

Mechanisms of selective cancer targeting exploiting distinct hallmarks of cancer cells

Der Naturwissenschaftlichen Fakultät
der Friedrich-Alexander-Universität Erlangen-Nürnberg
zur Erlangung des Doktorgrades Dr. rer. Nat.

Vorgelegt von

Insa Klemt

aus Ravensburg

Mechanisms of selective cancer targeting exploiting distinct hallmarks of cancer cells

Als Dissertation genehmigt von der Naturwissenschaftlichen Fakultät der
Friedrich-Alexander-Universität Erlangen-Nürnberg

Tag der mündlichen Prüfung:

08.12.2023

Gutachter/in:

Prof. Dr. Andriy Mohkir
Prof. Dr. Susanne Mühlich
Prof. Dr. Felix Zelder

Inhalt

Abstract	4
Zusammenfassung	6
1. Introduction	8
1.1 Cancer and its characteristics	8
1.2 The role of reactive oxygen species in normal and cancer cells	9
1.3 Cancer Treatment	13
2. Context and summary of the publications	17
2.1 Metal-based anti-cancer agents	17
2.2 3D binders of unfolded proteins inducing cancer cell-specific ER stress	19
2.3 Selective targeting of cancerous mitochondria via radical thiol-yne coupling.....	24
2.4 Prodrug concept.....	28
2.5 ROS-activatable siRNA prodrugs.....	29
2.6 Red light-triggered siRNA prodrugs.....	33
2.7 Aminoferrocene prodrugs.....	35
2.8 An aminoferrocene prodrug sequentially activated by ROS and OH ⁻	37
3. Publications and contributions of the author	43
Publication 1: 3D-shaped binders of unfolded proteins inducing cancer cell specific endoplasmic reticulum stress <i>in vitro</i> and <i>in vivo</i>	43
Publication 2: Synthesis and spectral characterization of the first fluorescein-tagged iron(II) clathrochelates, their supramolecular interactions with globular proteins, and cellular uptake.....	56
Publication 3: Cyanine- and Rhodamine-Derived Alkynes for the Selective Targeting of Cancerous Mitochondria via Radical Thiol-Yne Coupling in Live Cells	72
Publication 4: Reactive oxygen species-responsive RNA interference	85
Publication 5: Triggering RNA interference by photoreduction under red light irradiation	90
Publication 6: An Endoplasmic Reticulum Specific Pro-amplifier of Reactive Oxygen Species in Cancer Cells.....	102
Publication 7: A prodrug activated by H ₂ O ₂ and mitochondrial hydroxide: an improvement of cancer cells <i>versus</i> neutrophils selectivity	108
4. References	125

Abstract

Approximately 10 million people die of cancer every year. The genetic heterogeneity exhibited by different cancers on the one hand, and the physiological similarities between cancer and normal cells on the other hand pose challenges in the development of treatment options. Most chemotherapeutics available on the market exploit the fact that cancer cells typically rely on functional mitosis to a greater extent than normal cells. In that way, however, non-cancerous fast-dividing cells such as the precursor cells of leukocytes are also affected, leading to severe, dose-limiting side effects and impairment in the chemotherapy outcome. Hence, there is a demand for more selective chemotherapeutics, that effectively kill cancer cells while sparing all normal cells.

In the first part of this work, two different hallmarks of cancers are exploited as starting points for selective anti-cancer treatment. As the first hallmark, the fact that most cancer cells show a higher level of endoplasmic reticulum stress and higher amounts of un-/ misfolded proteins is leveraged. In particular, we demonstrated that a rigid, three-dimensional iron(II) clathrochelate binds unfolded proteins, causing their aggregation, increasing the endoplasmic reticulum stress levels selectively in cancer cells to the extent that apoptosis is induced. In an *in vivo* model, the clathrochelate not only cured a subgroup of cancer-bearing mice but in a different model also decreased the volume and number of metastases, while no side effects were detected. The work for this project is presented in Publication 1 and 2. The second project exploits increased levels of reactive oxygen species in cancerous mitochondria, which also increase the concentration of proteinogenic or small molecular thiyl radicals. Structure-guided mitochondrial accumulation combined with alkyne functionalization of small molecules thus enables radical thiol-yne coupling selectively in cancer cells. In Publication 3, the occurrence of this mechanism in cancerous mitochondria as well as the suitability of this approach for selective cancer targeting is presented for the first time.

In the second part of this work, we applied the prodrug concept to develop selective anti-cancer agents. Prodrugs that are designed to increase the selectivity of a parent drug are chemically modified to yield a pharmacologically inactive prodrug, which gets activated selectively at the tumor site/in the cancer cell or upon an external trigger. Reactive oxygen species-activatable small molecular prodrugs with an aryl boronic

acid as a promoiety have been reported previously. This prodrug approach was thus far, however, not transferable for oligonucleotide-based drugs such as siRNAs. We first reported on a siRNA prodrug with a 5' aryl boronic acid promoiety that gets selectively activated in the presence of high amounts of reactive oxygen species in Publication 4. In Publication 5, another siRNA prodrug is presented, that gets activated upon red light irradiation in the presence of the photosensitizer Sn(IV)(pyropheophorbide a)dichloride. In contrast to previously published red light activatable siRNA prodrugs, the activation is mediated by electrons and not cytotoxic $^1\text{O}_2$, with the latter inducing undesired side effects.

The cholic-acid-modified N-alkyl-aminoferrocene prodrug, presented in Publication 6, undergoes activation in response to high levels of reactive oxygen species in the endoplasmic reticulum, thereby exhibiting selectivity towards cancer cells. The activation of this prodrug leads to a further increase in oxidative stress, ultimately resulting in the induction of cancer cell death.

Since few normal cells such as primed neutrophils also show high levels of reactive oxygen species, a prodrug concept with a dual triggering mechanism for the activation of anticancer drugs is proposed in Publication 7. The promoiety is designed to be activated first by high levels of reactive oxygen species and secondarily by the basic pH present in mitochondria. Consequently, in (primed) neutrophils, which possess a very limited number of mitochondria, the prodrug remains incompletely activated. We implemented this prodrug concept using an exemplifying mitosis inhibitor camptothecin. Alongside the inherent cancer selectivity by targeting rapidly dividing cells, the prodrug concept enhances this selectivity by specifically targeting fast-dividing cells with elevated levels of reactive oxygen species and a high number of mitochondria. We validated the prodrug's activation mechanism and anti-cancer activity *in vitro*, as well as its efficacy and selectivity *in vivo*.

Altogether, in this thesis, several strategies for selective cancer targeting by small molecules are presented. These approaches exploit distinct hallmarks of cancer cells beyond their reliance on functional mitosis either as starting points of therapy or to selectively activate a prodrug within the cancerous environment.

Zusammenfassung

Etwa 10 Millionen Menschen sterben jedes Jahr an Krebs. Die genetische Individualität jeder Krebserkrankung und die physiologischen Ähnlichkeiten zwischen Krebs- und normalen Zellen stellen Herausforderungen bei der Entwicklung von Behandlungsmöglichkeiten dar. Die meisten auf dem Markt erhältlichen Chemotherapeutika basieren darauf, dass Krebszellen in der Regel stärker auf eine funktionierende Mitose angewiesen sind als normale Zellen. Auf diese Weise werden jedoch auch nicht-krebsartige, sich schnell teilende Zellen wie Vorläuferzellen der Leukozyten beeinträchtigt. Dies führt zu teils schwerwiegenden Nebenwirkungen, die die Medikamentendosis limitieren und somit das Ergebnis der Chemotherapie negativ beeinflussen können. Es besteht daher ein großer Bedarf an selektiveren Chemotherapeutika, die Krebszellen abtöten und gleichzeitig alle normalen Zellen verschonen.

Im ersten Teil dieser Doktorarbeit werden zwei unterschiedliche Charakteristika von Krebszellen als Ansatzpunkte für eine selektive Krebsbehandlung genutzt. Die Tatsache, dass Krebszellen generell ein höheres Maß an Stress im Endoplasmatischen Retikulum und eine größere Menge an un- bzw. fehlgefalteten Proteinen aufweisen, wird im ersten Projekt zu Nutze gemacht, was in Publication 1 und 2 veröffentlicht ist. Hier wird gezeigt, dass ein sterisch anspruchsvolles Eisen(II)-Clathrochelate ungefaltete Proteine bindet, diese aggregiert und dadurch den Stress des Endoplasmatischen Retikulums in den Krebszellen soweit erhöht, dass diese absterben. In zwei unterschiedlichen Mausmodellen wird zudem gezeigt, dass das Clathrochelate einige Mäuse, die an Krebs erkrankt sind, heilt und die Anzahl und Größe der Metastasen verringert. Im zweiten Projekt wird die erhöhte Konzentration radikaler Sauerstoffspezies in kanzerogenen Mitochondrien ausgenutzt. Diese erhöht auch die Anzahl an Thiyl-Radikalen in Proteinen und anderen Thiol-haltigen Biomolekülen. Die strukturbasierte Anreicherung von Alkin-funktionalisierten Verbindungen in Mitochondrien sollte daher radikalische Thiol-Alkin Reaktionen in Krebszellen ermöglichen. In Publication 3 wird gezeigt, dass diese Reaktion tatsächlich stattfindet und genutzt werden kann, um Krebszellen selektiv zu adressieren.

Im zweiten Teil dieser Doktorarbeit wird das Prodrug-Konzept angewandt, um selektive Antikrebsmittel zu entwickeln. Prodrugs, die darauf abzielen, die Selektivität

eines Ausgangswirkstoffs zu erhöhen, werden chemisch modifiziert, um pharmakologisch inaktive Prodrugs zu erzeugen. Im Milieu von Krebszellen oder durch einen externen Impuls werden diese Prodrugs gezielt aktiviert. Einige Verbindungen mit einer Phenylboronsäure-Schutzgruppe, welche selektiv durch reaktiven Sauerstoffspezies abgespalten wird, sind literaturbekannt. Dieses Konzept konnte allerdings bisher nicht auf Oligonukleotid-basierte Wirkstoffe wie siRNAs übertragen werden. Wie in Publication 4 dargestellt, wurde hier erstmals ein siRNA Prodrug mit einer Phenylboronsäure am 5' Ende des Leitstrangs hergestellt. In Publication 5 wird zudem ein anderes siRNA Prodrug präsentiert, welches durch die Bestrahlung mit rotem Licht in der Gegenwart von Sn(IV)(pyropheophorbide a)dichlorid als Photosensibilisator aktiviert wird. Im Gegensatz zu anderen Rotlicht-aktivierbaren siRNA Prodrugs wird die Abspaltung der Schutzgruppe durch Elektronenübertragung ausgelöst und es entsteht dabei kein toxisches $^1\text{O}_2$, welches unerwünschte Nebenwirkungen auslöst. Das in Publication 6 dargestellte Kohlsäure-Aminoferrocen Prodrug reichert sich im Endoplasmatischen Retikulum an, wo es durch die erhöhte Konzentration an reaktiven Sauerstoffspezies selektiv in Krebszellen aktiviert wird, was den oxidativen Stress weiter erhöht und die Krebszellen abtötet.

Da einige normale Zellen wie aktivierte Neutrophile ebenfalls hohe Mengen an reaktiven Sauerstoffspezies aufweisen, wird in Publication 7 ein Prodrug-Konzept mit einem dualen Aktivierungsmechanismus untersucht. Die hier eingeführte Schutzgruppe wird zuerst durch reaktive Sauerstoffspezies und anschließend durch das basische Milieu in Mitochondrien abgespalten. Folglich wird das Prodrug in Neutrophilen, die über eine sehr geringe Anzahl an Mitochondrien verfügen, nicht vollständig aktiviert. Das Konzept wurde auf den Mitoseinhibitor Camptothecin übertragen. Das daraus resultierende Prodrug weist eine dreifache Krebsselektivität auf, da es schnell proliferierende Zellen, mit erhöhtem oxidativem Stress und einer hohen Anzahl an Mitochondrien adressiert. Der Aktivierungsmechanismus und die Wirksamkeit wurden *in vitro* bewiesen und die Antikrebs-Aktivität und Selektivität *in vivo* aufgezeigt.

In dieser Doktorarbeit werden somit mehrere Strategien zur selektiven Krebszellenadressierung präsentiert. Die dargestellten Konzepte nutzen verschiedene Charakteristika von Krebszellen entweder als Ansatzpunkte für die Behandlung oder zur Aktivierung von Prodrugs aus.

1. Introduction

1.1 Cancer and its characteristics

Cancer constitutes the number one cause of premature death in Germany and 56 other well-developed countries worldwide (Figure 1). In fact, 19.3 million new cancer cases and almost 10.0 million cancer deaths have been reported to the world health organization in 2020. Even though the global cancer death rate has dropped by 32 % since 1991, sparing 3.5 million lives, the cancer burden is expected to rise in the future, with a predicted 28.4 million new cancer cases in 2040, mostly due to demographical changes^[1]. The most frequently diagnosed cancer in 2020 was female breast cancer (11.7 %) followed by lung cancer (11.4 %) and colorectal cancer (10.0 %). Lung cancer constitutes the most lethal cancer with a 5-year survival rate of e.g. non-small cell lung cancer of 28 % and small cell lung cancer of only 7 %. The main reason for the poor prognosis of cancer patients lies in the complexity of the disease as the average number of mutations in e.g. sporadic colorectal tumor cells has been estimated to be approximately 11,000 excluding epigenetic abnormalities^[2]. The individuality of the mutation pattern of every tumor constitutes a challenge in finding a suitable starting point for therapy to selectively kill cancer cells without harming normal cells.

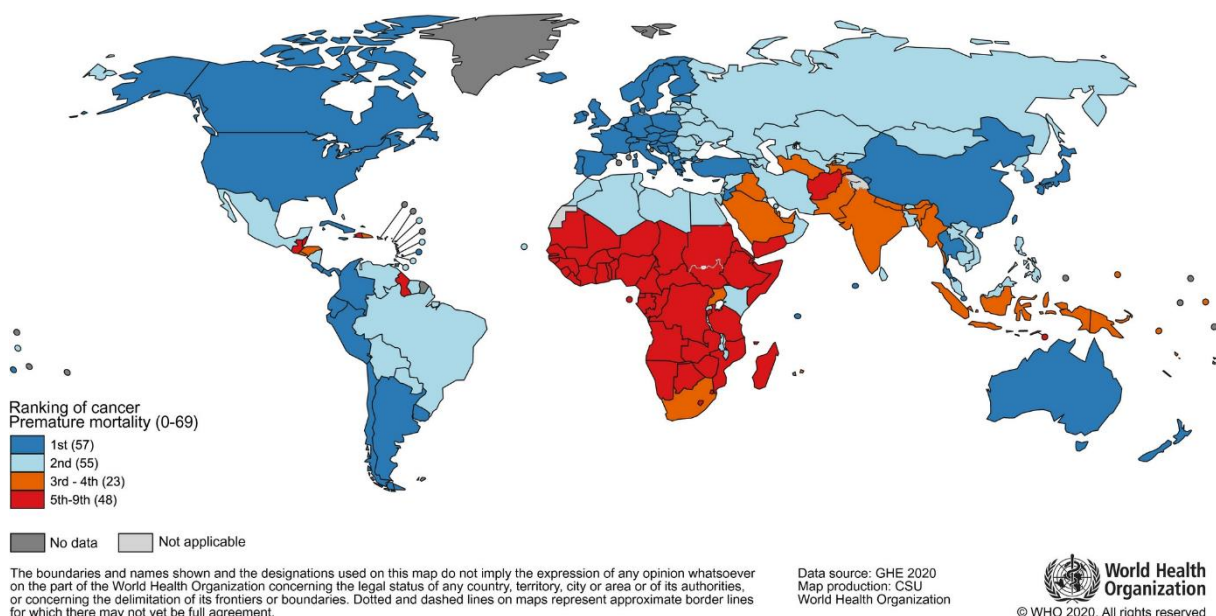


Figure 1: Global ranking of cancer as the cause of premature (<70 years) death in 2019^[1]. In countries colored dark and light blue, cancer constitutes the number one and two causes of premature death, respectively. In countries indicated in orange and red cancer ranks lower in premature mortality. This demonstrates the need for improved cancer treatments.

Despite the genetic heterogeneity, some common hallmarks are found in most cancers that could serve as differentiating factors in chemotherapy. First and foremost, cancer cells proliferate abnormally fast and unlimitedly, resisting antigrowth signals of the surrounding tissue^[3]. Fast tumor growth is further accelerated by the fact that cancer cells circumvent apoptosis and by their ability to invade surrounding tissues. In addition, metastasis formation by shedding clustered circulating tumor cells is also common, especially in hypoxic, solid tumors^[4]. To enable fast cell growth, most cancers show increased glycolysis rates and extensive blood vessel formation, called angiogenesis^[5]. Due to the fast metabolism, cancer cells show elevated stress levels especially in the endoplasmic reticulum (ER) because of the accelerated protein expression, in the mitochondria (Mit) as a result of the high energy demand, and in the lysosomes (LY), which play a crucial role in cell homeostasis and cancer progression. Also, in the cytosol, the levels of reactive oxygen species (ROS) in cancer cells are increased by up to 5,000-fold compared to normal cells, resulting in oxidative stress^[6].

1.2 The role of reactive oxygen species in normal and cancer cells

ROS are generally defined as oxygen-derived small molecules with short half-lives^[7]. Due to their high reactivity towards biological macromolecules, the generation, and decomposition of ROS are tightly regulated in cells. An overview is shown in Figure 2. A basal level of ROS (i.e. superoxide, $O_2^{\cdot-}$) is constantly produced in the mitochondria by electron leaks from complex I (NADH dehydrogenase) and III (CoQ-Cyt C reductase) of the electron transport chain^[8]. In addition, superoxide is generated upon stimuli by NADPH oxidases (NOX), xanthin oxidases (XO), and cytochrome P450 (CYPs). If nitric oxide (NO^{\cdot}) is present in close proximity to $O_2^{\cdot-}$, highly reactive peroxynitrite ($ONOO^{\cdot-}$) is formed. Superoxide can dismutate spontaneously or in an accelerated-manner by superoxide dismutases (SOD) to O_2 and H_2O_2 ^[9]. H_2O_2 is the chemically most stable of all ROS and can diffuse freely across membranes or is actively transported via aquaporins and can thus function as a signaling molecule. In neutrophils, myeloperoxidase (MPO) uses H_2O_2 to generate hypochlorous acid (HOCl). In the presence of metal ions such as iron or copper, hydroxyl radicals (OH^{\cdot}) are rapidly formed from H_2O_2 via *Fenton* reaction. As hydroxyl radicals are very reactive towards biological macromolecules and thus harmful, H_2O_2 is therefore degraded by several proteins of the antioxidant response such as peroxiredoxins and glutathione

peroxidases. In addition, in peroxisomes, H_2O_2 is decomposed in a dismutation reaction to oxygen and water. This reaction is catalyzed by catalase, one of the most efficient enzymes with an extremely high turnover number, underlining the importance of controlled ROS levels^[10]. Also, non-enzymatic antioxidants such as ascorbic acid, tocopherols, glutathione (GSH), and carotenoids play an important role in ROS homeostasis.

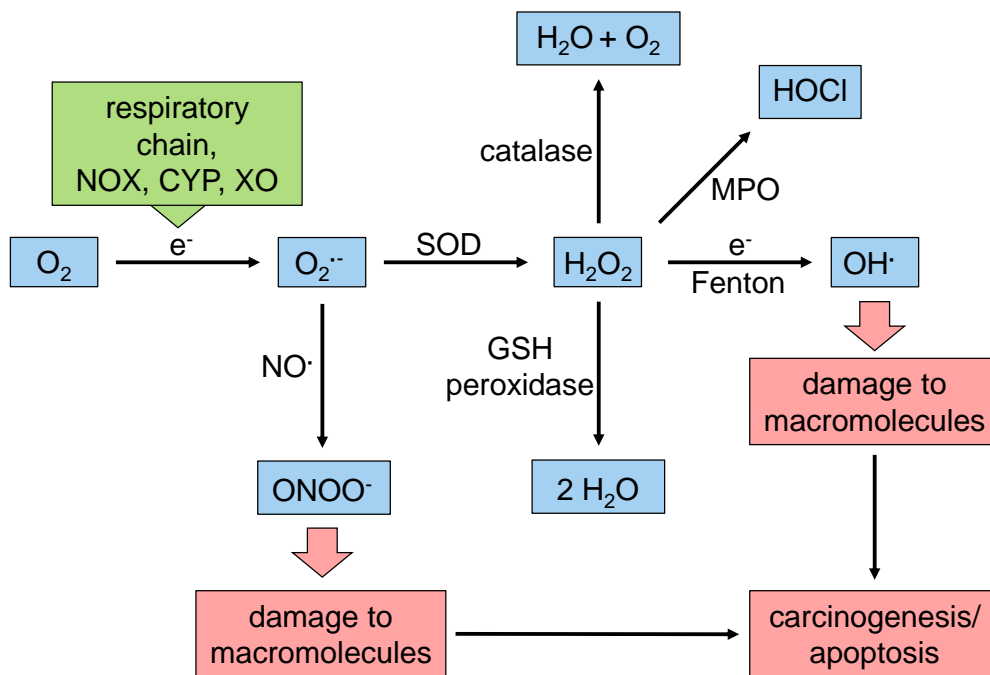


Figure 2: Overview of the generation, transition, and decomposition of different ROS in cells and the hazard that they pose. Superoxide ($\text{O}_2^{\cdot-}$) is generated by electron (e^-) transfer onto oxygen by NADPH oxidase (NOX), cytochrome P450 (CYP), xanthine oxidase (XO), or by e^- leakage from the respiratory chain. Reaction with nitric oxide (NO^{\cdot}) yields peroxynitrite (ONOO^-). $\text{O}_2^{\cdot-}$ spontaneously dismutates to hydrogen peroxide (H_2O_2) and oxygen (O_2). The reaction is additionally catalyzed by the superoxide dismutase (SOD). The resulting H_2O_2 is degraded by catalase, glutathione (GSH), or peroxidases. The myeloperoxidase (MPO) can convert H_2O_2 into hypochlorous acid (HOCl). Alternatively, in the presence of metal ions such as iron(II) or copper(I), hydroxide radicals (OH^{\cdot}) are generated via *Fenton* chemistry. ONOO^- and OH^{\cdot} are highly reactive towards macromolecules present in the cells, promoting carcinogenesis and toxicity which eventually leads to apoptosis induction.

As mentioned above, mitochondria play a major role in superoxide generation caused by electron leakage from complexes I and III of the respiratory chain. But also the ER has a great impact on ROS generation. The disulfide bond formations which are essential for proper protein folding are catalyzed by the enzyme protein disulfide isomerase (PDI) which is oxidized by oxidoreductase-1 (ERO1) which in turn is oxidized by molecular oxygen yielding H_2O_2 ^[11]. In addition, ER contains CYP family

enzymes responsible for steroid synthesis which can produce superoxide and H_2O_2 ^[12]. LYs also contain significant amounts of ROS, as H_2O_2 can freely diffuse into these organelles, where no ROS-degrading enzymes are present causing an accumulation of the small molecule^[13]. In addition, loosely bound iron ions found in LYs can catalyze the formation of hydroxyl radicals via *Fenton* reaction^[14]. In contrast, peroxisomes are the major site of ROS degradation mainly via high catalase activity^[15].

Despite these many antioxidant mechanisms, an imbalance towards higher ROS levels can occur, which is referred to as oxidative stress^[7]. High and prolonged oxidative stress levels are critical conditions as the oxidative damage in the cells is increasing. One common damage inflicted by ROS are DNA strand breaks, as the 4' hydrogen of the ribose is abstracted by hydroxyl radicals, resulting in the formation of a carbon-centered radical and subsequently the decomposition of the ribose (Figure 3)^[16]. Nucleobases, in particular the C₈-position of guanine, are prone to be attacked by hydroxyl radicals as well, resulting in either ring-opening degradation products or further oxidation to 8-hydroxyguanine. The latter is a commonly studied marker for oxidative stress. Also, thymidine is sensitive to oxidation by hydroxyl radicals at its C₅-position, since the resulting carbon radical is resonance-stabilized^[17]. Many more ROS-induced molecular modifications of nucleobases have been reported, all resulting in DNA replication failure, mutations, cell death, and hereditary diseases^[18].

Also, lipids are prone to oxidative damage, especially when they are unsaturated. The resulting alkyl radical can then further react with oxygen, resulting in a peroxide radical, which can further abstract one hydrogen, initiating a chain reaction called lipid peroxidation (Figure 3). As peroxidation drastically alters the lipophilicity of the fatty acid, the membrane integrity as well as its fluidity and the cellular structure can be impaired^[19]. Commonly observed by-products of lipid peroxidation include malondialdehyde and 4-hydroxynonenal which are, in turn, highly reactive towards amine groups of e.g. nucleobases and proteins^[20].

Proteins can also be directly affected by ROS as peptide bonds can be cleaved by a similar peroxidation reaction as observed for lipids. More commonly, amino acid side chains are oxidized. Peroxynitrite can, for example, nitrate tyrosine or tryptophan, which is believed to be irreversible in cells^[21]. Also, the oxidation of cysteine residues to disulfides, but also to sulfenic, sulfinic, and sulfonic acid is observed upon oxidative stress^[22]. Such side chain modifications can affect the protein structure and thus their

activity. In fact, the reversible oxidation of thiols to disulfides plays an important role in the regulation of protein activity. In that way, oxidative stress has a great, potentially hazardous, impact on cell homeostasis, as thousands of proteins were shown to be reversibly oxidized by ROS under oxidative stress conditions^[23]. At the same time, cells also use this mechanism for the adaptation to higher ROS levels. For example, if the redox-sensing protein keap1 cannot be kept in its reduced form (with free thiols) due to the lack of antioxidants/excess of ROS, the keap1-bound transcription factor Nrf2 is released and migrates into the nucleus to induce the expression of more proteins of the antioxidant response^[24]. In case, the antioxidant response gets overwhelmed, especially upon prolonged oxidative stress, apoptosis is induced in the cell^[7].

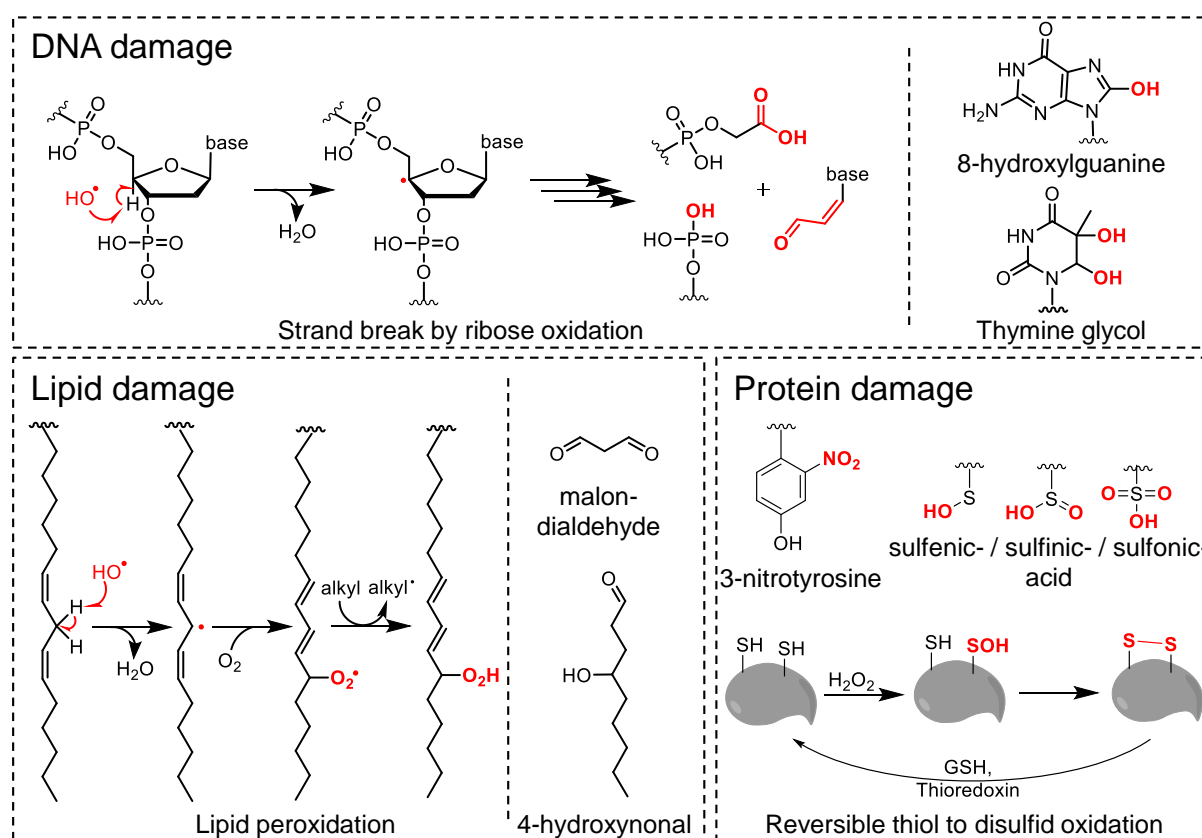


Figure 3: Overview of oxidative damage, commonly observed in stressed cells.

Despite their harmfulness, ROS are important signaling molecules, particularly H_2O_2 . As indicated above, it regulates the activity of proteins such as phosphatases and kinases by cysteine oxidation which in turn (in)activate other proteins. In fact, H_2O_2 was shown to be an essential second messenger for several cytokines and growth factors, promoting proliferation and cell migration^[25]. Also, superoxide was shown to mediate cell cycle progression via Ras induction^[26].

In cancer cells, ROS play a special role, as the pro-proliferative effects, as well as the higher mutation rates induced by ROS via DNA damage, are promoting cancer progression. Hence, compared to normal cells higher ROS levels are found in most cancer cells (see above). Especially in mitochondria, ROS production is increased in cancer cells, as the metabolism is accelerated and the respiratory chain overstrained. In most solid tumors, where the oxygen supply is low (hypoxia), the respiratory chain is even more exhausted, slowing down electron transfer, and increasing the probability of electron leakage^[27]. Also in cancerous ER, more ROS is produced due to the higher metabolism and protein expression rates. Consequently, many proteins that are involved in ROS generation are oncogenes. One well-studied example is RAC1, which upon activation stimulates NOX1 to produce superoxide. RAC1B, a constitutively activated RAC1 mutant is associated with lung cancer and melanoma^[28]. All these facts combined make the elevated ROS levels found in cancer cells (and in particular in the mitochondria and the ER) a good starting point for selective therapy.

1.3 Cancer Treatment

Currently, there are four major branches of cancer treatment, namely surgery, radiotherapy, immunotherapy, and chemotherapy, that can be applied individually or in combination. An overview of their (dis)advantages is shown in Figure 4. Surgical removal is the method of choice for solid, mostly isolated tumors. Ideally, the cancer can thus be fully eliminated. Early diagnosis is of high importance to pre-empt metastase formation and deep tissue penetration. As surrounding healthy tissue has to be removed to some extent as well, the aftereffects have to be carefully considered especially when the tumor is located in an important tissue or organ such as the brain. This method is often combined with either radiotherapy and/or chemotherapy, and lymph nodes are additionally removed to guarantee full cancer cell removal to avoid cancer relapse.

Radiotherapy can treat approximately 30-50 % of all cancer cases as the tumor has to be solid and accessible for radiation and different tumors vary in their radiosensitivity^[29]. Ionization radiation such as x-rays is aimed at the tumor to induce DNA damage and thus cell death. The energy absorption at the tumor site has to be maximized while the irradiation intensity in the surrounding tissue has to be minimized to avoid tissue damage and possible new tumorigenesis. Therefore, multiple beams of

radiation are usually applied, intersecting at the tumor site. For interior tumors, the side effects of x-rays are high as the delivered energy is reduced over the penetration distance. Here proton therapy is superior, as the irradiation energy is mostly released over the last few millimeters of the particle's range^[30]. In some cases also internal radiation (brachytherapy) is applied where a short-range-radiation source is applied at the tumor site^[31]. As large tumors are in general less sensitive to radiotherapy this method is oftentimes combined with surgical resection or chemotherapy.

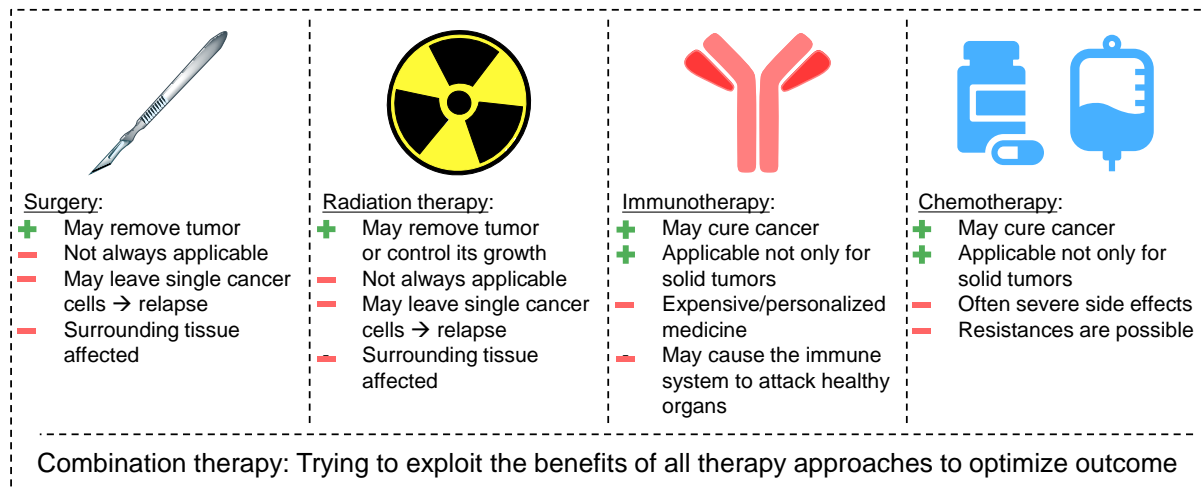


Figure 4: Advantages (+) and disadvantages (-) of the common cancer treatment methods.

An evolving field of cancer treatment is immunotherapy in which the patient's immune system is supported or even re-programmed to fight cancer. This can be achieved in multiple ways. First of all, cytokines or checkpoint inhibitors can be applied to counteract the immunosuppressive signals generated by the cancer cells and to boost a patient's immune system^[32]. Secondly, (monoclonal) antibodies that target mutated proteins on the cancer cell's surface can be applied to point out malignant cells to the immune cells^[33]. Thirdly, CAR T-cell therapy can be applied, which was first approved by the FDA in 2017^[34]. In 2018, the discoverers of this treatment concept, James P. Allison and Tasuku Honjo, were awarded the Nobel Prize in Physiology or Medicine^[35]. In this approach, T-cells are isolated from the cancer patient or a healthy donor and genetically engineered to express a specific chimeric antigen receptor (CAR) with affinity to a cancer cell's antigen that is not found in normal cells. After re-injection into the patient's blood, the T-cells then destroy the malignant cells selectively. To further enhance CAR T-cell therapy, combination therapy with chemotherapeutics that improve the susceptibility of the cancer cells is being developed.

Chemotherapy is defined as the application of anti-neoplastic drugs. Despite the above-mentioned characteristics that distinguish cancer cells from normal cells, it is difficult to selectively target cancer cells resulting in dose-limiting side effects of chemotherapeutics. Most chemotherapeutics are targeted against rapidly-dividing cells via four different mechanisms of which an overview is shown in Figure 5.

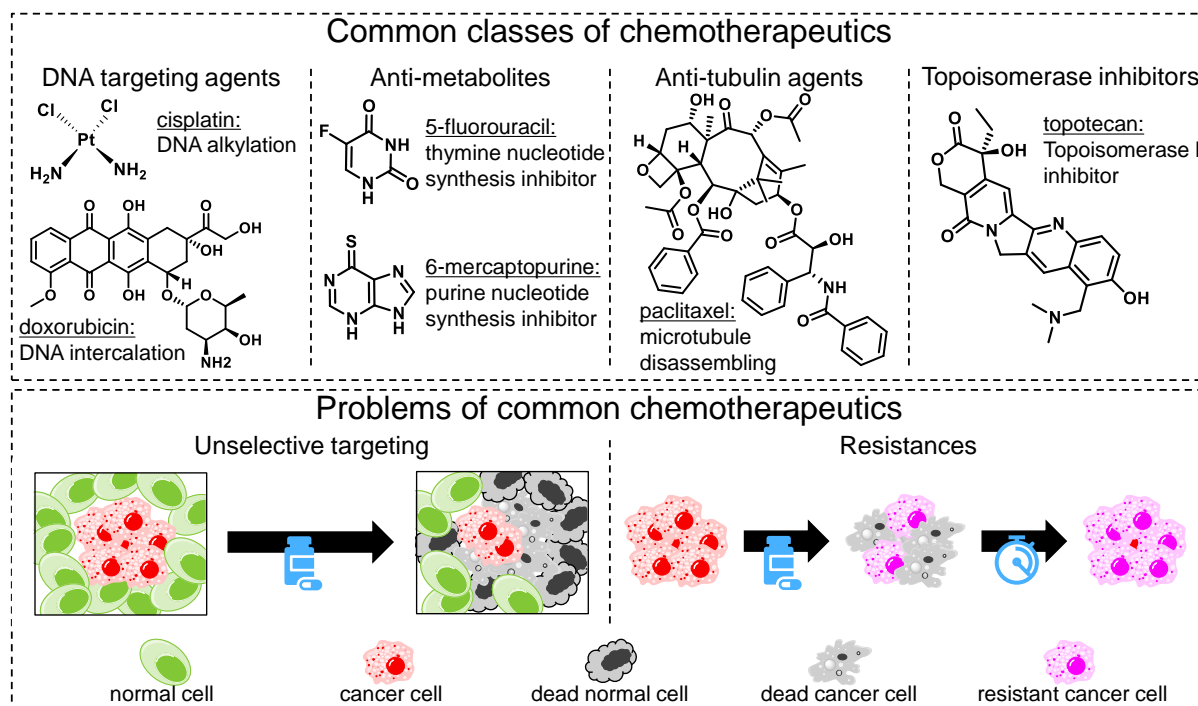


Figure 5: Overview of common classes of chemotherapeutics and prominent representatives of these groups and the general drawbacks of chemotherapy.

The first group of chemotherapeutics consists of DNA targeting agents including DNA alkylating agents such as dacarbazine, DNA cross-linking agents such as cisplatin, intercalating agents such as doxorubicin, and DNA cleaving agents such as bleomycin^[36]. All DNA targeting agents rely on interference with DNA replication and thus target primarily fast-dividing cells such as cancer cells. The second group of chemotherapeutics consists of anti-metabolites which impeded DNA and RNA synthesis. The most prominent example is 5-fluorouracil which inhibits thymidine monophosphate (TMP) synthesis, an essential building block for DNA synthesis^[37]. As rapidly-dividing cells rely on DNA synthesis to a larger extent than slow-dividing cells, this mechanism is again targeted towards fast-proliferating cells. The third class of chemotherapeutics consists of anti-tubulin agents such as paclitaxel (Taxol) which are interfering with the microtubule assembly/disassembly^[38]. As this part of the cytoskeleton is crucial for cell division, again rapidly dividing cells are affected the most. The last class of

chemotherapeutics consists of topoisomerase inhibitors such as camptothecin and its derivatives such as topotecan^[39]. During DNA replication, topoisomerase I is required for the release of tension of the DNA while it is unwound to make it accessible for polymerases, while topoisomerase II is responsible for DNA uncoiling. Inhibition of either topoisomerase results in failed replication, DNA strand breaks, and eventually induces apoptosis primarily in fast-dividing cells.

However, not only cancer cells but also cells of the bone marrow, the digestive tract, and hair follicles proliferate rapidly and are thus affected by chemotherapeutics (Figure 5, bottom left). Hence, side effects such as myelosuppression (reduced amount of blood cells leading to immunosuppression), peripheral neuropathy, alopecia (hair loss), nausea, and other gastrointestinal effects are very common amongst chemotherapeutics. In particular, due to the impaired immune system cancer patients often suffer from severe, or even lethal, infections that delay chemotherapy or require dose reduction which might jeopardize the treatment outcome^[40]. In addition to side effects, drug resistances can compromise treatment outcomes (Figure 5, bottom right). As cancer cells mutate frequently, it is probable that few cancer cells within a tumor are already resistant (intrinsic resistance) or can adapt to the chemotherapeutic agent (acquired resistance). While other cancer cells are effectively killed by the treatment, these few cells survive and constitute the seed of tumor relapse with mostly resistant cells. During the second treatment time, a higher chemotherapeutic dosage or a different drug is required to overcome the resistance^[41].

All these facts lead to the comprehension that further research is necessary to improve cancer therapy, particularly in terms of improving the selectivity of chemotherapeutics. The aim of this thesis was, therefore, to investigate novel anticancer agents with mechanisms of action different from the inhibition of mitosis, in order to exploit alternative, or even multiple, hallmarks of cancer cells to enhance cancer specificity. By employing this strategy, I explored several new approaches to chemotherapy and their corresponding (pro-)drugs, assessing their potency and suitability for selective cancer cell targeting. This marks an important first step towards the development of chemotherapeutics with a higher therapeutic index, improved treatment outcomes, and reduced side effects.

2. Context and summary of the publications

2.1 Metal-based anti-cancer agents

The discovery of the anti-cancer activity of cisplatin in the 1960s by Barnett Rosenberg represents a milestone in the development of chemotherapeutics^[42]. At the same time, it added coordinating compounds to the focus of attention of cancer research. Even though the field is still dominated by purely organic compounds, more and more metal-based substances are evolving, as they come with some major advantages and unique properties. First of all, metal complexes often possess the ability to bind biomolecules via the formation of coordinative bonds. As in the case of cis-platin, this can lead to ligand exchange reactions resulting in the cross-linkage of DNA bases and thus induction of apoptosis^[43]. Secondly, metal ions possess high electrophilicity due to a low-energy LUMO and thus Lewis acid properties. Most metal ions can, therefore, accept an electron pair from a Lewis base and thus polarize groups (e.g. peptide bonds) increasing their reactivity and facilitating certain reactions that would otherwise not be possible in cells, such as in hydrolysis in the active site of metalloproteinases^[44]. Thirdly, metal ions exhibit specific electronic properties, which can result in redox activity under physiological conditions. The application of redox-active substances, such as amino ferrocenes, initiates the generation of reactive oxygen species (ROS) finally leading to apoptosis in cancer cells (see chapter 2.7)^[45]. Some metal compounds, e.g. iron oxide, also show magnetic properties, which can be exploited in hyperthermia approaches^[46].

Another major advantage of metal-based compounds is their structural variability and complexity. For example, in octahedral metal complexes, the possibility of variation of six coordinating groups allows highly efficient probing of the structural space. In contrast, in purely organic compounds the maximal number of substituents around a single atom (e.g. sp^3 -carbon centers) is four. In that way, a metal backbone gives rise to a wide range of coordination geometries and unique shapes. At the same time, it facilitates the finetuning of the compound's activity and pharmacokinetic properties. This allows the synthesis of bulky, ball-shaped compounds which allows for different mechanisms of action, unique anti-cancer properties, and superior selectivity profiles.

This was already proven by Feng et al., who specifically exploit the superiority of metal-based complexes to form octahedral complexes with a sophisticated, preorganized structure^[47]. They complexed staurosporine, a two-dimensional, unselective kinase

inhibitor, to a ruthenium (II) backbone and screened the remaining four residues to achieve favorable interaction patterns with the binding pocket of certain kinases (Figure 6). In that way, Feng et al. inter alia developed selective inhibitors for PIM1, GSK3 α , and PAK1, which are all known to be potential targets for chemotherapy. So far, no organic compound was synthesized that inhibits either of these kinases selectively, as the binding pockets within the family of kinases resemble each other closely, demonstrating the advantage of exploiting the structural space by spherical coordinating compounds.

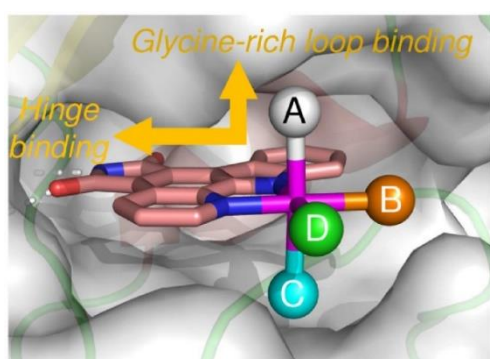


Figure 6: Probing the structural space to achieve selective kinase inhibitors. Staurosporine was conjugated to a ruthenium (II) backbone. The remaining four residues (A, B, C, D) were screened to achieve selective binding to a specific kinase active site. In that way, several selective kinase inhibitors were developed. Figure from Feng et al.^[47].

Apart from octahedral complexes, sandwiched complexes, so-called metallocenes, allow for the probing of the structural space in three dimensions and the formation of unique interaction patterns with e.g. protein binding sites^[48]. They are additionally interesting because of their above-mentioned redox activity and will be discussed in detail in Chapter 2.7.

Clathrochelates are even more superior to other, more simple, octahedral complexes in terms of bulkiness, structural pre-organization, and the number of substituents, as this class of metal complex contains a cage-like dioxime-based ligand with 8 variable substituents. The chelating ligand is shielding the iron(II) center rendering it highly

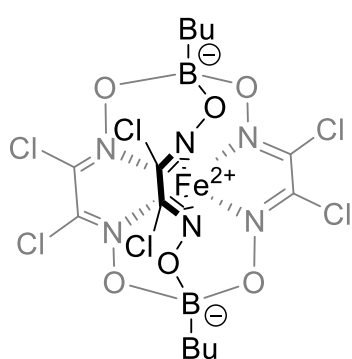


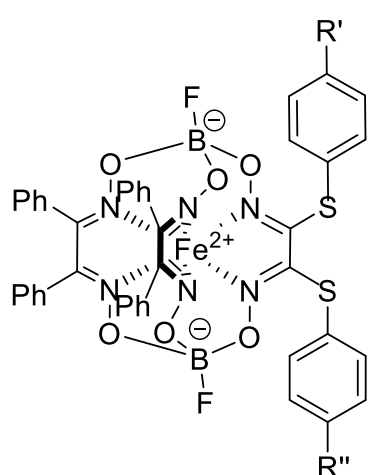
Figure 7: Structure of iron(II) clathrochelate^[49]

(redox) stable. One clathrochelate's anti-cancer activity has already been studied. Its structure is shown in Figure 7. This compound acts as an alkylating agent, as the six chlorine atoms can be substituted by nucleophilic residues, e.g. N- and S- nucleophiles, as shown in *in vitro* studies^[49]. Since the antioxidant glutathione (GSH) is one of the most abundant nucleophiles in cells, the administration of the compound results in the alkylation of GSH leading to an increase in oxidative stress and thus apoptosis,

predominantly in cancer cells, which was confirmed in human promyelocytic leukemia cells ($IC_{50} = 6.5 \pm 4.6 \mu\text{M}$ in HL-60 cells)^[50].

2.2 3D binders of unfolded proteins inducing cancer cell-specific ER stress

Chemically stable clathrochelates show similarity to the carbon allotrope fullerene C_{60} in terms of size and bulkiness (diameter of $C_{60} = 0.7 \text{ nm}$ vs 0.9 nm for clathrochelates). From the literature, it is known that C_{60} binds unfolded proteins (UPs)^[51]. This property could be exploited for anti-cancer treatment. As the ER in cancer cells shows higher stress levels than the one in normal cells (see above), the interference with the protein folding should increase this stress further, leading to apoptosis predominantly in cancer cells. However, C_{60} shows poor water solubility ($\log S = -11.0$)^[52] and is therefore challenging for medicinal application. Because of their eight modifiable substituents, clathrochelates can, however, be easily finetuned regarding water solubility and uptake



- 1: $R'=R''= -\text{CO}_2\text{H}$;
 2: $R'= -\text{CO}_2\text{H}$; $R''= -\text{H}$;
 3: $R'=R''= -\text{H}$;

Figure 8: Structures of FeCs 1-3 of Publication 1.

and could thus serve as a superior binder of unfolded proteins. In addition, in contrast to C_{60} , clathrochelates do not show redox activity under physiological conditions, excluding direct generation of ROS or other toxic reactive species, which would increase the probability of unwanted side effects and systemic toxicity. We, therefore synthesized a series of chemically stable clathrochelates and studied the hit candidate (FeC 2) in detail *in vitro* and *in vivo*. The structures of the hit compound and its two close chemical analogues (FeC 1 and FeC 3) are shown in Figure 8. The results are published in Publication 1 and are summarized in the following.

After initial toxicity studies that showed the high potency of the clathrochelate FeC 2, its stability was proven. This is of high importance, as the degradation yielding free iron ions would result in unselective toxicity towards cancer and normal cells. For this, we incubated the clathrochelate for 48 h in aqueous solutions containing bioavailable nucleophiles (5 mM GSH at pH 5 or pH 7.4), or oxidants (10 mM H_2O_2), or different pH levels (between 5 and 13). Subsequent analysis by LCMS revealed that FeC 2 was stable under the tested conditions. In

addition, we confirmed the lack of iron release in these solutions by applying the chelating agent ferrozine, which forms a colorful complex upon Fe²⁺ binding. The absence of iron ion release was additionally proven by testing whether 24 h or 48 h incubated solutions of FeC **2** catalyze *Fenton* chemistry, which was not the case. To assess the stability in cells, we incubated the clathrochelate with cells for 1 h or 24 h and, re-extracted out of the cell lysate for LCMS analysis. Only after 24 h, we observed minor degradation towards a glutathione adduct, proving that the clathrochelate indeed acts as an inert three-dimensional complex.

Next, we studied the cellular uptake of FeC **2** and its two analogs FeC **1** and FeC **3**, by incubation of cancer cells (either ovarian carcinoma A2780 or Burkitt lymphoma BL2 cells) with the clathrochelates. After thorough washing, the boron and iron content in the cell pellets were quantified by atomic emission spectroscopy (AES). Out of the three clathrochelates, only FeC **2** is uptaken efficiently (Figure 9, A; data for FeC **3** not shown), indicating that exactly one carboxylic acid residue is important for the uptake. This also explains FeC **2**'s superior toxicity towards cancer cells. Incubation at different temperatures (Figure 9, A) and in the presence of active uptake inhibitors (Figure 9, B) revealed that FeC **2** is actively uptaken via a clathrin- and caveolin-mediated mechanism. This could benefit its selectivity, since cancer cells, in general, show a higher active uptake rate caused by their fast metabolism. Staining of different organelles with organelle-specific dyes (ER staining over time: Figure 9, C), isolation of organelles after FeC **2** treatment, imaging of organelles by transition electron microscopy, and modification of the alkyne containing analog FeC **5** (with similar activity to FeC **2**) with a fluorescent dye in cells revealed that FeC **2** is first uptaken into the ER of cancer cells and later into mitochondria. Both organelles get destroyed by the clathrochelate treatment. In contrast, lysosomes are not affected.

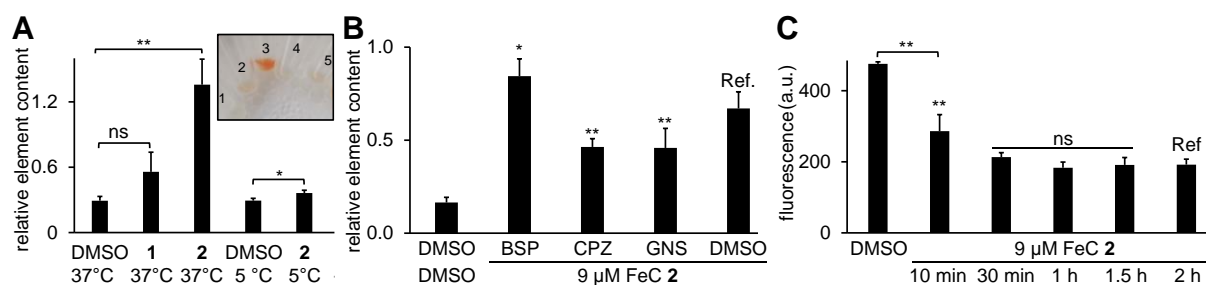


Figure 9: Uptake of FeCs **1** and **2** (9 μM, 4 h) in BL-2 cells at 37 °C or 5 °C by monitoring intracellular iron content (**A**). Uptake of FeC **2** (2 h, 9 μM) after pre-treated with the organic anion transporter inhibitor bromosulphthalein (bromo., 500 μM), with clathrin-mediated uptake inhibitor chlorpromazine (CPZ, 10 μg/mL) or with caveolin-mediated uptake inhibitor genistein

(400 μM) by monitoring intracellular iron amount (**B**). Effects of the time of FeC **2** (9 μM) incubation with A2780 cells on ER-specific staining of the cells. After treatment with FeC **2**, the ER-probe was added and the cells were incubated for an additional 20 min (**C**). For statistical analysis, an unpaired Student's t-test was performed *: $p < 0.05$; **: $p < 0.01$; ***: $p < 0.001$; ns ≥ 0.05 .

By studying FeC **1** and FeC **2** in cell-free settings, we indeed found that the clathrochelates bind unfolded proteins efficiently (Figure 10, A), as similarly described for the carbon allotrope C_{60} (see above). Moreover, FeC **2** accelerates the aggregation of insulin in the presence of denaturing agent dithiothreitol (DTT) as determined by dynamic light scattering (DLS) (Figure 10, B). The resulting aggregates also show striking size differences from DMSO-treated aggregates, which were visualized by atomic force microscopy (Figure 10, C-E).

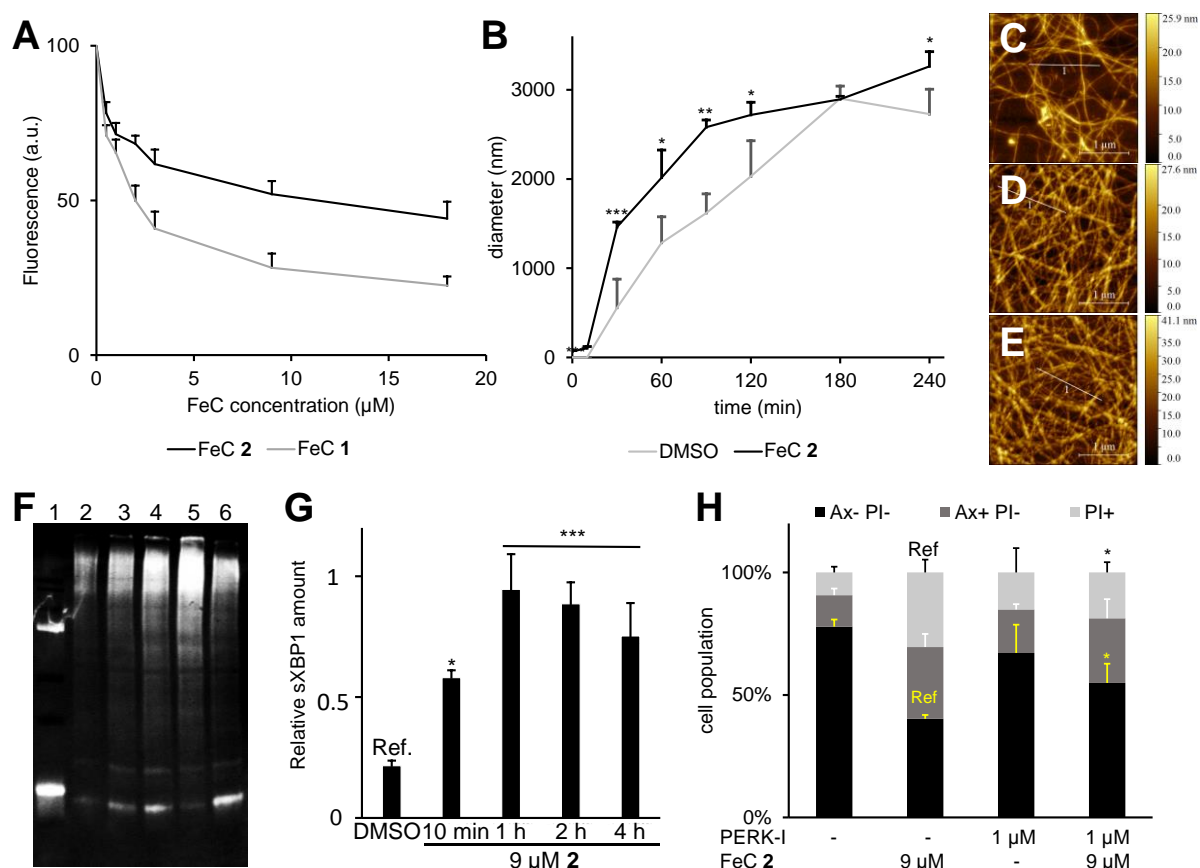


Figure 10: Dependence of fluorescence of thioflavin T (ThT, 10 μM , $\lambda_{\text{ex}} = 440 \text{ nm}$; $\lambda_{\text{em}} = 480 \pm 10 \text{ nm}$) from the concentration of FeC **2** in the presence of aggregated insulin (0.3 mg/mL, 3 h incubation, 20 mM DTT) (**A**). Kinetics of insulin (0.3 mg/mL) aggregation as monitored by DLS under conditions of (**A**), in the presence/absence of FeC **2** (9 μM) (**B**). AFM images of insulin samples after 4 h incubation at 65 $^{\circ}\text{C}$ and pH 2 in the absence (**C**) or presence of FeC **1** (9 μM) (**D**) or FeC **2** (9 μM) (**E**). Protein ubiquitination in A2780 lysates after treatment with DMSO (2); FeC **2** (9 μM , 30 min) (3); FeC **2** (9 μM , 4 h) (4); bortezomib (500 nM, 4 h) (5); control **1** (30 μM , 4 h) (6) as detected by western blotting using a α -ubiquitin mAB and an AlexaFluor488 secondary antibody (**F**), ER stress induction in A2780 cells after incubation for 10 min - 4 h with FeC **2** (9 μM) and subsequent determination of relative sXBP1 concentrations by qPCR (**G**), ER stress induction in A2780 cells after incubation for 10 min - 4 h with FeC **2** (9 μM) and subsequent determination of relative sXBP1 concentrations by qPCR (**H**).

(G). Rescuing effects of PERK-inhibitor (PERK-I) pre-treatment on the toxicity of FeC 2-treated A2780 cells. Annexin (Ax) and propidium iodide (PI) negative (Ax- PI-) cells are considered to be viable (H).

In cells, FeC 2 binds to previously formed protein aggregates, quenching the fluorescence of the protein aggregate-specific dye. Moreover, upon FeC 2 treatment, many proteins were ubiquitinated (Figure 10, F), indicating that misfolded or aggregated proteins accumulated. We additionally confirmed that the unfolded protein response (UPR) was activated already 10 min after FeC 2 treatment (Figure 10, G). In line with these findings, we observed that pre-treatment with a UPR inhibitor, the PERK-inhibitor GSK2606414, partially rescued the toxicity of the clathrochelate (Figure 10, H). These findings lead to the conclusion that FeC 2 acts as a binder of unfolded or partially folded proteins within the ER, most likely interfering with correct protein folding and causing aggregation of these proteins. In that way, the ER stress is induced and the unfolded protein response is activated, which fails to resolve the ER stress eventually leading the cell death. The mechanism of cell death was found to be apoptosis.

To get a more comprehensive understanding of the mechanism of action of FeC 2, we performed an unbiased, genome-wide RNAseq experiment that confirmed the activation of the unfolded protein response upon FeC 2 treatment and additionally revealed an impact on the cell cycle, the cytoskeleton, and the activation of the antioxidant response (Figure 11). We validated the RNAseq experiment by qPCR and investigated all pathways on a protein level. The activation of the antioxidant response was of high interest as the direct generation of ROS by the clathrochelate was already excluded (see above). And the oxidative damage (= carbonyl content) in cells treated with FeC 2 was even reduced. However, the clathrochelate is inducing mitochondrial ROS generation, which is a reported downstream effect of the UPR^[53].

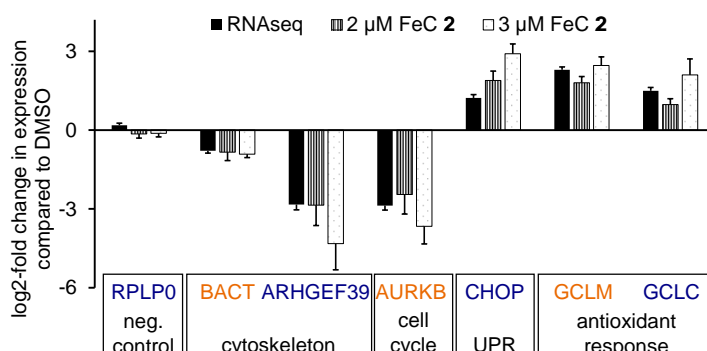


Figure 11: After an unbiased genome-wide RNAseq experiment, genes out of the mostly affected pathways, namely the β -actin cytoskeleton, the cell cycle, the UPR, and the antioxidant response were selected and their altered expression upon FeC 2 treatment (2 μ M or 3 μ M, 24 h) validated by qPCR.

After understanding the mechanism of action, FeC **2** was tested on its anti-cancer activity *in vivo*. Treatment with the clathrochelate more than doubled the mean survival of mice bearing NK/Ly sarcoma and three out of the 11 treated animals were found to be tumor-free after 93 days (Figure 12, A). Moreover, in a different model of murine Lewis lung carcinoma (LLC1)-bearing mice, FeC **2** not only reduced the relative tumor volume but also the number and size of metastases (Figure 12, B-C).

None of the treated mice showed weight loss or any other signs of systemic toxicity. Nevertheless, we assessed the selectivity of FeC **2**. For this, the FeC **2** activity in A2780 ovarian carcinoma cells was compared to the one in normal human fibroblast (SBLF9). In fact, the activation of the unfolded protein response, the mitochondrial ROS generation, and the NO generation were investigated, all of which were not or only marginally induced in the SBLF9 cells. For the selectivity tests *in vivo*, healthy mice were treated with FeC **2**. On day 7 of the treatment regime, blood cells as well as cells of the bone marrow that are prone to chemotherapy-induced side effects were counted. None of the investigated cells were affected by the clathrochelate treatment, proving excellent selectivity of FeC **2** (Figure 12, D).

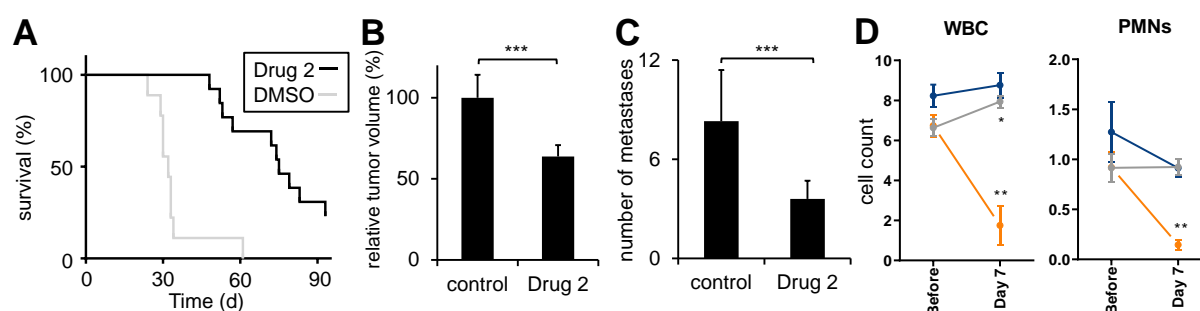


Figure 12: Survival of animals with NK/Ly sarcoma (A) in control (DMSO) and FeC **2**-treated groups. Antitumor (B) and antimetastatic (C) effects of FeC **2** in a murine Lewis lung carcinoma LLC1 model as observed on day 22 of the experiment. An unpaired Student's t-test was performed for statistical analysis: ***: $p < 0.001$. The number of white blood cells (WBC) and neutrophils (PMNs) in the blood of healthy mice, before and after 7 days of treatment with FeC **2** (grey), the negative control DMSO (blue), or the positive control camptothecin (orange) (D). Paired t-test was conducted between days 0 and 7. *: $p < 0.05$; **: $p < 0.01$.

Taken together, an alternative starting point of chemotherapy, namely the binding of unfolded proteins and the consequent induction of ER stress, was investigated. The mechanism was enabled by the application of an unusually bulky, three-dimensional, rigid iron (II) complex and finetuning of its hydrophilicity (number of carboxylic acid residues). This yielded a compound with pronounced anti-cancer and anti-metastatic

activity and high cancer selectivity. An overview of this cancer-selective mechanism of action and its downstream effects are shown in Figure 13.

During these studies, a fluorescein-tagged Clathrochelate, an analog of FeC 2, was synthesized, its localization in cancer cells was studied and the results were published in Publication 2.

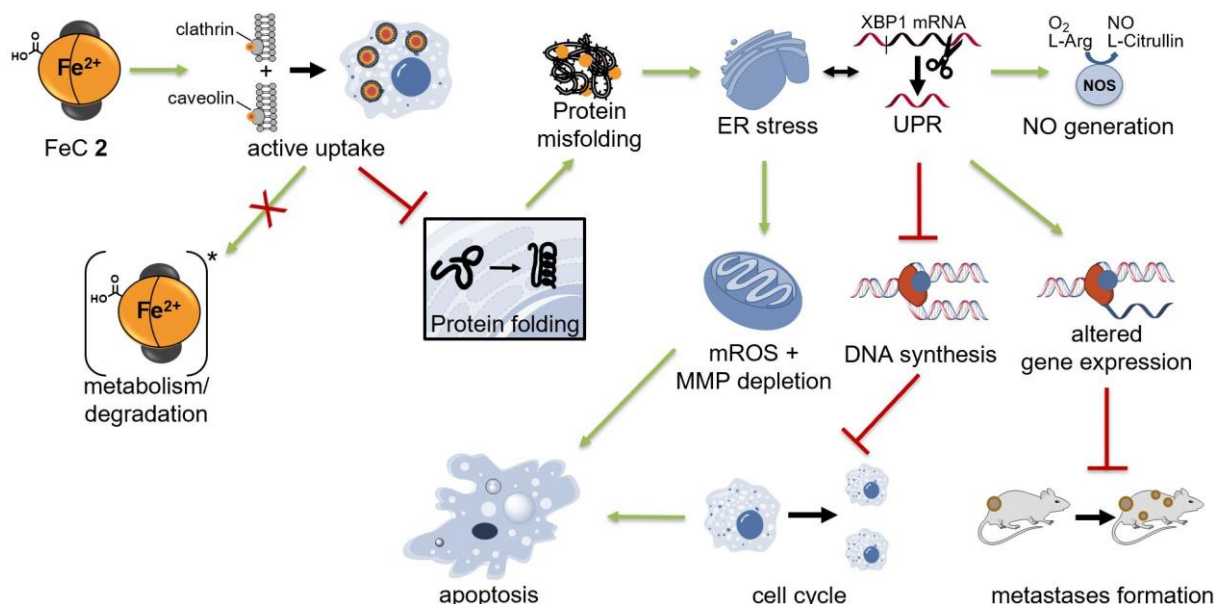


Figure 13: Selective targeting of cancer cells by clathrochelate FeC 2, a spherical binder of unfolded proteins, to increase ER stress in cancer cells.

2.3 Selective targeting of cancerous mitochondria via radical thiol-yne coupling

As described above, not only the ER is stressed in cancer cells, but cancerous mitochondria are also fraught with high metabolic rates and show high oxidative stress levels. This can be exploited for the selective targeting of cancer cells. Due to their relative negative charge, mitochondria in general can be easily targeted by hydrophobic compounds with a delocalized positive charge^[54]. To reach cancer selectivity, the elevated superoxide levels should additionally be exploited.

In general, alkyne moieties are considered bioorthogonal handles as they are not readily reactive towards biomolecules under physiological conditions^[55]. However, once the alkyne group is activated (by e.g. a carbonyl group in alpha position) decent reactivity towards nucleophilic thiols has been reported in the literature, mainly in the context of covalent kinase inhibitors^[56]. A few examples, of nucleophilic thiol-yne coupling with non-activated alkynes have additionally been reported where proximity factors increased the reaction probability^[57]. In contrast, radically driven thiol-yne

couplings towards bioavailable thiols have only been reported in cell-free settings^[58]. In theory, radical thiol-yne couplings should be feasible in the mitochondria of cancer cells due to the elevated ROS levels. As shown in Figure 14, the basic pH of mitochondria not only allows for spatial targeting but also facilitates thiol radical formation, as a higher percentage of thiols are deprotonated allowing single electron transfer of the thiolate ($R-S^-$) to yield the thiyl radical ($R-S^\bullet$), while protonated thiols ($R-SH$) have to undergo hydrogen transfer to yield thiyl radicals^[59].

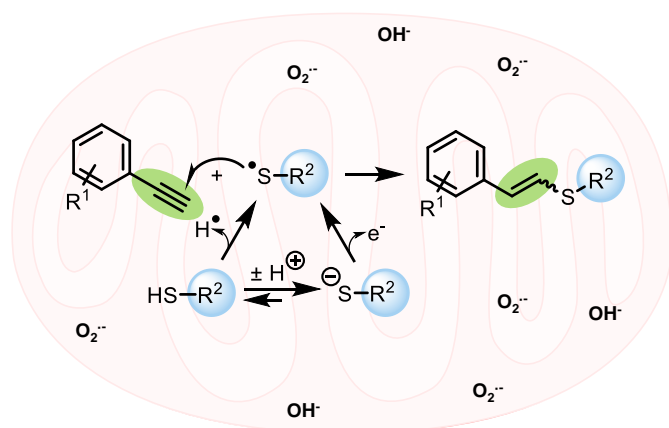


Figure 14: Selective targeting of cancerous mitochondria via radical thiol-yne coupling of which the mechanism is illustrated.

Achieving radical thiol-yne coupling in cancerous mitochondria with bioavailable thiols and artificially added alkyne probes could allow cancer treatment in three ways. First of all, GSH would be alkylated, impeding the antioxidant response, increasing oxidative stress and eventually inducing apoptosis in the cancer cells. Secondly, as outlined in chapter 1.2, proteinogenic thiols are critical in many metabolic reactions and regulatory mechanisms so that their alkylation strongly interferes with cell homeostasis eventually leading to cell death^[60]. Thirdly, alkyne-modified chemotherapeutics could get covalently fixed and thus accumulate in cancerous mitochondria, creating a pool of the drug. Upon protein turnover, the chemotherapeutics would be released over time, which could benefit the anti-cancer activity and facilitate the treatment regime.

In Publication 3^[61], this targeting strategy was implemented and tested. We synthesized a series of positively charged aryl-alkyne-containing fluorescent dyes (Figure 15) and confirmed their general ability to undergo radical thiol-yne couplings with bioavailable thiols and proteins in cell-free settings. Next, we analyzed the reactivity towards proteins by SDS PAGE and subsequent fluorescence imaging (Figure 17, A). Covalent binding of all tested dyes containing terminal aryl alkyne/alkene groups (**8**, **18**, **10**, **14**, **9**) was indeed detected selectively in the presence of H_2O_2 and $FeSO_4$.

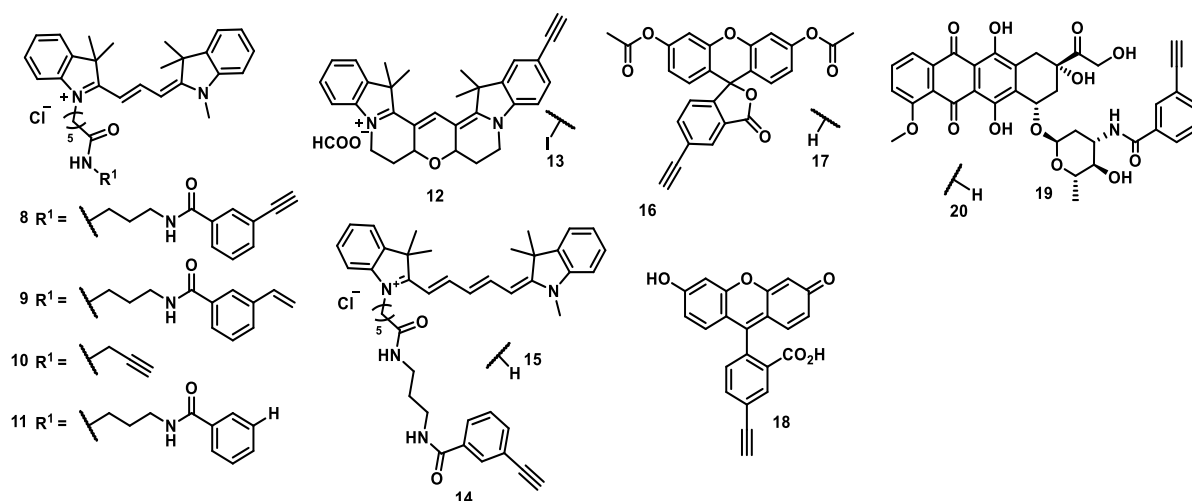


Figure 15: Overview of the applied Cy3-derivatives (**8-13**), Cy5-derivatives (**14-15**), fluorescein-derivatives (**16-17**), Fluorescein derivative (**18**), and doxorubicin-derivatives (**19-20**).

Encouraged by these results, we investigated the dye's covalent binding behavior in cells. Therefore, A2780 cancer cells were treated with the dye derivatives and subsequently fixed and washed with CH₃OH to remove all small molecules, leaving only those that bound covalently to macromolecules e.g. proteins. We analyzed the covalent binding efficacy by fluorescence microscopy (Figure 16, B) and quantified it by flowcytometry (Publication 3, Figure 2 B). A significantly higher fluorescence signal for all alkyne-derivatives was detected in comparison to their controls without alkyne groups. One exception is the Cy5 derivative alkyne **14**, which is most probably not stable in cells after covalent binding. In addition, the alkynyl doxorubicin derivative **19** also failed to covalently bind macromolecules (Publication 3, Figure 4).

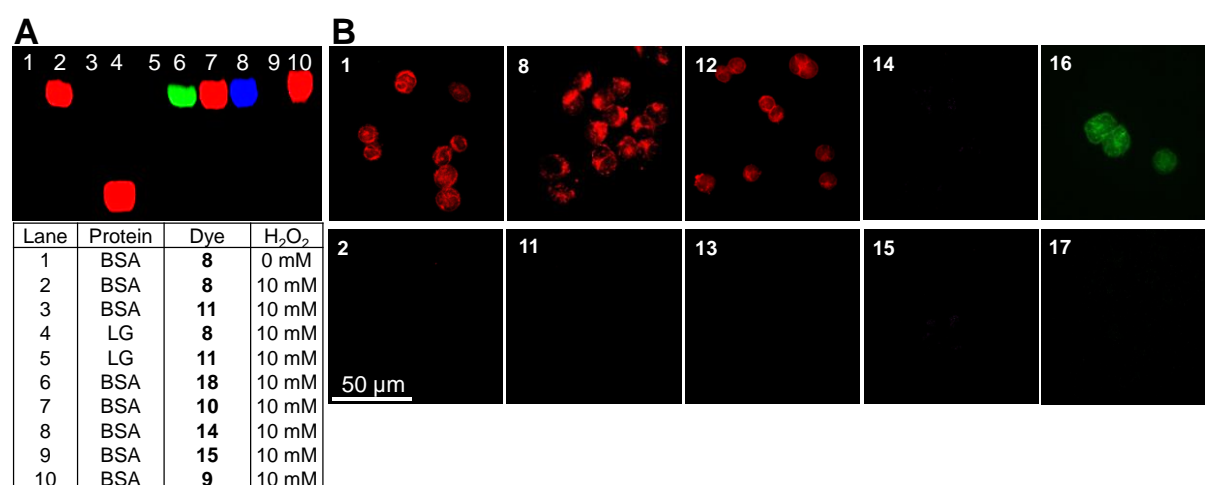


Figure 16: Covalent binding efficacy of alkyne fluorescence dyes (**1, 8, 9, 10, 12, 14, 16**) in contrast to the non-alkynyl dyes (**2, 11, 13, 15, 17**) to proteins in cell-free settings (**A**) and in A2780 cancer cells (**B**).

Colocalization experiments, however, revealed that the doxorubicin derivative, is not well taken up into the mitochondria, in contrast to all other studied compounds, (Publication 3, Figure 5). This confirms that the covalent binding is exclusively happening in mitochondria, and explains the missing signal of **19**. We validated this by isolating mitochondria from Cy3-alkyne **8**-pretreated cells and subsequent SDS-PAGE analysis. Here we detected high fluorescence, indicating covalent binding in these organelles (Figure 17, A). This was not observed for the control compound **11**. Next, we investigated the reactivity of the alkyne probe **8** in different cell lines, revealing the selectivity of the radical thiol-yne reaction for cancer cells (Du145, A2780, BL2) over normal cells (SBLF9) (Figure 17, B). This is explained by the higher concentration of mitochondrial ROS found in these fast-proliferating cells as determined by MitoSox™ staining (Figure 17, D). Finally, we investigated the toxicity of alkyne-containing Cy3 derivative **8** and its control compound **11** in A2780 cancer cells (Figure 17, C), which was significantly higher for alkyne **8** than for the control **11**, proving that this approach is indeed exploitable for chemotherapy. In conclusion, we presented a new chemotherapy strategy that combines compound-directed accumulation and stimuli-responsive reactivity to enable selective cancer targeting.

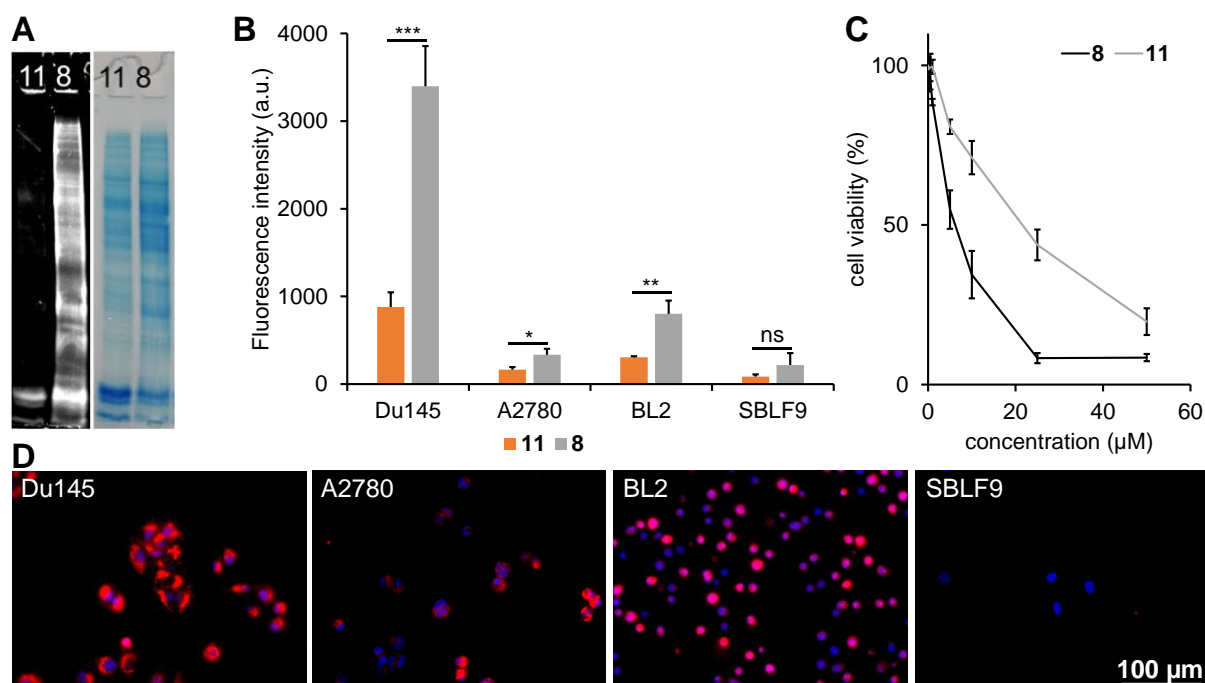


Figure 17: Fluorescence imaging and Coomassie staining of isolated mitochondria from cells pre-treated with Cy3-derived alkyne probe **8** or its control **11** after SDS PAGE (A). Covalent binding efficacy of probe **8** and control compound **11** in cancerous Du145, A2780, BL2 cells, and non-cancerous SBLF9 cells using flow cytometry (B). Relative cell viability of A2780 cell line after 4 h incubated Cy3-derived alkyne probe **8** or its control **11** as determined by MTT

assay (C). Determination of relative mitochondrial ROS concentrations in these cells by MitoSox™ staining (D).

2.4 Prodrug concept

One prominent approach to increase cancer selectivity is the chemical modification of a chemotherapeutic with a promoiety to yield a pharmacologically inactive prodrug. As illustrated in Figure 18, the prodrug is *in vivo* metabolized or chemically activated at the tumor site or inside a tumor cell to selectively release the active drug. Alternatively, the active drug can be released upon an external trigger, such as light irradiation.

In 2015, approximately 20 % of all FDA-approved small molecular drugs were considered prodrugs^[62]. However, the majority of these prodrugs were designed to increase the ADME (absorption, distribution, metabolism, and excretion) properties and not the specificity of the drug. One prominent example is L-DOPA, a dopamine prodrug, which in contrast to the actual neurotransmitter, can readily cross the blood-brain barrier. In the brain, L-DOPA is metabolized by the aromatic L-amino acid decarboxylase to the active dopamine^[63].

Several hallmarks of cancers, such as overexpressed enzymes, hypoxia, low/high pH, or increased ROS levels could be exploited as triggers for cancer-selective prodrug activation. One example of a chemotherapeutic prodrug on the market is capecitabine, a 5-fluorouracil prodrug that gets sequentially activated by carboxylesterases, cytidine deaminase, and finally by thymidine phosphorylase, an enzyme that is overexpressed in many cancers^[64]. Thus, conversion into the active drug takes place predominantly in cancer cells, reducing systemic toxicity. In 2010, the first ROS-activatable prodrug with an aryl boronic pinacol ester as the promoiety was reported for cancer-selective matrix metalloproteinase inhibitors^[65]. The mechanism is shown in Figure 18. The pinacol ester might be firstly hydrolyzed unspecifically. Then, the boronic acid is cleaved selectively in the presence of elevated ROS to yield the phenol. Upon deprotonation, the phenol undergoes 1,6-elimination yielding the active drug. Since its first successful implementation in a prodrug, the aryl boronic pinacol ester promoiety has been exploited frequently due to its moderate ROS (i.e. H₂O₂) responsiveness *in vivo* and its easy attachment to several functional groups that are important for the bioactivity of the actual drug.

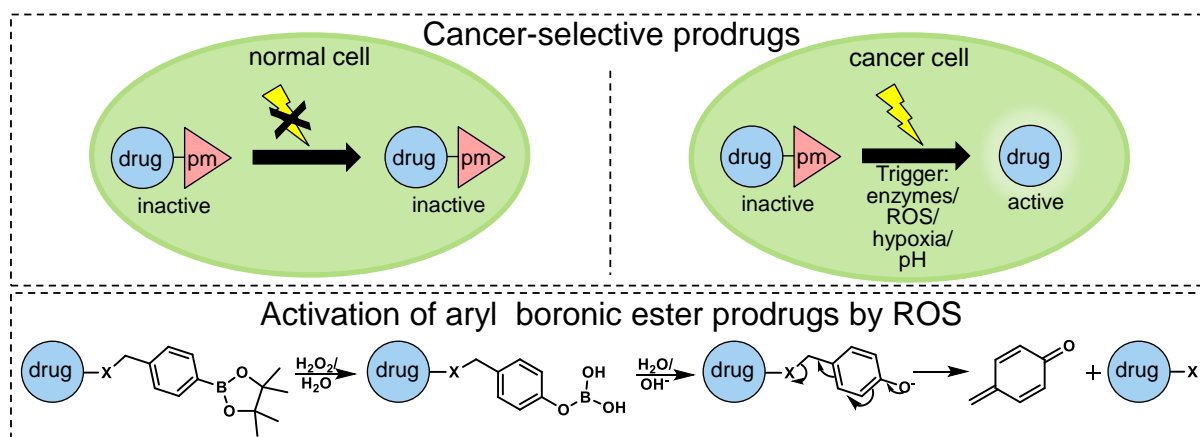


Figure 18: The mechanism of cancer-selective prodrug activation and the activation mechanism of aryl boronic ester prodrugs by ROS.

2.5 ROS-activatable siRNA prodrugs

While the aryl boronic ester promoiety has been exploited for many small molecules already, it was so far synthetically challenging to attach it to DNA/RNA oligonucleotides as the I₂-oxidation step required for oligonucleotide synthesis is cleaving the boronic acid. Nonetheless, a cancer-specific small interfering RNA (siRNA) prodrug approach is attractive for selective cancer targeting.

siRNAs are 21-25 base pair (bp) long RNA double strands, that usually come with a two-nucleotide overhang on the 3' ends. They act via the RNA interference (RNAi) mechanism as they are recognized by argonaut proteins that incorporate the siRNA into the RNA-induced silencing complex (RISC). The passenger strand is dissociating, while the guide strand is phosphorylated and thus activated at its 5' end. The activated strand then serves as a template for sequence-specific degradation of RNA in the cells. Via this catalytic mechanism, single genes can be selectively downregulated (=silenced). In research, RNAi is often exploited e.g. for drug screenings in cells. Regarding medicinal applications, the ability to target key genes in cancer progression selectively in cancer cells would greatly add to the toolbox of chemotherapeutics. However, the *in vivo* delivery of siRNAs and their cancer selectivity are major obstacles. Recently, progress in siRNA delivery has been made through the development of new siRNA carriers such as lipid nanoparticles^[66]. The cancer selectivity, however, remains challenging, although ROS-responsive lipid nanoparticles have been reported^[67]. The direct modification of siRNA with a ROS-activatable promoiety would simplify *in vivo* application as they could be formulated

with any carrier that already has been or will be developed in the future, and at the same time increases the selectivity via cancer-selective activation of the prodrug.

In a proof-of-concept study (Publication 4), we synthesized the first 5' aryl boronic acid modification of the guide strand of a siRNA. To avoid boronic acid cleavage during synthesis, a tridentate diethanolmethylamine boronic acid ester was used for the phosphoramidite synthesis, and upon attachment to the RNA strand, the phosphor (III) was mildly oxidized with 3-ethoxy-1,2,4-dithiazoline-5-one (EDITH) to yield the corresponding phosphorothioate, leaving the boronic acid intact. The 5' modification site was chosen to prevent activation of the siRNA in the RISC complex unless the boronic acid promoiety is cleaved by ROS. As a gene target, the *kinesin family member 11* (*kif11*) was selected, since the protein is essential for mitosis and its silencing leads to a cell cycle arrest in the prometaphase, which can be easily detected on a protein level. Because of its antimitotic effects, and because it is overexpressed in some cancers^[68], this gene is a promising target for cancer treatment. The concept is illustrated in Figure 19.

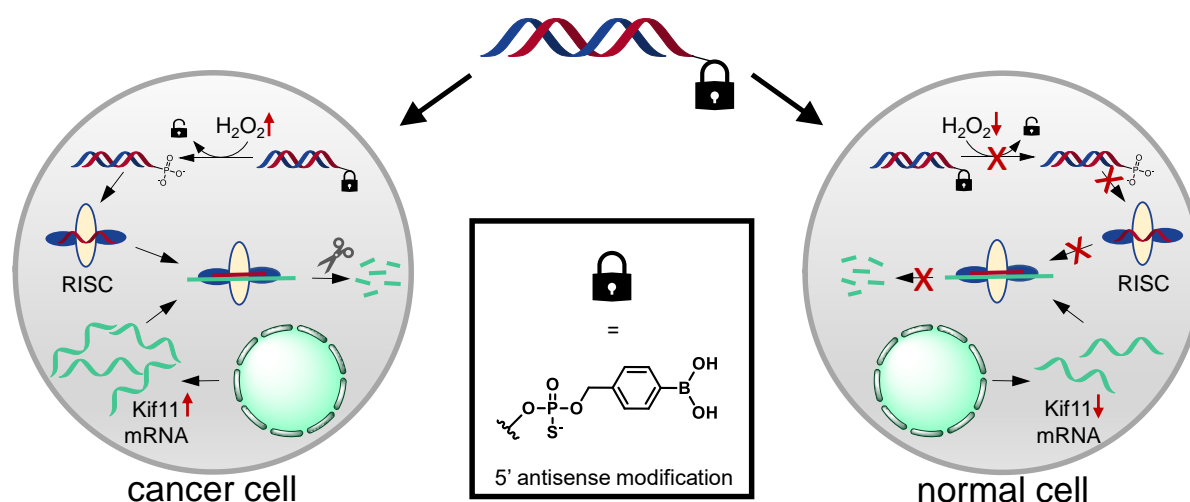


Figure 19: The ROS-responsive siRNA is selectively activated in cancer cells due to the higher levels of ROS. Upon cleavage of the promoiety, the guide strand of the siRNA is incorporated into the RISC complex, phosphorylated, and thus activated leading to the selective degradation of *kif11* mRNA. As correct mitosis fails in the absence of *kif11*, apoptosis is induced selectively in cancer cells.

We studied the activation mechanism (Figure 20, A) of the obtained oligonucleotide prodrugs, DNA **14** and RNA **7a** in the presence of H_2O_2 , by HPLC (Figure 20, B, D, respectively). In both cases, after 1h incubation, substantial amounts of the desired 5' phosphorylated oligonucleotide strand were formed. In contrast, the activation by other

reactive oxygen species was less pronounced (Figure 20, C), indicating the selectivity of the promoiety towards H_2O_2 .

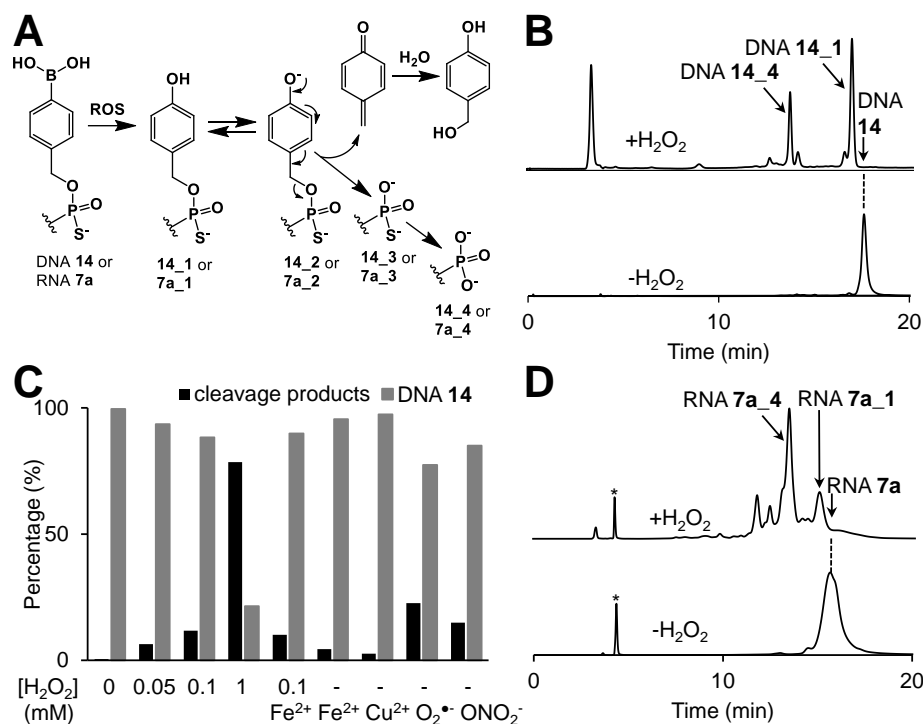


Figure 20: ROS-dependent activation mechanism of the aryl boronic ester promoiety (A). Activation of DNA 14 (B) and RNA 7a (D) in the presence (“+ H_2O_2 ”) and absence (“- H_2O_2 ”) of H_2O_2 as monitored by HPLC. *: impurity in RNA 7a (<10 %). Cleavage of DNA 14 by different oxidants: H_2O_2 (0–1 mM); FeSO_4 (10 μM), *N,N,N',N'*-ethylenediaminetetracetic acid (EDTA, 10 μM); CuSO_4 (10 μM); KO_2 (1 mM) and ONO_2^- (3-morpholinosydnonimine hydrochloride, SIN-1, 400 μM) (C) after 1 h incubation.

Encouraged by these results, we annealed RNA 7a with its sense strand (RNA 18) to yield the siRNA prodrug (siRNA 7a/18). We formulated it with a commercially available standard transfection reagent RNAiMAX for the treatment of A2780 cancer cells. In cells, we first studied the activation and knockdown efficacy of the siRNA prodrug by qPCR and compared it to the unmodified siRNA (19/18) and the negative controls that cannot be readily activated by H_2O_2 siRNAs (16/18 and 17/18). As shown in Figure 21, A, the siRNA prodrug 7a/18, induces a knockdown of *kif11* to a similar extent, if not even higher extent (which could be explained by higher stability, or transfection rate), than the positive control 19/18. Very similar results are observed on a protein level when quantifying the cells in the respective phase of the cell cycle (Figure 21, B). As expected, the prodrug is inhibiting the cell division in the G2 phase to a similar extent to the unmodified siRNA. By staining the DNA of transfected cells with Hoechst 33342 followed by fluorescence microscopy, we observed the same effects, as the chromatin

of the cells treated with the siRNA prodrug, and the positive control is clearly condensed without the cell division taking place (Figure 21, C).

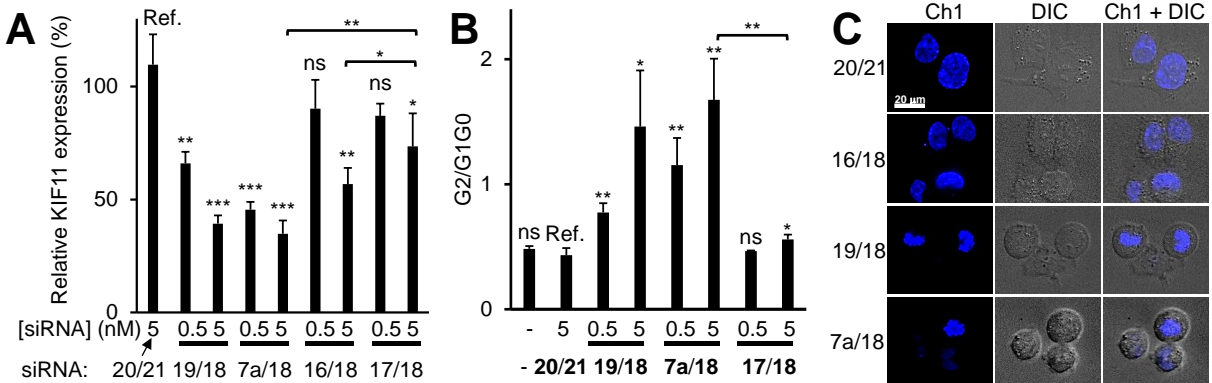


Figure 21: Quantification of relative *kif11* mRNA concentrations after transfection with siRNA prodrug (**7a/18**), the unmodified siRNA (**19/18**) as positive control, and the negative controls that cannot be readily activated by H₂O₂ siRNAs (**16/18** and **17/18**) or without a cellular target (**20/21**) (**A**). Effects of the same siRNAs G2/G1G0 ratio of the cell cycle of A2780 cells (**B**). Student's *t*-test: * $p < 0.05$, ** $p < 0.01$, *** $p < 0.001$, ns $p \geq 0.05$ (**A+B**). DNA staining of A2780 cells treated with the siRNA and subsequent confocal fluorescence microscopy (**C**).

Finally, the siRNA selectivity was challenged in an *in vivo* hepatectomy model, which increases the ROS concentration in the liver of healthy mice by sterile inflammation (Figure 22, A). Indeed, we observed selective activation of the siRNA prodrug upon hepatectomy, whereas the unmodified siRNA induced gene knockdown unselectively before and after hepatectomy (Figure 22, B). This demonstrates the suitability of this prodrug approach for selective targeting of cells with elevated ROS levels, such as cancer cells, reducing the effects on normal cells.

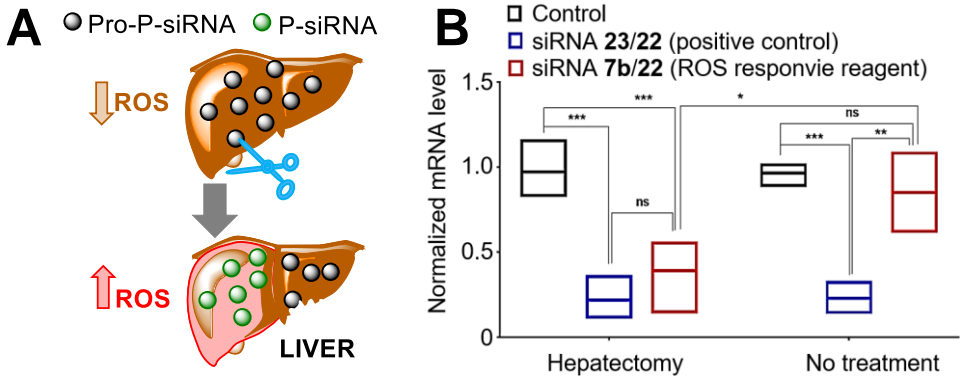


Figure 22: Partial hepatectomy induces a sterile inflammation and thus ROS increase (**A**). Relative eEF2 mRNA levels in the liver of FvB mice ("without treatment") and in the liver of FvB mice after partial hepatectomy using **23/22** (eEF2 siRNA) and **7b/22** (ROS-inducible eEF2 siRNA prodrug) (**B**). Student's *t*-test: * $p < 0.05$, ** $p < 0.01$, *** $p < 0.001$, ns $p \geq 0.05$.

2.6 Red light-triggered siRNA prodrugs

In addition to siRNA prodrugs that are activated in a specific microenvironment, approaches towards siRNA prodrugs that are activated upon an external trigger have also been reported in the literature^[69]. Ji et al., for example, developed a siRNA prodrug in which the 5' end of the antisense strand is caged with a vitamin E-derivative. Upon UV light irradiation (365 nm), the siRNA gets activated. UV light, however, is strongly cytotoxic and disadvantageous for *in vivo* application due to the very low tissue penetration^[70]. In contrast, red light is well tolerated, shows decent tissue penetration, and is, therefore, the preferred light trigger for biological applications. Hence, Meyer et al. reported on favorable red light activatable siRNA prodrug^[69c]. The 3' terminus of the sense strand of this prodrug is modified with a photosensitizer (In(pyropheophorbide a)chloride) that generates $^1\text{O}_2$ upon red light irradiation, which cleaves the caging group (9-anthracenyl residue) on the 5' end of the antisense strand, yielding the active siRNA and anthraquinone (see Figure 23, top). While the triggering mechanism works efficiently and the red light is well tolerated by the cells, the produced $^1\text{O}_2$ as well as the anthraquinone are strongly cytotoxic towards cells and surrounding tissue. To improve this, we developed an red light activatable siRNA prodrug where the 5' terminus of the antisense strand is caged with an electron-rich azobenzene (Publication 5, concept: Figure 23, bottom).

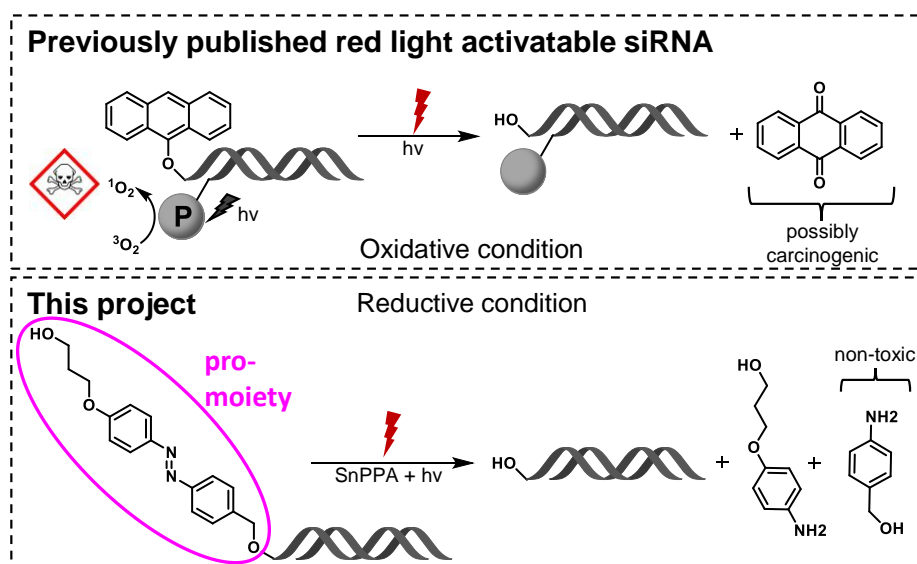


Figure 23: While previously published red light activatable siRNA prodrugs produce cytotoxic side products, the siRNA prodrug developed during this thesis is caged with an electron-rich azobenzene. The promoiety gets cleaved upon light trigger in the presence of photosensitizer SnPPA. The mediators of activation are electrons and no cytotoxic species are generated.

Upon red light irradiation, this cage group is cleaved off by photoreduction in the presence of the photosensitizer Sn(IV)(pyropheophorbide a)dichloride (SnPPA) and bulk-reducing agents such as ascorbate. In that way the promoiety allows on-demand activation of RNA interference, avoiding harmful side products.

In the first step, we synthesized a DNA model strand carrying the azobenzene-promoiety (DNA 1). In its analytical HPLC profile, shown in Figure 24 A, two peaks are seen corresponding to the *cis* and the *trans* stereoisomer. The activation of the DNA was initiated by red light irradiation in the presence of SnPPA and ascorbate as an electron source. The cleavage was monitored by HPLC and the resulting profile is shown in Figure 24 B. As expected, one prominent peak with a corresponding mass of the DNA strand after reduction and cleavage of the azobenzene with subsequent 1,6-elimination of the resulting aniline is observed (activation mechanism: Figure 24, E).

We then synthesized a siRNA antisense strand carrying the azobenzene-promoiety (RNA 2, Figure 24 C). As for the ROS-activatable siRNA in Publication 4, *kif11* was chosen as the gene target (see above) and a thiophosphate was introduced at the 5' end of the strand to increase stability towards phosphatases. We repeated the activation experiment in cell-free settings for the RNA strand. The resulting HPLC profile, shown in Figure 24 D, exhibits a double peak with masses corresponding to the thiophosphate- and phosphate-RNA strands. Both would lead to the activated RISC complex in cells. In addition, a few unidentifiable side products, showing small elution peaks, were formed.

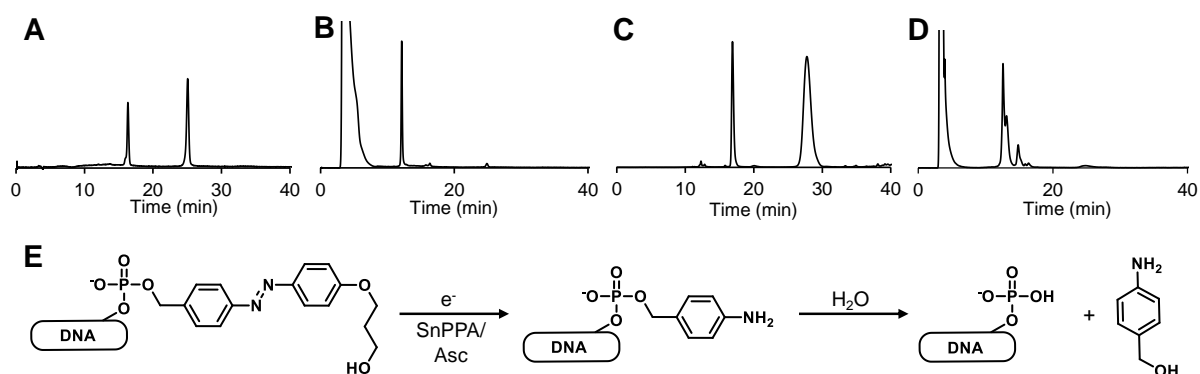


Figure 24: Reversed phase HPLC profile of the DNA 1 (A) and RNA 2 (C) carrying the azobenzene-promoiety and hence showing two peaks corresponding to the two stereoisomers. Red light irradiation of DNA 1 (B) and RNA 2 (D) in the presence of SnPPA and ascorbate yields the expected unmodified DNA/RNA strand with a 5' (thio-)phosphate group attached as seen in their HPLC profiles (B, D) and corresponding MALDI-TOF MS spectra (not shown). The activation mechanism of photoreduction and subsequent 1,6-elimination of the aniline (E).

To test the system in cells, we annealed RNA 2 with its sense strand (RNA 3) and transfected it into A2780 cells using RNAiMAX, a commercially available standard transfection reagent. As controls, the unmodified antisense strand (RNA 4) was also annealed with RNA 3 and transfected into the cells, alongside the negative control without cellular target RNA 5/6. After successful transfection, we treated indicated samples with the photosensitizer SnPPA, and all cell samples were irradiated. The *kif11* mRNA content was determined 38 h post-transfection by RT qPCR. As shown in Figure 25, the siRNA prodrug gets activated selectively in the presence of SnPPA resulting in a significant knockdown of the target gene.

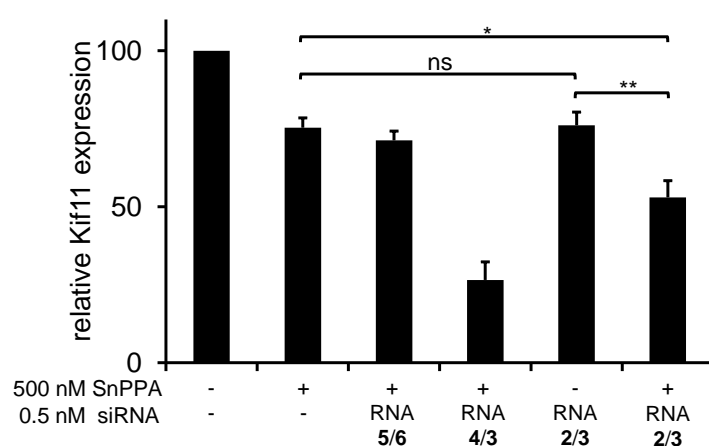


Figure 25: Quantification of relative *kif11* mRNA concentrations after transfection with the unmodified *kif11* siRNA 4/3, the siRNA prodrug RNA 2/3, or the negative control RNA 5/6, SnPPA addition, and red light irradiation. As a housekeeping gene, GAPDH was used. $2^{-\Delta Ct}$ values were calculated and normalized to the one of untreated cells. Three independent experiments were performed. Error bars indicate standard deviation. An unpaired Student's t-test was performed for statistical analysis: * - $p < 0.05$; ** - $p < 0.01$; ns - $p \geq 0.05$.

In conclusion, in this publication we presented a promoiety for oligonucleotides that allows on-demand activation of RNA interference by red light irradiation in the presence of photosensitizer SnPPA, triggering the knockdown of an essential gene in cancer cells. In contrast to previously published siRNA prodrugs, no cytotoxic side products are generated. The attachment of the promoiety directly onto the siRNA, allows the formulation with standard transfection reagents and potentially the modification of any siRNA sequence, making this promoiety a variable tool for on-demand siRNA activation.

2.7 Aminoferrocene prodrugs

As only a narrow window of ROS levels is promoting tumorigenesis (see above, and Figure 26) the manipulation of the redox state of cancer cells in the direction of cytostasis and slower cancer proliferation as well as in the direction of cell death has

been exploited in cancer treatment^[71]. However, these strategies come with disadvantages. While the reduction of ROS levels is only retarding cancer growth without curing it, the increase of ROS levels can potentially cure cancer by inducing cell death but at the same time promote the formation of new malignancies. The solution to this conflict would be to selectively increase ROS in those cells, which already exhibit a higher oxidative stress level, namely in cancer cells.

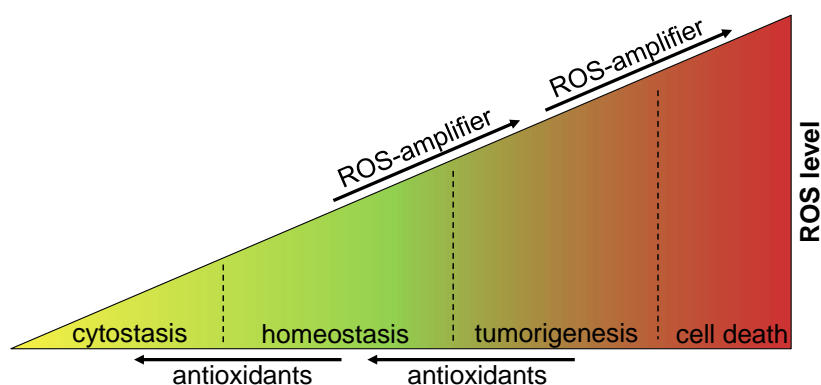


Figure 26: Antioxidants can decrease tumor growth, while ROS-amplifier can induce cell death in cancer cells. The unselective increase of ROS, however, promotes tumorigenesis in normal tissue.

As one possible solution, our group developed N-alkyl-aminoferrrocene (NAAF) prodrugs^[72]. As shown in Figure 27, these compounds carry the aryl boronic ester-based ROS-responsive promoiety, described above. Upon activation by H_2O_2 , the NAAF is released, which catalyzes the formation of hydroxyl radicals and superoxide via *Fenton* chemistry, thus inducing strong oxidative stress and apoptosis selectively in cells with already elevated ROS levels. As the ferrocenium can be re-reduced by GSH, a catalytic ROS-generating cycle is initiated. The N-alkyl moiety of these prodrugs can easily be exploited for intracellular targeting. In this way, non-targeting (propargyl- moiety)^[45], and mitochondria targeting NAAF prodrugs^[73] with a positively charged residue have been synthesized. To achieve lysosome targeting, an alkylated piperidine moiety was attached to the prodrug, which gets protonated in lysosomes due to the decreased pH, reducing its membrane permeability and thus trapping the prodrug in this organelle^[74]. In addition, cisplatin-aminoferrrocene codrugs have been synthesized and studied^[75].

As described above, the ER of cancer cells exhibits particularly high ROS levels. Hence, the targeting of this organelle by NAAF prodrugs is of high interest, which we accomplished in Publication 6. As hydrophobic compounds are known to accumulate in the ER^[76], we attached a cholic acid moiety to the aminoferrrocene. The intracellular accumulation of the prodrug in the ER was shown in A2780 cells. In addition, we

confirmed its ability to increase ROS and induce ER stress selectively in cancer cells. Finally, the activation of the prodrug in the ER of ascites of Nemeth-Kellner-Lymphoma-bearing mice was proven.

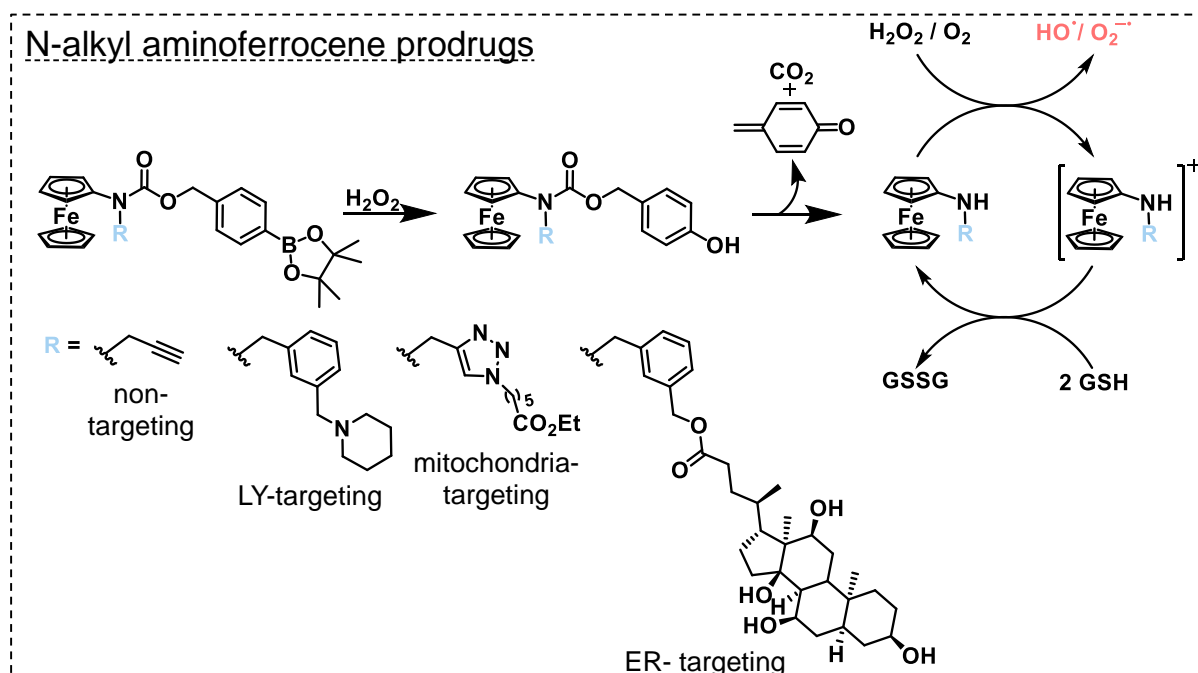


Figure 27: The general activation mechanism of NAAF prodrugs and their cycle of ROS generation via *Fenton* chemistry as well as the structures of their organelle-targeting moieties.

2.8 An aminoferrocene prodrug sequentially activated by ROS and OH⁻

Immune cells and their precursor cells are particularly affected by most chemotherapeutics as they divide rapidly and thus depend on functioning mitosis in a similar way as cancer cells do^[40b, 40c]. Hence, chemotherapy often leads to a condition called neutropenia which is characterized by a low number (<1500 cells/ μL blood) of neutrophils. As these leukocytes constitute the first line of defense against pathogens, even minor infections can become life-threatening to cancer patients exhibiting neutropenia. Consequently, chemotherapy is delayed or the dose reduced, which might jeopardize the treatment outcome^[77].

Unfortunately, “smarter” NAAF prodrugs can also be activated in neutrophils, as these leukocytes generate bursts of ROS as part of their immune response upon exposure to a trigger such as bacteria. Accordingly, partial activation and residual toxicity to neutrophils were also shown for a ROS-responsive gemcitabine prodrug by Matsushita et al.^[78]. Hence, the ROS activatable promoiety is not sufficient to discriminate between cancer cells and neutrophils.

One prominent distinguishing characteristic between these two cell types, however, is the substantially higher mass and total number of mitochondria in cancer cells^[79], which could be exploited for selective targeting. In previous studies, we observed that NAAF prodrugs migrate to the mitochondria upon oxidation to the positively charged ferrocenium product. Hereafter, the ferrocenium moiety is rapidly degraded, likely due to the elevated concentration of hydroxide ions in these organelles^[80]. Building on these findings, we developed a dual triggering mechanism for anti-neoplastic drugs by conjugating the drug to a NAAF backbone that serves as the promoiety. This should result in a prodrug that is activated only when exposed to both H₂O₂ (B-C bond cleavage: in cancer cells and neutrophils) and subsequently to OH⁻ (ferrocene degradation: in cancer cells, but not in neutrophils). Consequently, the drug is released selectively in the mitochondria of cancer cells.

Following this approach, we synthesized and characterized a camptothecin (cpt)-NAAF prodrug, by linking the drug via esterification of the hydroxyl group that is important for its activity to a NAAF backbone. Its activation mechanism was studied *in vitro* and the cpt-prodrug's activity, as well as its selectivity, was assessed *in vitro*, as well as *in vivo*. An overview of the concept is illustrated in Figure 28. The results are published in Publication 7 and will be outlined hereinafter.

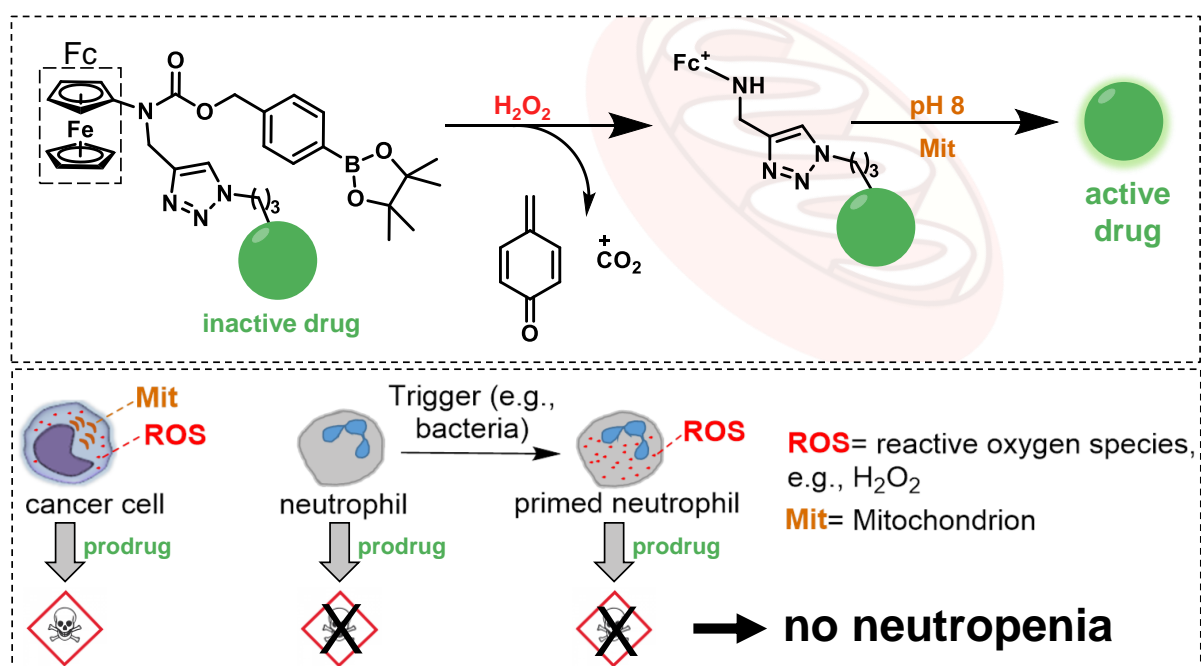


Figure 28: Improved cancer selectivity is achieved with a dual triggering mechanism. The prodrug is activated sequentially by ROS and OH⁻ to release the active chemotherapeutic drug selectively in the mitochondria of cancer cells. Thus, neutrophils even in a primed -ROS rich-state are not killed, avoiding neutropenia.

The cpt-prodrug ($\text{FcN}^{\text{PG2/PG1}}\text{-L-E-cpt}$) showed good stability in aqueous solution up to at least 48 h. The ester bonds of the compounds are most probably protected due to the compound's aggregation, which was observed by UV-vis and DLS (see Publication 7, Figure 3). Hence, even the pinacol ester of the promoiety is only hydrolyzed slowly (complete cleavage only after 24 h, whereas other NAAFs hydrolyze usually within less than 2 h^[80]). In contrast, upon H_2O_2 (10 mM) addition, $\text{FcN}^{\text{PG2/PG1}}\text{-L-E-cpt}$ is quickly activated. As anticipated, the main product after 1 h is, however, dependent on the pH. As shown in Figure 29, A, the aminoferrocenium [$\text{FcN}^+\text{-L-E-cpt}$] is formed at pH 7 (profile 1), whereas at pH 8 (profile 2), the ferrocenium is degraded to the amine [$\text{N}^+\text{-L-E-cpt}$] and potentially the free HO-cpt via an intermediate (*). The corresponding structures are shown in Figure 29, C.

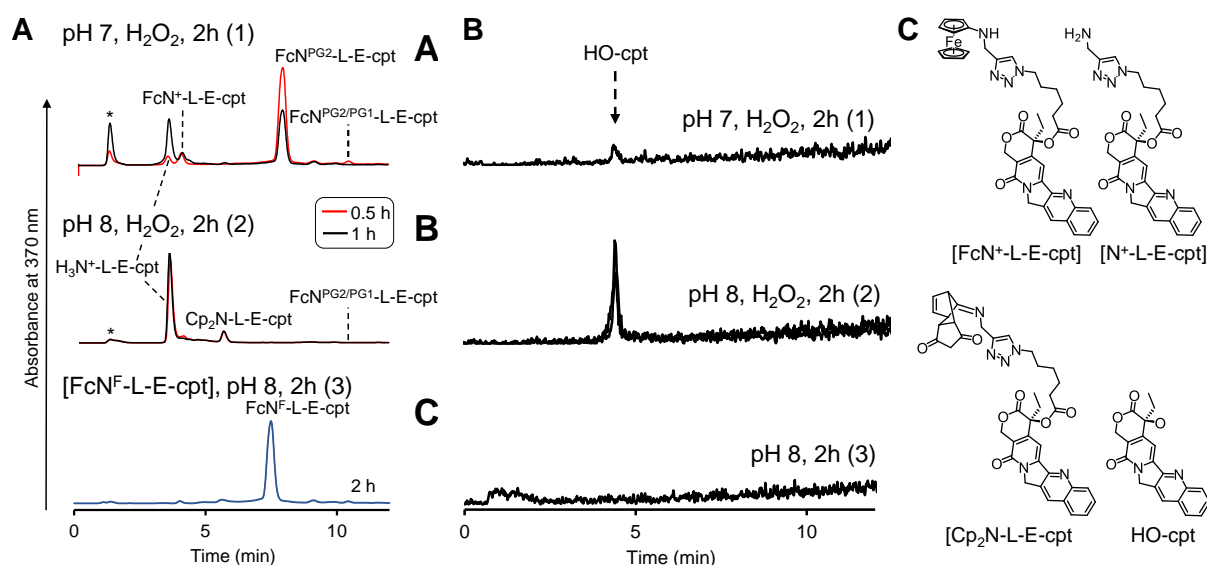


Figure 29: HPLC profiles (absorbance at 370 nm) of prodrug $\text{FcN}^{\text{PG2/PG1}}\text{-L-E-cpt}$ (1, 2) or $\text{FcN}^{\text{F}}\text{-L-E-cpt}$ (3) (20 μM , in 150 mM (Et_3NH)(OAc), acetonitrile (50 %), H_2O_2 (10 mM), pH 7 (1) or 8 (2, 3)) incubated for 0.5 h or 1 h (A). SIM ($m/z=349$) of solutions of prodrug $\text{FcN}^{\text{PG2/PG1}}\text{-L-E-cpt}$ (20 μM , in 150 mM (Et_3NH)(OAc), acetonitrile (15 %), pH 7 (1) or 8 (2)) incubated for 2 h in the presence (1, 2) or absence (3) of H_2O_2 (10 mM). Structures of the observed intermediates (C).

Unfortunately, the hydrophilicity of the amine [$\text{N}^+\text{-L-E-cpt}$] and HO-cpt is very similar, resulting in insufficient separation in this LCMS setting. However, applying a superior LC-MS system (UltiMate 3000 RS liquid chromatography system, coupled to a timsTOF Pro mass spectrometer, see Publication 7, S1) and plotting the Selected Ion Monitoring (SIM) of the corresponding mass (Figure 29, B) revealed that the free HO-cpt is indeed formed predominantly at pH 8 (profile 2), only minor traces were detected at pH 7 (profile 1), and no HO-cpt could be detected in the absence of H_2O_2 (profile 3).

The latter indicates good stability of the prodrug in the absence of H₂O₂. In contrast, the negative control, FcN^F-L-E-cpt, is not activated/degraded in the presence of H₂O₂ (Figure 29 A, profile 3). Altogether, these results demonstrate the selective activation of FcN^{PG2/PG1}-L-E-cpt in the presence of H₂O₂ in a basic milieu. We also demonstrated a very similar activation behavior for a model compound, where the HO-cpt moiety was replaced by another tertiary alcohol (1,1-dimethylbenzyl, dmb, Publication 7, Figure S30A, S), proving that the activation mechanism is not specific for HO-cpt.

We exploited the fact that the cpt fluorescence is quenched by the ferrocene due to photoinduced electron transfer, but is regained upon activation and oxidation to study the activation in cells. As shown by the cpt-fluorescence (blue) in Figure 30 A, FcN^{PG2/PG1}-L-E-cpt is efficiently activated in A2780 ovarian carcinoma cells. Pre-treatment of the cells with the ROS scavenger N-acetyl cysteine (NAC), however, leads to a reduction of the activation (Figure 30, A, right image). Figure 30, A and Figure 6, A in Publication 7, show that the activated compound accumulates in the mitochondria (Pearson's coefficient = 0.68, most likely the ferrocenium intermediate), as well as the nucleus (Pearson's coefficient = 0.81, most likely the fully activated HO-cpt at its target site). In contrast, in freshly isolated neutrophils of healthy donors, the compound is only activated upon exposure to phorbol myristate acetate (PMA) (compare Figure 30, B, left vs. right), which primes the neutrophils and induces an oxidative burst. From this data, it can, however, not be determined whether the ferrocenium is degraded which would mean full activation of the prodrug. Toxicity studies in neutrophils, however, suggest that the camptothecin is not released (Publication 7, Figure 6, D).

To confirm the release of HO-cpt in cancer cells, the distribution of cells in the respective phases of the cell cycle was determined upon treatment with FcN^{PG2/PG1}-L-E-cpt, HO-cpt, a NAAF (ROS generator) or just the carrier DMSO. As shown in Figure 30, C, HO-cpt induces a strong arrest of the cell cycle in the G2/S phase, whereas the ROS-generating agent does not. The prodrug FcN^{PG2/PG1}-L-E-cpt acts via cpt activity. On the other hand, FcN^{PG2/PG1}-L-E-cpt does not induce the generation of ROS, while the NAAF efficiently increases the ROS level in the cancer cells (see Figure 30, R). Taken together, this proves that the prodrug is efficiently activated in cancer cells where it acts via cpt release.

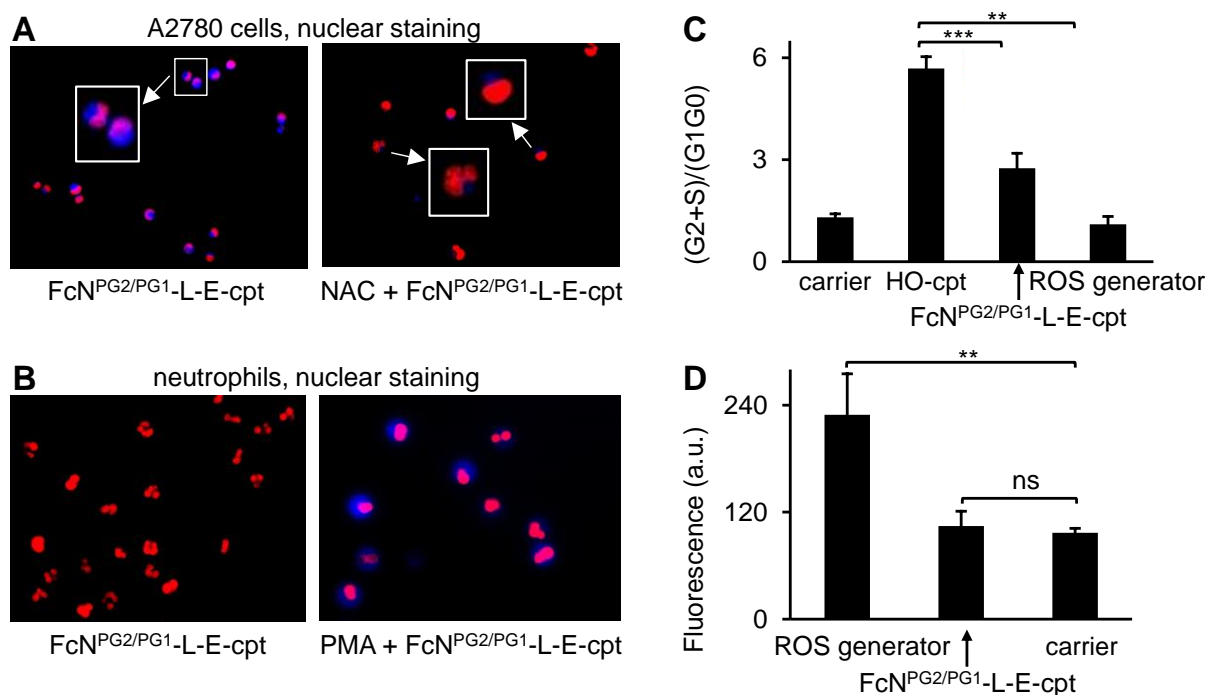


Figure 30: Fluorescence microscopy of A2780 cells (**A**) and neutrophils incubated (**B**) with prodrug FcN^{PG2/PG1}-L-E-cpt (20 μ M) and NUCLEAR-ID® Red dye (NIRD). In A2780 cells, ROS levels and thus compound activation were reduced by the ROS-scavenger N-acetyl cysteine (NAC, 2 mM) (**A**). In neutrophils, ROS and thus compound activation were increased by the addition of phorbol myristate acetate (PMA, 50 nM) (**B**). Effects of FcN^{PG2/PG1}-L-E-cpt, a control NAAF (“ROS generator”) and DMSO (“carrier”) on intracellular ROS in A2780 cells as determined by CM-H₂DCFDA staining (**C**). Quantification of the cell cycle distribution of A2780 cells after 72 h treatment with carrier only (DMSO, 1 %, v/v), or HO-cpt (5 nM), or FcN^{PG2/PG1}-L-E-cpt (0.5 μ M) (**D**). Student’s t test: ns= p>0.05, *: p< 0.05, **: p< 0.01, ***: p< 0.001.

Encouraged by the *in vitro* results, we studied the anti-cancer activity and cancer selectivity *in vivo*. In a preliminary study, healthy mice were treated over seven days with 24 mg/kg FcN^{PG2/PG1}-L-E-cpt, while another group received a four times lower dose of 6 mg/kg cpt. As shown in Figure 31, A the HO-cpt-treated mice lost weight, indicating acute toxicity, while the FcN^{PG2/PG1}-L-E-cpt-treated mice maintained their body weight, a sign of good tolerability. To avoid prodrug precipitation, the following experiments were conducted with 12 mg/kg FcN^{PG2/PG1}-L-E-cpt. First, the anti-cancer activity was assessed in C57/BL6N mice bearing Nemeth-Kellner Lymphoma. Here, FcN^{PG2/PG1}-L-E-cpt treatment could significantly increase the mean mice survival ($t_{1/2}$) (Figure 31, B). To investigate whether the prodrug design indeed spares neutrophils and other immune cells, healthy mice were treated for 7 days (3 injections each) with prodrug FcN^{PG2/PG1}-L-E-cpt (12 mg/kg), HO-cpt (6 mg/kg) or just the carrier DMSO and the number of various types of cells in the blood and bone marrow were counted. The results for the neutrophils in the blood are shown in Figure 31, C. Cpt is affecting the

neutrophils substantially, whereas the number of neutrophils in the FcN^{PG2/PG1}-L-E-cpt-treated mice did not differ before and after the treatment in comparison to the DMSO treated mice.

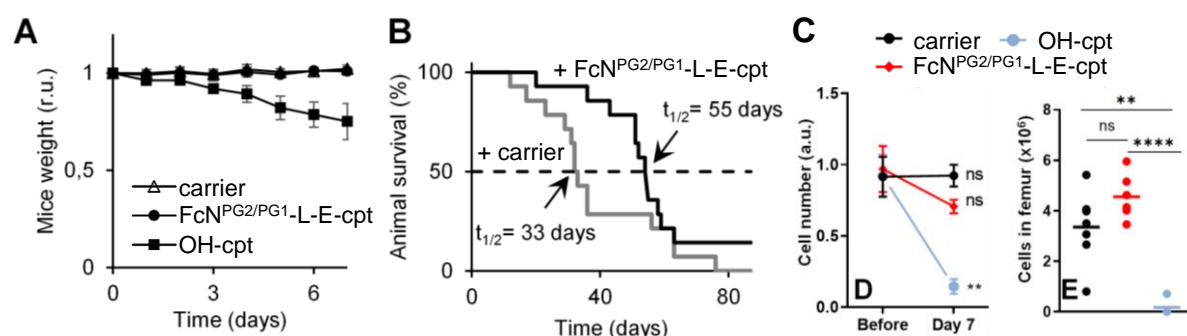


Figure 31: Weight of healthy mice treated with DMSO (“carrier“), or FcN^{PG2/PG1}-L-E-cpt (12 mg/kg), or HO-cpt (6 mg/kg), injected intraperitoneal (i.p.) on days 0, 2 and 4 (A). Effects of FcN^{PG2/PG1}-L-E-cpt (12 mg/kg) injected i.p. on days 1, 3, 6, 8, 10, 13, 15, 17, 20 and 22 in comparison to just DMSO (“carrier”) injections on the survival of mice carrying Nemeth-Kellner lymphoma (B). Monitoring of the number of neutrophils in the blood of healthy mice treated as described for (A). The analysis was conducted before the first treatment and on day 7 of the treatment plan (C).

Altogether, these experiments demonstrate the selectivity of the developed prodrug and thus the suitability of the dual triggering mechanism for the sequential activation of prodrugs first by ROS via B-C bond cleavage, and secondly by hydroxide ions via ferrocenium degradation. This prodrug approach spares normal cells (low ROS levels) and even activated neutrophils (high ROS levels, but a low number and mass of mitochondria and thus no increased levels of hydroxide ions). In this way, neutropenia can be avoided. By applying the promoiety to a model compound containing a tertiary alcohol (1,1-dimethylbenzyl, dmb, Publication 7, Figure S30, A, S1) and a drug (HO-cpt), we demonstrate that this approach is generalizable, and in theory, can be applied for any chemotherapeutic drug with a hydroxyl group that is important for its activity.

3. Publications and contributions of the author

Publication 1:

3D-shaped binders of unfolded proteins inducing cancer cell specific endoplasmic reticulum stress *in vitro* and *in vivo*

Insa Klemt,^[a] Oleg Varzatskii,^{[b],[c]} Roman Selin,^[a] Serhii Vakarov,^{[b],[c]} Vladyslava Kovalska,^{[b],[d]} Galyna Bila,^{[e],[f]} Rostyslav Bilyy,^{[e],[f]} Yan Voloshin,^[g] Itziar Cossío Cuartero,^[h] Andrés Hidalgo,^[h] Benjamin Frey,^[i] Ina Becker,^[i] Bernhard Friedrich,^[j] Rainer Tietze,^[j] Ralf P. Friedrich,^[j] Christoph Alexiou,^[j] Elena-Laura Ursu,^[k] Alexandru Rotaru,^[k] Iris Solymosi,^[a] M. Eugenia Pérez-Ojeda,^[a] and Andriy Mokhir^[a]

^[a]Friedrich-Alexander-University of Erlangen-Nürnberg (FAU), Department of Chemistry and Pharmacy, Organic Chemistry II, 91058 Erlangen, Germany

^[b]Princeton Biomolecular Research Labs, 26A Saperne Pole St., Kyiv, Ukraine

^[c]V.I. Vernadsky Institute of General and Inorganic Chemistry, NASU, 32/34 Palladin Av., 03142 Kyiv, Ukraine

^[d]Institute of Molecular Biology and Genetics, NASU, 150 Zabolotnogo St., 03143 Kyiv, Ukraine

^[e]Danylo Halytsky Lviv National Medical University, Department of Histology, Cytology and Embryology Pekarska str. 69, 79010 Lviv, Ukraine

^[f]Lectinotest R&D, Mechanichna Str 2, 79024, Lviv, Ukraine

^[g]Nesmeyanov Institute of Organoelement Compounds, RAS, 28 Vavilova St., Moscow, Russia

^[h]Program of Cardiovascular Regeneration, Centro Nacional de Investigaciones Cardiovasculares Carlos III (CNIC), C. Melchor Fernández Almagro, 3, 28029 Madrid, Spain

^[i]Friedrich-Alexander-University of Erlangen-Nürnberg (FAU), Universitaetsklinikum Erlangen, Department of Radiation Oncology, Translational Radiobiology, Glueckstrasse 4A, 91054 Erlangen, Germany

^[j]Friedrich-Alexander-University of Erlangen-Nürnberg (FAU), University Hospital, Department of Otorhinolaryngology, Head and Neck Surgery, Section of Experimental Oncology and Nanomedicine (SEON), Glückstraße 10a, 91054 Erlangen, Germany

^[k]“Petru Poni” Institute of Macromolecular Chemistry, Romanian Academy, Centre of Advanced Research in Bi-nanoconjugates and Biopolymers, Grigore Ghica Voda Alley 41 A, 700487 Iasi, Romania

Contribution of I. Klemt:

All experiments performed in cell-free settings, except AFM and ITC experiments. All cellular experiments performed in A2780, BL-2, SBLF9 and SK-MES-1 cells. Data processing, figure design, manuscript preparation and revision, abstract image design.

The publication and supporting information are found under: DOI: [10.1021/jacs.3c08827](https://doi.org/10.1021/jacs.3c08827).

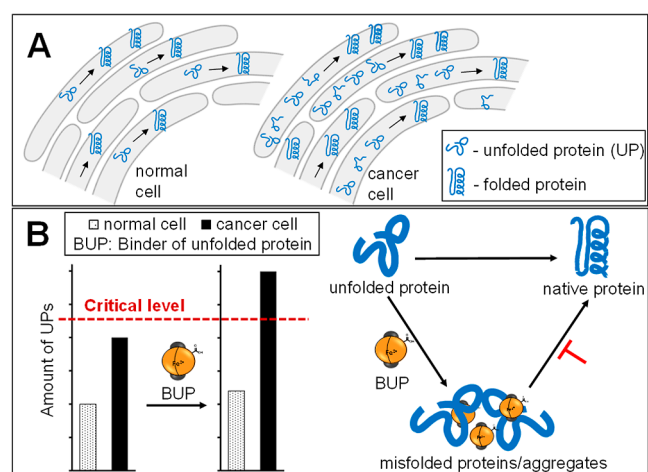


Figure 1. (A) Illustration of a hallmark of cancer cells: a higher intracellular amount of UPs and enhanced ER stress. (B) Approach to selectively kill cancer cells by inducing the ER stress by a binder of UPs (BUP). The critical level of the ER stress is indicated with a red line.

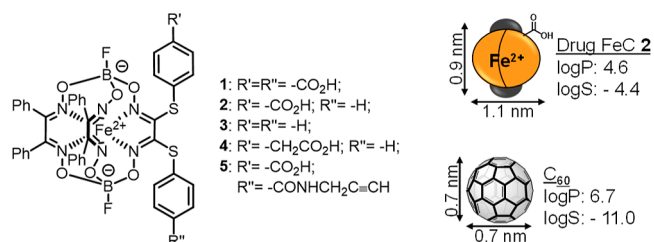
63 which catalyze generation of reactive oxygen species (ROS)
 64 $O_2^{\bullet-}$ and $HO\bullet$ from O_2 and H_2O_2 , respectively. A
 65 representative of the complexes of the latter type is the half-
 66 sandwich Ru^{2+} arene complex, which catalyzes oxidation of
 67 glutathione (GSH) to GSSG.¹¹ Third, metal complexes induce
 68 generation of toxic products via photoinduced energy or
 69 electron transfers, e.g., VO^{2+} , bimetallic Cu^+-Fe^{2+} , and Ir^{3+}
 70 complexes,^{12–14} all act as photosensitizers by generating ROS
 71 including either 1O_2 or $O_2^{\bullet-}$ or both of them. Fourth,
 72 positively charged lipophilic compounds, e.g., cyclometalated
 73 Ir^{3+} complexes,¹⁵ are accumulated in the negatively charged
 74 membrane of mitochondria (Mit) causing Mit dysfunction and
 75 ROS production. In all of these cases, either coordination of
 76 CUCs to nucleophilic sites of biological macromolecules or
 77 direct or indirect intracellular ROS generation or both take
 78 place not only in cancer but also in normal cells, which leads to
 79 undesired toxicity.

80 In search of alternative ER stress inducers, which are not
 81 CUCs and do not cause systemic ROS production, we were
 82 drawn to binders of UPs (BUPs). These could stabilize UPs,
 83 eventually leading to their accumulation or/and aggregation,
 84 thereby inducing the ER stress (Figure 1B). The interaction of
 85 BUP and UPs is at least a bimolecular reaction. As such, it is
 86 strongly dependent on concentrations of both BUP and UPs.
 87 In cancer cells containing the high level of UPs, the
 88 equilibrium $BUP + UPs \rightarrow BUP/UPs$ is shifted to the BUP/
 89 UPs, leading to ER stress. In contrast, in normal cells
 90 containing the low level of UPs, this equilibrium is shifted
 91 toward the unbound UPs, which can be normally processed.
 92 Thus, the optimized BUP will be toxic to cancer cells, but not
 93 affect normal cells (Figure 1B), thereby solving the problem of
 94 side effects of common ER stress inducers.^{3–15}

95 Several synthetic binders of UPs have been identified
 96 previously, e.g., chemical chaperones 4-phenylbutyrate and
 97 lysophosphatidic acids¹⁶ as well as a molecular tweezer
 98 CLR01.¹⁷ In contrast to the suggested BUPs, they reduce
 99 the intracellular load of UPs, thereby attenuating rather than
 100 enhancing the ER stress.¹⁸ Correspondingly, the anticancer
 101 activity of these compounds is low.¹⁹ Another potential BUP is
 102 the carbon allotrope fullerene C_{60} . Though it is known to bind
 103 strongly UPs,²⁰ medicinal applications of C_{60} are limited by its

poor solubility in water ($\log S = -11.0$ ²¹). A better water-
 soluble metal-containing carbon allotrope $Gd-C_{82}(OH)_{22}$
 exhibits moderate anticancer activity.²² However, its mode of
 action is not related to binding UPs. We have previously
 prepared and studied Fe-clathrochelates (FeCs), which are
 coordination compounds with a 3D-shaped structure having
 dimensions similar to that of C_{60} (Scheme 1).²³ We have

Scheme 1. Structures and Some Properties of Drugs/
 Controls FeCs 1–5 and C_{60} ²¹



found that, similarly to C_{60} , the FeCs functionalized with either
 six (Vz375,²⁴ Scheme S1, Supporting Information) or two
 carboxylic acid moieties (FeC 1,²⁵ Scheme 1) bind to model
 UPs. Their anticancer activity has not been studied before.
 Compared to C_{60} , FeCs exhibit several favorable properties. In
 particular, as less hydrophobic compounds, the FeCs are more
 water soluble (e.g., $\log S = -4.4$ for FeC 2, Scheme 1).
 Furthermore, in contrast to C_{60} , they are not redox active at
 physiological conditions and therefore are not expected to
 directly generate ROS or other toxic reactive species that could
 adversely affect normal cells. Importantly, chemical modifica-
 tion of the exterior of FeCs is straightforward and can be
 achieved by the variation of the substituents of the dioxime
 ligands and boron-containing cap groups that allows fine-
 tuning of the properties of FeCs for medicinal applications.²³
 All of the factors mentioned above make FeCs a suitable
 scaffold for the development of the BUPs. A single previously
 reported FeCs exhibiting some anticancer activity is electro-
 philic FeC-Cl₆ (Scheme S1, Supporting Information).²⁶ The
 latter compound alkylates intracellular glutathione (GSH),
 leading to the ROS increase in both cancer and normal cells
 and, therefore, is not suitable for further development as a
 drug.

In this paper, we report on optimized BUP FeC 2. It binds
 model UPs, induces the ER stress, as well as increases the
 levels of mitochondrial ROS and nitric oxide (NO) in cancer
 cells. In contrast, it does not affect normal cells. Further, FeC
 is nontoxic in vivo up to a dose of 147 mg/kg and exhibits strong
 anticancer and antimetastatic activities in three murine models
 of cancer.

RESULTS AND DISCUSSION

**Preliminary Studies, Synthesis, and Properties of the
 Selected FeCs in Cell-Free Settings.** Though previously
 reported Vz375²⁴ and 1²⁵ bind UPs, they are either inactive
 (Vz375, half-maximal inhibitory concentration (IC_{50}) > 50 μM
 for human ovarian carcinoma A2780 cells) or exhibit weak
 anticancer activity toward a range of cancer cell lines: The IC_{50}
 value of 1 for human acute promyelocytic leukemia HL-60,
 A2780, Burkitt's lymphoma BL-2, T-cell leukemia Jurkat, and
 lung cancer SK-MES-1 cells is >32 μM , whereas the IC_{50} value
 for murine lung cancer LLC1 cells is >15 μM (Table 1).

Table 1. Effects of FeCs on the Viability of Selected Cancer Cell Lines^a

FeC	IC50 (μM) ^d for cell lines					
	HL-60	A2780	BL-2	Jurkat	SK-MES1	LLC1
1	40 \pm 2	40 \pm 1	32 \pm 5	>50 ^b	43 \pm 3	>15 ^c
2	1.3 \pm 0.3	2.6 \pm 0.6	0.6 \pm 0.1	3 \pm 1 ^b	21 \pm 2	12.0 \pm 0.4 ^c
4		2.9 \pm 0.2				
5		4.7 \pm 0.0				

^aThe cells were incubated with the compounds for 48 h, except of data indicated with. ^b(24 h) and. ^c(72 h). FeC = clathrochelate. ^dIC50: half-maximal inhibitory concentration.

Since these FeCs are relatively polar due to the presence of six (Vz375) or two (1) carboxylic acid groups, their low activity could be caused by the inefficient membrane permeability. To determine whether this is the case, we investigated the uptake of one of these compounds in BL-2 cells. By using atomic emission spectroscopy (AES), we observed no statistically significant increase of the intracellular amount of both iron and boron in BL-2 cells incubated for 4 h with 1 (9 μM) as compared to untreated BL-2 cells (Figure 2A).

These data confirm that the uptake of FeC 1 by BL-2 cells is poor. In search for membrane-permeable FeCs, we explored potentially more lipophilic compounds containing one (2) or no carboxylic acids (3²⁷) (Scheme 1). The previously unknown FeC 2 was prepared starting from the electrophilic FeC intermediate S1 by the nucleophilic substitution reaction using thiophenol in the presence of triethylamine (NEt₃) as described in the Supporting Information. To evaluate the lipophilicity of FeCs 2 and 3, we determined their *n*-octanol/water partition coefficients (log *P*'s, Table S1, Supporting Information). As expected, both compounds (log *P*(2) = 4.6 \pm 0.2 and log *P*(3) = 5.6 \pm 0.3) are more lipophilic than the reference FeC 1 (log *P* = 3.7 \pm 0.1). Importantly, despite its higher lipophilicity, the solubility of FeCs 2 in aqueous solutions is still sufficient for the studies of its biological activity: 40 \pm 8 μM in aqueous phosphate-buffered saline (PBS) solution and 74 \pm 10 μM in Roswell Park Memorial Institute 1640 (RPMI 1640) medium containing fetal bovine serum (FBS, 5%), L-glutamine (Gln, 1%), and penicillin/streptomycin (1%) (Table S2, Supporting Information). In contrast, FeC 3 is insoluble at >10 μM in the aqueous solutions that precluded its further tests. All further studies focused on FeC 2 and its analogues 4 and 5.

Anticancer Effects, the Active Form of FeC 2. The reference FeC 1 is weakly toxic toward several human and murine cancer cell lines originating from blood (HL-60, BL-2, Jurkat), ovary (A2780), and lungs (SK-MES1, LLC1). We tested the effects of FeC 2 on the same set of cells to be able to compare the anticancer efficacies of 2 and reference 1. We found that FeC 2 is a substantially more potent anticancer agent than 1, affecting cell viability at IC₅₀ ranging from 0.6 μM for the most sensitive BL-2 cells to 21 μM for the least sensitive SK-MES1 cells (Table 1). These data show that the presence of one rather than two or six CO₂H groups is required for the anticancer activity of FeC. We conducted further in vitro studies mostly with A2780 cells as a representative cancer cell line. In few cases, the same experiments were also done for BL-2 cells to confirm that the effects observed are not restricted to a single cell line.

To find out whether it is critical for the activity that the CO₂H group is directly attached to the phenyl ring, we prepared an analogue FeC 4 containing a methylene bridge

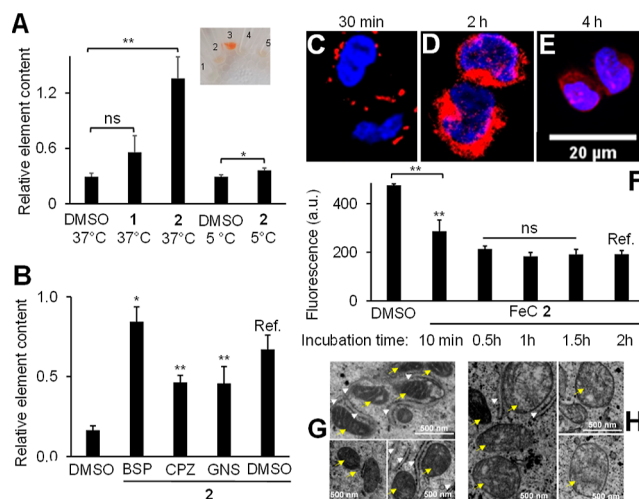


Figure 2. (A) Uptake of FeCs 1 and 2 (each 9 μM , incubation: 4 h) in BL-2 cells at 37 or 5 °C by monitoring intracellular iron content (data on the boron content: Figure S16, Supporting Information). Inset: a photo of BL-2 cells incubated with FeC or controls (orange color indicates accumulation of FeCs): (1) DMSO, 37 °C; (2) FeC 1, 37 °C; (3) FeC 2, 37 °C; (4) DMSO, 5 °C; and (5) FeC 2, 5 °C. (B) Cells were pretreated with the OAT inhibitor bromsulphthalein (BSP, 500 μM , 5 min preincubation), with the clathrin-mediated uptake inhibitor chlorpromazine (CPZ, Ten $\mu\text{g}/\text{mL}$, 2 h preincubation) or with the caveolin-mediated uptake inhibitor genistein (GNS, 400 μM). After the preincubation, the cells were treated with FeC 2 for 2 h in the medium at 37 °C. The uptake was evaluated by determination of intracellular iron amount. (C–E) Visualization of the intracellular distribution of FeC 5 (9 μM) in A2780 cells after 0.5, 2, and 4 h incubation. FeC was labeled by Alexa Fluor 594 Azide. The nuclei of the cells were costained with Hoechst 33342. Ch1 (red)— λ_{ex} : 561 nm; λ_{em} : 595 \pm 50 nm; Ch2 (blue)— λ_{ex} : 355 nm; and λ_{em} : 450 \pm 50 nm. (F) Effects of the time of FeC 2 (9 μM) incubation with A2780 cells (10 min–2 h) on ER-specific staining of the cells. After the cells were incubated with the FeC for the specified time, the ER probe was added, and the cells were incubated for an additional 20 min (Supporting Information). For (A,B,F), unpaired Student's *t*-test *: *p* < 0.05; **: *p* < 0.01; ***: *p* < 0.001; ns > 0.05. (G,H) TEM images of A2780 cells. (G) Control (no FeC added). (H) FeC 2 (9 μM), preincubation for 4 h. White arrowheads indicate ER, and yellow arrows indicate mitochondria (Mit).

between the phenyl ring and the CO₂H group. This compound was obtained in two steps (Supporting Information). First, the nucleophilic substitution reaction between the electrophilic intermediate S2 and 2-(4-mercaptophenyl)acetic acid in the presence of NEt₃ furnished intermediate S3. Second, S3 was reacted with thiophenol in the presence of NEt₃ to obtain FeC 4. We found that the anticancer efficacy of FeC 4 in A2780 cells (IC₅₀ = 2.6 \pm 0.6 μM) is identical to that of FeC 2 (IC₅₀ = 2.9 \pm 0.2 μM , Student's *t*-test, *p* > 0.05). These data might

213 indicate that the binding sites of **2** and **4** in their putative target
214 can tolerate at least small structural changes that would be in
215 agreement with binding to unstructured UPs. The latter
216 conclusion is further supported by the fact that FeC **5**,²⁸
217 containing a larger propargylaminocarbonyl moiety in the para-
218 position of one of the phenyl residues, is only slightly less
219 active than its analogue **2**: IC₅₀ = 4.7 ± 0.0 μM versus 2.6 ±
220 0.6 μM, correspondingly (Table 1). We used FeC **5** for the
221 study of the intracellular distribution of FeCs as described
222 below.

223 Lipophilic drugs can form aggregates in aqueous solutions,
224 which may destabilize the protein structure, leading to their
225 unfolding, thereby causing both cell- and target-unspecific
226 toxicity.²⁹ To exclude this possibility, we investigated whether
227 FeC **2** forms aggregates by using UV–visible spectroscopy and
228 dynamic light scattering (DLS). We observed that the
229 absorbance at 487 nm (*A*_{max}) of solutions of **2** in aqueous
230 PBS (pH 7.4) is linearly dependent on the compound
231 concentration up to at least 30 μM (*R*² = 0.9986, Figure
232 S10, Supporting Information), indicating that only one species
233 exists in this concentration range. Further, we did not detect
234 aggregated species in aqueous solutions of FeC **2** at <30 μM by
235 using DLS. These data indicate that **2** exists in the monomeric
236 form in aqueous solutions at <30 μM concentrations. Since
237 IC₅₀ values for the tested cancer cell lines are also <30 μM
238 (Table 1), we conclude that the monomeric form rather than
239 the aggregates is responsible for the anticancer activity of the
240 FeC.³⁰

241 A single previously described clathrochelate exhibiting
242 strong anticancer activity is an electrophilic derivative
243 FeC₆-Cl₆ (Scheme S1, Supporting Information). Its mode of
244 action relies on the covalent modification of GSH via the
245 nucleophilic substitution of the chlorides in the FeC.²⁶
246 Potentially, FeC **2** could exhibit similar chemical reactivity
247 via the substitution of a PhS[−] moiety with GS[−] derived from
248 GSH. It is a less likely reaction because PhS[−] is not as good
249 leaving group as Cl[−]. However, in cancer cells, the latter
250 reaction can be facilitated by the follow-up oxidation of PhS[−]
251 to PhSSPh, thereby shifting the equilibrium toward the
252 product. By using LC–MS (Figure S11, Supporting
253 Information) as well as by monitoring the release of free
254 Fe²⁺ and Fe³⁺ ions (Table S3, Supporting Information), we
255 confirmed that FeC **2** is chemically stable both in the absence
256 and presence of GSH. We also found that this compound is
257 stable under other conditions, which it could encounter in
258 cancer cells: pH 7.4 (cytoplasm), pH 5 (lysosome), and in the
259 presence of H₂O₂ (ER) (Figure S11 and Table S3, Supporting
260 Information). The high stability of the FeC is also retained in
261 cells. In particular, we analyzed the extract of A2780 cells
262 incubated with this compound (3 μM) for 1 and 24 h by using
263 LC–MS (Figures S12–S14, Supporting Information). We
264 detected only the parent compound after 1 h of incubation,
265 whereas at the longer incubation time (24 h), we additionally
266 detected metabolite **2a** (educt of **2** with GSH), which was
267 formed with 10% yield. As discussed below, the biological
268 effects, including the induction of the ER stress, occur already
269 after 10 min of the incubation of **2** with cells. Therefore, the
270 metabolite **2a** that formed much later is not expected to play a
271 critical role in the activity of **2**. These data confirm that **2** acts
272 via the different mechanism than the previously reported
273 FeC₆-Cl₆.²⁶

274 **Uptake Mechanism, Intracellular Distribution, and**
275 **Effects of FeC **2** on Intracellular Organelles.** For the

uptake studies, we selected 9 μM FeC's as the highest drug
276 concentration not causing significant cell death at short
277 incubation times (<8 h). In contrast to FeC **1**, the uptake of
278 FeC **2** by BL-2 and A2780 cells is substantial at 37 °C (Figure
279 2A). That explains why **2** is a more potent anticancer agent
280 than **1** (Table 1 and Figures S8 and S9, Supporting
281 Information). The uptake of **2** is strongly inhibited at 5 °C
282 (Student's *t*-test, *p* < 0.01, Figures 2A, S15, and S16,
283 Supporting Information). The latter data indicate that the
284 cellular transport of the FeC requires energy and, therefore,
285 occurs via the active mechanism or mechanisms. We identified
286 these to be clathrin- and caveolin-mediated endocytosis since
287 chlorpromazine (CPZ) and genistein (GNS), which are
288 inhibitors of these biochemical processes, suppress the uptake
289 of **2** significantly (*p* < 0.01, Figures 2B and S18, Supporting
290 Information). A mixture of CPZ and GNS affects the uptake of
291 FeC **2** even more strongly than the individual inhibitors,
292 indicating additive clathrin- and caveolin-mediated endocytosis
293 (Figure S19, Supporting Information). In contrast, the
294 inhibitor of organic anion transporters (OATs) bromsultha-
295 lein (BSP) does not suppress the uptake, indicating that OATs
296 are not involved in the transport of **2** (Figure 2B).
297

To evaluate the intracellular distribution of FeC **2**, we
298 prepared its analogue containing a terminal alkyne moiety—
299 FeC **5**, whose synthesis was described elsewhere.²⁹ Incubation
300 of A2780 cells with FeC **5** (9 μM) for 0.5, 2, and 4 h followed
301 by their fixation, treatment with either Alexa Fluor 488 azide or
302 Alexa Fluor 594 azide under the conditions of Cu⁺-catalyzed
303 alkyne–azide cycloaddition “click” reaction, washing, and
304 monitoring the signal of the Alexa Fluor dyes allowed
305 visualization of the transport of the FeC (Figure 2C–E). We
306 found that the fluorescence signal observed in A2780 cells
307 treated with FeC **5** can be suppressed by the coincubation of **5**
308 with the unlabeled **2**, indicating that both **5** and **2** bind to the
309 same intracellular target or targets (Figure S20, Supporting
310 Information). After incubation for 30 min, the FeC is located
311 in the cellular periphery, which can be the cellular membrane
312 and/or the FeC bound to the components of the active
313 transport associated with the membrane (Figures 2C and S21,
314 Supporting Information). At the longer incubation time (2 h),
315 the FeC is located in the proximity of the nucleus that can be
316 either ER or Golgi or both (Figures 2D and S21, Supporting
317 Information). Attempts to conduct the colocalization experi-
318 ments of these in situ formed dye conjugates with known ER-
319 and lysosome (LY)-staining probes were not successful since
320 the stringent washing used in such experiments affected the
321 intracellular distribution of the conjugates. At the longest
322 incubation time (4 h), the FeC is distributed evenly within the
323 cell. For example, its signal is partially colocalized with the
324 nuclear stain (Pearson's coefficient 0.55, Figures 2E and S21,
325 Supporting Information).
326

Within cells, UPs are formed, processed, and eventually
327 accumulated mostly in the ER and LYs. Correspondingly, if
328 FeC **2** induces the accumulation of UPs (Figure 1B), one of
329 these organelles or both of them might be stressed. We
330 observed that after only 10 min of incubation with FeC **2**, the
331 fluorescence of A2780 cells, stained with the ER-specific dye
332 ER-tracker Green for an additional 20 min, is significantly
333 reduced (*p* < 0.01), indicating that the ER is affected. The
334 effect is saturated after 30 min of incubation (Figure 2F). In
335 contrast, FeC **2** (up to 24 h incubation) does not change the
336 fluorescence of the cells labeled with LY-specific dye acridine
337 orange (Figures S22 and S23, Supporting Information) that
338

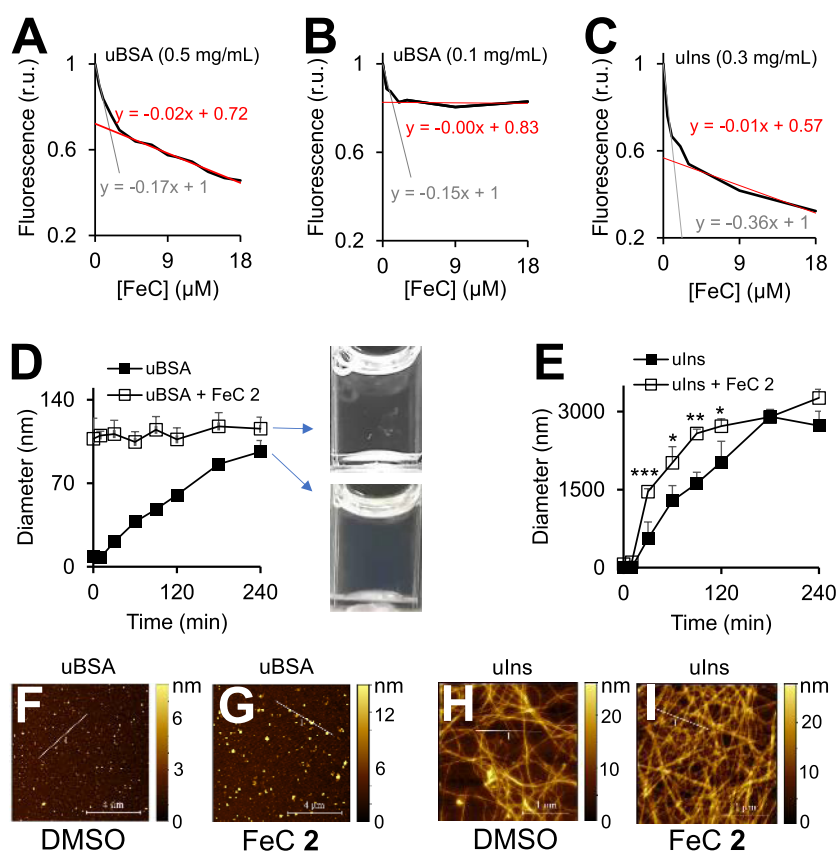


Figure 3. (A–C) Dependence of the fluorescence of associates of UPs (unfolded bovine serum albumin: uBSA or unfolded insulin: uIns) with thioflavin T (ThT, 10 μM , $\lambda_{\text{ex}} = 440 \text{ nm}$; $\lambda_{\text{em}} = 480 \pm 10 \text{ nm}$) from the concentration of FeC 2. Other conditions: incubation time, 100 min; temperature, 45 $^{\circ}\text{C}$; DTT (1 mM for uBSA and 20 mM for uIns); and DMSO (1% (v/v)). (D) Kinetics of uBSA (0.5 mg/mL) aggregation in the presence of DTT (1 mM) at 45 $^{\circ}\text{C}$ were monitored by DLS. [FeC 2] = 9 μM . The measurement at time point 0 min was performed before DTT addition. The size of the main peak was plotted vs the incubation period. Photos of cuvettes with uBSA and uBSA/FeC 2 samples after 240 min incubation are included. (E) Kinetics of uIns (0.3 mg/mL) aggregation in the presence of DTT (20 mM). Other conditions are as described in (D). AFM images of uBSA in the absence (F) and presence (G) of FeC 2. AFM images of uIns in the absence (H) and presence (I) of FeC 2. Height profiles along traces labeled with “I” are given in Figure S33, Supporting Information.

339 excludes LYs as the primary target of the FeC. Interestingly,
 340 treatment of the cells loaded with the Mit-specific dye
 341 rhodamine 123 (R123) with FeC 2 for 4 and 24 h also leads
 342 to the strong decrease of the R123 fluorescence, indicating that
 343 the FeC affects the Mit (Figures S22 and S23, Supporting
 344 Information). The latter effect is secondary to that on the ER
 345 since it appears at a substantially longer incubation time. In
 346 particular, the effect on the ER is saturated after 30 min
 347 incubation, whereas that on Mit is not saturated even after 4 h
 348 incubation (Figure S24, Supporting Information). By using JC-
 349 1, a dye sensitive to Mit membrane potential (MMP), we
 350 found that the FeC induces the decrease of MMP (Figures S25
 351 and S26, Supporting Information).

352 Next, we determined whether the FeC is physically
 353 accumulated in particular organelles or whether the observed
 354 effects are indirect. These experiments required large cell
 355 numbers (5×10^7 cells) due to the technical limitations of the
 356 analytical method (AES) applied for monitoring Fe and B
 357 derived from the FeC in organelles (Supporting Information).
 358 We used BL-2 rather than A2780 cells since the former cells
 359 can be easily obtained in large quantities. We analyzed the
 360 content of ER, Mit, and LYs from the cells, which were
 361 preincubated with FeC 2 (9 μM) for 1 h, and found that only
 362 ER and Mit, but not LY fractions contain FeC 2 (Figures S27

and S28, Supporting Information). These data indicate that 363
 FeC is directly accumulated in the ER and Mit. 364

By using TEM (Figure 2G,H; more detailed images are 365
 provided in Figure S29, Supporting Information), we visualized 366
 morphological changes of the intracellular organelles in 367
 response to the FeC treatment. We found that the short (10 368
 min) treatment of A2780 cells causes changes of morphology 369
 of Mit including the alteration of the cristae membrane and 370
 intracrystal space from typical parallel orientation (Figures 2G 371
 and S29A, Supporting Information) to less ordered intra-Mit 372
 structures (Figure S29C, Supporting Information). Further- 373
 more, the FeC-treated cells contain ER's of irregular width and 374
 those exhibiting interruptions (Figure S29D, Supporting 375
 Information). These effects are strengthened under the 376
 prolonged treatment (4 h). For example, under the latter 377
 conditions, the cristae membrane is practically fully destroyed 378
 (Figures 2H and S29E, Supporting Information) and a number 379
 of swollen ER's are present (Figure S29F, Supporting 380
 Information). 381

Thus, according to the data described in this section, we 382
 could identify the ER as a primary target and Mit as a 383
 secondary target of FeC 2. 384

**Mechanism of Anticancer Activity of FeC 2. Studies in 385
 Cell-Free Settings.** We considered two possible modes of 386
 action of FeC 2, which could cause an effect on the ER, leading 387

388 to the anticancer activity. First, this FeC can first bind UPs,
389 inhibiting their maturation or inducing aggregation, thereby
390 causing the ER stress. This possibility is based on the fact that
391 the previously described analogues of **2**, clathrochelates
392 Vz375,²⁴ and **1**²⁵ are binders of UPs in cell-free settings.
393 Second, since FeC **2** is a complex of Fe²⁺, it can potentially
394 induce the generation of highly toxic species O₂^{•-} and HO• by
395 donating an electron from the metal ion to the less toxic
396 species O₂ and H₂O₂, thereby inducing oxidative stress in the
397 ER and disturbing its function. It has been previously reported
398 that ROS inducers can cause the ER stress, leading to cancer
399 cell death.^{10,11} In this section, the experiments will be
400 described, which allowed us to confirm one of these
401 possibilities.

402 To evaluate whether FeC **2** binds to UPs, we first selected
403 unfolded bovine serum albumin (further uBSA) as a
404 representative protein. uBSA was obtained by incubation of
405 BSA with a dithiothreitol (DTT, 1 mM) at 45 °C. We
406 confirmed formation of uBSA under these conditions by using
407 thioflavin T probe (ThT, 10 μM), whose fluorescence is
408 increased in the presence of unfolded and aggregated
409 proteins³¹ (Figure S30, Supporting Information). The increase
410 of the fluorescence of the ThT/uBSA solutions (F100) is
411 >90% complete after 100 min incubation. In further studies, we
412 used normalized values of F100, which were obtained by
413 dividing the fluorescence in the presence of FeC **2** at the
414 concentration from 3 to 18 μM by the fluorescence in its
415 absence (Figure 3A,B). F100 is strongly quenched by FeC in a
416 dose-dependent fashion. Since in the absence of uBSA the FeC
417 does not affect the fluorescence of ThT (Figure S31A,
418 Supporting Information), the latter data indicate that the
419 FeC binds to uBSA. The quenching curve obtained at the
420 higher concentration of uBSA (0.5 mg/mL) is represented by
421 two linear regions: the first one is steeper (F100 = -0.17 ×
422 [FeC **2**] + 1, black trendline), while the second one is more flat
423 (F100 = -0.02 × [FeC **2**] + 0.72, red trendline) (Figure 3A).
424 At a lower uBSA concentration (0.1 mg/mL), the latter region
425 is absent. These data might indicate that the first region
426 corresponds to binding of the FeC to uBSA and the second
427 region to binding of the FeC to aggregated uBSA, whose
428 formation is expected to be strongly concentration dependent.
429 Interestingly, the same trend is observed in the quenching
430 experiment, where uBSA was replaced with unfolded insulin
431 (uIns, Figure 3C).

432 Due to limitations in solubility of FeC **2**, saturation of the
433 quenching curves could not be reached (Figure 3A–C).
434 Furthermore, binding of FeC **2** to products obtained after
435 protein unfolding, followed by protein aggregation, is a
436 complex process that makes it difficult to suggest a suitable
437 model for fitting the experimental data. Due to these reasons,
438 estimation of the binding constant of the FeC with the UPs
439 was not possible based on the data shown in Figure 3A–C. In
440 an attempt to address this issue, we applied isothermal titration
441 calorimetry. We selected uIns rather than uBSA as a model
442 protein due to its better water solubility. According to the
443 baseline-corrected and blank-subtracted data, uIns binds FeC **2**
444 in an exothermic process (Figure S32, Supporting Informa-
445 tion). Unfortunately, the heat differences observed as well as
446 the *c*-value were too small for the reliable determination of
447 thermodynamic parameters of the uIns/FeC **2** interaction
448 (Supporting Information). Reasons for that are limitations in
449 the solubility of the reactants and heat compensation caused by
450 the endothermic process of uIns dilution upon titration.

To study aggregation of the UPs in the presence of FeC **2**,
we used DLS. We observed that the aggregates with a size of
110 ± 4 nm are formed immediately after mixing BSA (0.5
mg/mL) and FeC **2** (9 μM). Larger aggregates are not
detected by DLS. However, they are also generated and, due to
the low solubility in water, precipitated in the form of flakes
(Figure 3D). In contrast, the uBSA aggregates grow
substantially slowly (*t*_{1/2} ~ 120 min) in the absence of the
FeC, and precipitation is not observed (Figure 3D). Aggregates
of uIns are more soluble and do not precipitate. Therefore,
steady growth of these species up to 3 μm in the presence of
FeC **2** is observed within 240 min. In contrast, the growth rate
of uIns is slower in the absence of FeC **2**. The latter data are
confirmed by atomic force microscopy (AFM). In particular,
uBSA forms <10 nm (in height) nanoparticles, whereas in the
presence of FeC **2**, the size of the nanoparticles is increased up
to 60 nm (Figures 3F,G and S33, Supporting Information).
uIns form fibrils rather than nanoparticles. We observed that in
the presence of FeC **2**, more fibrils were formed (Figure 3H,I).
Moreover, the thickness of the fibrils is larger in the presence
of FeC **2** than in the absence of FeC **2** (Figure S33, Supporting
Information).

We observed that FeC **2** also binds the native proteins BSA
and insulin. It is reflected in FeC **2**-induced quenching of the
native protein fluorescence (Figure S34A, Supporting
Information). The binding induces quick (<10 min) formation
of aggregates of <110 nm diameter for both BSA and insulin
(Figure S34B, Supporting Information). However, the amount
of these aggregates seems to be small since they are not
detected by AFM. Furthermore, in contrast to uBSA and uIns,
no larger aggregates/precipitates are formed from native
proteins and FeC **2** as evidenced by monitoring of light
scattering of the corresponding suspensions (Figure S35,
Supporting Information). This reaction will occur in normal
cells lacking large amounts of UPs and can lead to undesired
toxicity. Since only minute amounts of the aggregates will be
formed, the negative impact is expected to be limited.

Next, we investigated whether FeC **2** can induce generation
of highly reactive O₂^{•-} and HO• from less toxic O₂ and H₂O₂
in cell-free settings under the conditions resembling the
intracellular medium: aqueous buffer, pH 7.4, GSH 5 mM. In
this experiment, we used a nonfluorescent probe 2',7'-
dichlorodihydrofluorescein (DCFH), which is oxidized to
fluorescent 2',7'-dichlorofluorescein (DCF) in the presence of
O₂^{•-} and HO•, but not O₂ and H₂O₂ (Figure S36, Supporting
Information). We observed that FeC **2** does not accelerate the
oxidation of DCFH at all. The reason for this behavior is its
high redox potential of >1 V versus Ag/AgCl reference
electrode as determined by cyclic voltamperometry (CV,
Figure S37, Supporting Information).

Cellular Assays. We investigated whether FeC **2** binds to
unfolded/aggregated proteins in living A2780 cells. The latter
proteins were stained by ThT as described by Beriault and
Werstuck.^{31b} Additionally, the cells were loaded with
LysoTracker Deep Red to stain lysosomes. The latter signal
is not affected by FeC **2** (Figures S22 and S23, Supporting
Information); therefore, it was used as a reference. We
observed that the A2780 cells labeled in this way feature
nonoverlapping green (ThT bound to unfolded/aggregated
proteins) and red (lysosomes) signals. The treatment with FeC
2 (9 μM) leads to strong quenching of the green signal (Figure
4A,B, controls are provided in Figure S38, Supporting
Information). By using flow cytometry, we confirmed that

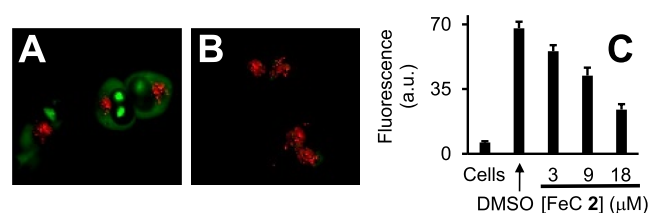


Figure 4. A2780 cells loaded with ThT (5 μM) and LysoTracker Deep Red (100 nM, reference) and treated either with carrier (DMSO, 1%, v/v) (A) or FeC 2 (9 μM) (B). Fluorescence images shown in A and B are both combinations of the green channel output ($\lambda_{\text{ex}} = 470 \pm 40$ nm and $\lambda_{\text{em}} = 525 \pm 50$ nm (monitoring ThT)) and red channel output ($\lambda_{\text{ex}} = 640 \pm 30$ nm and $\lambda_{\text{em}} = 690 \pm 50$ nm (monitoring LysoTracker Deep Red)). (C) Monitoring fluorescence of ThT-loaded A2780 cells ($\lambda_{\text{ex}} = 405$ nm and $\lambda_{\text{em}} = 450 \pm 45$ nm) treated with either carrier (“DMSO”) or FeC 2 (3–18 μM). Data for nonloaded cells (“cells”) are shown for comparison. Error bars indicate the standard deviation. An unpaired Student’s *t*-test was performed for statistical analysis. FeC 2 induces quenching of ThT-loaded cells: for 3 μM FeC 2: $p < 0.05$; for 9 and 18 μM FeC 2: $p < 0.001$.

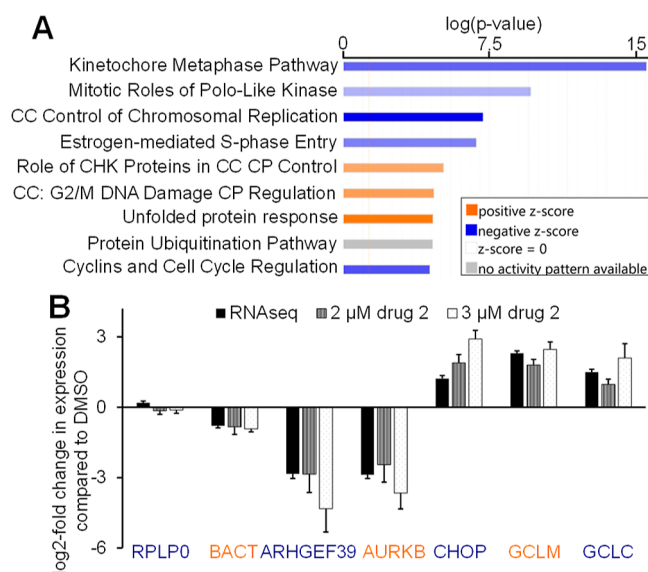


Figure 5. Impact of FeC 2 (2 μM, 1% DMSO, 24 h) on the transcriptome of A2780 cancer cells. (A) Most significantly altered canonical pathways. CC and CP are abbreviations for cell cycle and checkpoint, respectively. (B) Validation of the RNaseq experiment by determination of relative gene expression of the selected genes in the presence of 2 μM or 3 μM FeC 2 by using PCR. The data were normalized to GAPDH mRNA levels ($N = 3$, error bars indicate standard deviations).

514 this effect is dose dependent in the concentration range of 3–
515 18 μM of FeC 2 (Figure 4C). These data indicate that FeC 2
516 binds to unfolded/aggregated proteins in living A2780 cells at
517 the selected experimental conditions.

518 To get an overview of the signaling pathways that are
519 affected by FeC 2, we evaluated its effects on gene expression
520 in A2780 cells by using next-generation sequencing (RNA-
521 Seq). We determined the ratios of amounts of RNAs derived
522 from known genes in the untreated and treated groups (FeC 2:
523 2 μM, 24 h incubation) and defined these parameters as
524 FoldChange. We selected the genes fulfilling the condition of
525 \log_2 FoldChange < -2 and > 2 for further analysis (Figure S40,
526 Supporting Information). Based on the obtained data set and
527 by using Ingenuity Pathway Analysis (IPA), we identified nine
528 top scored canonical pathways induced or suppressed by the
529 FeC (IPA, Figure 5A).

530 In agreement with the previous experiments (Figure 2), two
531 of these pathways are related to ER stress: UPR and protein
532 ubiquitination pathways. The detailed effect of FeC 2 on the
533 expression of genes belonging to these pathways is outlined in
534 Figure S41A,B, Supporting Information. We validated the
535 latter result in the following four groups of independent
536 experiments. First, we confirmed the overexpression of C/EBP
537 homologous protein (CHOP) mRNA in A2780 cells treated
538 with FeC 2 using PCR (Figure 5B). CHOP(GADD153) is a
539 transcription factor known to be activated under the ER
540 stress.² Second, we observed that the level of ubiquitinated
541 proteins increased in the treated A2780 cells (Figure 6A). The
542 latter data indicated that the treatment with the FeC leads to
543 the amplification of UPs prepared for removal via the ER-
544 associated protein degradation (ERAD) system including the
545 ubiquitin–proteasome pathway.² Third, we detected the
546 formation of the elevated amount of spliced XBP1 (sXBP1)-
547 mRNA transcript 10 min after the treatment of A2780 cells
548 with FeC 2 (Figures 6B and S43, Supporting Information).
549 These data indicate the activation of eukaryotic translation
550 initiation factor 2 alpha kinase 3 (PERK) and inositol requiring
551 enzyme 1 (IRE1) arms of UPR.^{2a} In contrast, the activating
552 transcription factor 6 (ATF6) arm seems to be activated to a
553 lesser extent (Figure S41 and the summary afterward,
554 Supporting Information). Fourth, we observed the upregula-

tion of the antioxidant intracellular system controlled by
555 nuclear factor erythroid-2 related factor 2 (NRF2). This was
556 evident from the enhanced expression of NRF2 target genes
557 glutamate–cysteine ligase regulatory protein (GCLM) and
558 glutamate–cysteine ligase catalytic subunit (GCLC)³² (Figure
559 5B).
560

Further, we found that in A2780 cells treated with FeC 2,
561 the levels of mitochondrial ROS (mROS) (Figures 6C and,
562 S44, Supporting Information) and NO are increased in dose-
563 and incubation time-dependent ways (Figure S46, Supporting
564 Information). mROS ($\text{O}_2^{\bullet-}$) and NO can combine in cells
565 with the formation of a highly reactive peroxynitrite anion
566 (ONOO^-).³³ The latter chemical species induce strong
567 oxidative stress in the cancer cells that should be the cause
568 of the activation of the NRF2 system. Potentially, ROS can be
569 produced either indirectly as a consequence of the ER stress³⁴
570 or directly by donation of an electron from FeC 2 to O_2 and
571 H_2O_2 . We excluded the latter possibility based on two
572 experiments. First, we confirmed that the redox potential of
573 FeC 2 is too high to act as a catalyst in ROS generation
574 (Figures S36 and S37, Supporting Information). Second, we
575 observed that FeC 2 does not induce production of total ROS
576 (tROS) in A2780 cells, which is detected using 5-(and-6)-
577 chloromethyl-2',7'-dichlorodihydrofluorescein diacetate
578 (CMDCFH-DA) as a probe (Figure S47, Supporting
579 Information). In contrast, known iron-containing compounds
580 capable of the direct ROS generation in cell-free settings and in
581 cells, e.g., aminoferrocene-based prodrugs, usually increase the
582 level of intracellular tROS.^{11,35,36}
583

Next, we studied the effects of FeC 2 in representative
584 normal cells SBLF9. These cells were selected since they
585 contain the lower level of intracellular unfolded/aggregated
586 proteins compared to cancer A2780 cells (Figure S43,
587 Supporting Information). According to the suggested mode
588 of action (Figure 1B), we expected that FeC 2 would induce
589

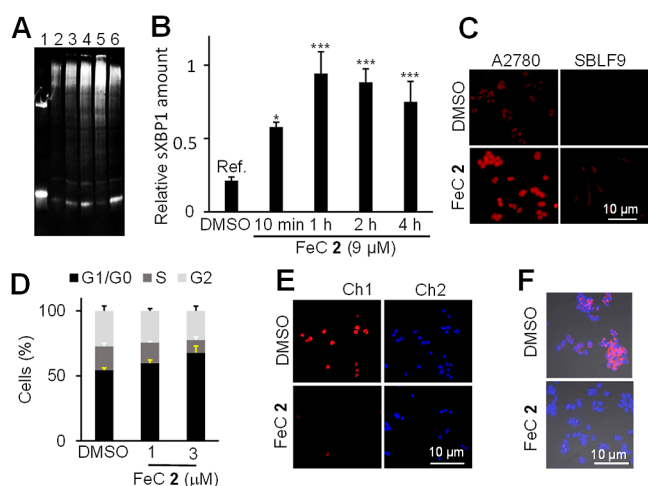


Figure 6. (A) Protein ubiquitination in A2780 cells upon treatment with DMSO (2); FeC 2 (9 μM , 30 min incubation) (3); as (2) except for 4 h incubation (4); upon treatment with bortezomib (500 nM); 4 h incubation (5); control 1 (30 μM); and 4 h incubation (6) as detected by western blotting using antiubiquitin (E412J) rabbit mAb and anti-rabbit AlexaFluor488 secondary antibodies. Fluorescence imaging was performed with an iBright FL1000 $\lambda_{\text{ex}} = 455\text{--}485$ nm and $\lambda_{\text{em}} = 510\text{--}555$. (B) Kinetics of ER stress induction in A2780 cells after incubation for 10 min–4 h with FeC 2 (9 μM) and subsequent determination of relative sXBP1 concentrations by qPCR using RPLP0 as a housekeeping gene. (C) Fluorescence of MitoSOX-loaded A2780 and SBLF9 cells incubated either with DMSO (1%, v/v) or FeC 2 (9 μM , incubation time 2 h) determined by fluorescence microscopy. (D) Effects of FeC 2 on the cell cycle of A2780 cells: incubation time 24 h. (E) Effects of FeC 2 (9 μM , incubation time 4 h) on the *de novo* synthesis of DNA as determined by using deoxyethynyluridine treatment (2 mM, 2 h) and subsequent reaction of all DNA-incorporated alkyne groups with an Alexa Fluor 594 azide. Red channel Ch1: $\lambda_{\text{ex}} = 545 \pm 25$ nm and $\lambda_{\text{em}} = 605 \pm 70$ nm. Blue channel, Ch2: $\lambda_{\text{ex}} = 365$ nm and $\lambda_{\text{em}} = 445 \pm 50$ nm. (F) A2780 cells were treated with either DMSO (1%, v/v) or FeC 2 (3 μM , 1% DMSO) for 24 h followed by fixation and staining with phalloidin-Atto655 (red signal: $\lambda_{\text{ex}} = 640 \pm 30$ nm and $\lambda_{\text{em}} = 690 \pm 50$ nm) and Hoechst 33342 (blue signal: $\lambda_{\text{ex}} = 365$ nm and $\lambda_{\text{em}} = 445 \pm 50$ nm). An unpaired Student's *t*-test was performed for statistical analysis (*: $p < 0.05$; **: $p < 0.01$; and ***: $p < 0.001$).

590 less or no effect in SBLF9 cells. In agreement with this
591 expectation, we observed that FeC 2 (9 μM) does not increase
592 intracellular levels of spliced XBP1, mROS, and NO at 1 h
593 incubation time. In contrast, under the same conditions,
594 spliced XBP1, mROS, and NO are significantly upregulated in
595 cancer A2780 cells (Figures 6C, S43C, S45, and S46B,
596 Supporting Information). Thus, these data support the concept
597 of BUPs introduced above (Figure 1B).

598 A known effect of the ER stress is the growth arrest in the
599 G1 phase of the cell cycle³⁷ as well as the inhibition of
600 expression of many related to these process genes.³⁸ In
601 agreement with this expectation, we observed that seven of
602 nine top-scored pathways affected by the FeC in A2780 cells,
603 as identified by RNA-Seq, are related to the cell cycle and
604 DNA and RNA synthesis (Figure 5A). We validated this result
605 by the following two experiments. First, we observed that the
606 cell cycle arrest in the G1 phase is induced upon treatment of
607 A2780 cells with FeC 2 (Figure 6D). Second, we found that
608 the FeC inhibits the *de novo* synthesis of DNA (Figure 6E,
609 Supporting Information) and RNA (Figure S49, Supporting
610 Information) in A2780 cells. Furthermore, Rho Guanine

Nucleotide Exchange Factor 39 (ARHGEF39) is down- 611
regulated by FeC 2 according to RNA-Seq and PCR (Figure 612
5). ARHGEF39 protein is known to promote cell proliferation. 613
All these data (G1 phase cell cycle arrest, inhibition of 614
the DNA and RNA synthesis, as well as the effect on 615
ARHGEF39) contribute to antiproliferative properties of the 616
FeC. 617

Surprisingly, FeC 2 treatment of A2780 cells leads to 618
downregulation of expression of β -actin (ACTB) as confirmed 619
by RNA-Seq and validated by PCR (Figure 5B). We also 620
observed that it is accompanied by a decrease of the level of 621
intracellular β -actin protein (Figure 6F). Since β -actin is 622
upregulated in the majority of cancer cells and is associated 623
with invasiveness and metastasis of cancer,⁴⁰ these data could 624
indicate that the FeC has a potential as an antimetastatic drug. 625
We confirmed that it is indeed the case in two experiments. 626
First, we observed that FeC 2 (3 μM) substantially slows down 627
the migration of human lung cancer SK-MES-1 cells in wound 628
healing assay (Figure S50, Supporting Information). Second, 629
we found that the FeC exhibits antimetastatic activities *in vivo*, 630
as described in the next section. 631

Together with the ER stress and the associated oxidative 632
stress, the effects of the FeC on cell cycle, DNA/RNA 633
synthesis, and cell proliferation induce cancer cell death (Table 634
1). We determined that the FeC 2 mediated death of A2780 635
and BL-2 cells occurs via apoptosis and necrosis (Figures S51– 636
S57, Supporting Information). The cells can be rescued by 637
PERK-inhibitor I and scavengers of ROS (N-acetylcysteine, 638
NecroX5 methanesulfonate, and ascorbic acid). In contrast, the 639
 Ca^{2+} scavenger BAPTA and the NOX2 inhibitor DPI exhibit 640
no effect. These data indicate that the upregulated UPR and 641
ROS, but not Ca^{2+} and NOX2, play important roles in the 642
anticancer activity of FeC 2. Despite ROS being involved, 643
according to our data discussed above, the upstream factor of 644
the activity of FeC 2 is the amplification of UPs caused by the 645
ER stress and eventually the cell death in cancer cells. 646

Next, we benchmarked FeC 2 with respect to the known 647
inducers of ER stress. In particular, effects of FeC 2 (9 μM), an 648
inhibitor of 26S proteasome bortezomib (0.5 μM), and an 649
inhibitor of sarcoplasmic/ER calcium ATPase (SERCA) 650
thapsigargin (0.5 μM) were compared with each other in 651
four selected assays. Nontoxic concentrations of the inhibitors 652
were selected. A summary of inhibitor rankings corresponding 653
to their performance in these assays (first, second, and third 654
place) is provided in Table 2. 655

In particular, we found that FeC 2 strongly enhances mROS 656
in A2780 cells (2.5 fold, $p < 0.001$), whereas bortezomib is 657
inactive ($p < 0.05$), and thapsigargin even slightly reduces the 658
amount of mROS ($p < 0.05$) (Figure S58A, Supporting 659

Table 2. Efficacy of Drugs Inducing ER Stress (first to third Places)^a in Four Selected Assays

drug ^b	ranking of drugs in the following assays			
	mROS level	ER staining	CHOP expression	XBP1 splicing
FeC 2	1st	1st	3rd	2nd
thapsigargin	2nd	2nd	1st	1st
bortezomib	2nd	3rd	2nd	3rd

^a1st place: a drug with the strongest effect. 3rd place: a drug with the weakest effect. ^b[FeC 2] = 9 μM , [thapsigargin] = [bortezomib] = 0.5 μM .

660 Information). Similarly, FeC 2 has the strongest effect on ER
 661 staining among this group of drugs (Figure S58B, Supporting
 662 Information). In contrast, thapsigargin is the most potent
 663 enhancer of CHOP expression ($p < 0.001$), followed by
 664 bortezomib ($p < 0.001$), whereas FeC 2 exhibits the weakest
 665 effect ($p < 0.01$) (Figure S58C, Supporting Information).
 666 Finally, thapsigargin is the strongest inducer of the XBP1
 667 splicing ($p > 0.001$), followed by FeC 2 ($p < 0.05$), whereas
 668 bortezomib is inactive under the selected conditions (Figure
 669 S58D, Supporting Information). These data indicate that FeC
 670 2 exhibits the unique action profile as reflected in Table 2,
 671 which indicates that its mechanism of action is different from
 672 that of the known ER stress inducers tested here.

673 **Antitumor and Antimetastatic Activity of FeC 2 and**
 674 **Its Toxicity toward Blood Cells and Bone Marrow In**
 675 **Vivo.** Encouraged by excellent anticancer activity (Table 1)
 676 and cancer cell specificity (Figures 6C, S43C, S45, and S46B,
 677 Supporting Information) observed in vitro, we studied whether
 678 FeC 2 retains these favorable properties in vivo. First, we found
 679 that the lethal dose (LD) of FeC 2, injected intraperitoneally
 680 (i.p.) in C57/BL6 mice, is between 147 and 246 mg/kg (Table
 681 S16, Supporting Information). The lethality of the FeC at the
 682 high dose can be caused by its activation by low amounts of
 683 unfolded/aggregated proteins or by its direct effect on proteins
 684 (Figure S34, Supporting Information).

685 Next, we investigated the antitumor effect of FeC in
 686 Nemeth-Kellner lymphoma (NK/Ly), grown as solid tumors
 687 of myeloid sarcoma. This is a standard model for testing new
 688 chemotherapeutics in our laboratories.^{33,39} Untreated animals
 689 had a half-life of 32 days. For this therapy experiment, we
 690 selected the dose of 12 mg/kg for a single injection. The
 691 compound was injected ip every second day for 10 times. The
 692 treatment did not cause any adverse effects. For example, the
 693 animals did not lose weight over 93 days of the experiment
 694 (Figure S59, Supporting Information). Moreover, the internal
 695 organs of animals dissected at the end of the experiment did
 696 not show any abnormalities (Figure S62, Supporting
 697 Information). The resulting Kaplan–Meier (survival) plot is
 698 shown in Figure 7A.

699 The mean survival time is statistically significantly increased
 700 in the group treated with the FeC as compared to the group,
 701 which received only the carrier: from 32 to 75 days ($p <$
 702 0.0001). On day 93, three survived mice in the treated group
 703 (27% from the initial number of the animals: 11) were killed
 704 and dissected. We detected no signs of tumors, indicating that
 705 these animals were completely cured (Figure S62, Supporting
 706 Information). This is an exciting result, which we have
 707 previously never observed for other Fe-containing drugs.^{35,41}
 708 Due to the excellent performance in the standard tumor model,
 709 we have also investigated its effects in the second, more
 710 challenging NK/Ly model, in which the cancer cells grow in
 711 the abdomen as ascites. This cancer is very aggressive, and
 712 untreated animals have a half-life of only 18 days. We were
 713 pleased to observe the moderate activity of FeC 2. In
 714 particular, treatment with the FeC prolonged the life span of
 715 mice from 18 to 22 days ($p < 0.05$) (Figure 7B). On day 13 of
 716 this experiment, we collected ascites from the mice (0.3 mL,
 717 lymphoma tumor cells), treated them with TBMS-306⁴² (20
 718 nM), a probe sensitive to MMP, and detected their
 719 fluorescence by fluorescence microscopy. We observed a
 720 strong signal in the control group and practically no signal in
 721 the FeC 2-treated group (Figure 7C). In a similar experiment,
 722 in which TBMS-306 was replaced with an MMP-independent

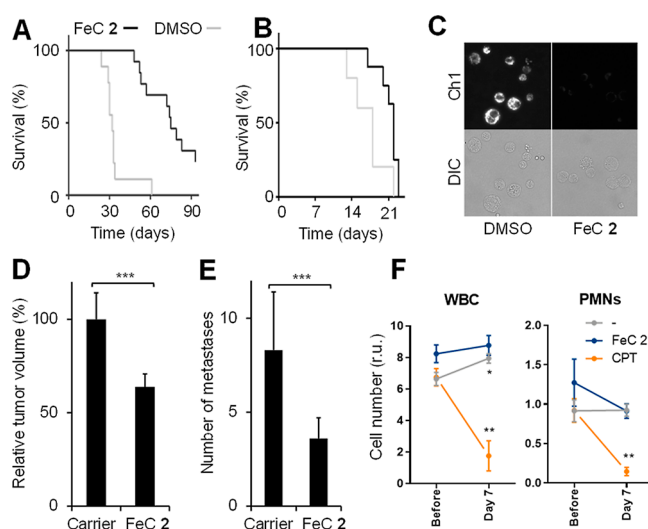


Figure 7. (A) Survival of animals with NK/Ly myeloid sarcoma (A) and lymphoma (B) in the control (DMSO) and FeC 2-treated groups. Experimental details are provided in the Supporting Information. (C) Fluorescent microscopy of NK/Ly lymphoma cells grown in the abdominal cavity of mice isolated after 13 days of treatment either with the carrier (DMSO) or FeC 2 and stained with TBMS-306 (20 nM, 10 min) ($\lambda_{\text{ex}} = 630$ nm and $\lambda_{\text{em}} = 720$ nm, Ch1). DIC = brightfield images. (D,E) Antitumor (C) and antimetastatic (D) effects of FeC 2 in a murine Lewis lung carcinoma LLC1 model were observed on 22 day of the experiment. An unpaired Student's *t*-test was performed for statistical analysis: *— $p < 0.05$; **— $p < 0.01$; and ns— $p > 0.05$. (F) Monitoring of the number of white blood cells (WBC) and neutrophils (PMNs) in blood. The analysis was conducted on day 7. Paired *t*-test was conducted between days 0 and 7. *: $p < 0.05$; **: $p < 0.01$; and ***: $p < 0.001$. The data for other blood and BM cells are provided in Figure S53, Supporting Information.

723 Mit-probe TBMS-52⁴³ (20 nM), no difference between both
 724 groups was observed (Figure S60, Supporting Information).
 725 These data indicate that in vivo, the FeC acts via the reduction of
 726 MMP, whereas the shape and size of Mit are not affected.
 727 Similar effects of the FeC on the MMP of A2780 cells were
 728 also observed in vitro (Figures S25 and S26, Supporting
 729 Information).

730 On day 23 of the experiment with the myeloid sarcoma
 731 model, one mouse from the control, and one from the treated
 732 groups were killed, and histology of tumor slices was
 733 conducted. We observed an increase in the number of cancer
 734 cells with fragmented nuclei in the treated group, indicating
 735 that the FeC promotes cancer cell apoptosis in vivo (Figure
 736 S61, Supporting Information). As described above, FeC also
 737 induces apoptosis of A2780 and BL-2 cells in vitro (Figures
 738 S51–S57, Supporting Information). Thus, at least two effects
 739 of FeC including the decrease of MMP and cell death via
 740 apoptosis are observed both in vivo and in vitro. These data
 741 may indicate that the modes of action of FeC in vitro and in
 742 vivo are similar. Importantly, we observed that also in this
 743 more challenging NK/Ly model, treatment with FeC 2 does
 744 not induce the loss of animal weight, indicating its good
 745 tolerability (Figure S59, Supporting Information).

746 The FeC affects the expression of β -actin and inhibits cell
 747 migration in vitro (Figure S50, Supporting Information).
 748 These preliminary studies justified the evaluation of anti-
 749 metastatic properties of FeC in vivo. We selected murine Lewis
 750 lung carcinoma LLC1 model, in which LLC1 cells grow as a

751 primary tumor and form numerous metastases in lungs. The
752 treatment included the i.p. injection of the FeC (48 mg/kg)
753 twice per week for 3 weeks. On the 22nd day, the tumor
754 volume as well as the number and volume of metastases were
755 evaluated (Figures 7D,E and S63, Supporting Information).
756 We observed significant reduction of volume of the primary
757 tumor ($p < 0.001$) and the number ($p < 0.001$) and volume (p
758 < 0.05) of metastases in the treated group as compared to the
759 control group.

760 Finally, we investigated the in vivo toxicity of the FeC
761 toward a range of noncancerous cells at the therapeutically
762 active dose of 12 mg/kg. They included white blood cells
763 (WBC), red blood cells (RBC), platelets, polymorphonuclear
764 neutrophils (PMNs), monocytes (MONO), and lymphocytes
765 (LYM) from blood. We also studied the effect of the FeC on
766 BM cellularity and on the following BM cells: CD45+ cells,
767 PMNs, MONO, B and T cells, LineageNEG Sca-1+ c-Kit+
768 cells, and myeloid progenitors. As a positive control, we
769 applied camptothecin (CPT), which exhibited strong toxicity
770 toward the majority of these cells (Figures 7F and S64,
771 Supporting Information). In contrast, no statistically significant
772 toxicity of FeC was observed (Figures 7F and S64, Supporting
773 Information) that is in agreement with good tolerability of this
774 compound and its inability to generate mROS and NO and
775 induce the ER stress (no sXBP1 upregulation) in representa-
776 tive normal SBLF9 cells as observed in vitro (Figures 6C, S43,
777 S45, and S46B, Supporting Information).

778 ■ CONCLUSIONS

779 Known Fe²⁺-clathrochelates binding UPs (e.g., FeC 1) are not
780 cell membrane permeable and, therefore, do not exhibit
781 anticancer activity. By the variation of their structure, we
782 discovered FeC 2 containing a critical carboxylic acid moiety.
783 Structurally, FeC resembles fullerene C₆₀. However, in contrast
784 to the latter carbon allotrope, it is more water soluble. The FeC
785 can be considered as an inorganic mimic of C₆₀ suitable for
786 medicinal applications. The FeC exhibits high to moderate
787 anticancer activity toward a range of cancer cell lines derived
788 from blood (HL-60, BL-2, Jurkat), ovary (A2780), and lungs
789 (SK-MES1, LLC1). Furthermore, its activity is retained in vivo,
790 as confirmed for two Nemeth-Kellner lymphoma models and
791 an LLC1 lung cancer model. In cells, the FeC acts as a
792 monomer rather than an aggregate. It is stable in cells at the
793 shorter incubation time (1 h) but is partially (10%)
794 metabolized to its educt with glutathione at the longer
795 incubation time (24 h). The latter metabolite does not
796 contribute to the anticancer activity since the initial cellular
797 effects of the FeC, including the induction of the ER stress,
798 appear very quickly at <10 min incubation time. The FeC is
799 efficiently uptaken by cancer cells via the active mechanism
800 mediated by clathrin and caveolin. In cells, it first induces the
801 ER stress due to the accumulation of UPs as evidenced by the
802 activation of the protein ubiquitination pathway, which is
803 reflected in the upregulation of its genes and the increase of the
804 amount of intracellular ubiquitinated proteins. The initial effect
805 on the ER leads later onto the decrease of mitochondrial
806 membrane potential, induction of oxidative stress including the
807 formation of mitochondrial ROS, upregulation of NO as well
808 as growth arrest in the G1 phase, and inhibition of DNA and
809 RNA synthesis. All these factors cause cell apoptosis and
810 partially necrosis. Importantly, in contrast to cancer cells, the
811 FeC does not affect the ROS, NO, and sXBP1 levels in
812 representative noncancerous SBLF9 cells, indicating its cancer

cell specificity. We confirmed that at its active dose of 12 mg/
kg, the FeC does not induce any toxic effects on a range of cells
in blood (white and red blood cells, platelets, neutrophils,
monocytes, and lymphocytes) and bone marrow (CD45+ cells,
neutrophils, monocytes, B and T cells, lineageNEG Sca-1+ c-
Kit+ cells, and myeloid progenitors). Finally, the FeC exhibits
significant antimetastatic activity in the LLC1 lung cancer
model. These data are in agreement with the FeC-mediated
inhibition of β -actin expression and reduction of β -actin levels
in cells observed in vitro.

In summary, FeC is a metal-containing anticancer agent
acting via a novel mechanism based on the intracellular UP
amplification in the ER and exhibiting high cancer cell
specificity and, correspondingly, low toxicity as confirmed in
vitro and in vivo.

■ ASSOCIATED CONTENT

Supporting Information

The Supporting Information is available free of charge at
<https://pubs.acs.org/doi/10.1021/jacs.3c08827>.

Synthesis protocols, analytics, experimental details, in
vitro experiments not described in the main paper, and
detailed in vivo data (PDF)

■ AUTHOR INFORMATION

Corresponding Author

Andriy Mokhir – Department of Chemistry and Pharmacy,
Organic Chemistry II, Friedrich-Alexander-University of
Erlangen-Nürnberg (FAU), 91058 Erlangen, Germany;
orcid.org/0000-0002-9079-5569;
Email: Andriy.Mokhir@fau.de

Authors

Insa Klemt – Department of Chemistry and Pharmacy,
Organic Chemistry II, Friedrich-Alexander-University of
Erlangen-Nürnberg (FAU), 91058 Erlangen, Germany
‡‡Oleg Varzatskii – Princeton Biomolecular Research
Laboratories, 01042 Kyiv, Ukraine; V.I. Vernadsky Institute
of General and Inorganic Chemistry, NASU, 03142 Kyiv,
Ukraine
Roman Selin – Department of Chemistry and Pharmacy,
Organic Chemistry II, Friedrich-Alexander-University of
Erlangen-Nürnberg (FAU), 91058 Erlangen, Germany
Serhii Vakarov – Princeton Biomolecular Research
Laboratories, 01042 Kyiv, Ukraine; V.I. Vernadsky Institute
of General and Inorganic Chemistry, NASU, 03142 Kyiv,
Ukraine
‡‡Vladyslava Kovalska – Princeton Biomolecular Research
Laboratories, 01042 Kyiv, Ukraine; Institute of Molecular
Biology and Genetics, NASU, 03143 Kyiv, Ukraine
Galyna Bila – Department of Histology, Cytology and
Embryology, Danylo Halytsky Lviv National Medical
University, 79010 Lviv, Ukraine; Lectinotest R&D, 79024
Lviv, Ukraine
Rostyslav Bilyy – Department of Histology, Cytology and
Embryology, Danylo Halytsky Lviv National Medical
University, 79010 Lviv, Ukraine; Lectinotest R&D, 79024
Lviv, Ukraine; orcid.org/0000-0002-2344-1349
Yan Voloshin – Nesmeyanov Institute of Organoelement
Compounds, RAS, 119334 Moscow, Russia; orcid.org/0000-0003-2823-6560

- 871 **Itziar Cossío Cuartero** – Program of Cardiovascular
872 Regeneration, Centro Nacional de Investigaciones
873 Cardiovasculares Carlos III (CNIC), 28029 Madrid, Spain
874 **Andrés Hidalgo** – Program of Cardiovascular Regeneration,
875 Centro Nacional de Investigaciones Cardiovasculares Carlos
876 III (CNIC), 28029 Madrid, Spain
877 **Benjamin Frey** – Department of Radiation Oncology,
878 Translational Radiobiology, Universitätsklinikum Erlangen,
879 Friedrich-Alexander-University of Erlangen-Nürnberg
880 (FAU), 91054 Erlangen, Germany
881 **Ina Becker** – Department of Radiation Oncology,
882 Translational Radiobiology, Universitätsklinikum Erlangen,
883 Friedrich-Alexander-University of Erlangen-Nürnberg
884 (FAU), 91054 Erlangen, Germany
885 **Bernhard Friedrich** – Department of Otorhinolaryngology,
886 Head and Neck Surgery, Section of Experimental Oncology
887 and Nanomedicine (SEON), University Hospital, Friedrich-
888 Alexander-University of Erlangen-Nürnberg (FAU), 91054
889 Erlangen, Germany
890 **Rainer Tietze** – Department of Otorhinolaryngology, Head
891 and Neck Surgery, Section of Experimental Oncology and
892 Nanomedicine (SEON), University Hospital, Friedrich-
893 Alexander-University of Erlangen-Nürnberg (FAU), 91054
894 Erlangen, Germany; orcid.org/0000-0001-9306-633X
895 **Ralf P. Friedrich** – Department of Otorhinolaryngology, Head
896 and Neck Surgery, Section of Experimental Oncology and
897 Nanomedicine (SEON), University Hospital, Friedrich-
898 Alexander-University of Erlangen-Nürnberg (FAU), 91054
899 Erlangen, Germany
900 **Christoph Alexiou** – Department of Otorhinolaryngology,
901 Head and Neck Surgery, Section of Experimental Oncology
902 and Nanomedicine (SEON), University Hospital, Friedrich-
903 Alexander-University of Erlangen-Nürnberg (FAU), 91054
904 Erlangen, Germany
905 **Elena-Laura Ursu** – “Petru Poni” Institute of Macromolecular
906 Chemistry, Romanian Academy, Centre of Advanced
907 Research in Bionanoconjugates and Biopolymers, 700487
908 Iasi, Romania
909 **Alexandru Rotaru** – “Petru Poni” Institute of Macromolecular
910 Chemistry, Romanian Academy, Centre of Advanced
911 Research in Bionanoconjugates and Biopolymers, 700487
912 Iasi, Romania
913 **Iris Solymosi** – Department of Chemistry and Pharmacy,
914 Organic Chemistry II, Friedrich-Alexander-University of
915 Erlangen-Nürnberg (FAU), 91058 Erlangen, Germany
916 **M. Eugenia Pérez-Ojeda** – Department of Chemistry and
917 Pharmacy, Organic Chemistry II, Friedrich-Alexander-
918 University of Erlangen-Nürnberg (FAU), 91058 Erlangen,
919 Germany

920 Complete contact information is available at:
921 <https://pubs.acs.org/10.1021/jacs.3c08827>

922 Funding

923 We thank European Commission (861878: NeuroCure;
924 778245: Clathroprobes; and 872331: NoBiasFluors),
925 Schmauser-Stiftung; and Friedrich-Alexander-Universität Er-
926 lingen-Nürnberg for funding this study. IK acknowledges the
927 support of Studienstiftung for a doctoral fellowship. RS
928 acknowledges the support of Alexander von Humboldt-
929 Stiftung for a postdoctoral fellowship. The CNIC is supported
930 by the MCIN and the Pro CNIC Foundation and is a Severo
931 Ochoa Center of Excellence (CEX2020-001041-S). We

gratefully acknowledge the generous support by the Manfred 932
Roth-Stiftung, Fürth (Germany), as well as by the 933
Forschungstiftung Medizin am Universitätsklinikum Erlan- 934
gen (Germany). 935

936 Notes

The authors declare no competing financial interest. 937

††O. Varzatskii: date of death—20.12.2017; V Kovalska: date 938
of death—03.12.2020. 939

940 ACKNOWLEDGMENTS

We thank Prof. Dr. Andreas Hirsch for allowing the extensive 941
usage of the infrastructure of his chair Organic Chemistry II at 942
FAU. Confocal microscopy was performed on a Zeiss Spinning 943
Disc Axio Observer Z1, funded by Deutsche Forschungsge- 944
meinschaft (DFG, German Research Foundation)—project 945
248122450. Tumor tissue imaging was done using infra- 946
structure established under National Research Foundation of 947
Ukraine grant 2020.02.0131. 948

949 ABBREVIATIONS

ACTB, β -actin; AES, atomic emission spectroscopy; AFM, 950
atomic force microscopy; ARHGEF39, Rho Guanine Nucleo- 951
tide Exchange Factor 39; BSA, bovine serum albumin; BUP, 952
binders of Ups; BSP, bromsulphthalein; CHOP, C/EBP 953
homologous protein; CMDCFH-DA, 5-(and-6)- 954
chloromethyl-2',7'-dichlorodihydrofluorescein; CPT, campto- 955
thecin; CPZ, chlorpromazine; CUC, coordinatively unsatu- 956
rated complexes; CV, cyclic voltamperometry; DCFH, 2',7'- 957
dichlorodihydrofluorescein; DCF, 2',7'-dichlorofluorescein; 958
DLS, dynamic light scattering; DTT, dithiothreitol; ER, 959
endoplasmic reticulum; ERAD, ER-associated protein degra- 960
dation; FBS, fetal bovine serum; GCLC, glutamate–cysteine 961
ligase catalytic subunit; GCLM, glutamate–cysteine ligase 962
regulatory protein; Gln, glutathione; GNS, genistein; GSH, 963
glutathione; LD, lethal dose; LY, lysosome; Mit, mitochondria; 964
MMP, mitochondrial membrane potential; MONO, mono- 965
cytes; mROS, mitochondrial ROS; NO, nitric oxide; NRF2, 966
nuclear factor erythroid-2 related factor 2; PBS, phosphate 967
buffered saline; PMN, neutrophils; RBC, red blood cells, R123, 968
rhodamine 123; ROS, reactive oxygen species; sXBP1, spliced 969
XBP1 mRNA; TEM, transmission electron microscopy; ThT, 970
thioflavin T; tROS, total ROS; uINS, unfolded insulin; UP, 971
unfolded proteins; UPR, unfolded protein response; WBS, 972
white blood cells; WBC, white blood cells 973

974 REFERENCES

- (1) (a) Hurley, L. H. DNA and its associated processes as targets for 975
cancer therapy. *Nat. Rev. Cancer* **2002**, *2*, 188–200. (b) Palchadhuri, 976
R.; Hergenrother, P. J. DNA as a target for anticancer compounds: 977
methods to determine the mode of binding and the mechanism of 978
action. *Curr. Opin. Biotechnol.* **2007**, *18*, 497–503. (c) van den 979
Boogaard, W. M. C.; Komninos, D. S. J.; Vermeij, W. P. 980
Chemotherapy Side-Effects: Not All DNA Damage Is Equal. *Cancers* 981
2022, *14*, 627. 982
- (2) (a) Chen, X.; Cubillos-Ruiz, J. R. Endoplasmic reticulum stress 983
signals in the tumour and its microenvironment. *Nat. Rev. Cancer* 984
2021, *21*, 71–88. (b) King, A. P.; Wilson, J. J. Endoplasmic reticulum 985
stress: an arising target for metal-based anticancer agents. *Soc. Rev.* 986
2020, *49*, 8113–8136. 987
- (3) Richardson, P. G.; Sonneveld, P.; Schuster, M. W.; Irwin, D.; 988
Stadtmauer, E. A.; Facon, T.; Harousseau, J.-L.; Ben-Yehuda, D.; 989
Lonial, S.; Goldschmidt, H.; Reece, D.; San-Miguel, J. F.; Bladé, J.; 990
Boccardo, M.; Cavenagh, J.; Dalton, W. S.; Boral, A. L.; Esseltine, D. 991
L.; Porter, J. B.; Schenkein, D.; Anderson, K. C. Bortezomib or high- 992

- 993 dose dexamethasone for relapsed multiple myeloma. *N. Engl. J. Med.*
994 **2005**, *352*, 2487–2498.
- 995 (4) (a) Usmani, S. Z.; Quach, H.; Mateos, M. V.; Landgren, O.;
996 Leleu, X.; Siegel, D.; Weisel, K.; Gavriatopoulou, M.; Oriol, A.; Rabin,
997 N.; Nooka, A.; Qi, M.; Beksac, M.; Jakubowiak, A.; Ding, B.; Zahlten-
998 Kumeli, A.; Yusuf, A.; Dimopoulos, M. Carfilzomib, dexamethasone,
999 and daratumumab versus carfilzomib and dexamethasone for patients
1000 with relapsed or refractory multiple myeloma (CANDOR): updated
1001 outcomes from a randomised, multicentre, open-label, phase 3 study.
1002 *Lancet Oncol.* **2022**, *23*, 65–76. (b) Dimopoulos, M. A.; Goldschmidt,
1003 H.; Niesvizky, R.; Joshua, D.; Chng, W. J.; Oriol, A.; Orłowski, R. Z.;
1004 Ludwig, H.; Facon, T.; Hajek, R.; Weisel, K.; Hungria, V.; Minuk, L.;
1005 Feng, S.; Zahlten-Kumeli, A.; Kimball, A. S.; Moreau, P. Carfilzomib
1006 or bortezomib in relapsed or refractory multiple myeloma
1007 (ENDEAVOR): an interim overall survival analysis of an open-
1008 label, randomised, phase 3 trial. *Lancet Oncol.* **2017**, *18*, 1327–1337.
- 1009 (5) (a) Chen, X.; Yang, Q.; Xiao, L.; Tang, D.; Dou, Q. P.; Liu, J.
1010 Metal-based proteasomal deubiquitinase inhibitors as potential
1011 anticancer agents. *Met. Rev.* **2017**, *36*, 655–668. (b) Zhang, Z.;
1012 Wang, H.; Yan, M.; Wang, H.; Zhang, C. Novel copper complexes as
1013 potential proteasome inhibitors for cancer treatment. *Mol. Med. Rep.*
1014 **2017**, *15*, 3–11. (c) Karges, J.; Stokes, R. W.; Cohen, S. M. Metal
1015 complexes for therapeutic applications. *Trends Chem.* **2021**, *3* (7),
1016 523–534. (d) Zhang, L.; Montesdeoca, N.; Karges, J.; Xiao, H.
1017 Immunogenic cell death inducing metal complexes for cancer therapy.
1018 *Angew. Chem., Int. Ed.* **2023**, *62*, No. e202300662.
- 1019 (6) (a) Mandic, A.; Hansson, J.; Linder, S.; Shoshan, M. C. Cisplatin
1020 induces endoplasmic reticulum stress and nucleus-independent
1021 apoptotic signaling. *J. Biol. Chem.* **2003**, *278*, 9100–9106. (b) John-
1022 stone, T. C.; Suntharalingam, K.; Lippard, S. J. The Next Generation
1023 of Platinum Drugs: Targeted Pt(II) Agents, Nanoparticle Delivery,
1024 and Pt(IV) Prodrugs. *Chem. Rev.* **2016**, *116*, 3436–3486.
- 1025 (7) Fiskus, W.; Saba, N.; Shen, M.; Ghias, M.; Liu, J.; Gupta, S. D.;
1026 Chauhan, L.; Rao, R.; Gunewardena, S.; Schorno, K.; Austin, C. P.;
1027 Maddocks, K.; Byrd, J.; Melnick, A.; Huang, P.; Wiestner, A.; Bhalla,
1028 K. N. Auranofin induces lethal oxidative and endoplasmic reticulum
1029 stress and exerts potent preclinical activity against chronic
1030 lymphocytic leukemia. *Cancer Res.* **2014**, *74*, 2520–2532.
- 1031 (8) Ramos, R.; Gilles, J. F.; Morichon, R.; Przybylski, C.; Caron, B.;
1032 Botuha, C.; Karaiskou, A.; Salmain, M.; Sobczak-Thépot, J. Cytotoxic
1033 BODIPY-Appended Half-Sandwich Iridium(III) Complex Forms
1034 Protein Adducts and Induces ER Stress. *J. Med. Chem.* **2021**, *64*,
1035 16675–16686.
- 1036 (9) Neuditschko, B.; Legin, A. A.; Baier, D.; Schintlmeister, A.;
1037 Reipert, S.; Wagner, M.; Keppler, B. K.; Berger, W.; Meier-Menches,
1038 S. M.; Gerner, C. Die Wechselwirkung mit ribosomalen Proteinen
1039 begleitet die Stressinduktion des Wirkstoffkandidaten BOLD-100/
1040 KP1339 im endoplasmatischen Retikulum. *Angew. Chem.* **2021**, *133*,
1041 5121–5126.
- 1042 (10) (a) Vidimar, V.; Meng, X.; Klajner, M.; Licon, C.; Fetzer, L.;
1043 Harlepp, S.; Hébraud, P.; Sidhoum, M.; Sirlin, C.; Loeffler, J. P.;
1044 Mellitzer, G.; Sava, G.; Pfeffer, M.; Gaiddon, C. Induction of caspase 8
1045 and reactive oxygen species by ruthenium-derived anticancer
1046 compounds with improved water solubility and cytotoxicity. *Biochem*
1047 *Pharmacol.* **2012**, *84*, 1428–1436. (b) Xu, H. G.; Schikora, M.; Sisa,
1048 M.; Daum, S.; Klemm, I.; Janko, C.; Alexiou, C.; Bila, G.; Bilyy, R.;
1049 Gong, W.; Schmitt, M.; Sellner, L.; Mokhir, A. An Endoplasmic
1050 Reticulum Specific Pro-amplifier of Reactive Oxygen Species in
1051 Cancer Cells. *Angew. Chem., Int. Ed.* **2021**, *60*, 11158–11162.
- 1052 (11) Dougan, S. J.; Habtemariam, A.; McHale, S. E.; Parsons, S.;
1053 Sadler, P. J. Catalytic organometallic anticancer complexes. *Proc. Natl.*
1054 *Acad. Sci. U.S.A.* **2008**, *105* (33), 11628–11633.
- 1055 (12) Banerjee, S.; Dixit, A.; Shridharan, R. N.; Karande, A. A.;
1056 Chakravarty, A. R. Endoplasmic reticulumtargeted chemotherapeutics:
1057 the remarkable photo-cytotoxicity of an oxovanadium(IV) vitamin-B6
1058 complex in visible light. *Chem. Commun.* **2014**, *50*, 5590–5592.
- 1059 (13) Goswami, T. K.; Gadadhar, S.; Balaji, B.; Gole, B.; Karande, A.
1060 A.; Chakravarty, A. R. Ferrocenyl-L-amino acid copper(II) complexes
showing remarkable photo-induced anticancer activity in visible light. *1061*
Dalton Trans. **2014**, *43*, 11988–11999. *1062*
- (14) (a) Nam, J. S.; Kang, M. G.; Kang, J.; Park, S. Y.; Lee, S. J.;
1063 Kim, H. T.; Seo, J. K.; Kwon, O. H.; Lim, M. H.; Rhee, H. W.; Kwon,
1064 T. H. Endoplasmic Reticulum-Localized Iridium(III) Complexes as
1065 Efficient Photodynamic Therapy Agents via Protein Modifications. *1066*
Chem. Soc. **2016**, *138*, 10968–10977. (b) Yuan, B.; Liu, J.; Guan, R.;
1067 Jin, C.; Ji, L.; Chao, H. Endoplasmic reticulum targeted cyclo-
1068 metalated iridium(III) complexes as efficient photodynamic therapy
1069 photosensitizers. *Dalton Trans.* **2019**, *48*, 6408–6415. *1070*
- (15) Tripathy, S. K.; De, U.; Dehury, N.; Laha, P.; Panda, M. K.;
1071 Kim, H. S.; Patra, S. Cyclometallated iridium complexes inducing
1072 paraptotic cell death like natural products: synthesis, structure and
1073 mechanistic aspects. *Dalton Trans.* **2016**, *45*, 15122–15136. *1074*
- (16) (a) Cortez, L.; Sim, V. The therapeutic potential of chemical
1075 chaperones in protein folding diseases. *Prion* **2014**, *8*, 197–202. *1076*
(b) Perlmutter, D. H. Chemical chaperones: a pharmacological
1077 strategy for disorders of protein folding and trafficking. *Pediatr. Res.*
1078 **2002**, *52*, 832–836. *1079*
- (17) (a) Di, J.; Siddique, I.; Li, Z.; Malki, G.; Hornung, S.; Dutta, S.;
1080 Hurst, I.; Ishaaya, E.; Wang, A.; Tu, S.; Boghos, A.; Ericsson, I.;
1081 Klärner, F. G.; Schrader, T.; Bitan, G. The molecular tweezer CLR01
1082 improves behavioral deficits and reduces tau pathology in P301S-tau
1083 transgenic mice. *Alzheimer's Res. Ther.* **2021**, *13*, 6. (b) Bengoa-
1084 Vergniory, N.; Faggiani, E.; Ramos-Gonzalez, P.; Kirkiz, E.; Connor-
1085 Robson, N.; Brown, L. V.; Siddique, I.; Li, Z.; Vingill, S.; Cioroch, M.;
1086 Cavaliere, F.; Threlfell, S.; Roberts, B.; Schrader, T.; Klärner, F. G.;
1087 Cragg, S.; Dehay, B.; Bitan, G.; Matute, C.; Bezdard, E.; Wade-Martins,
1088 R. CLR01 protects dopaminergic neurons in vitro and in mouse
1089 models of Parkinson's disease. *Nat. Commun.* **2020**, *11*, 4885. *1090*
- (c) Herrera-Vaquero, M.; Bouquio, D.; Kallab, M.; Biggs, K.; Nair, G.;
1091 Ochoa, J.; Heras-Garvin, A.; Heid, C.; Hadrovic, I.; Poewe, W.;
1092 Wenning, G. K.; Klärner, F. G.; Schrader, T.; Bitan, G.; Stefanova, N.
1093 The molecular tweezer CLR01 reduces aggregated, pathologic, and
1094 seeding-competent α -synuclein in experimental multiple system
1095 atrophy. *Biochim. Biophys. Acta, Mol. Basis Dis.* **2019**, *1865*, 165513. *1096*
- (18) Özcan, U.; Yilmaz, E.; Özcan, L.; Furuhashi, M.; Vaillancourt,
1097 E.; Smith, R. O.; Görgün, C. Z.; Hotamisligil, G. S. Chemical
1098 chaperones reduce ER stress and restore glucose homeostasis in a
1099 mouse model of type 2 diabetes. *Science* **2006**, *313*, 1137–1140. *1100*
- (19) (a) Herzog, G.; Shmueli, M. D.; Levy, L.; Engel, L.; Gazit, E.;
1101 Klärner, F. G.; Schrader, T.; Bitan, G.; Segal, D. The Lys-Specific
1102 Molecular Tweezer, CLR01, Modulates Aggregation of the Mutant
1103 p53 DNA Binding Domain and Inhibits Its Toxicity. *Biochemistry*
1104 **2015**, *54*, 3729–3738. (b) Sinha, S.; Lopes, D. H.; Du, Z.; Pang, E. S.;
1105 Shanmugam, A.; Lomakin, A.; Talbiersky, P.; Tennstaedt, A.;
1106 McDaniel, K.; Bakshi, R.; Kuo, P. Y.; Ehrmann, M.; Benedek, G. B.;
1107 Loo, J. A.; Klärner, F. G.; Schrader, T.; Wang, C.; Bitan, G. Lysine-
1108 specific molecular tweezers are broad-spectrum inhibitors of assembly
1109 and toxicity of amyloid proteins. *J. Am. Chem. Soc.* **2011**, *133*, 16958–
1110 16969. *1111*
- (20) Siepi, M.; Politi, J.; Dardano, P.; Amoresano, A.; De Stefano, L.;
1112 Maria Monti, D.; Notomista, E. Modified denatured lysozyme
1113 effectively solubilizes fullerene c60 nanoparticles in water. *Nano-*
1114 *technology* **2017**, *28*, 335601. *1115*
- (21) Jafvert, C. T.; Kulkarni, P. P. Buckminsterfullerene's (C60)
1116 octanol-water partition coefficient (Kow) and aqueous solubility. *Sci.*
1117 *Technol.* **2008**, *42*, 5945–5950. *1118*
- (22) (a) Meng, J.; Liang, X.; Chen, X.; Zhao, Y. Biological
1119 characterizations of [Gd@C82(OH)22]n nanoparticles as fullerene
1120 derivatives for cancer therapy. *Integr. Biol.* **2013**, *5*, 43–47. (b) Lin, J.;
1121 Cai, R.; Sun, B.; Dong, J.; Zhao, Y.; Miao, Q.; Chen, C. Gd@
1122 C82(OH)22 harnesses inflammatory regeneration for osteogenesis of
1123 mesenchymal stem cells through JNK/STAT3 signaling pathway. *J.*
1124 *Mater. Chem. B* **2018**, *6*, 5802–5811. *1125*
- (23) (a) Voloshin, Y. Z.; Kostromina, N. A.; Krämer, R.;
1126 *Clathrochelates: Synthesis, Structure and Properties*; Elsevier Science,
1127 2002. (b) Voloshin, Y.; Belaya, I.; Krämer, R. *Cage Metal Complexes:*
1128 *Clathrochelates Revisited*; Springer, 2017. *1129*

- 1130 (24) Kovalska, V.; Chernii, S.; Cherepanov, V.; Losytskyy, M.;
1131 Chernii, V.; Varzatskii, O.; Naumovets, A.; Yarmoluk, S. The impact
1132 of binding of macrocyclic metal complexes on amyloid fibrillization of
1133 insulin and lysozyme. *J. Mol. Recognit.* **2017**, *30*, No. e2622.
- 1134 (25) Kovalska, V. B.; Losytskyy, M. Y.; Varzatskii, O. A.;
1135 Cherepanov, V. V.; Voloshin, Y. Z.; Mokhir, A.; Yarmoluk, S. M.;
1136 Volkov, S. V. Study of anti-fibrillogenic activity of iron(II)
1137 clathrochelates. *Bioorg. Med. Chem.* **2014**, *22*, 1883–1888.
- 1138 (26) Blechinger, J.; Varzackii, O. A.; Kovalska, V.; Zelinskii, G. E.;
1139 Voloshin, Y. Z.; Kinski, E.; Mokhir, A. Cytotoxicity of electrophilic
1140 iron(II)–clathrochelates in human promyelocytic leukemia cell line.
1141 *Med. Chem. Lett.* **2016**, *26*, 626–629.
- 1142 (27) Belov, A. S.; Belaya, I. G.; Novikov, V. V.; Starikova, Z. A.;
1143 Polshin, E. V.; Dolganov, A. V.; Lebed, E. G. Structure, spectral and
1144 electrochemical properties of the 2,6-di-tert-butylphenol-function-
1145 alized iron and cobalt(ii) clathrochelates and their phenylsulfide
1146 analogs. *Inorg. Chim. Acta* **2013**, *394*, 269–281.
- 1147 (28) (a) Selin, R.; Chornenka, N.; Chernii, V. Ya.; Mokhir, A.;
1148 Vologzhanina, A. V.; Belov, A. S.; Pomadchik, A. L.; Voloshin, Y. Z.
1149 Chemical design of the heterodifunctionalized iron(II) clathrochelates
1150 with terminal biorelevant carboxyl group and reactive triple C≡C
1151 bond: Synthesis, structure, redox properties and their stability in
1152 various media. *Inorg. Chim. Acta* **2019**, *496*, 119047. (b) Selin, R.;
1153 Klemt, I.; Chernii, V. Ya.; Losytskyy, M. Yu.; Chernii, S.; Mular, A.;
1154 Gumienna-Kontecka, E.; Kovalska, V. B.; Voloshin, Y. Z.;
1155 Vologzhanina, A. V.; Dorovatovskii, P. V.; Mokhir, A. Synthesis and
1156 spectral characterization of the first fluorescein-tagged iron(ii)
1157 clathrochelates, their supramolecular interactions with globular
1158 proteins, and cellular uptake. *RSC Adv.* **2021**, *11*, 8163–8177.
- 1159 (29) Coan, K. E.; Maltby, D. A.; Burlingame, A. L.; Shoichet, B. K.
1160 Promiscuous aggregate-based inhibitors promote enzyme unfolding. *J.*
1161 *Med. Chem.* **2009**, *52*, 2067–2075.
- 1162 (30) Selin, R. A.; Chornenka, N. V.; Chernii, V.; Mokhir, A.;
1163 Vologzhanina, A. V.; Belov, A. S.; Pomadchik, A. L.; Voloshin, Y. Z.
1164 Chemical design of the heterodifunctionalized iron(II) clathrochelates
1165 with terminal biorelevant carboxyl group and reactive triple C≡C
1166 bond: synthesis, structure, redox properties and their stability in
1167 various media. *Inorg. Chim. Acta* **2019**, *496*, 119047.
- 1168 (31) (a) Shen, D.; Coleman, J.; Chan, E.; Nicholson, T. P.; Dai, L.;
1169 Sheppard, P. W.; Patton, W. F. Novel Cell- and Tissue-Based Assays
1170 for Detecting Misfolded and Aggregated Protein Accumulation
1171 Within Aggregates and Inclusion Bodies. *Cell Biochem. Biophys.*
1172 **2011**, *60*, 173–185. (b) Beriault, D. R.; Werstuck, G. H. Detection
1173 and quantification of endoplasmic reticulum stress in living cells using
1174 the fluorescent compound, Thioflavin T. *Biochim. Biophys. Acta* **2013**,
1175 *1833*, 2293–2301.
- 1176 (32) Rooney, J. P.; Chorley, B.; Hiemstra, S.; Wink, S.; Wang, X.;
1177 Bell, D. A.; van de Water, B.; Corton, J. C. Mining a human
1178 transcriptome database for chemical modulators of NRF2. *PLoS* **2020**,
1179 *15*, No. e0239367.
- 1180 (33) Ríos, N.; Prolo, C.; Álvarez, M. N.; Piacenza, L.; Radi, R.
1181 Peroxynitrite Formation and Detection in Living Cells. *Nitric Oxide*
1182 *Biology and Pathobiology*; Academic Press, 2017; pp 271–288.
- 1183 (34) Santos, C. X.; Tanaka, L. Y.; Wosniak, J.; Laurindo, F. R.
1184 Mechanisms and implications of reactive oxygen species generation
1185 during the unfolded protein response: roles of endoplasmic reticulum
1186 oxidoreductases, mitochondrial electron transport, and NADPH
1187 oxidase. *Antioxid. Redox Signaling* **2009**, *11*, 2409–2427.
- 1188 (35) Daum, S.; Reshetnikov, M. S. V.; Sisa, M.; Dumych, T.;
1189 Lootsik, M. D.; Bilyy, R.; Bila, E.; Janko, C.; Alexiou, C.; Herrmann,
1190 M.; Sellner, L.; Mokhir, A. Lysosome-Targeting Amplifiers of Reactive
1191 Oxygen Species as Anticancer Prodrugs. *Angew. Chem., Int. Ed.* **2017**,
1192 *56*, 15545–15549.
- 1193 (36) Reshetnikov, V.; Daum, S.; Janko, C.; Karawacka, W.; Tietze,
1194 R.; Alexiou, C.; Paryzhak, S.; Dumych, T.; Bilyy, R.; Tripal, P.;
1195 Schmid, B.; Palmisano, R.; Mokhir, A. ROS-Responsive N-
1196 Alkylaminoferrocenes for Cancer-Cell-Specific Targeting of Mito-
1197 chondria. *Angew. Chem., Int. Ed.* **2018**, *57*, 11943–11946.
- (37) Han, C.; Jin, L.; Mei, Y.; Wu, M. Endoplasmic reticulum stress
inhibits cell cycle progression via induction of p27 in melanoma cells.
Cell Signal **2013**, *25*, 144–149.
- (38) Ma, Y.; Hendershot, L. M. The role of the unfolded protein
response in tumour development: friend or foe? *Nat. Rev. Cancer*
2004, *4*, 966–977.
- (39) Wang, H.; Li, Y.; Wang, Y.; Han, Z. G.; Cai, B. C9orf100, a new
member of the Dbl-family guanine nucleotide exchange factors,
promotes cell proliferation and migration in hepatocellular carcinoma.
Mol. Med. Rep. **2012**, *5*, 1169–1174.
- (40) Guo, C.; Liu, S.; Wang, J.; Sun, M. Z.; Greenaway, F. T. ACTB
in cancer. *Clin. Chim. Acta* **2013**, *417*, 39–44.
- (41) Özkan, H. G.; Thakor, V.; Xu, H. G.; Bila, G.; Bilyy, R.; Bida,
D.; Böttcher, M.; Mougiakakos, D.; Tietze, R.; Mokhir, A. Anticancer
Aminoferrrocene Derivatives Inducing Production of Mitochondrial
Reactive Oxygen Species. *Chem.—Eur. J.* **2022**, *28*, No. e202104420.
- (42) Bříza, T.; Rimpelová, S.; Králová, J.; Záruba, K.; Kejřík, Z.;
Ruml, T.; Martásek, P.; Král, V. Pentamethinium fluorescent probes:
The impact of molecular structure on photophysical properties and
subcellular localization. *Dyes Pigm.* **2014**, *107*, 51–59.
- (43) Chazotte, B. Labeling mitochondria with TMRM or TMRE.
Cold Spring Harb. Protoc. **2011**, *2011*, 895–897.

Publication 2:

Synthesis and spectral characterization of the first fluorescein-tagged iron(II) clathrochelates, their supramolecular interactions with globular proteins, and cellular uptake

Roman Selin,^[a] Insa Klemt,^[b] Viktor Ya. Chernii,^[a] Mykhaylo, Yu. Losytskyy,^[c] Svitlana Chernii,^[c] Andrzej Mular,^[d] Elzbieta Gumienna-Kontecka,^[d] Vladyslava B. Kovalska,^[c] Yan Z. Voloshine,^[f] Anna V. Vologzhanina,^[f] Pavel V. Dorovatovskij,^[g] and Andriy Mokhir^[b]

^[a] Vernadskii Institute of General and Inorganic Chemistry NASU, 32/34 Palladin Prosp., 03080 Kiev, Ukraine.

^[b] Department of Chemistry and Pharmacy, Organic Chemistry II, Friedrich-Alexander-Universität Erlangen-Nürnberg, Nikolaus-Fiebiger-Str. 10, 91058 Erlangen, Germany

^[c] Institute of Molecular Biology and Genetics, NASU, 150 Zabolotnogo St., 03143 Kyiv, Ukraine

^[d] Faculty of Chemistry, University of Wrocław, 14 F. Joliot-Curie St., 50-383 Wrocław, Poland

^[e] Kurnakov Institute of General and Inorganic Chemistry of the Russian Academy of Sciences, 31 Leninsky Prosp., 119991 Moscow, Russia

^[f] Nesmeyanov Institute of the Organoelement Compounds of the Russian Academy of Sciences, 28 Vavilova St., 119991 Moscow, Russia

^[g] National Research Center Kurchatov Institute, 1 Kurchatova Pl., 123098 Moscow, Russia

Contribution of I. Klemt:

Design, performance, and data processing of microscopy experiment with A2780 cells, contribution to Publication writing and revision of the manuscript.

The publication and supporting information are found under: DOI: **10.1039/D0RA10502C**.


 Cite this: *RSC Adv.*, 2021, 11, 8163

Synthesis and spectral characterization of the first fluorescein-tagged iron(II) clathrochelates, their supramolecular interactions with globular proteins, and cellular uptake†

 Roman O. Selin, ^{‡a} Insa Klemt, ^b Viktor Ya. Chernii, ^{*a}
 Mykhaylo Yu. Losytskyi, ^c Svitlana Chernii, ^c Andrzej Mular, ^d
 Elzbieta Gumienna-Kontecka, ^d Vladyslava B. Kovalska, ^c Yan Z. Voloshin, ^{ef}
 Anna V. Vologzhanina, ^f Pavel V. Dorovatovskii ^g and Andriy Mokhir ^b

A fluorescein-tagged iron(II) cage complex was obtained in a moderate total yield using a two-step synthetic procedure starting from its propargylamine-containing clathrochelate precursor. An 11-fold decrease in fluorescence quantum yield is observed in passing from the given fluorescein-based dye to its clathrochelate derivative. An excitation energy transfer from the terminal fluorescent group of the macrobicyclic molecule to its quasiaromatic highly π -conjugated clathrochelate framework can explain this effect. The kinetics of the hydrolysis of the acetyl groups of acetylated fluorescein azide and its clathrochelate derivative in the presence of one equivalent of BSA evidenced no strong supramolecular host–guest interactions between BSA and the tested compounds. Study of a chemical stability of the deacetylated iron(II) clathrochelate suggested the formation of a supramolecular 1 : 1 BSA–clathrochelate assembly. Moreover, an addition of BSA or HSA to its solution caused the appearance of strong clathrochelate-based ICD outputs. The fluorescence emission anisotropy studies also evidenced the supramolecular binding of the fluorescein-tagged iron(II) clathrochelate to the BSA macromolecule, leading to a high increase in this type of anisotropy. Subcellular uptake of the fluorescein-tagged molecules was visualized using fluorescence microscopy and showed its distribution to be mainly in the cytosol without entering the nucleus or accumulating in any other organelle. An X-rayed crystal of the above propargylamide macrobicyclic precursor with a reactive terminal $C\equiv C$ bond contains the clathrochelate molecules of two types, A and B. The encapsulated iron(II) ion in these molecules is situated in the center of its FeN_6 -coordination polyhedron, the geometry of which is intermediate between a trigonal prism (TP) and a trigonal antiprism (TAP). The Fe–N distances vary from 1.8754(6) to 1.9286(4) Å and the heights h of their distorted TP–TAP polyhedra are very similar (2.30 and 2.31 Å); their values of φ are equal to 25.3 and 26.6°. In this crystal, the molecules of types A and B participate in different types of hydrogen bonding, giving H-bonded clathrochelate tetramers through their carboxylic and amide groups, respectively; these tetramers are connected to H-bonded chains.

 Received 14th December 2020
 Accepted 2nd February 2021

DOI: 10.1039/d0ra10502c

rsc.li/rsc-advances

Introduction

Clathrochelates¹ are a unique class of cage metal complexes, with their central metal ion(s) encapsulated in the three-

dimensional cavity of an appropriate macropolycyclic organic or organoelement ligand. Designed clathrochelates with terminal reactive group(s) or atom(s) in their molecules possess high flexibility for their easy chemical functionalization in up to

^aVernadskii Institute of General and Inorganic Chemistry NASU, 32/34 Palladin Prosp., 03080 Kiev, Ukraine. E-mail: v.chernii@gmail.com

^bOrganic Chemistry II, Friedrich-Alexander-University of Erlangen-Nuremberg, Nikolaus-Fiebiger-Straße 10, 91058 Erlangen, Germany

^cInstitute of Molecular Biology and Genetics, NASU, 150 Zabolotnogo St., 03143 Kyiv, Ukraine

^dFaculty of Chemistry, University of Wrocław, 14 F. Joliot-Curie St., 50-383 Wrocław, Poland

^eKurnakov Institute of General and Inorganic Chemistry of the Russian Academy of Sciences, 31 Leninsky Prosp., 119991 Moscow, Russia

^fNesmeyanov Institute of the Organoelement Compounds of the Russian Academy of Sciences, 28 Vavilova St., 119991 Moscow, Russia

^gNational Research Center Kurchatov Institute, 1 Kurchatova Pl., 123098 Moscow, Russia

† CCDC 2041069. For crystallographic data in CIF or other electronic format see DOI: 10.1039/d0ra10502c

‡ The authors dedicate this paper to the memory of Prof. O. Varzatskii who initiated this work, but suddenly passed away on 20 December 2017.



four directions, using up to eight sites in the case of mononuclear cage metal complexes (Fig. 1). As it can be seen from Fig. 1, there are six ribbed and two apical potential sites for transformations which can be directly chemically modified using a wide range of organic substituents. This opens a path to different practical applications, including various biological activities, depending on the nature and geometrical positions of these substituents in the cage framework. However, for a long time, the metal complexes of this type were not considered to be prospective biologically active compounds for modern drug therapy because of “classic” requirements^{2–4} for therapeutic prodrugs, despite the presence of a number of exceptions to these rules.^{5–7} In particular, the designed cage metal complexes are reported^{8–11} to be low- and sub-micromolar transcription inhibitors in the transcription systems of T7 RNA and Taq DNA polymerases; they are also able to quench the protein fluorescence of a series of globular proteins.¹² An *in vitro* study¹³ revealed the high cytotoxicity of an electrophilic iron(II) hexachloroclathrochelate against the human promyelocytic leukemia cell line; antifibrillogenic activity of the designed carboxyl-terminated iron(II) mono- and bis-clathrochelates toward insulin and lysozyme has also been observed.^{14,15} Moreover, an ability of the inherently CD-silent iron(II) clathrochelates to give a strong CD output (induced CD (ICD) signals) in the presence of globular proteins was reported^{16,17} for the first time. The appearance of highly intense clathrochelate-localized ICD spectra for a series of iron(II) cage complexes as macrobicyclic guests upon their supramolecular binding to bovine and human serum albumins (BSA and HSA) and β -lactoglobulin (BLG) as the hosts suggests their prospective ICD-reporter properties for probing the spatial structure of macromolecules of a wide range of globular proteins and their structural alternations. Regardless of obtaining the above valuable experimental results, the true mechanism of the cytotoxicity and other types of biological activity of these cage complexes remains unknown. Molecular imaging is an efficient prospective method for the detection of the subcellular

localization of target molecules.^{18,19} At the same time, a large variety of prospective optical tags (optically active labeling substituents or groups) has been extensively elaborated.²⁰ Functionalization of a given clathrochelate molecule with a fluorescent labelling group can be used to monitor its localization in cells; it also allows *in vivo* testing of these cage complexes for a better understanding of their mode of bioactivity. In this paper, we report an efficient synthetic strategy for obtaining the first fluorescein-tagged iron(II) clathrochelates, whose molecules are functionalized with a terminal fluorophore group, their luminescent properties, and data on their chemical stability in various media, their interaction with globular proteins, and the uptake and localization of these cage metal complexes in cancer cells.

Experimental

Materials and apparatus

The reagent tris((1-benzyl-4-triazolyl)methyl)amine (TBTA), CuI, lipase, CALB-L (Novozyme), sorbents, organic bases, and solvents used were obtained commercially. Propargylamide clathrochelate precursor **2** was prepared as described elsewhere.²¹ Diacetyl *N*-(4-azobutyl)-fluorescein-5(6)-carboxamide was obtained using a known synthetic procedure.²² Bovine Serum Albumin (BSA) and human serum albumin (HAS) were obtained commercially (SAF® and Fisher Bioreagents, respectively). β -Lactoglobulin (BLG), lysozyme (LYZ), human insulin, trypsin, and analytical grade DMSO were also purchased from SAF®. 50 mM Tris-HCl aqueous buffer with pH 7.9 was used as the solvent for all optical studies. All these experiments were performed in a standard 1 × 1 cm quartz cell.

Analytical data (C, H, N contents) were obtained with a Carlo Erba model 1106 microanalyzer. High-resolution APPI mass spectra were obtained using a maXis 4G UHR TOF mass spectrometer (Bruker Daltonik).

¹H and ¹³C{¹H} NMR spectra of the complexes under study were recorded from their solutions in acetone-*d*₆ and DMSO-*d*₆ with a Bruker Avance 400 spectrometer. The ¹H and ¹³C (¹H) NMR measurements were obtained using the residual signals of these solvents.

CD spectra were recorded on a Jasco J-1500CD spectrometer in the range 300–600 nm in 0.1 nm steps with a scan of 3001 points; three scans were averaged for each of the ICD spectra in the visible and near UV ranges. For the latter measurements, stock 5 mM solutions of compounds **1**, **3**, **4**, and **5** in DMSO and 0.2 mM solutions of BSA, HSA, BLG, and LYZ in 50 mM Tris-HCl aqueous buffer with pH 7.9 were prepared. Mixtures of 0.8 mL of this buffer, 0.2 mL of a protein solution, and 4 μ L of the stock solution of a given compound were used for the fluorescence experiments. Fluorescence excitation, emission, and anisotropy spectra were measured using a Cary Eclipse fluorescence spectrophotometer (Varian, Australia); the coupled UV-vis experiments were performed with a Shimadzu UV-3600 UV-vis-NIR spectrophotometer. Quantum yields for compounds **4** and **5** were obtained in 50 mM Tris-HCl aqueous buffer with pH 7.9 using a solution of fluorescein in ethanol as the reference fluorophoric standard (its quantum yield ϕ_{FL} is equal to 0.97). For

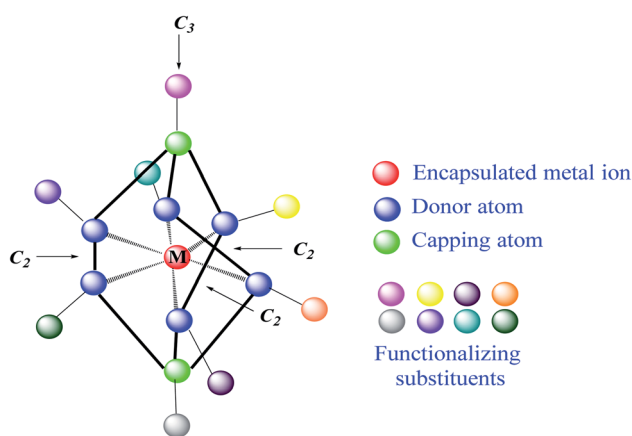


Fig. 1 Functionalization of a mononuclear metal-encapsulating clathrochelate framework. The marked symmetry elements appear if the corresponding functionalizing apical and/or ribbed substituents are the same groups.



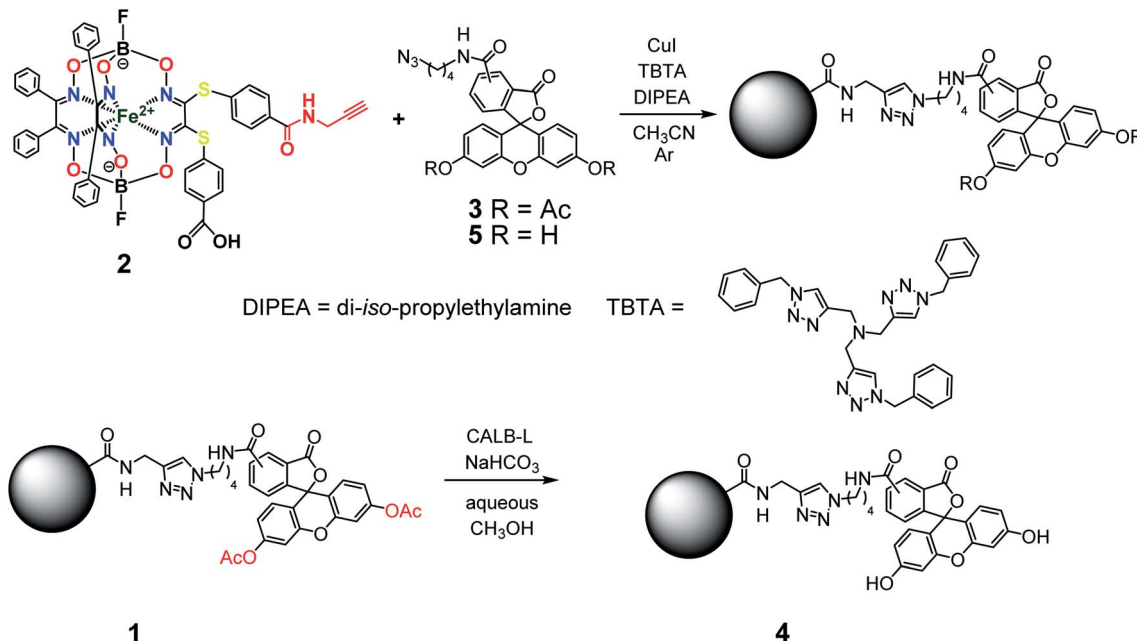


Fig. 2 Elaborated synthetic pathway to obtain a given monoribbed-functionalized iron(II) clathrochelate molecule containing a single terminal fluorescent group in one of its ribbed substituents.

this purpose, the DMSO stock solutions of clathrochelate 4 and modified fluorescein 5 were diluted in 50 mM Tris-HCl aqueous buffer with pH 7.9 to concentrations possessing equal optical densities at 472 and 490 nm, respectively, to that of fluorescein; due to the dilution in the above buffer, the quantity of DMSO in the final solutions was negligibly small. Fluorescence of all the obtained solutions was excited at the corresponding wavelengths (472 nm for complex 4 and fluorescein and 490 nm for compound 5 and fluorescein) and the area below each of these spectra (S_{dye} for 4 and 5 and S_{FL} for fluorescein as reference) was calculated. Then, the fluorescence quantum yields ϕ_{dye} for these compounds were calculated using the following equation: $\phi_{\text{dye}} = \phi_{\text{FL}} \times (S_{\text{dye}}/S_{\text{FL}}) \times (n_{\text{H}_2\text{O}}/n_{\text{EtOH}})^2$, where $n_{\text{H}_2\text{O}}$ and n_{EtOH} are the refractive indexes of water and ethanol, respectively.

Study of uptake and subcellular localization of iron(II) clathrochelate with fluorescent labelling group

Human ovarian cancer A2780 cells (Merck, 93112519), selected as a representative cancer cell line, were cultured according to the recommendations of Deutsche Sammlung von Mikroorganismen und Zellkulturen GmbH (DSMZ) in Roswell Park Memorial Institute (RPMI) 1640 medium supplemented with 10% FBS (fetal bovine serum), 1% L-glutamine and 1% penicillin/streptomycin (all SAF®). One day before the experiment, A2780 cells were seeded at a concentration of 80 cells per μL in 500 μL of culture medium on a 35 mm-diameter imaging dish ($\mu\text{-Dish}$, high, SAF® GmbH, Germany) and incubated overnight. The next day, the cells were washed two times with Dulbecco's Phosphate-Buffered Saline (DPBS) and incubated for 4 h with 9 μM of complex 4 in growth medium containing 5%

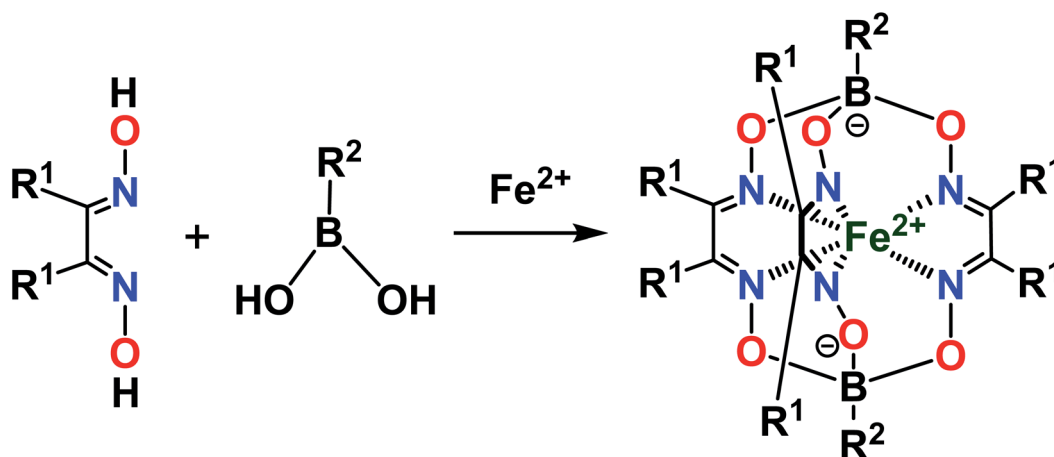


Fig. 3 Template synthesis of the boron-capped iron(II) clathrochelates with equivalent apical cross-linking and ribbed chelating fragments.



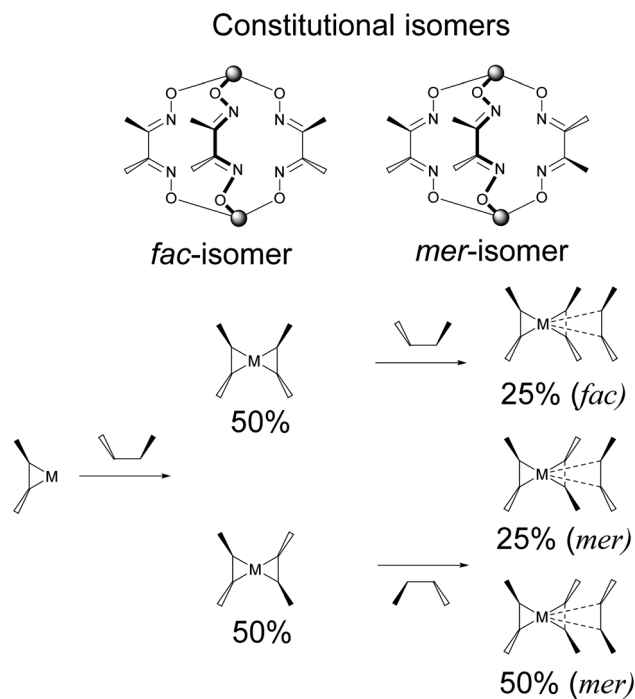


Fig. 4 Statistical formation of the constitutional *fac*- and *mer*-isomers of a clathrochelate complex—the derivative of a chelating ligand's synthon with non-equivalent substituents.

FBS, 1% L-glutamine, 1% penicillin/streptomycin, and 1% DMSO. Subsequently, the cells were washed two times with DPBS, then 4 ng mL⁻¹ Hoechst 33342 in culture medium was added and incubated for 30 min. The cells were washed again two times with DPBS and images were obtained using a Zeiss Axio Vert.A1 equipped with two filter sets (excitation/emission 365/445(50) nm for the 49 DAPI channel and excitation/emission 470(40)/525(50) nm for the 38 blue channel) using the objective 40×/1.30 and an oil DIC.

Synthesis, analysis and spectral characteristics of the fluorescein-tagged iron(II) clathrochelates

The general synthetic pathway to obtain the new cage iron(II) complexes is presented in Fig. 2.

Complex 1. Clathrochelate precursor **2** (15 mg, 14.7 μmol), fluorescein azide **3** (8.2 mg, 14.7 μmol), CuI (0.3 mg, 1.47 μmol) and TBTA (0.78 mg, 1.47 μmol) were dissolved in acetonitrile (0.6 mL) under argon, then di-iso-propylethylamine (12.8 μL, 73.57 μmol) was added. The reaction mixture was stirred for 4 h at 60 °C and then 1 M aqueous hydrochloric acid (1 mL) was added. The obtained solution was extracted with dichloromethane (3 mL in three portions). The combined extract was washed with a brine solution, dried with Na₂SO₄ and separated using column chromatography on silica gel (eluent: ethyl acetate–methanol 7 : 3 mixture), giving the red solid target product with *R_f* = 0.28 after evaporation of the corresponding major elute. Yield: 7.8 mg (5.0 μmol, 34%). Calc. for C₇₆H₅₇B₂F₂FeN₁₁O₁₇S₂: C, 57.90; H, 3.65; N, 9.78; S, 4.07. Found (%): C, 57.59; H, 3.69; N, 9.55; S, 3.99. MS APPI (positive range) *m/z*: Calcd. for C₇₆H₅₇B₂F₂FeN₁₁O₁₇S₂: 1575.29, found: 1576.2944 [M + H]⁺. ¹H NMR (400 MHz, acetone-*d*₆) δ 0.97 (d, *J*_{H-H} = 6.1 Hz, 6H, CH₃), 1.54 (p, *J* = 7.1 Hz, 2H, CH₂), 1.86 (q, *J*_{H-H} = 7.3 Hz, 2H, CH₂), 3.36 (dt, *J*_{H-H} = 7.1, 3.7 Hz, 2H, CH₂), 4.32 (t, *J*_{H-H} = 7.0 Hz, 2H, CH₂), 4.48 (d, *J*_{H-H} = 4.9 Hz, 2H, CH₂), 6.86–6.75 (m, 4H, 2*H*-Ar + *H*-N), 7.10–7.04 (m, 2H, *H*-Ar), 7.12 (d, *J*_{H-H} = 8.3 Hz, 2H, *H*-Ar), 7.31–7.15 (m, 23H, *H*-Ar), 7.37–7.31 (m, 1H, *H*-Ar), 7.75–7.67 (m, 2H, *H*-Ar), 7.82–7.74 (m, 2H, *H*-Ar), 8.11 (s, 1H, *H*-Ar), 8.18 (dd, *J* = 8.0, 1.6 Hz, 1H, *H*-Ar), 8.39–8.33 (m, 1H, *H*-Ar). ¹³C{¹H} NMR (101 MHz, acetone-*d*₆) δ 20.10, 24.87, 26.37, 27.56, 28.38, 28.57, 28.76, 28.96, 29.15, 29.34, 29.53, 29.70, 39.02, 49.39, 81.33, 110.47, 116.23, 118.40, 123.54, 124.34, 126.61, 128.00, 128.03, 128.30, 129.11, 129.18, 129.28, 130.31, 130.61, 134.70, 135.27, 151.41, 152.70, 154.76, 157.70, 167.78, 168.45, 205.35.

Complex 4. Complex **1** (10 mg, 6.34 μmol) was suspended in methanol (1 mL), then NaHCO₃ aqueous solution (25%, 1 mL) and lipase CALB-L (0.1 mL) were added. The reaction mixture was stirred for 48 h at 40 °C, then the solid product was filtered off and recrystallized from methanol. Yield: 6 mg (4.02 μmol, 63%). MS APPI (positive range) *m/z*: Calcd. for C₇₂H₅₃B₂F₂FeN₁₁O₁₅S₂: 1491.27. Found: 1492.2752 [M + H]⁺. ¹H NMR (400 MHz, DMSO-*d*₆) δ 1.48 (dt, *J*_{H-H} = 42.7 and 7.7 Hz, 4H, CH₂), 1.98–1.66 (m, 4H, CH₂), 3.41–3.16 (m, 4H, CH₂), 4.35 (dt, *J*_{H-H} = 29.1 and 7.0 Hz, 4H, CH₂), 4.50 (dd, *J*_{H-H} = 11.2 and 5.4 Hz, 4H, CH₂), 6.57 (tq, *J*_{H-H} = 6.0, 3.7 and 2.8 Hz, 10H, *H*-Ar), 6.70

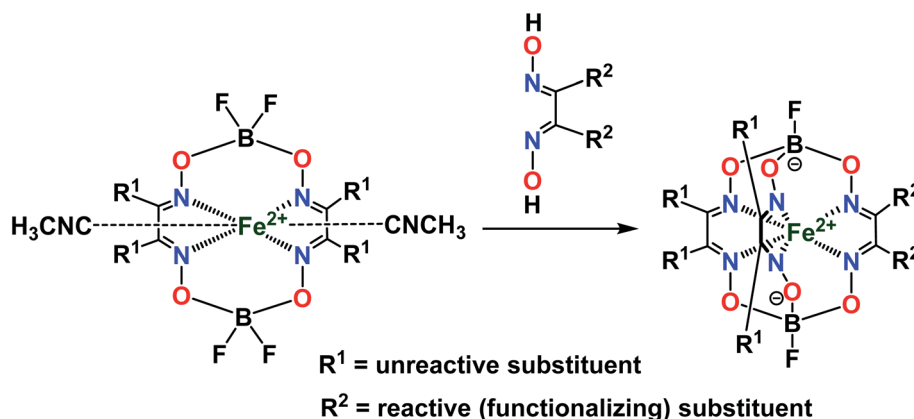


Fig. 5 General synthetic approach for preparation of the monoribbed-functionalized iron(II) clathrochelates.



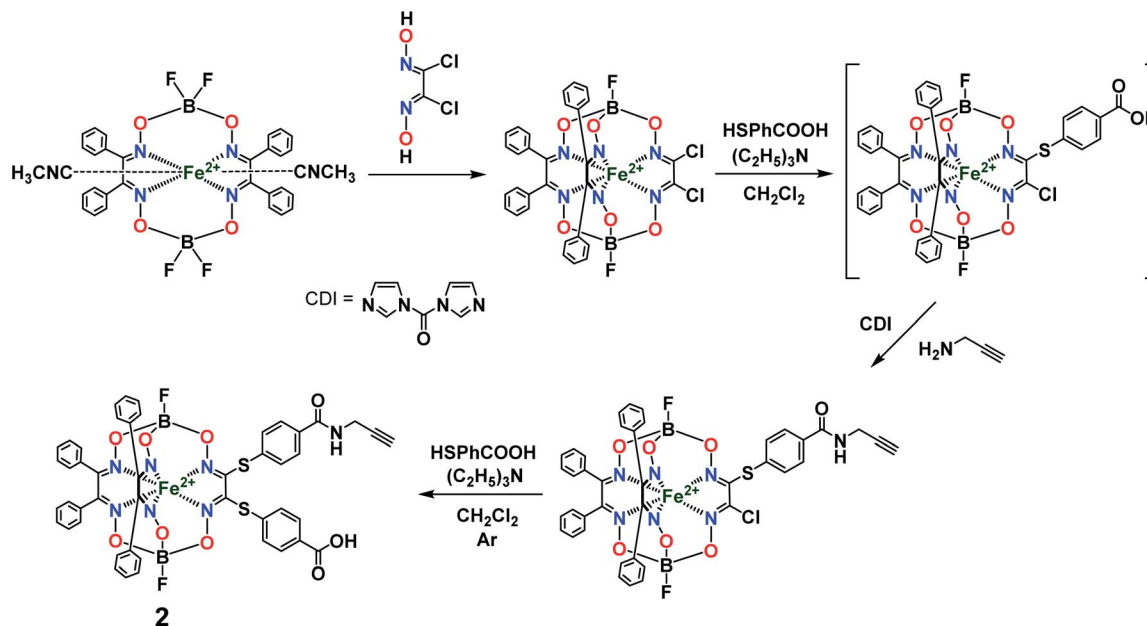


Fig. 6 General synthetic pathway to a monocarboxylomonopropargylamine iron(II)-encapsulating clathrochelate precursor.

(*t*, $J_{\text{H-H}} = 2.4$ Hz, 4H, *H-N*), 7.29 (d, $J_{\text{H-H}} = 8.1$ Hz, 8H, *H-Ar*), 7.38 (d, $J_{\text{H-H}} = 5.3$ Hz, 40H, *H-Ar*), 7.67 (s, 1H, *H-Ar*), 7.92–7.82 (m, 8H, *H-Ar*), 7.95 (d, $J_{\text{H-H}} = 2.5$ Hz, 2H, *H-Ar*), 8.00 (d, $J_{\text{H-H}} = 2.4$ Hz, 1H, *H-Ar*), 8.07 (d, $J_{\text{H-H}} = 8.0$ Hz, 1H, *H-Ar*), 8.16 (d, $J_{\text{H-H}} = 8.1$ Hz, 1H, *H-Ar*), 8.23 (d, $J_{\text{H-H}} = 8.2$ Hz, 1H, *H-Ar*), 8.45 (s, 1H, *H-Ar*), 8.70 (t, $J_{\text{H-H}} = 5.6$ Hz, 1H, *H-Ar*), 8.85 (t, $J_{\text{H-H}} = 5.6$ Hz, 1H, *H-Ar*), 9.07 (dd, $J_{\text{H-H}} = 11.4$ and 6.1 Hz, 2H, *H-Ar*), 10.16 (d, $J_{\text{H-H}} = 2.6$ Hz, 4H, *H-Ar*), 13.11 (s, 2H, *HOOC*).

Single crystal X-ray diffraction experiment

A single crystal of the complex $2 \cdot 0.75\text{C}_7\text{H}_{16}$ suitable for the synchrotron X-ray diffraction experiment was grown from a chloroform–heptane 1 : 5 mixture. Intensities of the reflections for this crystal were collected with the K4.4 Belok

beamline of the Kurchatov Synchrotron Radiation Source (NRC Kurchatov Institute, Moscow, Russia) at the wavelength of 0.7927 Å using a Rayonix CCD 165 detector. Data collection was performed at the low temperature of 100.0(2) K using an Oxford CryoJet (Oxford Cryosystems). Image integration was performed using iMosflm software.²³ The integrated intensities were empirically corrected for absorption using the Scala program.²⁴ Crystal data for $2 \cdot 0.75\text{C}_7\text{H}_{16}$ at 100.0(2) K: $\text{C}_{52.5}\text{H}_{45.5}\text{B}_2\text{F}_2\text{FeN}_7\text{O}_9\text{S}_2$, $M = 1098.05$, triclinic, space group $P\bar{1}$, $a = 13.293(3)$ Å, $b = 18.175(4)$ Å, $c = 22.565(5)$ Å, $\alpha = 104.83(3)^\circ$, $\beta = 103.52(3)^\circ$, $\gamma = 90.14(3)^\circ$, $V = 5113(2)$ Å³, $Z = 4$, $D_{\text{calc}} = 1.427$ g cm⁻³, $\mu = 0.579$ mm⁻¹, 17347 independent reflections ($R_{\text{int}} = 0.241$), 7195 observed reflections, final convergence factors $R_1[I > 2\sigma(I)] = 0.096$, $wR(F^2) = 0.227$ and GOF = 0.992. The structure was solved by the direct method and refined by full-matrix least

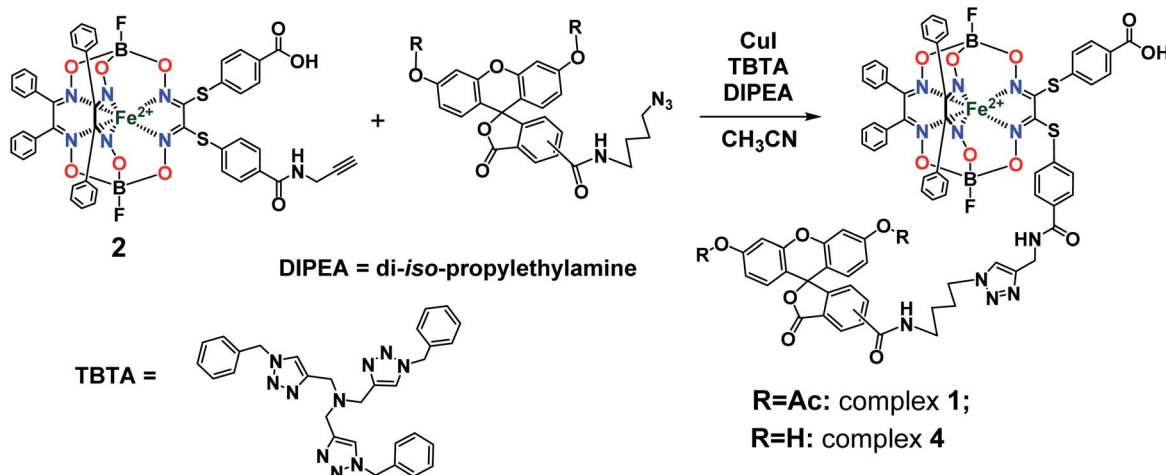


Fig. 7 Functionalization of an iron(II)-encapsulating clathrochelate precursor with the single terminal fluorescein group.



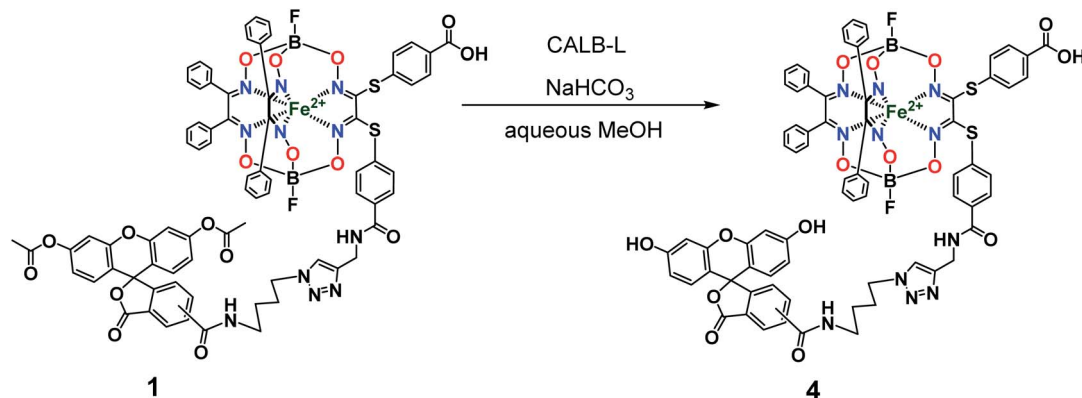


Fig. 8 Chemical transformation of an iron(II) clathrochelate molecule with the single acylated fluorescein group giving its deprotected macrobicyclic derivative.

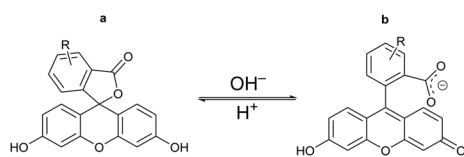


Fig. 9 Chemical drawings of the closed (a) and open (b) tautomeric forms of the fluorescein molecule.

squares against F^2 . Non-hydrogen atoms were refined anisotropically; the positions of hydrogen atoms were calculated and all hydrogen atoms were included in the refinement by the riding model using $U_{\text{iso}}(\text{H}) = 1.5U_{\text{eq}}(\text{X})$ for methyl groups and $1.2U_{\text{eq}}(\text{X})$ for the other atoms. The crystal structure was refined as a twin using HKLF 5 refinement. All calculations were made using the SHELXL2014 (ref. 25) and OLEX2 (ref. 26) program packages. CCDC 2041069 contains the ESI[†] crystallographic data for this paper.

Results and discussion

Synthetic strategy towards the target tagged iron(II) cage complexes and their preparation

The designed clathrochelate tris- α -dioximate molecules with reactive inherent or terminal groups or atoms are quasiaromatic macropolycyclic systems and, therefore, can be easily functionalized using the classical methods of modern organic chemistry.¹ Very few synthetic approaches for obtaining metal clathrochelates of this type have been developed to date. Despite the metal-promoted C-C cross- and homo-coupling reactions of the suitable halogenoclathrochelate precursors that have been recently developed,^{9,10,27–29} only three main synthetic approaches have been successfully used to date for effective preparation in a reasonable yield. The first of them is based on template condensation on a suitable metal ion as a matrix³⁰ (Fig. 3) with a statistical mixture of a given α -dioxime and an appropriate Lewis acid (in particular, a suitable boronic acid or its ester). This method, based on direct *one-pot* condensation, is reported^{1,30} to be the most widely used for

the synthesis of a number of cage metal complexes of this type, the molecules of which contain equivalent apical cross-linking and ribbed chelating fragments in their encapsulating macropolycyclic ligands. Unfortunately, its use is substantially limited or even prohibited in the case of the functionalized α -dioximate ligand's synthons, the additional donor group(s) of which are able to form strong coordination bond(s) with a templating metal ion, thus competing with the two N-donor oxime groups of this synthon and causing a decrease in the yield of the target clathrochelate complex. Moreover, such uncoordinated oxime groups are highly reactive towards various ketones, aldehydes, unsaturated bonds, *etc.*³¹ As a result, the triribbed-functionalized metal clathrochelates with equivalent chelate and apical fragments have been prepared mainly by exploring the reactivity of their hexahalogenoclathrochelate precursors (including in metal-catalyzed (promoted) processes) in various nucleophilic substitution and cross-coupling reactions.^{1,30}

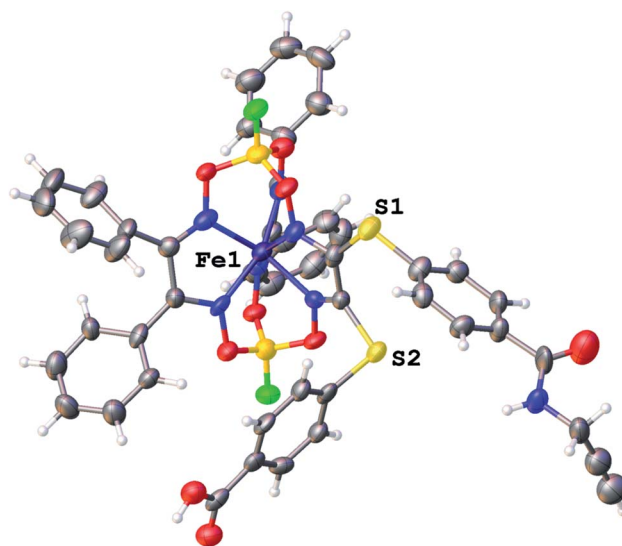


Fig. 10 General view of an independent molecule of 2 (type A) in a representation of its atoms as thermal ellipsoids ($p = 50\%$).



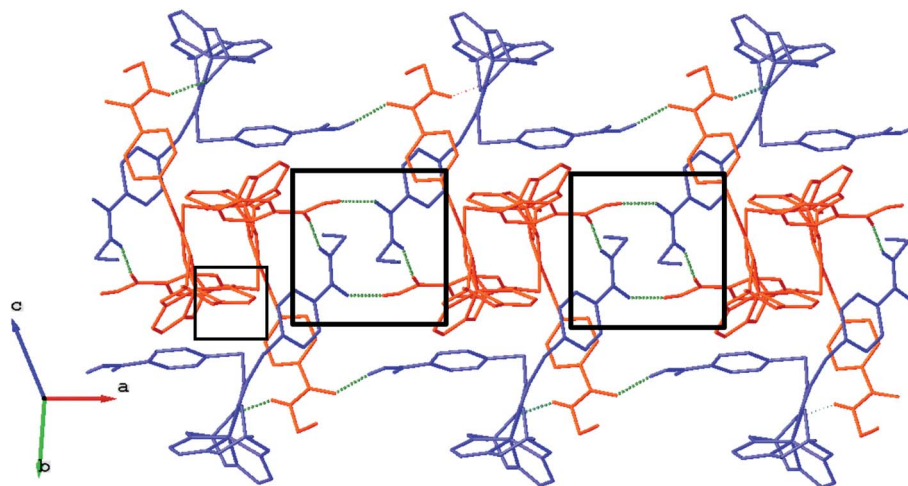


Fig. 12 Fragment of the H-bonded clathrochelate chains in the X-rayed crystal $2 \cdot 0.75\text{C}_7\text{H}_{16}$. The clathrochelate molecules of types A and B are shown in red and blue colors, respectively; solvent molecules, phenyl rings and all H(C) atoms are omitted for clarity. H-bonded clathrochelate tetramers, which are formed within the above chains, are marked using the black squares.

The third synthetic method to obtain the target cage complexes with non-equivalent ribbed chelate fragments is based on a stepwise nucleophilic substitution of their reactive halogenoclathrochelate precursors with various *S,N,O,S,P*-nucleophiles.^{1,30,37–42} The nature of the clathrochelate products of these reactions is described in literature^{1,30,38,41} as affected not only by the nature of a given nucleophilic agent but also those of the solvent used and of the reaction conditions.

Previously, we obtained²¹ the propargylamide iron(II) cage complex **2** as a prospective clathrochelate precursor for the

metal-promoted reactions, the molecule of which contains a terminal $\text{C}\equiv\text{C}$ bond. Complex **2** was synthesized using a combination of template condensation and stepwise nucleophilic substitution with an *in situ* chemical transformation of the terminal carboxyl group of its macrobicyclic intermediate (Fig. 6). From a general point of view, it is possible to obtain the corresponding difunctionalized iron(II) clathrochelate with two terminal carboxyl groups and then implement its further modification with a propargylamine group. However, the order of chemical transformations of a given dichloroclathrochelate precursor shown in Fig. 6 gave the target macrobicyclic complex **2** in an higher overall yield.

So, the fluorescein-functionalized iron(II) cage complex **4** with a terminal fluorophoric group was obtained from its propargylamide-containing clathrochelate precursor **2** using a two-step synthetic procedure shown in Fig. 7. During our preliminary experiments, we tried to perform a direct reaction of this macrobicyclic precursor with the appropriate fluorescein-containing azide component. However, we failed to obtain the target clathrochelate product **4** in a reasonable yield, if any, using different reaction conditions (probably because the presence of hydroxyl groups in this fluorescein-based molecule prevents a formation of the corresponding intermediate copper complex, thus inhibiting the target copper-catalyzed “click”-reaction). Therefore, we initially performed acetylation of the

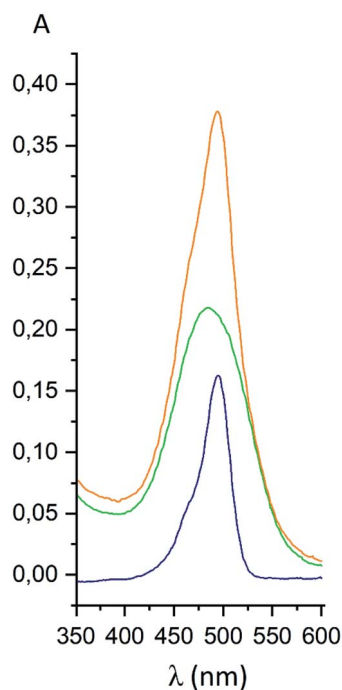


Fig. 13 UV-vis spectra of fluorescein azide **5** (shown in blue), the tag-less clathrochelate **4** (shown in green) and their equimolar mixture (shown in orange).

Table 2 Fluorescence characteristics of compounds **4** and **5** measured in two different media

Compound	Tris-HCl aqueous buffer			Methanol		
	λ_{ex} (nm)	λ_{em} (nm)	<i>I</i> (a.u.)	λ_{ex} (nm)	λ_{em} (nm)	<i>I</i> (a.u.)
4	497	523	368	490	521	57
5	495	522	10181	487	523	1045



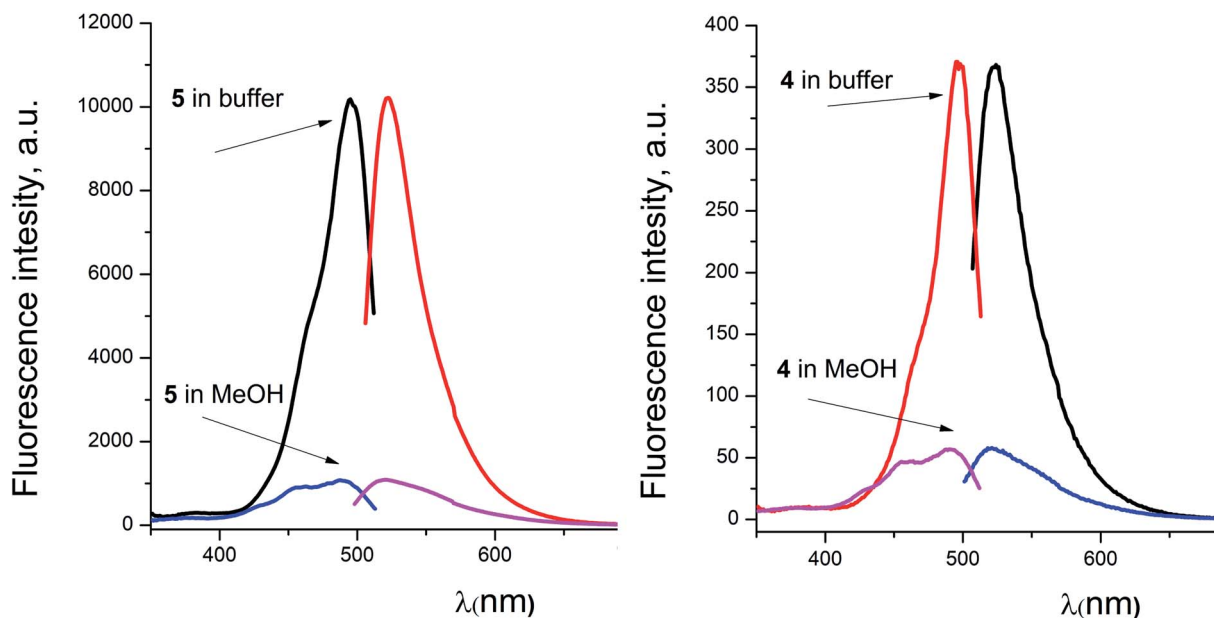


Fig. 14 Excitation and fluorescence emission spectra of fluorescein azide **5** (left) and the fluorescein-tagged iron(II) clathrochelate **4** (right) measured from their solutions in 0.05 M Tris–HCl aqueous buffer with pH 7.9 and in methanol.

hydroxyl groups and the corresponding acetylated fluorescein-containing clathrochelate intermediate **1** was obtained in a moderate yield of approximately 30%. The formation of substantial amounts of by-products in this 1,3-dipolar cycloaddition could be caused by partial hydrolysis of the acetyl groups of its fluorescein-containing azide component under the reaction conditions used. We tested various synthetic approaches to deprotect the acetylated hydroxyl groups of **1** to obtain the target cage complex **4**. Their partial hydrolysis, which easily proceeds under these reaction conditions, also causes a competing parallel process of the complete destruction of **1**. Indeed, its clathrochelate tris-dioximate framework is chemically unstable under the “classical” aqueous basic conditions of a hydrolysis reaction of these groups and undergoes complete destruction with elimination of the functionalizing fluorescein group. Such a side process can be easily detected by naked eye as it causes the appearance of the characteristic green coloration in aqueous basic media. To prevent a complete destruction of the cage framework of **1**, we used, for the first time, enzymatic hydrolysis with lipase CALB-L as a catalyst, thus giving the target deacetylated clathrochelate **4** in almost quantitative yield (Fig. 8).

The obtained complexes were characterized using elemental analysis, HR-APPI mass spectrometry; UV-vis, fluorescence, and ^1H and $^{13}\text{C}\{^1\text{H}\}$ NMR spectra; and single-crystal X-ray diffraction (for clathrochelate precursor **2**).

Single crystal X-ray structure of a monocarboxyl-containing clathrochelate precursor with the single terminal reactive $\text{C}\equiv\text{C}$ group

We failed to grow single crystals of the new fluorescein-containing iron(II) cage complexes, but unexpectedly succeeded in a growing those of their clathrochelate precursor **2**

which were suitable for the synchrotron X-ray diffraction (XRD) experiment. The X-rayed crystal of $2\cdot 0.75\text{C}_7\text{H}_{16}$ contains the clathrochelate molecules of types **A** and **B**; a general view of one of these molecules is shown in Fig. 10, while the main geometrical parameters of their cage frameworks, as well as those of analogous fluoroboron-capped monoribbed-functionalized arylsulfide iron(II) clathrochelates with known XRD structures, are listed in Table 1. The encapsulated iron(II) ion in all these cage molecules is situated in the centre of its FeN_6 -coordination polyhedron, the geometry of which is intermediate between a trigonal prism (TP, distortion angle $\varphi = 0^\circ$) and a trigonal antiprism (TAP, $\varphi = 60^\circ$). Fe–N distances in the macrobicyclic molecules **2** of types **A** and **B** vary from 1.8754(6) to 1.9286(4) Å and the heights h of their distorted TP–TAP polyhedra are very similar, equal to 2.30 and 2.31 Å, respectively. The values of their bite (chelate N–Fe–N) angles α are characteristic of the boron-capped aromatic α -dioximate iron(II) clathrochelates,^{1,30} while their values of φ are equal to 25.3 and 26.6°, respectively. A comparison of the general views of **A** and **B** is displayed in Fig. 11. Free rotation along their ordinary C–S bonds without any steric clashes is allowed and their conformations are different mainly in an orientations of the arylsulfide ribbed substituents at a cage framework. These clathrochelate molecules **A** and **B** in the X-rayed crystal of $2\cdot 0.75\text{C}_7\text{H}_{16}$ have different types of hydrogen bonding. Two molecules **2** of type **A** with an encapsulated Fe1 ion and two molecules **2** of type **B** with a caged Fe2 cation form the H-bonded clathrochelate tetramers shown in Fig. 12 through their carboxylic and amide groups, respectively. These tetramers are connected into the H-bonded chains *via* the N–H \cdots O interactions of an amide fragment of the clathrochelate molecule of type **A** and oxygen atom of a cage framework of the neighbouring macrobicyclic molecule of type **B**. As a result, in the X-rayed crystal $2\cdot 0.75\text{C}_7\text{H}_{16}$, each of the macrobicyclic

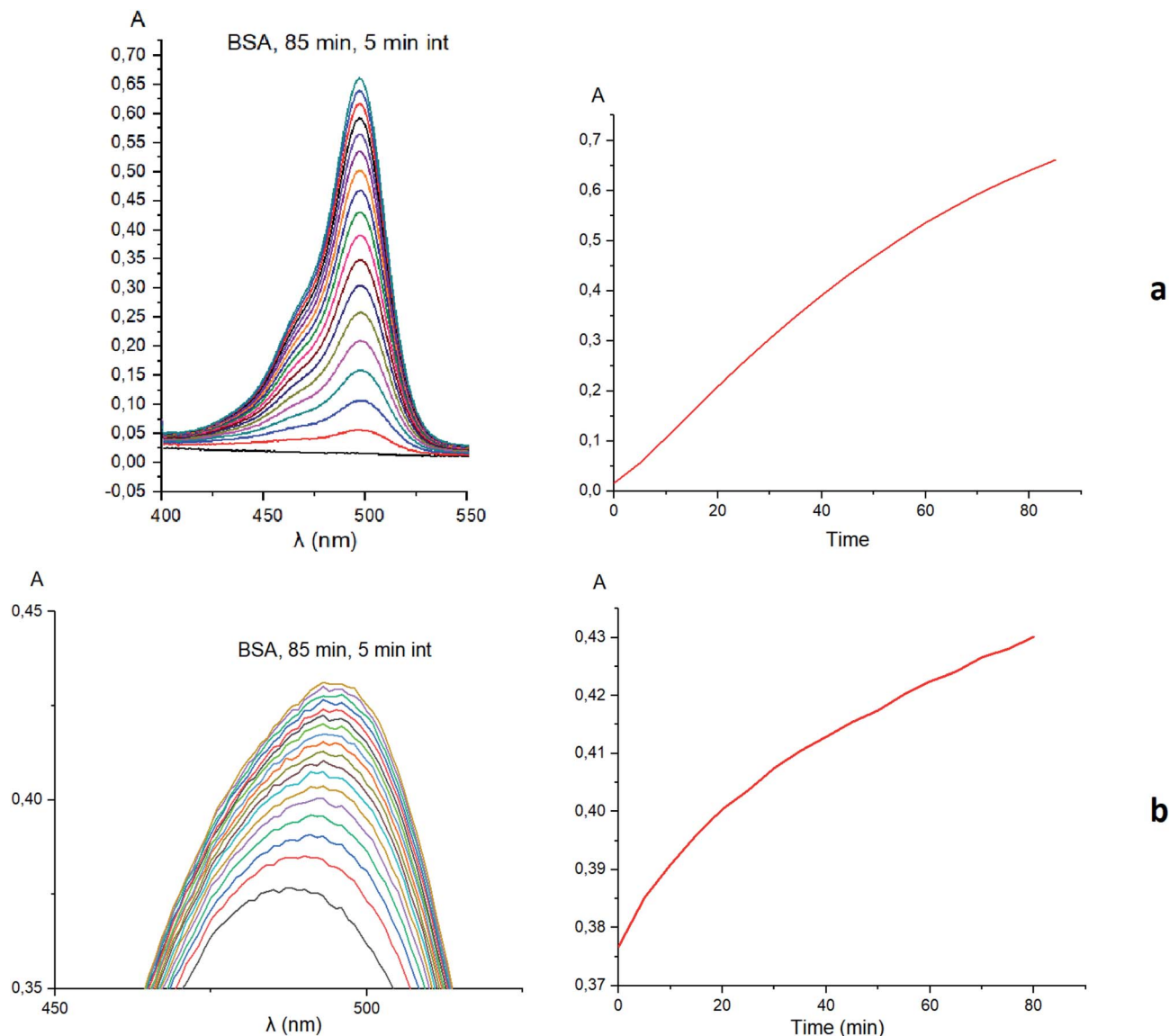


Fig. 15 Kinetic UV-vis experiments and the corresponding plots illustrating the supramolecular host–guest binding of fluorescein azide **3** (a) and clathrochelate complex **1** (b) as the guests to BSA macromolecule as a host.

molecules **2** of type **A** is connected with four clathrochelate molecules **2** of type **B**, and each of the macrobicyclic molecules **2** of type **B** is H-bonded to four cage molecules **2** of type **A**.

UV-vis and fluorescence spectra and UV-vis kinetic studies

The presence of highly intense metal-to-ligand charge transfer (MLCT) $\text{Fe } d \rightarrow L\pi^*$ bands in the visible range is a characteristic of the UV-vis spectra of the tris-dioximate iron(II) clathrochelates.^{1,30} The maxima of these bands are affected by the nature of the σ - and π -conjugated substituents in the chelating ribbed fragments of their quasaromatic cage frameworks. In the case of the bis- α -benzildioximate iron(II) clathrochelates, one absorption band has been observed from 400 to 550 nm with a maximum at approximately 470 nm.¹⁶ The presence of this broad and highly intense asymmetric band may result in

a substantial decrease in a quantum yield or even in a complete quenching of the intrinsic fluorescence of the standard fluorescently active compounds, caused either by an excitation energy transfer or by reabsorption of their emission in a wide spectral range. Earlier, we succeeded in the preparation of a coumarin-functionalized iron(II) clathrochelate; however, it was found to be a fluorescently silent compound. So, in the present study, we tested another fluorescently active group, a fluorescein residue, one of the most common and widely used fluorophore dyes, for target functionalization of the iron(II) clathrochelates. This dye is known²⁰ to possess relatively high molar extinction (approximately $8.8 \times 10^4 \text{ mol}^{-1} \text{ L cm}^{-1}$ at 499 nm in its basic aqueous solution⁴³), with an excellent fluorescence quantum yield of 0.93 and good water solubility as well.



For the fluorescein azide **5** and its tagged clathrochelate derivative **4**, the UV-vis absorption and fluorescent spectra were measured from their 3 μM solutions both in 0.05 M Tris-HCl aqueous buffer with pH 7.9 and in methanol (Fig. 13); the obtained spectral data are collected in Table 2. Both these fluorescein derivatives were initially isolated in acidic media and, therefore, their dye fragment adopts its closed form (Fig. 9). As it can be seen from Fig. 14, compounds **4** and **5** possess different spectral characteristics in solvents of different polarity and H-donor ability. In their methanol solutions, a closed form of this dye fragment persists in both these molecules, while, in a slightly basic medium of the buffer solution, this labeling group adopts its open tautomeric form (Fig. 14), which possesses a higher fluorescence quantum yield. The calculated quantum yields for **5** and **4** are equal to 0.8 and 0.07, respectively, suggesting an 11-fold decrease in fluorescence quantum yield from the fluorescein dye **5** to its clathrochelate derivative **4**. This effect can be explained by an excitation energy transfer from a terminal fluorescein group of labeled molecule **4** to its quasiaromatic highly π -conjugated clathrochelate framework.

Taking into account the well-known^{44,45} esterase-like activity of serum albumins, we performed a study of kinetics of a hydrolysis of the acetyl groups of molecules **1** and **3** in the presence of one equivalent of BSA. Both molecules underwent this reaction, leading to a transformation of their fluorescein-containing closed fragment into its opened tautomeric form, as well as causing an increase in the intensities of their absorptions. Similar optical outputs were observed for both compounds **1** and **3** (Fig. 15), thus suggesting the absence of their (as the guests) strong supramolecular host-guest interactions with the binding centres of BSA macromolecule as a host. On the other hand, the study of a chemical stability of complex **4** showed an increase in the intensity of its characteristic visible absorption band over time in the presence of one equivalent of

BSA (Fig. 16); this spectral effect was not observed in the absence of this transport protein. Therefore, it could be caused by formation of a supramolecular BSA-clathrochelate **4** assembly in the Tris-HCl aqueous buffer solution. Due to the very high halfwidth of the abovementioned visible absorption band, we were not able to assign the components that appeared because of the formation of this non-covalent associate. On the other hand, its dissociation caused an increase in the optical density of the obtained solution. This also evidenced the formation of a supramolecular host-guest assembly between the hosting BSA macromolecule and the clathrochelate guest **4**. Without BSA, no significant change in the measured spectrum was observed for the same period of time. The UV-vis spectrum of the solution of complex **4** in 0.05 M Tris-HCl aqueous buffer with pH 7.9 was measured after 7 days of being kept at room temperature and a 3.5% decrease in its maximal adsorption was observed. We explained this effect by the slow precipitation (agglomeration) of this complex in the given buffer solution while retaining its cage structure.

Clathrochelate-based ICD spectra

No signals were observed in the CD spectra of the initial acetylated compounds **1**, **3**, and **5**. On the other hand, because of a lipase activity of globular proteins, the CD silence of acetylated complex **1** in the presence of these proteins and the appearance of CD signals for its deacetylated derivative **4** under the same reaction conditions suggest their supramolecular binding as clathrochelate guests to the different binding sites of their macromolecules. Indeed, in the case of macrobicyclic complex **4**, the addition of BSA or HSA caused the appearance of strong clathrochelate-based ICD outputs with two positive (maxima at approximately 350 and 520 nm) and one negative (maximum at

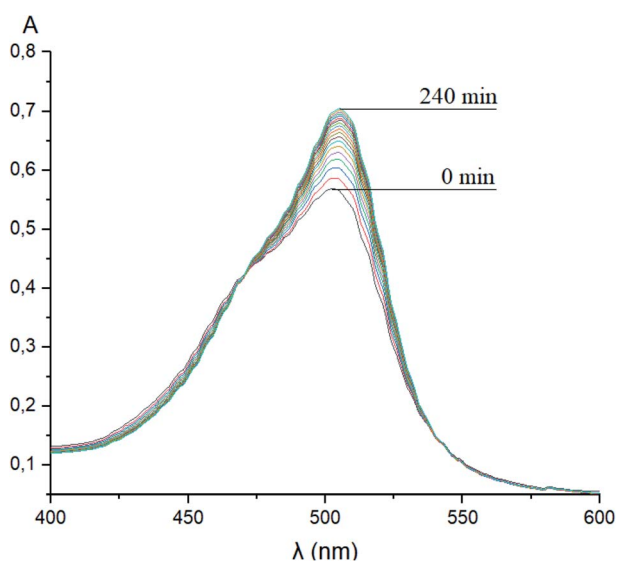


Fig. 16 Changes over time of the solution UV-vis spectrum of complex **4** in the presence of BSA; 0.05 M Tris-HCl aqueous buffer with pH 7.9 was used as a solvent.

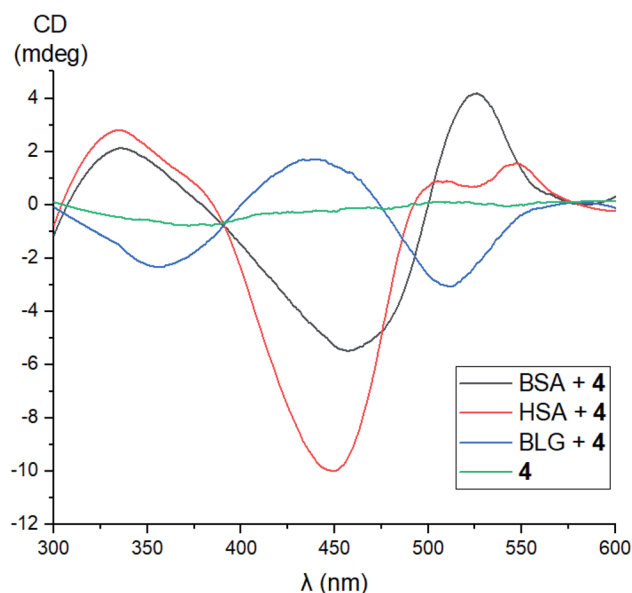


Fig. 17 CD spectra of the supramolecular assemblies of proteins HSA, BSA, BLG and LYZ as the hosts with iron(II) clathrochelate **4** as the guest, measured in 0.05 M Tris-HCl aqueous buffer with pH 7.9 at 25 °C.



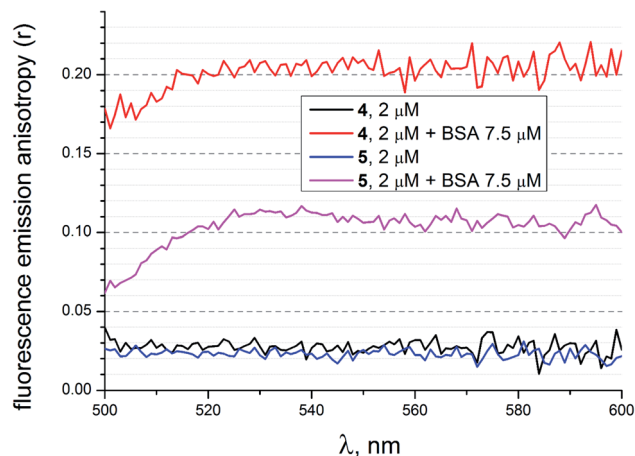


Fig. 18 Fluorescence emission anisotropy spectra of compounds 4 and 5 with excitation at 475 nm alone and those in the presence of BSA, measured in 50 mM Tris-HCl aqueous buffer with pH 7.9.

approximately 450 nm) bands possessing various intensities (Fig. 17). The shapes of these ICD spectra are very similar to those observed earlier⁴⁶ for their untagged clathrochelate analogs. Host-guest binding of molecule 4 to the BLG macromolecule caused the appearance of two negative (maxima at approximately 350 and 520 nm) and one positive (maximum at approximately 450 nm) bands possessing similar intensities. In the case of LYZ as a hosting macromolecule, the corresponding CD spectra were not informative because of the formation of an insoluble LYZ-clathrochelate 4 supramolecular assembly.

Fluorescence emission anisotropy data

To evaluate additional evidence of the supramolecular binding of a given guest molecule to the hosting BSA macromolecule, we performed fluorescence emission anisotropy studies of compounds 4 and 5 (2 μ M) in the absence and presence of BSA (7.5 μ M) in 50 mM Tris-HCl aqueous buffer with pH 7.9, using an excitation at 475 nm (Fig. 18). As it can be seen from Fig. 18, the presence of BSA led to a high increase in anisotropy in the

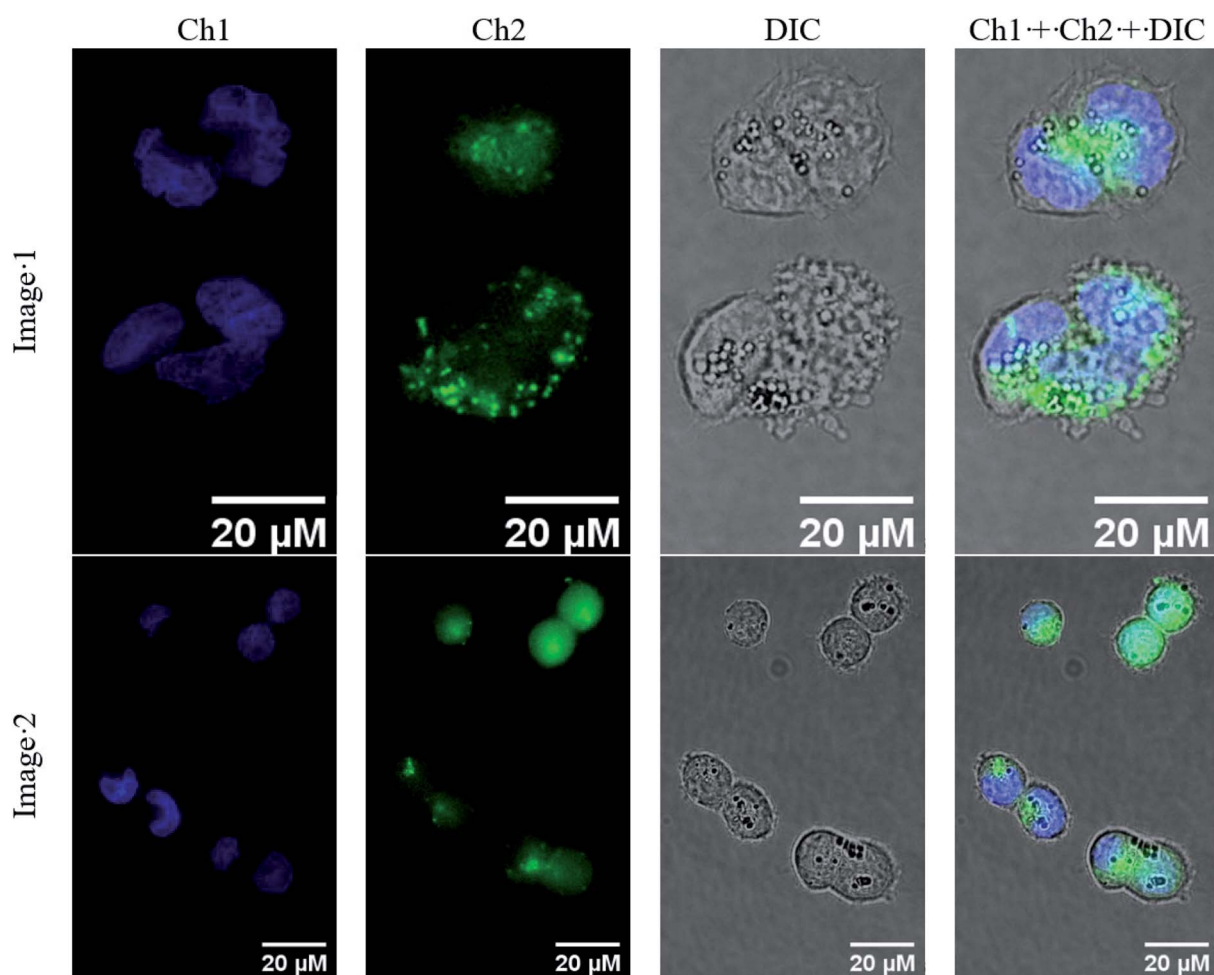


Fig. 19 Accumulation of fluorescein-tagged iron(II) clathrochelate 4 in A2780 cancer cells. Cells were treated with 4 for 4 h and subsequently stained with Hoechst 33342. Fluorescence images were taken in addition to brightfield images (DIC). Fluorescence channels: Channel 1 (Ch1, blue), λ_{ex} : 365 nm; λ_{em} : 445/50 nm (detection of Hoechst in nuclei); Channel 2 (Ch2, green): λ_{ex} : 470/40 nm; λ_{em} : 525/50 nm (detection of compound 4). Images were processed and merged (Ch1 + Ch2 + DIC) using ImageJ.



cases of both the fluorescein-tagged clathrochelate **4** and the fluorescein-based compound **5**. This suggests that their molecules as the guests form stable supramolecular assemblies with the BSA macromolecule. The observed decrease in fluorescence anisotropy for the solutions of **4** and **5** in the presence of BSA at wavelengths lower than 520 nm can be explained by the greater contribution of these initial non-bonded molecules (*i.e.* those which are not included in the formation of the host-guest assemblies) to their fluorescence spectra in the corresponding shorter-wavelength spectral range.

Molecular imaging of fluorescein-tagged iron(II) clathrochelate in cancer cells

The obtained novel fluorescently active iron(II) clathrochelate **4** was additionally characterized in a cellular context. For this purpose, A2780 cancer cells were incubated with **4** for 4 h and their nuclei were stained using Hoechst 33342; the subcellular localization of this tagged cage complex was visualized using fluorescence microscopy. Despite the observed fluorescence quenching behaviour of the quasiaromatic metal clathrochelates (see above), a reasonable fluorescent signal of the fluorescein group of the corresponding functionalized cage molecule is expected to be detectable because of both its high quantum yield and its high emission intensity. Indeed, an intense optical signal was detected for complex **4** in the 38 blue channel (Fig. 19, shown in green) which is not colocalized with the corresponding Hoechst signal in the 49 DAPI channel (Fig. 10, shown in blue). This suggests that fluorescein-tagged clathrochelate **4** is efficiently taken up by cancer cells, where it is evenly distributed in the cytosol. This fluorescein-tagged iron(II) cage complex does not seem to enter the nucleus and no accumulation in any other organelle is apparent. Unfortunately, no toxicity was observed for tagged clathrochelate **4**.

Conclusions

We elaborated an efficient synthetic strategy to obtain the first fluorescein-tagged iron(II) clathrochelates functionalized with a terminal fluorophore group and studied their chemical stability in various media, their self-assembly with globular proteins, and their localization in cancer cells.

In the X-rayed crystal of clathrochelate precursor **2**, molecules of two types, **A** and **B**, were found.

It was shown that fluorescein azide and its clathrochelate derivative possess different spectral characteristics: an 11-fold decrease in a fluorescence quantum yield is observed between a given fluorescein-based dye and this macrobicyclic complex.

A study of kinetics of a hydrolysis of the acetyl groups of acetylated fluorescein azide and its clathrochelate derivative in the presence of one equivalent of BSA evidenced that there are no strong supramolecular host-guest interactions between the BSA macromolecule and these tested compounds. At the same time, during the study of a chemical stability of the deacetylated clathrochelate, the formation of a supramolecular 1 : 1 BSA-clathrochelate assembly was detected. Moreover, the addition of BSA or HSA to its solution caused the appearance of strong

clathrochelate-based ICD outputs with two positive and one negative bands possessing different intensities. The fluorescence emission anisotropy studies also evidenced the supramolecular binding of fluorescein-tagged iron(II) clathrochelate to the BSA macromolecule, leading to a high increase in such anisotropy.

The cellular uptake of the fluorescein-tagged molecules was visualized using fluorescence microscopy which showed that the compound was mainly distributed in the cytosol without entering into the nucleus or accumulating in any other organelle.

Thus, the designed fluorescently active cage complexes seem to be prospective molecular probes for studies of subcellular localization. As a result, the use of the obtained fluorescent clathrochelates in further experiments can give new insights into the mechanism of bioactivity of clathrochelate-based drug candidates, which are promising therapeutically active compounds to fight viral, neurodegenerative, and cancerous diseases.

Author contributions

The manuscript was written through the contributions of all authors. All authors read and approved its final version; they all contributed equally.

Conflicts of interest

There are no conflicts of interest to declare.

Acknowledgements

The project leading to these results has received funding from the European Union's Horizon 2020 Research and Innovation Programme under the Marie Skłodowska-Curie grant agreement no. 778245. The synthesis of cage complexes was supported by Russian Science Foundation (project 16-13-10475). Y. Z. V. also thanks the financial support of the Russian Foundation for Basic Research (grant 18-29-23007).

References

- 1 Y. Voloshin, I. Belaya and R. Krämer, *Cage metal complexes: clathrochelates revisited*, Springer, 2017.
- 2 C. A. Lipinski, F. Lombardo, B. W. Dominy and P. J. Feeney, Experimental and computational approaches to estimate solubility and permeability in drug discovery and development settings, *Adv. Drug Delivery Rev.*, 1997, **23**, 3–25.
- 3 K. Gunasekaran, B. Ma and R. Nussinov, Is allostery an intrinsic property of all dynamic proteins?, *Proteins: Struct., Funct., Bioinf.*, 2004, **57**, 433–443.
- 4 G. M. Lee and C. S. Craik, Trapping Moving Targets with Small Molecules, *Science*, 2009, **324**(5924), 213–215.
- 5 S. Taniguchi, N. Suzuki, M. Masuda, S. Hisanaga, T. Iwatsubo, M. Goedert and M. Hasegawa, Inhibition of heparin-induced tau filament formation by phenothiazines,



- polyphenols, and porphyrins, *J. Biol. Chem.*, 2005, **280**, 7614–7623.
- 6 D. A. Kocisko, W. S. Caughey, R. E. Race, G. Roper, B. Caughey and J. D. Morrey, A porphyrin increases survival time of mice after intracerebral prion infection, *Antimicrob. Agents Chemother.*, 2006, **50**, 759–761.
 - 7 G. R. Lamberto, A. Binolfi, M. L. Orcellet, C. W. Bertocini, M. Zweckstetter, C. Griesinger and C. O. Fernandez, Structural and mechanistic basis behind the inhibitory interaction of PcTS on alpha-synuclein amyloid fibril formation, *Proc. Natl. Acad. Sci. U. S. A.*, 2009, **106**, 21057–21062.
 - 8 V. V. Novikov, O. A. Varzatskii, V. V. Negrutska, Y. N. Bubnov, L. G. Palchykovska, I. Y. Dubey and Y. Z. Voloshin, Size matters, so does shape: inhibition of transcription of T7 RNA polymerase by iron(II) clathrochelates, *J. Inorg. Biochem.*, 2013, **124**, 42–45.
 - 9 O. A. Varzatskii, V. V. Novikov, S. V. Shulga, A. S. Belov, A. V. Vologzhanina, V. V. Negrutska, I. Y. Dubey, Y. N. Bubnov and Y. Z. Voloshin, Copper-promoted reductive homocoupling of quasi-aromatic iron(II) clathrochelates: boosting the inhibitory activity in a transcription assay, *Chem. Commun.*, 2014, **50**, 3166–3168.
 - 10 O. A. Varzatskii, S. V. Shul'ga, A. S. Belov, V. V. Novikov, A. V. Dolganov, A. V. Vologzhanina and Y. Z. Voloshin, Copper(I)- and copper(0)-promoted homocoupling and homocoupling–hydrodehalogenation reactions of dihalogenoclathrochelate precursors for C–C conjugated iron(II) bis-cage complexes, *Dalton Trans.*, 2014, **43**, 17934–17948.
 - 11 O. A. Varzatskii, A. V. Vologzhanina, V. V. Novikov, S. V. Vakarov, R. V. Oblap and Y. Z. Voloshin, Inhibition of DNA synthesis in the transcription system of Taq DNA polymerase by various iron and cobalt(II) tris-dioximate clathrochelates: *in vitro* study and X-ray structure of leader inhibitors, the carboxyl-terminated macrobicyclic complexes, *Inorg. Chim. Acta*, 2018, **482**, 90–98.
 - 12 M. Y. Losytskyy, V. B. Kovalska, O. A. Varzatskii, A. M. Sergeev, S. M. Yarmoluk and Y. Z. Voloshin, Interaction of the Iron(II) Cage Complexes With Proteins: Protein Fluorescence Quenching Study, *J. Fluoresc.*, 2013, **23**, 889–895.
 - 13 J. Blechinger, O. A. Varzatskii, V. Kovalska, G. E. Zelinskii, Y. Z. Voloshin, E. Kinski and A. Mokhir, Cytotoxicity of electrophilic iron(II)-clathrochelates in human promyelocytic leukemia cell line, *Bioorg. Med. Chem. Lett.*, 2016, **26**, 626–629.
 - 14 V. B. Kovalska, M. Y. Losytskyy, O. A. Varzatskii, V. V. Cherepanov, Y. Z. Voloshin, A. A. Mokhir, S. M. Yarmoluk and S. V. Volkov, Study of anti-fibrillogenic activity of iron(II) clathrochelates, *Bioorg. Med. Chem.*, 2014, **22**, 1883–1888.
 - 15 V. Kovalska, S. Chernii, V. Cherepanov, M. Losytskyy, V. Chernii, O. Varzatskii, A. Naumovets and S. Yarmoluk, The impact of binding of macrocyclic metal complexes on amyloid fibrillation of insulin and lysozyme, *J. Mol. Recognit.*, 2017, **30**, e2622.
 - 16 V. B. Kovalska, S. V. Vakarov, M. V. Kuperman, M. Y. Losytskyy, E. Gumienna-Kontecka, Y. Z. Voloshin and O. A. Varzatskii, Induced chirality of cage metal complexes switched by their supramolecular and covalent binding, *Dalton Trans.*, 2018, **47**, 1036–1052.
 - 17 V. Kovalska, M. Kuperman, M. Losytskyy, S. Vakarov, S. Potocki, S. Yarmoluk, Y. Voloshin, O. Varzatskii and E. Gumienna-Kontecka, Induced CD of iron(II) clathrochelates: sensing of the structural and conformational alterations of serum albumins, *Metalomics*, 2019, **11**, 338–348.
 - 18 X. Michalet, F. F. Pinaud, L. A. Bentolila, J. M. Tsay, S. Doose, J. J. Li, G. Sundaresan, A. M. Wu, S. S. Gambhir and S. Weiss, Quantum dots for live cells, *in vivo* imaging, and diagnostics, *Science*, 2005, **307**(5709), 538–544.
 - 19 A. M. Achimovich, H. Ai and A. Gahlmann, Enabling technologies in super-resolution fluorescence microscopy: reporters, labeling, and methods of measurement, *Curr. Opin. Struct. Biol.*, 2019, **58**, 224–232.
 - 20 M. S. T. Gonçalves, Fluorescent Labeling of Biomolecules with Organic Probes, *Chem. Rev.*, 2009, **109**, 190–212.
 - 21 R. A. Selin, N. V. Chornenka, V. Y. Chernii, A. Mokhir, A. V. Vologzhanina, A. S. Belov, A. L. Pomadchik and Y. Z. Voloshin, Chemical design of the heterodifunctionalized iron(II) clathrochelates with terminal biorelevant carboxyl group and reactive triple C≡C bond: synthesis, structure, redox properties and their stability in various media, *Inorg. Chim. Acta*, 2019, **496**, 119047.
 - 22 R. Selin, V. Chernii and A. Mokhir, Synthesis of modified fluorescein for click reactions, *Ukr. Biochem. J.*, 2020, **86**, 3–8.
 - 23 T. G. G. Battye, L. Kontogiannis, O. Johnson, H. R. Powell and A. G. W. Leslie, iMOSFLM: a new graphical interface for diffraction-image processing with MOSFLM, *Acta Crystallogr., Sect. D: Biol. Crystallogr.*, 2011, **67**, 271–281.
 - 24 P. Evans, Scaling and assessment of data quality, *Acta Crystallogr., Sect. D: Biol. Crystallogr.*, 2006, **62**, 72–82.
 - 25 G. Sheldrick, SHELXT – Integrated space-group and crystal-structure determination, *Acta Crystallogr., Sect. A: Found. Adv.*, 2015, **71**, 3–8.
 - 26 O. V. Dolomanov, L. J. Bourhis, R. J. Gildea, J. A. K. Howard and H. Puschmann, OLEX2: a complete structure solution, refinement and analysis program, *J. Appl. Crystallogr.*, 2009, **42**, 339–341.
 - 27 I. N. Denisenko, O. A. Varzatskii, R. A. Selin, A. S. Belov, E. G. Lebed, A. V. Vologzhanina, Y. V. Zubavichus and Y. Z. Voloshin, Extension and functionalization of an encapsulating macrobicyclic ligand using palladium-catalyzed Suzuki–Miyaura and Sonogashira reactions of iron(II) dihalogenoclathrochelates with inherent halogen substituents, *RSC Adv.*, 2018, **8**, 13578–13587.
 - 28 S. V. Svidlov, O. A. Varzatskii, T. V. Potapova, A. V. Vologzhanina, S. S. Bukalov, L. A. Leites, Y. Z. Voloshin and Y. N. Bubnov, C-carboranylation of a quasi-aromatic iron(II) cage complex and its organic aromatic analog by the metal-catalyzed (promoted) cross-



- coupling reactions, *Inorg. Chem. Commun.*, 2014, **43**, 142–145.
- 29 O. A. Varzatskii, I. N. Denisenko, A. S. Belov, A. V. Vologzhanina, Y. N. Bubnov, S. V. Volkov and Y. Z. Voloshin, Metal-catalyzed cross-coupling reactions of iron(II) cage complexes: New furyl-containing macrobicyclic scaffold, a reactive halogenoclathrochelate precursor and its ribbed-functionalized derivatives, *Inorg. Chem. Commun.*, 2014, **44**, 134–138.
- 30 Y. Z. Voloshin, N. A. Kostromina and R. Krämer, *Clathrochelates: synthesis, structure and properties*, Elsevier, Amsterdam, 2002.
- 31 A. R. Katritzky, L. Huang, M. Chahar, R. Sakhuja and C. D. Hall, The Chemistry of *N*-Hydroxyamidoximes, *N*-Aminoamidoximes, and Hydrazidines, *Chem. Rev.*, 2012, **112**, 1633–1649.
- 32 M. D. Wise, A. Ruggi, M. Pascu, R. Scopelliti and K. Severin, Clathrochelate-based bipyridyl ligands of nanoscale dimensions: easy-to-access building blocks for supramolecular chemistry, *Chem. Sci.*, 2013, **4**, 1658–1662.
- 33 O. M. Planes, S. M. Jansze, R. Scopelliti, F. Fadaei-Tirani and K. Severin, Two-Step Synthesis of Linear and Bent Dicarboxylic Acid Metalloligands with Lengths of up to Three Nanometers, *Inorg. Chem.*, 2020, **59**, 14544–14548.
- 34 Y. Z. Voloshin, O. A. Varzatskii, A. V. Palchik, E. V. Polshin, Y. A. Maletin and N. G. Strizhakova, Synthesis, spectral and electrochemical characteristics of asymmetrical iron(II) tris-dioximates, *Polyhedron*, 1998, **17**, 4315–4326.
- 35 Y. Z. Voloshin, V. E. Zavodnik, O. A. Varzatskii, V. K. Belsky, A. V. Palchik, N. G. Strizhakova, I. I. Vorontsov and M. Y. Antipin, Clathrochelate monoribbed-functionalized iron(II) α -dioximates: synthetic pathways and structural and electrochemical features, *Dalton Trans.*, 2002, 1193–1202.
- 36 Y. Z. Voloshin, A. S. Belov, A. V. Vologzhanina, G. G. Aleksandrov, A. V. Dolganov, V. V. Novikov, O. A. Varzatskii and Y. N. Bubnov, Synthesis, structure, properties and immobilization on a gold surface of the monoribbed-functionalized tris-dioximate cobalt(II) clathrochelates and an electrocatalytic hydrogen production from H⁺ ions, *Dalton Trans.*, 2012, **41**, 6078–6093.
- 37 Y. Z. Voloshin, O. A. Varzatskii, D. I. Kochubey, I. I. Vorontsov and Y. N. Bubnov, Synthesis and structure of monoribbed-functionalized disulfide iron(II) clathrochelates and their coordination as the ligands toward platinum(II) and platinum(IV) ions, *Inorg. Chim. Acta*, 2009, **362**, 149–158.
- 38 V. E. Zavodnik, O. A. Varzatskii, V. K. Belsky, I. I. Vorontsov and M. Y. Antipin, Reactions of chloride iron(II) clathrochelates with aliphatic amines: an unexpected influence of the nature of the amine and solvent on the reaction products, *Inorg. Chim. Acta*, 2001, **321**, 116–134.
- 39 I. G. Belaya, G. E. Zelinskii, A. S. Belov, O. A. Varzatskii, V. V. Novikov, A. V. Dolganov, H. Kozłowski, L. Szyrwił, Y. N. Bubnov and Y. Z. Voloshin, Synthesis, spectra and properties of the first protono- and ionogenic tris-dioximate iron(II) clathrochelates, *Polyhedron*, 2012, **40**, 32–39.
- 40 G. E. Zelinskii, A. S. Belov, A. V. Vologzhanina, A. A. Pavlov, V. V. Novikov, O. A. Varzatskii and Y. Z. Voloshin, Synthesis, structure and ADMET properties of the monoribbed-functionalized iron(II) clathrochelates with terminal DNA-relevant groups, *Inorg. Chim. Acta*, 2016, **448**, 7–15.
- 41 O. I. Artyushin, I. L. Odinets, E. V. Matveeva, A. V. Vologzhanina, O. A. Varzatskii, S. E. Lubimov and Y. Z. Voloshin, Clathrochelates meet phosphorous. 1. Thiophosphorylation of an iron(II) dichlathrochelate precursor, synthesis of N,S-donor clathrochelate ligands and their palladium(II) complexes as potent catalysts of Suzuki cross-coupling reaction, *Dalton Trans.*, 2014, **43**, 9677–9689.
- 42 A. S. Belov, I. G. Belaya, V. V. Novikov, Z. A. Starikova, E. V. Polshin, A. V. Dolganov and E. G. Lebed, Structure, spectral and electrochemical properties of the 2,6-di-*tert*-butylphenol-functionalized iron and cobalt(II) clathrochelates and their phenylsulfide analogs, *Inorg. Chim. Acta*, 2013, **394**, 269–281.
- 43 P. G. Seybold, M. Gouterman and J. Callis, Calorimetric, photometric and lifetime determinations of fluorescence yields of fluorescein dyes, *Photochem. Photobiol.*, 1969, **9**, 229–242.
- 44 B. M. Liederer and R. T. Borchardt, Enzymes involved in the bioconversion of ester-based prodrugs, *J. Pharm. Sci.*, 2006, **95**, 1177–1195.
- 45 T. Peters Jr, Serum Albumin, *Adv. Protein Chem.*, 1985, **37**, 161–245.
- 46 V. Kovalska, S. Vakarov, M. Losytskyy, M. Kuperman, N. Chornenka, Y. Toporivska, E. Gumienna-Kontecka, Y. Voloshin, O. Varzatskii and A. Mokhir, Dicarboxyl-terminated iron(II) clathrochelates as ICD-reporters for globular proteins, *RSC Adv.*, 2019, **9**, 24218–24230.



Publication 3:

Cyanine- and Rhodamine-Derived Alkynes for the Selective Targeting of Cancerous Mitochondria via Radical Thiol-Yne Coupling in Live Cells

Johannes Köckenberger,^{#, [a]} Insa Klemt,^{#, [b]} Caroline Sauer,^[a] Anton Arkhypov,^[b] Viktor Reshetnikov,^[b] Andriy Mokhir,^{*, [b]} Markus R. Heinrich^{*, [a]}

^[a] Department of Chemistry and Pharmacy, Pharmaceutical Chemistry, Friedrich-Alexander-Universität Erlangen-Nürnberg, Nikolaus-Fiebiger-Str. 10, 91058 Erlangen, Germany

^[b] Department of Chemistry and Pharmacy, Organic Chemistry II, Friedrich-Alexander-Universität Erlangen-Nürnberg, Nikolaus-Fiebiger-Str. 10, 91058 Erlangen, Germany

[#]equal contribution

Contribution of I. Klemt:

Design and performance of experiment of compounds with proteins in cell free settings and all cellular experiments. Contribution to Publication writing, revision of the manuscript and cover image design.

The publication and supporting information are found under: DOI: [10.1002/chem.202301340](https://doi.org/10.1002/chem.202301340).



Cyanine- and Rhodamine-Derived Alkynes for the Selective Targeting of Cancerous Mitochondria through Radical Thiol-Yne Coupling in Live Cells

Johannes Köckenberger⁺,^[a] Insa Klemt⁺,^[b] Caroline Sauer,^[a] Anton Arkhypov,^[b] Viktor Reshetnikov,^[b] Andriy Mokhir,^{*[b]} and Markus R. Heinrich^{*[a]}

Abstract: Despite their long history and their synthetic potential underlined by various recent advances, radical thiol-yne coupling reactions have so far only rarely been exploited for the functionalization of biomolecules, and no examples yet exist for their application in live cells - although natural thiols show widespread occurrence therein. By taking advantage of the particular cellular conditions of mitochondria in cancer cells, we have demonstrated that radical thiol-yne coupling represents a powerful reaction principle for the selective targeting of these organelles. Within our studies,

fluorescently labeled reactive alkyne probes were investigated, for which the fluorescent moiety was chosen to enable both mitochondria accumulation as well as highly sensitive detection. After preliminary studies under cell-free conditions, the most promising alkyne-dye conjugates were evaluated in various cellular experiments comprising analysis by flow cytometry and microscopy. All in all, these results pave the way for improved future therapeutic strategies relying on live-cell compatibility and selectivity among cellular compartments.

Introduction

Thiyl radical additions to aryl alkynes have a long history, in which early studies were mainly focused on stereochemistry.^[1] In addition, various suitable reaction conditions were discovered, among which photoredox catalysis recently became of major interest.^[2] Important synthetic applications comprise macrocyclizations,^[3] polymerizations,^[4] peptide chemistry^[3b,5] and multicomponent reactions,^[6] among others.^[7] Although the high rate constants under which thiyl radicals add to aryl alkynes are basically advantageous, such reactions are also considered difficult to control as up to six different adducts can arise from the radical addition of a thiol to a terminal alkyne.^[8]

As a result, radical thiol-yne couplings did by far not gain the same importance as nucleophilic thiol-yne couplings, which are even categorized as click reactions.^[9] This preference for nucleophilic over radical thiol-yne chemistry is also observed in synthetic biology and in medicinal applications.^[10]

In related biological settings, activated alkynes show increased reactivity in nucleophilic conjugate additions of thiolate anions^[10–11] (Scheme 1A), which has been exploited in numerous applications such as the development of irreversible inhibitors for Bruton tyrosine kinase,^[12] serine/threonine-protein kinase Nek2,^[13] ATPase p97^[14] and the epidermal growth factor receptor (EGFR).^[15]

Non-activated alkynes are considered largely unreactive towards intermolecular nucleophilic addition of thiols under

[a] J. Köckenberger,⁺ Dr. C. Sauer, Prof. Dr. M. R. Heinrich
Department of Chemistry and Pharmacy
Pharmaceutical Chemistry

Friedrich-Alexander-Universität Erlangen-Nürnberg
Nikolaus-Fiebiger-Str. 10, 91058 Erlangen (Germany)
E-mail: markus.heinrich@fau.de

Homepage: <http://www.medchem.uni-erlangen.de/heinrichlab>

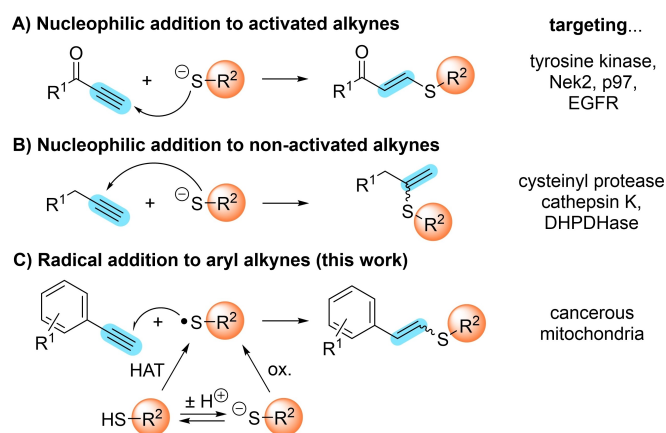
[b] I. Klemt,⁺ A. Arkhypov, Dr. V. Reshetnikov, Prof. Dr. A. Mokhir
Department of Chemistry and Pharmacy, Organic Chemistry II
Friedrich-Alexander-Universität Erlangen-Nürnberg

Nikolaus-Fiebiger-Str. 10, 91058 Erlangen (Germany)
E-mail: andriy.mokhir@fau.de
Homepage: <https://chemie.nat.fau.de/ak-mokhir>

[⁺] These authors contributed equally to this work.

Supporting information for this article is available on the WWW under <https://doi.org/10.1002/chem.202301340>

© 2023 The Authors. Chemistry - A European Journal published by Wiley-VCH GmbH. This is an open access article under the terms of the Creative Commons Attribution Non-Commercial License, which permits use, distribution and reproduction in any medium, provided the original work is properly cited and is not used for commercial purposes.



Scheme 1. Thiol-yne coupling reactions applied in medicinal chemistry and chemical biology. HAT: hydrogen atom transfer.

physiological conditions, which makes them useful bioorthogonal handles (Scheme 1B).^[5b,16] Nevertheless, conjugate additions to such alkynes can be achieved if particular effects such as proximity driven reactivity,^[17] activation through allene isomerization^[18] or enzyme templated adduct stabilization come into play.^[18b,19]

Although radical thiol-yne couplings to aryl alkynes (Scheme 1C) would be basically suited for biological applications due to the widespread natural abundance of thiols, the pronounced bioorthogonal reactivity of alkynes^[16,20] and the mild conditions required for thiyl radical generation,^[21] the above-mentioned negative aspect that product formation is difficult to control has yet impeded such application in a cellular setting. Only under cell-free conditions, a radical carbohydrate-alkyne conjugation to bioavailable thiols has so far been reported by Dondoni,^[22] which nevertheless nicely underlines the bioorthogonality of the reaction type.^[22–23] The assumption that poor reaction control may have been a key issue in preventing applications of radical thiol-yne chemistry in living cells is also supported by successful examples of thiol-ene reactions,^[24] which are less prone to side-product formation.

Against this background and our general interest in transferring radical reactions to biomimetic conditions and biological applications^[25,26] it was a challenging question how to perform radical thiol-yne couplings in live cells. If successful, such reactions would significantly enlarge the yet available toolbox for medicinal chemistry and chemical biology (Scheme 1) and pave the way for new bioactive molecules and targeting principles. Herein, we now show that radical thiol-yne chemistry can indeed be performed in live cells and that the particular cellular conditions of cancerous mitochondria offer an excellent means to achieve target selectivity.

When aiming at radical thiol-yne couplings in live cells, we chose mitochondria as target organelles for two major reasons. At first, both the level of reactive oxygen species (ROS) and the pH are elevated in cancerous mitochondria,^[27] which can be expected to lead to a strongly preferred thiyl radical formation in this organelle.^[21] While the increased pH shifts the acid-base equilibrium towards the thiolate anions, the elevated ROS level is likely to promote thiyl radical formation both from the thiol (by hydrogen atom transfer) and from the thiolate (by oxidation; Scheme 1C).^[21] Secondly, and due to their importance as centers of metabolic activity and their involvement in many diseases, mitochondria are of increasing interest as potential target for therapeutics, in particular for cancer treatment. For targeting mitochondria in a therapeutic manner, different strategies have already evolved, among which mitochondria-targeted drug-free agents currently appear as one of the most promising, as high selectivity may then be achieved at small concentrations and along with only few side effects.^[27]

By selecting radical thiol-yne coupling as reaction type for the implementation of this strategy, a noteworthy aspect is in how far C–S bond formation to mitochondria-abundant, metabolically critical thiols^[28] can be achieved in the presence of the natural thiol glutathione (GSH). GSH can occur in live cells in concentrations of up to 10 mM, but is most often found in a lower range of 1–2 mM.^[29] Notably, cytosolic and mitochon-

drial (mainly matrix-bound) GSH concentrations do not differ significantly, which remains true for cancerous mitochondria.^[30] Given the particular importance of mitochondrial GSH for cancer cells, targeting GSH in this particular compartment has even been proposed as a potential therapeutic strategy for the treatment of cancer.^[27] In turn, a major preference of an acetylene warhead for a particular mitochondrial thiol functionality, and over GSH, is not required as long as the overall thiol-yne coupling remains selective for cancerous mitochondria.

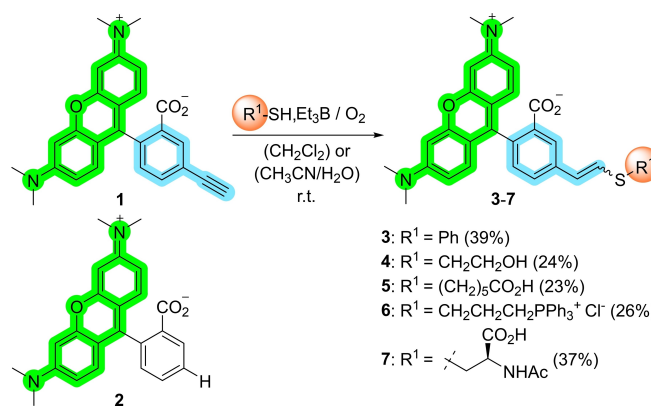
To promote spatial selectivity of the thiol-yne coupling for mitochondria in addition to the above mentioned, favorable conditions of elevated pH and ROS, the rhodamine-alkyne dye **1**^[31] was chosen for the first series of experiments along with control compound **2** (Scheme 2). Due to their permanent but delocalized positive charge, rhodamines show pronounced mitochondria localization,^[32] and their fluorescent properties strongly facilitate detection in biological settings by analytical methods such as microscopy or flow cytometry.

Results and Discussion

Through a row of preliminary reactions, the general ability of rhodamine-alkyne **1** to undergo radical thiol-yne couplings was initially confirmed (Scheme 2). Using triethylborane as radical initiator,^[33] five vinyl thioethers **3–7** were obtained as mixtures of *cis* and *trans* stereoisomers,^[34] thereby demonstrating tolerance of the reaction towards the thiol component. Moreover, the successful coupling of **1** to *N*-acetyl cysteine being performed in aqueous acetonitrile (1:1), provided a particularly valuable prerequisite regarding the targeting of naturally abundant thiols in live cells.

Based on these promising initial results, we next expanded our study to cyanine-3-, cyanine-5-, fluorescein- and doxorubicin-derived fluorescent probes (Figure 1).

As before, control compounds (**11**, **13**, **15**, **17** and **20**) were prepared along with the reactive alkyne and alkene probes **8**, **9**, **10**, **12**, **14**, **16**, **18** and **19** (see Experimental Section and Supporting Information for synthetic procedures and characterization). While the cyanine-3-, cyanine-5- and fluorescein-



Scheme 2. Thiol-yne coupling reactions of rhodamine-alkyne **1** to various thiols.

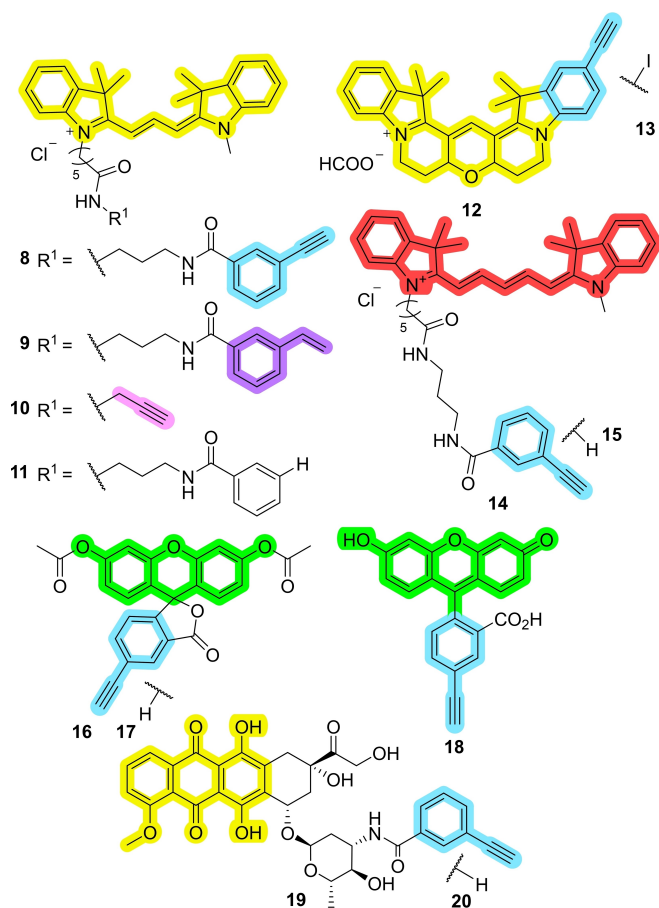


Figure 1. Reactive alkyne and alkene probes **8**, **9**, **10**, **12**, **14**, **16**, **18** and **19** and related control compounds derived from cyanine-3, cyanine-5, fluorescein or doxorubicin.

derived probes **8**, **9**, **10**, **12**, **14**, **16** and **18** were selected due to their favorable fluorescent properties^[37] and known accumulation in mitochondria,^[38] the doxorubicin-derived alkyne **19** was deliberately chosen as a negative control, as doxorubicin has been shown to be largely unable to enter mitochondria.^[39] Within a first series of experiments, the reactivity of the alkyne and alkene probes **1**, **8**, **9**, **10**, **12**, **14**, **18** and **19** towards thiol-ene coupling was evaluated under oxidative conditions simulating those in cancerous mitochondria.^[31,40] Using iron(II) sulfate in the presence of hydrogen peroxide for the generation of reactive oxygen species (ROS) at pH 8, the coupling of GSH to the individual probes was monitored by LC-MS (Table 1).

Validation of the overall method was achieved by comparing the thiol-yne adduct formation from **1** (Table 1, entry 1) with an authentic sample, which had earlier been obtained by the reaction of rhodamine-alkyne **1** and GSH under the alternative conditions shown in Scheme 2.

While the probes **8**, **9**, **12**, **18** and **19** provided the respective glutathione conjugates **8-SG**, **9-SG**, **12-SG**, **18-SG** and **19-SG** in basically useful reactant-to-product ratios, the rhodamine-, the alkyl alkyne and the cyanine-5-derived probes **1**, **10** and **14** led to only low amounts or traces of the expected conjugates. In particular, the row of cyanine-3-derived probes **8**, **9** and **10**

nicely reflects the expected reactivity towards thiyl radicals with the phenyl alkene **9** being the most reactive and the alkyl alkyne **10** being the least.^[21] Notably, and due to the occurrence of a benzyl radical intermediate, the coupling of **9** provides a hydroperoxide **9-SG**, thereby strongly supporting the overall radical mechanism.

Regarding probe **14**, a conjugate **14-SG*** with a slightly lower mass (*M*-2) was observed as major product. At first, and based on literature,^[41] we reasoned that the glutathione thiyl radical attack had occurred on the polymethine system of the cyanine-5 probe **14** followed by oxidation. As control experiments with the alkyne-free cyanine dyes **11**, **13** and **15** did not show any conjugation under identical conditions, thus proving that the alkyne moiety is required for the coupling of these probes, a thiyl radical attack on the polymethine system of **14** and **15** could be excluded. Consequently, we now assume that the thiyl radical addition to the aryl alkyne subunit of **15** is not - as otherwise typical - followed by hydrogen atom transfer to provide a vinyl thioether, but by a further attack of the reactive vinyl radical intermediate on the proximate cyanine-5 polymethine system.

Further control reactions with the alkyne probes **1**, **8**, **12** and **14**, GSH and iron(II) sulfate, but in the absence of H₂O₂ did not lead to conjugate formation. This again supports the assumed radical mechanism for the thiol-yne coupling, which requires ROS for thiyl radical formation, and excludes an alternative nucleophilic Michael addition pathway.^[9] Notably, and due to strongly reduced solubility in the presence of iron(II) ions, all experiments with doxorubicin alkyne **19** and its control compound **20** had to be performed under alternative conditions employing UV irradiation and DMPA as radical initiator. In the absence of light irradiation, alkyne probe **19** was also unreactive towards GSH, which similarly excluded the Michael addition pathway.

In the next step to approach more cell-like settings, we evaluated the reactivity of the alkene and alkyne probes **8**, **9**, **10**, **14** and **18** towards the cysteine-containing proteins bovine serum albumin (BSA) and β-lactoglobulin (LG; Figure 2A).

Analysis of the reactions by SDS-PAGE and fluorescence imaging showed that no coupling occurs in the absence of H₂O₂ (lane 1) and for control compounds **11** and **15** (lanes 3, 5 and 9), which again supports the radical mechanism. In contrast, if thiyl radicals are generated, covalent binding of all alkyne-containing probes occurred. No remarkable difference in coupling could be observed among the phenyl alkyne probes **8**, **14** and **18** derived from cyanine-3, cyanine-5 and fluorescein, respectively (lanes 2, 4, 6, 8), and not even among the probes **8**, **9** and **10** (lanes 2, 7, 10), which had earlier given divergent results when coupled to GSH (Table 1). Encouraged by the successful thiol-yne coupling of various dyes to proteins under cell-like conditions, we then moved to *in vitro* studies in cancer cells. To determine the relative degree of *in-cell* conjugation, cancerous A2780 cells were incubated with the cyanine-3 derived probes **8**–**10** and their related control compound **11** and analyzed by flow cytometry. In addition, cells were treated in the same way followed by treatment with methanol (at –20 °C) to fix the cells and permeabilize their membranes.

Table 1. Thiol-yne coupling under oxidative conditions simulating cancerous mitochondria.

	Probe	Reactant/product ratio ^[a]	Detected mass (<i>m/z</i>) ^[b]
1	1	94/6	359.64 [1-SG + H] ²⁺ , 718.23 [1-SG] ⁺
2	8	75/25	474.87 [8-SG + H] ²⁺
3	9	28/72	491.85 [9-SG + H] ²⁺ , 982.41 [9-SG] ⁺
4	10	98/2	417.28 [10-SG + H] ²⁺ , 833.26 [10-SG] ⁺
5	12	54/46	377.70 [12-SG + H] ²⁺ , 755.38 [12-SG] ⁺
6	14	n.d. (traces)	487.91 [14-SG + H] ²⁺ , 486.82 [14-SG* + H] ²⁺
7	18	83/17	332.56 [18-SG + H] ²⁺ , 664.16 [18-SG] ⁺
8	19	51/49	979.33 [19-SG + H] ⁺

[a] Reactant-to-product ratios determined by LC-MS analysis based on the integration of corresponding peaks at $\lambda = 550$ nm (for 1, 8, 9, 10 and 12), at $\lambda = 650$ nm (for 14), $\lambda = 450$ nm (for 18) and $\lambda = 480$ nm (for 19). [b] LC-MS analysis in the Supporting Information.

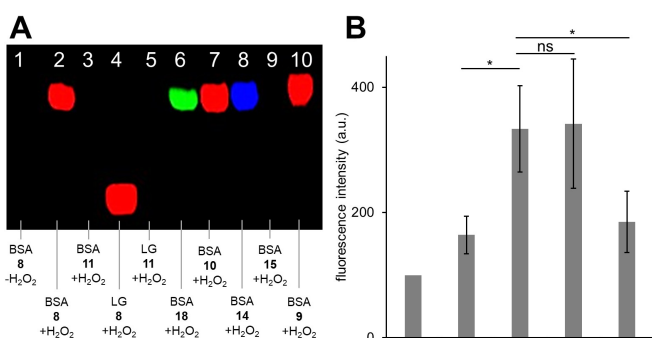


Figure 2. A) BSA or LG (5 mg mL⁻¹) incubated with the indicated dyes (10 μ M) in the presence or absence of H₂O₂ (10 mM). Overlay of Images after SDS-PAGE: iBright FL1000 $\lambda_{\text{ex}} = 455\text{--}485$ nm, $\lambda_{\text{em}} = 510\text{--}555$ nm (for 18), $\lambda_{\text{ex}} = 515\text{--}545$ nm, $\lambda_{\text{em}} = 568\text{--}617$ nm (for 8, 9, 10, 11) and $\lambda_{\text{ex}} = 608\text{--}632$ nm, $\lambda_{\text{em}} = 675\text{--}720$ nm (for 14, 15). B) Fluorescence of cyanine-3 derived dyes (8, 9, 10, 11) detected in A2780 cells before (see the Supporting Information) and after MeOH washing using flow cytometry ($\lambda_{\text{ex}} = 488$ nm, $\lambda_{\text{em}} = 543\text{--}627$ nm). A Student's t-test was performed in GraphPad Prism (ns: $p > 0.05$, * $p < 0.05$, ** $p < 0.01$, *** $p < 0.001$; $n = 3$).

Under these conditions small molecules (unreacted dye) are washed away. Subsequent flow cytometry measurements allowed the quantification of covalently bound dye and thus of the efficiency of thiol-yne coupling (Figure 2B). In these advanced experiments, the phenyl alkyne **8** and the phenyl alkene **9** again revealed their superiority as both probes displayed the most distinct covalent binding. As phenyl alkynes

are, however, known for more suitable bioorthogonal properties than phenyl alkenes,^[5b,16,41] we decided to focus on phenyl alkynes from now on.

Having shown that covalent binding of the phenyl alkyne probe **8** in cancerous cells is feasible, it remained to be established whether - and as initially intended - mitochondria indeed play a key role in this covalent fixation. First insights into the cellular distribution were obtained by MeOH-washing experiments (as described above) combined with confocal microscopy (Figure 3). These experiments included the phenyl alkyne-derived probes **1**, **8**, **12**, **14** and **16**, whereat the diacetylated fluorescein **16** was now chosen due to assumingly facilitated cellular uptake.

Among these probes, only the cyanine-5 derivative **14** failed to give significant covalent binding, which coincides with the uncommon behavior under cell-free conditions (Table 1). Accordingly, thiol-yne coupling can as well take place for alkyne probe **14** (Figure 2A), but a probably less stable conjugate (c.f. mass difference) is then formed. In addition, the particular conditions of cancerous mitochondria as well as blinking or quenching effects of reactive thiol groups attached to cyanine-5 derivatives have been reported.^[42,43] Overlay images with bright-field images are included in the Supporting Information. Importantly, control compounds **2**, **11**, **13**, **15** and **17** only gave minor background signals after the washing step.

To obtain further evidence for the key role of mitochondria, doxorubicin and its derivatives **19** and **20** were evaluated with

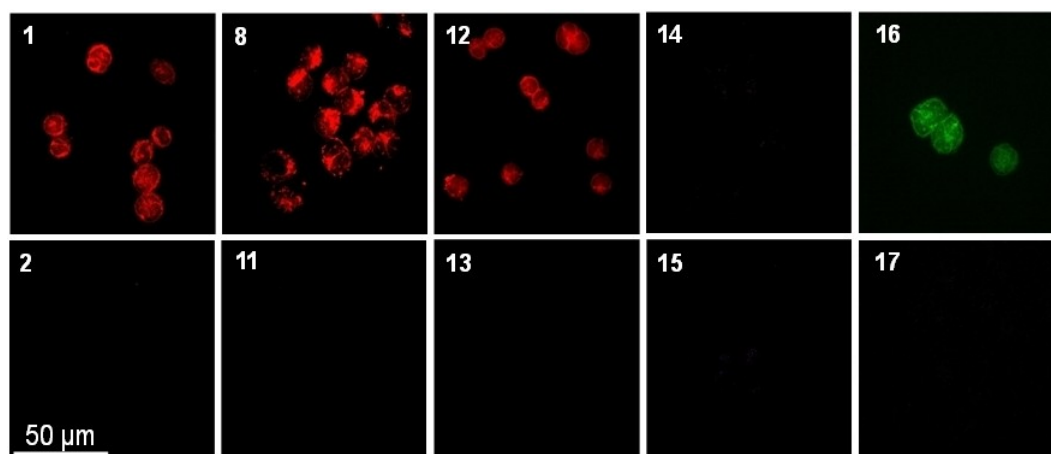


Figure 3. Confocal images (channel 2: λ_{ex} : 488 nm; λ_{em} : 525/50 (for 16, 17); channel 3: λ_{ex} : 561 nm; λ_{em} : 595/50 (for 1, 2, 8, 11, 12, 13); channel 4: λ_{ex} : 638 nm; λ_{em} : 690/50 (for 14, 15)) of cancerous A2780 cells previously incubated with reactive alkynyl probes 1, 8, 12, 14, 16, or control compounds 2, 11, 13, 15, 17 after fixation and washing with MeOH for 30 min at -20°C .

regard to cellular uptake using the established incubation-fixation-washing sequence. As shown in Figure 4, doxorubicin, the alkyne probe 19 and the control compound 20 were all able to enter cancerous A2780 cells, but remained fully washable after cell fixation. As the doxorubicin probe 19 however exhibits comparable reactivity towards thiols in cell-free settings as the non-washable cyanine- or rhodamine-derived probes (Table 1 and Figure 3), this strongly indicates that 19 was unable to reach a cellular compartment suitable for thiol-yne coupling.^[39]

That this cellular compartment, which could not be reached by 19 but by the TAMRA-derived probe 1, the cyanine-3-derived probes 8 and 12 and by the fluorescein-derived probe 16 is indeed the mitochondrion, was then further confirmed by colocalization experiments (Figure 5). As a reference compound, for which mitochondria-localization was validated with MitoTracker™ Green FM (see the Supporting Information), the cyanine-5-derived, alkyne-free probe 15 was used.

As summarized in Figure 5, the reactive alkyne probes 1, 8 and 16 display a similar spatial distribution as reference 15, and can thus be considered to accumulate in mitochondria. The

doxorubicin alkyne 19, on the other hand, showed a significantly divergent distribution, which is in agreement with the known reluctance of doxorubicin to enter mitochondria.^[39] These results, in combination with the washing experiments conducted with doxorubicin-alkyne 19 (Figure 4), strongly support the assumption that mitochondria localization in combination with the favorable conditions being present in cancerous mitochondria (elevated pH and ROS) are the key factors enabling covalent fixation of the alkyne probes 1, 8 and 16 by radical thiol-yne coupling.

To additionally confirm covalent binding of the alkyne probes to cellular proteins in mitochondria, isolated mitochondria from pre-treated A2780 cells were analyzed by SDS-PAGE (Figure 6A). In comparison with the alkyne-free probe 11, covalent binding of the reactive probe 8 to a range of mitochondrial proteins could be unambiguously detected.

As mitochondria are of increasing interest as potential target for therapeutics, in particular for cancer treatment,^[27] we evaluated the impact of radical thiol-yne coupling of probe 8 on the cell viability of A2780 cancer cells (Figure 6B). The alkyne probe 8 indeed displayed enhanced toxicity with an IC_{50} value 2.5 times lower than the alkyne-free control compound 11 (IC_{50} of 8 = $8.7 \pm 0.8 \mu\text{M}$ vs. IC_{50} of 11 = $21.5 \pm 2.7 \mu\text{M}$ after 4 h incubation), which can - based on the previous results - be attributed to covalent binding to mitochondria-abundant, metabolically critical thiols.

Finally, and to get insights into the covalent binding of the reactive probes in different cancer cells, the three cancerous cell lines Du145, A2780 and BL2 were evaluated in comparison to the noncancerous cell line SBLF9 using flow cytometry (Figure 7A, B). In the larger Du145 and SBLF9 cells, a slight difference in uptake between probe 8 and control 11 was detectable, whereas the smaller cells (A2780 and BL2) showed no significant difference (Figure 7A). After methanol washing, all cancer cell lines display a significantly higher fluorescence when previously treated with 8 than with 11 (Figure 7B). In contrast, no significant difference in fluorescence read-out was

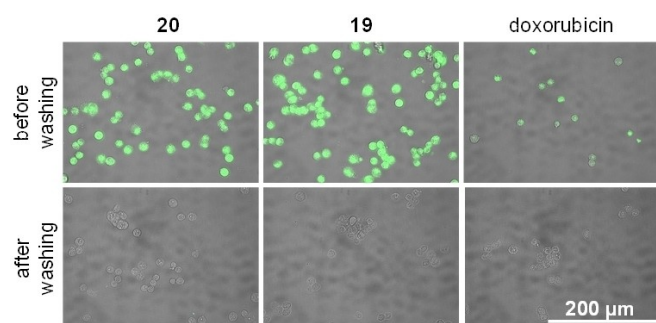


Figure 4. Non-confocal images of cancerous A2780 cells previously incubated with doxorubicin-alkynyl probes 19, control compounds 20 or unmodified doxorubicin, with and without washing with MeOH and PBS.

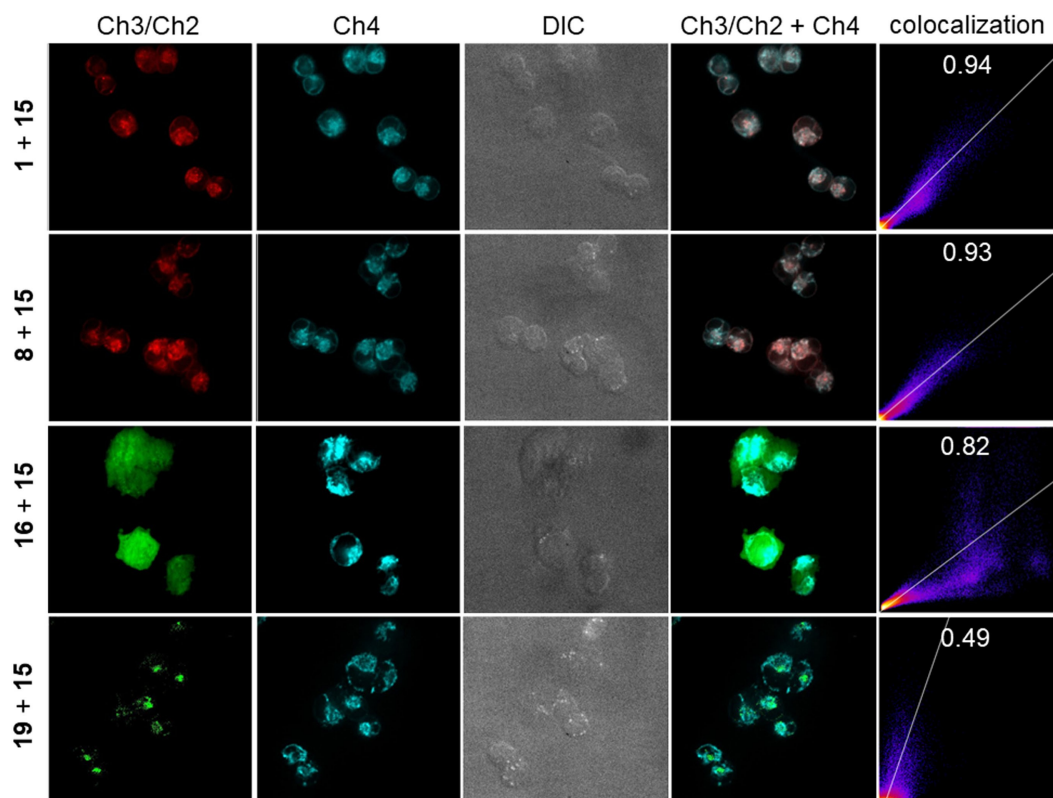


Figure 5. Colocalization experiments in cancerous A2780 cells using the alkyne probes **1**, **8** (channel 3: Ch3 = λ_{ex} : 561 nm; λ_{em} : 595/50), **16** (channel 2: λ_{ex} : 488 nm; λ_{em} : 525/50) and **19** (channel 2: Ch2 = λ_{ex} : 488 nm; λ_{em} : 595/50; 10 μM , 2 h incubation) and the mitochondrion-accumulating reference compound **15** (channel 4: Ch4 = λ_{ex} : 638 nm; λ_{em} : 690/50; 1 μM , 15 min). Colocalization and Pearson coefficient calculated in imageJ (diagram and coefficient shown on the right). For controls of single dye staining and colocalization of **15** with MitoTracker Green FM, see the Supporting Information.

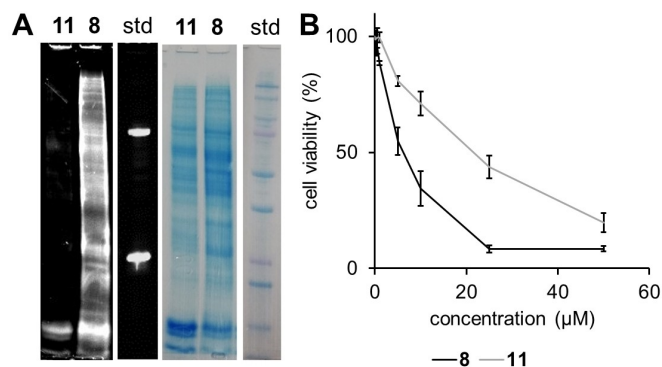


Figure 6. A) SDS-PAGE analysis of isolated mitochondria of A2780 cells previously incubated with reactive alkynyl probe **8** or control compound **11** and protein standard (std) after washing with PBS. Fluorescent image (λ_{ex} = 515–545 nm, λ_{em} = 568–617 nm) and image of subsequent Coomassie staining are shown. B) Relative cell viability of an A2780 cell line incubated with various concentrations of the cyanine-3-derived alkyne probe **8** (IC_{50} = $8.7 \pm 0.8 \mu\text{M}$) or **11** (IC_{50} = $21.5 \pm 2.7 \mu\text{M}$) for 4 h. Viability measured by using MTT and UV/Vis detection. Three independent experiments were each performed in triplicate.

detectable in the non-cancerous SBLF9 fibroblasts despite the initial difference before MeOH washing.

As shown in Figure 7C, the preferred covalent binding of probe **8** to cancerous cells nicely corresponds to the degree of

mitochondrial ROS concentration, which is - as expected - substantially higher in cancer cells than in SBLF9 as determined by MitoSox™ staining. Besides being a further proof for an underlying radical thiol-yne coupling mechanism, this result demonstrates a more general ROS-based cancer selectivity.

Conclusion

In conclusion, we have shown that radical thiol-yne coupling reactions, which have so far not been applied in live-cell chemistry, can provide the basis for a novel strategy to induce selective dysfunction of mitochondria in cancer cells. Our approach relies on the combination of two major principles, that are, compound-directed accumulation in mitochondria and stimuli responsive reactivity. In particular, structural units such as cyanines enable mitochondrial accumulation of an attached aryl alkyne probe, in which thiol-yne coupling to naturally abundant thiols is then favored by ROS and pH levels being particularly elevated in cancerous mitochondria. Cell experiments show the covalent fixation of the alkyne probes, and a preference of this fixation towards cancerous cells was observed. Furthermore, mitochondria targeting was confirmed by colocalization studies, and higher cytotoxicity of an alkyne probe compared to its reference was determined. Ongoing

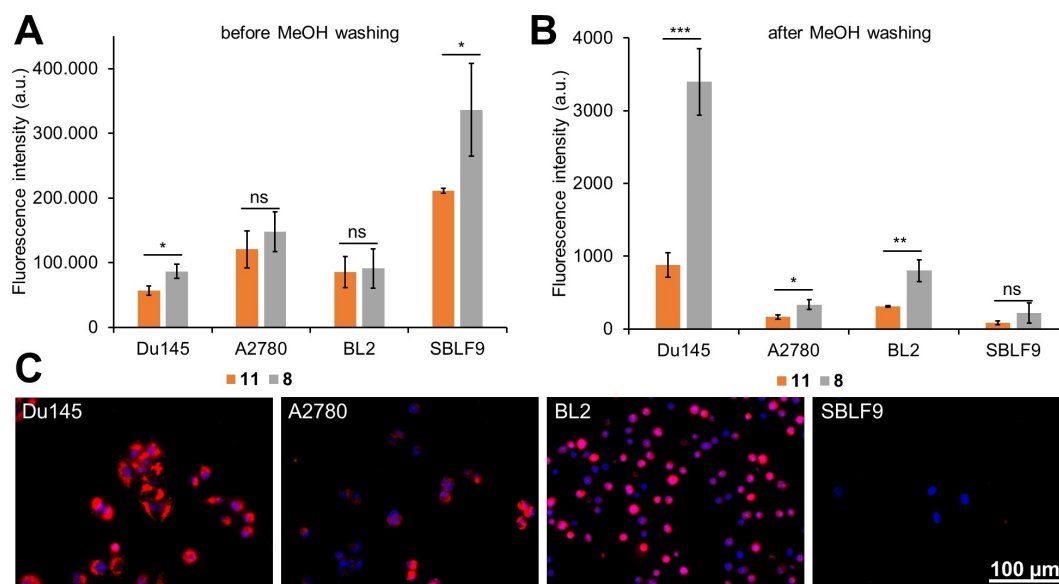


Figure 7. Fluorescence of probe **8** and control compound **11** detected in various cell lines A) before and B) after washing with MeOH using flow cytometry ($\lambda_{\text{ex}} = 488 \text{ nm}$, $\lambda_{\text{em}} = 543\text{--}627 \text{ nm}$). A Student's t-test was performed in GraphPad Prism (ns: $p > 0.05$, * $p < 0.05$, ** $p < 0.01$, *** $p < 0.001$; $n = 3$). C) Relative mitochondrial ROS concentrations in Du145, A2780, BL2 and SBLF9 cells as determined by MitoSox activation (red signal, $\lambda_{\text{ex}} = 545/25 \text{ nm}$; $\lambda_{\text{em}} = 605/70 \text{ nm}$). Cells were co-incubated with Hoechst 33342 (blue signal, $\lambda_{\text{ex}} = 365 \text{ nm}$; $\lambda_{\text{em}} = 445/50 \text{ nm}$). Images taken with Zeiss Observer with the 40x/1.30 Oil DIC objective. Due to their very high signal, BL2 images were edited differently.

research is now directed towards the development of further mitochondrion-directed aryl alkyne probes and the precise elucidation of the mitochondrion-abundant thiols that are targeted by the radical thiol-yne chemistry.

Experimental Section

Materials and methods: Solvents and reagents are obtained from commercial sources and used as received. ^1H NMR and ^{13}C NMR spectra are recorded on Bruker Avance 600 (^1H : 600 MHz; ^{13}C : 151 MHz), and Bruker Avance 400 (^1H : 400 MHz or 600 MHz; ^{13}C : 101 MHz) spectrometers. For ^1H NMR spectra, CDCl_3 is used as solvent referenced to tetramethylsilane (TMS, 0 ppm): CDCl_3 (7.26 ppm), $(\text{CD}_3)_2\text{SO}$ (2.50 ppm), and CD_3OD (3.31 ppm). Chemical shifts are reported in parts per million (ppm). Coupling constants are in Hertz (Hz). The following abbreviations are used for the description of signals: s (singlet), d (doublet), t (triplet), q (quartet), m (multiplet), and bs (broad singlet). ^{13}C NMR or DEPTQ spectra are recorded in CDCl_3 using CHCl_3 (77.2 ppm) and in $(\text{CD}_3)_2\text{SO}$ using $(\text{CD}_3)(\text{CD}_2\text{H})\text{SO}$ (39.52 ppm) as standard, respectively. Chemical shifts are given in parts per million (ppm). Mass spectra are recorded using electron spray ionization (ESI) and atmospheric pressure photoionization (APPI) and a TOF-mass analyzer for HRMS measurements. Analytical thin-layer chromatography (TLC) is carried out on Merck silica gel plates using short-wave (254 nm) UV light to visualize components. Silica gel (Kieselgel 60, 40–63 μm , Merck) is used for flash column chromatography. The purity of the substances was determined using an analytical HPLC: System A: Waters analytical system equipped with either A1: Waters XBridge C_{18} analytical column, 4.6 mm \times 50 mm, 3.5 μm , or A2: Phenomenex Gemini[®] 5 μm NX-C18, 50 \times 2 mm LC column, a DAD detector for UV Vis detection and an ESI quadrupole mass detector. Flow rate: 0.5 mL min^{-1} , Eluent: CH_3CN in $\text{H}_2\text{O} + 0.1\% \text{HCO}_2\text{H}$ (0–15 min 10–90%, 15–20 min 90%). The purity of all biologically tested

compounds **1**, **2** and **8–15** was determined as $> 95\%$. System B: Agilent 1100 Preparative Series which is equipped with a VWD detector with wavelengths of $\lambda = 230 \text{ nm}$, 254 nm and 550 nm. B1: Column from Macherey-Nagel Varioprep VP 250/32 Nucleodur C_{18} H Tec with 5 μm particles [C_{18}] with a flow rate of 32 mL min^{-1} was applied. B2: Phenomenex Gemini[®] 5 μm NX-C18, 100 \times 21.2 mm LC-Column with a flow rate 30.0 mL min^{-1} was applied. System C: Phenomenex Gemini[®] 5 μm NX-C18, 250 \times 46 mm LC column, flow rate: 2.0 mL min^{-1} , DAD detector. Diacetyl fluorescein **17** was purchased from Sigma Aldrich and used without further purification or chemical analysis.

For the characterization of the coupling products **3–7**, as well as spectra of all compounds see the Supporting Information.

Synthesis and characterization of reactive alkyne probes **1**, **8**, **9**, **10**, **12**, **14**, **16**, **18**, **19**

5-Ethynyltetramethylrhodamine (1): 5-Ethynyltetramethyl-rhodamine (**1**) was synthesized as reported in literature.^[31] Briefly, TMS-protected 5-ethynyltetramethyl-rhodamine (358 mg, 0.74 mmol) was dissolved in methanol (40 mL) and potassium carbonate (460 mg, 3.33 mmol) was added. The reaction was monitored by LC-MS. After stirring at room temperature for 3 h, the solvent was removed under reduced pressure and the crude product was purified by column chromatography ($\text{CH}_2\text{Cl}_2/\text{MeOH}$ 10:1 \rightarrow 5:1) to yield **1** (191 mg, 0.47 mmol, 64%) as a purple solid. R_f : 0.4 ($\text{CH}_2\text{Cl}_2/\text{MeOH}$ 7:1) [UV]. ^1H NMR (400 MHz, CD_3OD): $\delta = 3.23$ (s, 12H), 3.75 (s, 1H), 6.83 (q, $J = 2.7, 2.3 \text{ Hz}$, 2H), 6.97 (dt, $J = 9.5, 2.3 \text{ Hz}$, 2H), 7.21–7.27 (m, 3H), 7.69 (dd, $J = 7.8, 1.7 \text{ Hz}$, 1H), 8.19 ppm (d, $J = 1.7 \text{ Hz}$, 1H). ^{13}C NMR (151 MHz, CD_3OD): $\delta = 40.8, 80.7, 83.4, 97.4, 114.9, 115.0, 125.4, 130.8, 132.6, 133.8, 134.2, 134.4, 141.7, 158.6, 159.0, 162.1, 172.0$. HRMS (ESI) calcd. for $\text{C}_{26}\text{H}_{22}\text{N}_2\text{O}_3$: 411.1703 [$M + \text{H}$]⁺; found: 411.1701.

1-(6-((3-(3-Ethynylbenzamido)propyl)amino)-6-oxohexyl)-3,3-dimethyl-2-((E)-3-((E)-1,3,3-trimethylindolin-2-ylidene)prop-1-en-1-yl)-3H-indol-

1-ium chloride (Cy3-alkyne; 8): To a solution of Cy3-COOH (100 mg, 0.22 mmol) in dry DMF (2 mL) and dry THF (2 mL), DIPEA (77.0 μ L, 0.45 mmol, 2.1 equiv.) and *N,N'*-disuccinimidyl carbonate (67.5 mg, 0.26 mmol, 1.2 equiv.) were added, and the mixture was stirred at rt for 2.5 h under argon in the dark. The progress was monitored by LC-MS and TLC. Upon full conversion of Cy3-COOH to Cy3-NHS, a solution of amine **21** (58.5 mg, 0.29 mmol, 1.3 equiv.) in dry DMF (1.5 mL) was added dropwise and the reaction was stirred overnight at room temperature, under argon, and in the dark. Upon completion, the reaction mixture was diluted with CH₂Cl₂ (100 mL). The resulting solution was successively washed with aq. HCl (1 M, 2 \times 100 mL), H₂O (1 \times 100 mL) and brine (3 \times 100 mL), dried over Na₂SO₄ and the solvent was removed under reduced pressure. Purification of the crude product by flash column chromatography (CH₂Cl₂/MeOH 0 \rightarrow 1 \rightarrow 2 \rightarrow 5 \rightarrow 7 \rightarrow 10 \rightarrow 15% MeOH) gave the title compound **8** (Cy3-alkyne) (93.0 mg, 0.14 mmol, 63% yield) as a dark red solid. *R*_f: 0.7 (CH₂Cl₂/MeOH 10:1) [UV]. ¹H NMR (400 MHz, CDCl₃): δ = 1.60 (p, *J* = 7.2 Hz, 2H), 1.70 (s, 6H), 1.71 (s, 6H), 1.75–1.98 (m, 6H), 2.54 (t, *J* = 7.2 Hz, 2H), 3.03 (s, 1H), 3.36–3.44 (m, 2H), 3.51 (p, *J* = 6.7, 6.3 Hz, 2H), 3.61 (s, 3H), 4.09 (t, *J* = 7.8 Hz, 2H), 6.97 (d, *J* = 13.4 Hz, 1H), 7.03 (dt, *J* = 8.0, 0.8 Hz, 1H), 7.10 (d, *J* = 7.9 Hz, 1H), 7.19 (d, *J* = 13.4 Hz, 1H), 7.21–7.31 (m, 2H), 7.31–7.44 (m, 5H), 7.50 (dt, *J* = 7.7, 1.4 Hz, 1H), 8.09–8.20 (m, 2H), 8.40 (t, *J* = 13.4 Hz, 1H), 8.96 (s, 1H), 9.45 ppm (s, 1H). DEPTQ (101 MHz, CDCl₃): δ = 25.3, 26.3, 26.8, 28.2 (2 \times CH₃), 28.3 (2 \times CH₃), 28.4, 32.0, 36.0, 36.1, 36.4, 44.7, 49.1, 49.2, 53.6, 77.8, 100.1, 104.1, 105.0, 111.0, 111.1, 122.1, 122.3, 125.6, 128.1, 128.4, 129.1, 129.2, 131.7, 134.4, 135.2, 140.5, 140.6, 141.9, 142.6, 151.0, 166.4, 173.9, 174.6, 174.9 ppm. One signal missing. HRMS (ESI) calcd. for C₄₂H₄₉N₄O₂: 641.3850 [M]⁺; found: 641.3848.

3,3-Dimethyl-1-(6-oxo-6-((3-(3-vinylbenzamido)propyl)amino)-hexyl)-2-((E)-3-((E)-1,3,3-trimethylindolin-2-ylidene)prop-1-en-1-yl)-3H-indol-1-ium chloride (Cy3-alkene; 9): To a solution of Cy3-NHS (30.0 mg, 0.05 mmol) in dry DMF (3 mL), DIPEA (41.4 μ L, 0.15 mmol, 3 equiv.) the amine **23** (25.0 mg, 0.12 mmol, 1.5 equiv.) was added. The reaction mixture was stirred overnight at room temperature under argon in the dark. Upon completion, the reaction mixture was diluted with CHCl₃ (50 mL). The resulting solution was successively washed with aq. HCl (1 M, 2 \times 50 mL), H₂O (1 \times 50 mL) and brine (3 \times 50 mL), dried over Na₂SO₄ and the solvent was removed under reduced pressure. Purification of the crude product by flash column chromatography (CH₂Cl₂/MeOH 0 \rightarrow 2 \rightarrow 4 \rightarrow 6 \rightarrow 10 \rightarrow 20% MeOH) gave the title compound **9** (Cy3-alkene; 22.2 mg, 32.2 μ mol, 64% yield) as a dark red solid. *R*_f: 0.7 (CH₂Cl₂/MeOH 10:1) [UV]. ¹H NMR (400 MHz, CD₃OD): δ = 1.44–1.55 (m, 2H), 1.68–1.79 (m, 16H), 1.86 (p, *J* = 7.7 Hz, 2H), 2.24 (t, *J* = 7.7 Hz, 2H), 3.25 (t, *J* = 6.8 Hz, 2H), 3.40 (t, *J* = 6.8 Hz, 2H), 3.64 (s, 3H), 4.16 (t, *J* = 7.7 Hz, 2H), 5.30 (dd, *J* = 11.0, 0.9 Hz, 1H), 5.86 (dd, *J* = 17.6, 0.9 Hz, 1H), 6.43 (dd, *J* = 14.8, 13.5 Hz, 2H), 6.77 (dd, *J* = 17.6, 11.0 Hz, 1H), 7.26–7.48 (m, 7H), 7.53 (ddt, *J* = 7.4, 1.5, 0.6 Hz, 2H), 7.58 (dt, *J* = 7.7, 1.5 Hz, 1H), 7.70 (ddd, *J* = 7.7, 1.9, 1.1 Hz, 1H), 7.89 (t, *J* = 1.9 Hz, 1H), 8.39 (s, 1H), 8.53 ppm (t, *J* = 13.5 Hz, 1H). DEPTQ (151 MHz, CD₃OD): δ = 26.5, 27.3, 28.2 (2 \times CH₃), 28.2, 28.3 (2 \times CH₃), 30.3, 31.7, 36.8, 37.8, 38.3, 45.1, 50.6, 50.6, 103.6, 103.7, 112.3, 112.5, 115.5, 123.4, 123.5, 126.0, 126.7, 126.8, 127.5, 129.9, 129.9, 130.0, 130.3, 136.0, 137.4, 139.4, 142.1, 142.2, 143.4, 144.0, 152.1, 168.2, 170.0, 176.0, 176.0, 176.6 ppm. HRMS (ESI) calcd. for C₄₂H₅₁N₄O₂: 643.4007 [M]⁺; found: 643.4009.

3,3-Dimethyl-1-(6-oxo-6-(prop-2-yn-1-ylamino)hexyl)-2-((E)-3-((E)-1,3,3-trimethylindolin-2-ylidene)prop-1-en-1-yl)-3H-indol-1-ium chloride (Cy3-alkyl-alkyne; 10): To a solution of Cy3-NHS (40.0 mg, 0.07 mmol) in dry DMF (4 mL), DIPEA (35.7 μ L, 0.21 mmol, 3 equiv.) propargylamine (6.51 μ L, 0.10 mmol, 1.5 equiv.) was added. The reaction mixture was stirred overnight at room temperature under argon in the dark. Upon completion, the reaction mixture was diluted with CHCl₃ (50 mL). The resulting solution was successively

washed with aq. HCl (1 M, 2 \times 50 mL), H₂O (1 \times 50 mL) and brine (3 \times 50 mL), dried over Na₂SO₄ and the solvent was removed under reduced pressure. Purification of the crude product by flash column chromatography (CH₂Cl₂/MeOH 0 \rightarrow 2 \rightarrow 4 \rightarrow 6 \rightarrow 10 \rightarrow 20% MeOH) gave the title compound **10** (Cy3-alkyl-alkyne) (31.2 mg, 58.9 μ mol, 87% yield) as a dark red solid. *R*_f: 0.7 (CH₂Cl₂/MeOH 10:1) [UV]. ¹H NMR (400 MHz, [D₆]DMSO): δ = 1.39 (p, *J* = 8.3 Hz, 2H), 1.57 (p, *J* = 7.4 Hz, 2H), 1.65–1.77 (m, 14H), 2.10 (t, *J* = 7.4 Hz, 2H), 3.08 (t, *J* = 2.5 Hz, 1H), 3.66 (s, 3H), 3.82 (dd, *J* = 5.5, 2.5 Hz, 2H), 4.10 (t, *J* = 7.6 Hz, 2H), 6.49 (d, *J* = 13.5 Hz, 2H), 7.25–7.36 (m, 2H), 7.39–7.51 (m, 4H), 7.64 (dt, *J* = 7.1, 1.4 Hz, 2H), 8.26–8.40 ppm (m, 2H). DEPTQ (101 MHz, [D₆]DMSO): δ = 24.8, 25.8, 26.8, 27.3 (2 \times CH₃), 27.5 (2 \times CH₃), 27.7, 31.4, 34.8, 43.7, 48.9, 72.9, 81.3, 102.4, 103.0, 111.5, 111.6, 122.4, 122.6, 125.1, 125.3, 128.6, 128.7, 140.6 (2 \times C_q), 141.9, 142.7, 149.7, 171.7, 173.6, 174.5 ppm. One signal missing. HRMS (ESI) calcd. for C₃₃H₄₀N₃O: 494.3166 [M]⁺; found: 494.3170.

Cy3B-alkyne (12): Cy3B-alkyne (**12**) was synthesized according to literature.^[44] *R*_f: 0.4 (CH₂Cl₂/MeOH 8:1) [UV]. ¹H NMR (400 MHz, CD₃OD): δ = 1.59–1.73 (m, 1H), 1.76–1.78 (m, 12H), 1.96–2.11 (m, 1H), 2.61 (q, *J* = 6.8, 5.2 Hz, 2H), 3.60 (s, 1H), 3.95 (dtd, *J* = 26.3, 13.4, 4.1 Hz, 3H), 4.29–4.44 (m, 2H), 4.69 (dt, *J* = 11.1, 5.4 Hz, 2H), 7.22–7.27 (m, 1H), 7.33–7.38 (m, 2H), 7.44–7.50 (m, 1H), 7.56 (ddd, *J* = 10.9, 8.0, 1.3 Hz, 2H), 7.64 (d, *J* = 1.5 Hz, 1H), 8.20 (s, 1H), 8.29 ppm (s, 1H). DEPTQ (151 MHz, CD₃OD): δ = 24.8, 27.6, 27.7, 27.8, 27.9, 28.3, 28.5, 42.4, 42.7, 49.6, 50.3, 71.1, 71.1, 79.5, 111.1, 111.6, 112.2, 112.3, 120.7, 123.5, 127.0, 127.3, 130.0, 134.1, 139.7, 142.2, 142.3, 143.1, 143.4, 168.9, 170.7 ppm. HRMS (ESI) calcd. for C₃₁H₃₁N₂O: 447.2431 [M]⁺; found: 447.2431.

1-(6-((3-(3-Ethynylbenzamido)propyl)amino)-6-oxohexyl)-3,3-dimethyl-2-((1E,3E)-5-((E)-1,3,3-trimethylindolin-2-ylidene)penta-1,3-dien-1-yl)-3H-indol-1-ium chloride (Cy5-alkyne) (14): To a solution of Cy5-NHS (50.0 mg, 0.08 mmol) in dry DMF (2 mL), DIPEA (41.4 μ L, 0.24 mmol, 3 equiv.) the amine **21** (25.0 mg, 0.12 mmol, 1.5 equiv.) was added. The reaction mixture was stirred overnight at room temperature under argon in the dark. Upon completion, the reaction mixture was diluted with CH₂Cl₂ (50 mL). The resulting solution was successively washed with aq. HCl (1 M, 2 \times 50 mL), H₂O (1 \times 50 mL) and brine (3 \times 50 mL), dried over Na₂SO₄ and the solvent was removed under reduced pressure. Purification of the crude product by flash column chromatography (CH₂Cl₂/MeOH 0 \rightarrow 2 \rightarrow 4 \rightarrow 6 \rightarrow 10 \rightarrow 20% MeOH) gave the title compound **14** (Cy5-alkyne; 26.9 mg, 38.2 μ mol, 47% yield) as a dark blue solid. *R*_f: 0.8 (CH₂Cl₂/MeOH 10:1) [UV]. ¹H NMR (400 MHz, CDCl₃): δ = 1.53 (p, *J* = 7.1 Hz, 2H), 1.65 (s, 6H), 1.69 (s, 6H), 1.83–1.95 (m, 6H), 2.47 (t, *J* = 7.1 Hz, 2H), 2.99 (s, 1H), 3.39 (q, *J* = 6.0 Hz, 2H), 3.45 (s, 3H), 3.54 (q, *J* = 5.8 Hz, 2H), 4.15 (t, *J* = 7.4 Hz, 2H), 6.15 (d, *J* = 13.0 Hz, 1H), 6.65 (d, *J* = 13.0 Hz, 1H), 6.88 (t, *J* = 13.0 Hz, 1H), 7.04 (d, *J* = 7.9 Hz, 1H), 7.12 (d, *J* = 8.0 Hz, 1H), 7.18–7.24 (m, 1H), 7.26 (dd, *J* = 7.4, 0.8 Hz, 1H), 7.29–7.43 (m, 5H), 7.48 (dt, *J* = 7.7, 1.4 Hz, 1H), 7.73 (t, *J* = 13.0 Hz, 1H), 7.79 (t, *J* = 13.0 Hz, 1H), 8.20 (t, *J* = 1.7 Hz, 1H), 8.28 (dt, *J* = 8.0, 1.4 Hz, 1H), 9.11 (s, 1H), 9.15 ppm (s, 1H). DEPTQ (101 MHz, CDCl₃): δ = 25.3, 26.1, 26.9, 28.2 (2 \times CH₃), 28.3 (2 \times CH₃), 28.4, 31.3, 35.9, 36.0, 36.4, 44.6, 49.0, 49.5, 77.7, 103.6, 105.1, 110.3, 111.3, 122.1, 122.2, 122.3, 125.1, 125.7, 126.5, 128.2, 128.5, 128.8, 129.0, 131.9, 134.4, 135.0, 140.7, 141.2, 141.9, 142.8, 152.3, 153.5, 166.4, 172.4, 173.6, 174.5 ppm. One signal missing. HRMS (ESI) calcd. for C₄₄H₅₁N₄O₂: 667.4007 [M]⁺; found: 667.4008.

Diacetyl-5-ethynyl-fluorescein (16): 5-Ethynyl-fluorescein (**17**; 40.0 mg, 0.11 mmol) was dissolved in THF (4 mL) and acetic anhydride (1 mL) was added. The reaction was stirred for 2 h at room temperature and monitored by using TLC. Upon completion, the reaction mixture was diluted with ethyl acetate (50 mL), washed with H₂O (3 \times 50 mL) and brine (2 \times 50 mL), and the solvent was removed under reduced pressure. The crude product was purified by flash column chromatography (EtOAc/hexanes 3:7) to yield the

title compound **16** (41.7 mg, 94.7 μ mol, 84% yield). R_f : 0.6 (EtOAc/hexanes 3:7) [UV] $^1\text{H NMR}$ (400 MHz, CDCl_3): δ = 2.32 (s, 6H), 3.24 (s, 1H), 6.82 (d, J = 1.4 Hz, 4H), 7.10 (t, J = 1.4 Hz, 2H), 7.15 (dd, J = 8.0, 0.8 Hz, 1H), 7.77 (dd, J = 8.0, 1.5 Hz, 1H), 8.12 ppm (dd, J = 1.5, 0.8 Hz, 1H). DEPTQ (101 MHz, CDCl_3): δ = 169.0 ($2 \times \text{C}_q$), 168.2, 152.7, 152.3 ($2 \times \text{C}_q$), 151.6 ($2 \times \text{C}_q$), 138.9, 129.0 ($2 \times \text{CH}$), 128.9, 126.6, 124.7, 124.4, 118.0 ($2 \times \text{CH}$), 116.0 ($2 \times \text{C}_q$), 110.6 ($2 \times \text{CH}$), 81.9, 80.0, 21.3 ppm ($2 \times \text{CH}_3$). HRMS (ESI) calcd. for $\text{C}_{26}\text{H}_{17}\text{O}_7$: 441.0969 [$M + \text{H}$] $^+$; found: 441.0967.

5-Ethynyl-fluorescein (18): 5-Ethynyl-fluorescein **18** was synthesized according to literature.^[45] R_f : 0.4 (MeOH/ CH_2Cl_2 1:10) [UV] $^1\text{H NMR}$ (400 MHz, CD_3OD): δ = 3.77 (s, 1H), 6.54 (dd, J = 8.7, 2.4 Hz, 2H), 6.61 (d, J = 8.7 Hz, 2H), 6.68 (d, J = 2.4 Hz, 2H), 7.20 (dd, J = 8.0, 0.8 Hz, 1H), 7.83 (dd, J = 8.0, 1.5 Hz, 1H), 8.06 ppm (dd, J = 1.5, 0.8 Hz, 1H). DEPTQ (101 MHz, CD_3OD): δ = 64.7, 81.2 ($2 \times \text{C}_q$), 82.7, 103.6 ($2 \times \text{CH}$), 110.8, 113.6, 125.7, 125.8 ($2 \times \text{C}_q$), 128.7, 129.1, 130.2 ($2 \times \text{CH}$), 139.7 ($2 \times \text{CH}$), 154.0, 170.4 ppm. One C_q signal missing. HRMS (ESI) calcd. for $\text{C}_{22}\text{H}_{13}\text{O}_5$: 357.0757 [$M + \text{H}$] $^+$; found: 357.0758.

Doxorubicin-3-ethynylbenzamide (DOX-alkyne; 19): To a stirred solution of doxorubicin hydrochloride (60.0 mg, 0.10 mmol) and diisopropylethylamine (DIPEA, 35.1 μ L, 0.21 mmol, 2.0 equiv.) in dry DMF (3 mL), 2,5-dioxopyrrolidin-1-yl benzoate (68.1 mg, 0.31 mmol, 3.0 equiv.) was added and the resulting mixture was stirred under argon at room temperature for 16 h. The resulting mixture was poured into cold (0°C) methyl *tert*-butyl ether (150 mL), the precipitate was collected by filtration, washed with methyl *tert*-butyl ether (3 \times 20 mL) and dried *in vacuo*. The crude product was purified by preparative HPLC ($\text{CH}_3\text{CN}/\text{H}_2\text{O}$: 20–60%, 15 min, system B) to yield the title compound **20** (21.5 mg, 33.2 μ mol, 32% yield) as a red solid. R_f : 0.6 ($\text{CH}_2\text{Cl}_2/\text{MeOH}$ 10:1) [UV]. $^1\text{H NMR}$ (400 MHz, CD_3OD): δ = 1.30 (d, J = 6.6 Hz, 3H), 1.82 (dd, J = 13.0, 4.5 Hz, 1H), 2.08–2.24 (m, 2H), 2.40 (d, J = 14.6 Hz, 1H), 2.94 (d, J = 18.6 Hz, 1H), 3.07 (d, J = 18.6 Hz, 1H), 3.75 (d, J = 2.4 Hz, 1H), 3.99 (s, 3H), 4.30–4.41 (m, 2H), 4.76 (d, J = 4.5 Hz, 2H), 5.11 (s, 1H), 5.46 (d, J = 3.8 Hz, 1H), 5.49 (s, 1H), 7.37–7.45 (m, 2H), 7.45–7.53 (m, 2H), 7.74–7.82 (m, 3H), 7.87 ppm (d, J = 7.7 Hz, 1H). DEPTQ (101 MHz, CD_3OD): δ = 17.3, 30.5, 34.0, 37.4, 47.9, 57.1, 65.7, 68.6, 69.9, 71.3, 77.3, 102.3, 112.2, 112.5, 120.2, 120.5, 121.6, 128.4 ($2 \times \text{CH}$), 129.5 ($2 \times \text{CH}$), 132.6, 135.2, 135.7, 135.8, 136.4, 137.2, 156.2, 157.4, 162.4, 169.8, 187.8, 188.2, 214.7 ppm. HRMS (ESI) calcd. for $\text{C}_{34}\text{H}_{32}\text{NO}_{12}$: 646.1930 [$M - \text{H}$] $^-$; found: 646.1931.

The control compounds **2**, **11**, **13**, **15**, **17**, and **20** were synthesized in analogy to their corresponding reactive alkyne probes. Characterization and procedures are reported in the Supporting Information.

Biomimetic assay: Experimental for Table 1

Coupling of 1, 8, 9, 10, 12, 14 or 18: In a small capped vial, glutathione (50.0 μ L, 4 mM in H_2O) and the reactive probe **1**, **8**, **9**, **10**, **12**, **14** or **18** (50.0 μ L, 2.0 mM in DMSO) were added to Tris-HCl buffer (875 μ L, 0.1 M, pH 8.0) containing diethylenetriaminepentaacetic acid (DTPA, 20 mM). To the resulting mixture $\text{FeSO}_4 \times 7 \text{H}_2\text{O}$ (27.8 μ L, 10 mg mL^{-1} in H_2O) and in the last step H_2O_2 (11.3 μ L, 30%) were added. The mixture was stirred for 10 min at room temperature, and a sample was analyzed by LC-MS (System A2). Cyanine-3 and TMR probes **1**, **8**, **9**, **10** and **12** as well as the conjugates **1-SG**, **8-SG**, **9-SG**, **10-SG** and **12-SG** were detected at λ = 550 nm. Cyanine-5-alkyne **14** and the related conjugates **14-SG** and **14-SG*** where detected at λ = 650 nm. Fluorescein-alkyne **18** and the related conjugate **18-SG** was detected at λ = 450 nm.

Coupling of 19: In a sealed vial glutathione (50.0 μ L, 4.0 mM in H_2O) and the doxorubicin alkyne **19** (50.0 μ L, 2.0 mM in DMSO) were stirred in a mixture of H_2O (500 μ L) and DMSO (400 μ L). DMPA (10.0 μ L, 20 mM in DMSO) was added and the mixture was

irradiated with 365 nm single LED (Thorlabs[®] M365D2, 1150 mW (Min), 1700 mA) for 10 min at room temperature. A sample was drawn from the reaction mixture and analyzed by LC-MS (System A2). Doxorubicin alkyne **19** and the formed conjugate **19-SG** were detected at λ = 480 nm (see the Supporting Information for LC-MS).

Reaction of compounds with proteins in cell-free settings: Bovine serum albumin (BSA) or β -lactoglobulin (LG, both: 5 mg mL^{-1}) was incubated in Tris-HCl (0.1 M, 10 mM DTPA, 1 mM FeSO_4 , 1% DMSO (v/v), pH 8) for 1 h with the respective dyes (10 μ M) in the presence or absence of 10 mM H_2O_2 . Equal volumes of 2x Laemmli Sample Buffer was added and incubated at 95°C for 5 min. The samples (7.5 μ L) were loaded onto a pre-cast SDS gel and run at 200 V until the front ran out. Fluorescence images were taken with the iBright FL1000 λ_{ex} = 455–485 nm, λ_{em} = 510–555 nm (fluorescein-based dye), λ_{ex} = 515–545 nm, λ_{em} = 568–617 nm (Cy3- and rhodamine-based dyes) and λ_{ex} = 608–632 nm, λ_{em} = 675–720 nm (Cy5-based dyes). Images of the different fluorescent channels were overlapped using ImageJ Fiji. Results are shown in Figure 2.

Cell experiments

General: Human ovarian cancer cell line A2780 was purchased from Sigma-Aldrich and cultivated in Roswell Park Memorial Institute (RPMI) 1640 medium supplemented with 10% FBS, 1% (v/v) L-glutamine and 1% (v/v) penicillin/streptomycin. Human Burkitt lymphoma cell line BL2 was cultivated in Roswell Park Memorial Institute (RPMI) 1640 medium, supplemented with 20% FBS, 1% (v/v) L-glutamine and 1% (v/v) penicillin/streptomycin. The prostate cancer cell line Du145 was kindly gifted by Prof. Dr. Olaf Prante and was cultivated in Dubecco's modified Eagle medium (DMEM), supplemented with 10% FBS, 1% (v/v) L-glutamine and 1% (v/v) penicillin/streptomycin, respectively. Normal human skin fibroblasts (SBLF9)-courtesy of the group of PD Dr. rer. nat. habil. Udo Gaipl, Chair of Radiation Therapy, University Hospital Erlangen, Germany, were cultivated in Ham's F-12 Nutrient Mix (F-12) medium supplemented with 15% FBS, 2% nonessential amino acid mix (v/v) and 1% (v/v) penicillin/streptomycin. Adherent cells were cultivated to around 80% confluence. SBLF9 cells were cultivated to around 50% confluence. For the experiments, the cells were washed and incubated with their respective cultivation medium containing reduced amounts of FBS (5%) improve compound uptake.

Flow cytometry: A2780 and Du145 cells were seeded in a 6-well microtiter plate at a density of 200 cells/ μ L (total volume 2 mL) in RPMI 1640 or DMEM medium (5% FBS, 1% L-glutamine, 1% penicillin/streptomycin) one day before the experiment. SBLF9 cells were seeded in a 6-well microtiter plate at a density of 40 cells/ μ L (total volume 2 mL) in Ham's F-12 nutrient mix (F-12) medium supplemented with 15% FBS, 2% nonessential amino acid mix (v/v) and 1% (v/v) penicillin/streptomycin. On the next day, the cells were washed with PBS buffer (2 \times 2 mL) and a fresh portion of RPMI 1640 or DMEM (5% FBS, 1% L-glutamine, 1% penicillin/streptomycin, 2 mL) was added. BL2 cells were diluted to 500 cells/ μ L and a 1 mL aliquot was prepared for each sample in Eppendorf tubes. Dyes (20 μ L, 1 mM in DMSO) were added and incubated for 2 h at 37°C and 5% CO_2 . Then the cells were washed with PBS (2 \times 2 mL) and detached from the surface by trypsin (0.05%, v/v)/EDTA (0.02%, w/v) solution (0.5 mL). Then, the cells were re-suspended in RPMI 1640 medium (5% FBS, 1% L-glutamine, 1% penicillin/streptomycin; 1 mL), transferred to 1.5 mL Eppendorf tubes. For the BL2 suspension cells the trypsination step was skipped and the samples washed twice by centrifugation (3 min, 1000 relative centrifugal force, rcf). The mean fluorescence of live cells of a total of 5000 events (PE-channel, λ_{ex} = 488 nm, λ_{em} = 585/42 nm for Cy3-based dyes) was determined by using the flow cytometer. The fluorescence intensity of each sample was normalized by the one of

DMSO-treated cells, which was set to 100. Three independent experiments were performed.

Fixation of the cells was done in the following way. After trypsination, cells were centrifuged for 3 min at 22 °C (1000 rcf). The supernatant was removed and the remaining cell pellet was washed with PBS (0.5 mL). Each cell pellet was re-suspended in 400 μ L of PBS and then 800 μ L of precooled (−20 °C methanol) was added. Cells were incubated for 20 min at −20 °C in the dark (in case of Du145 cells, the fixation step was prolonged to 30 min). The cells were centrifuged for 3 min at 22 °C (5000 rpm), washed with PBS (0.5 mL) and suspended in medium containing 5% FBS, 1% L-glutamine and 1% penicillin/streptomycin (150 μ L). Flow cytometry was performed as for the living cells.

An overview of dye **8** and its control **11** in all cell lines is shown in Figure 7. A comparison of all cyanine-3 derived dyes (**8**, **9**, **10**, **11**) is shown in Figure 2 and Figure S1 in the Supporting Information. Student's t-test was performed in GraphPad Prism (ns: $p > 0.05$, * $p < 0.05$, ** $p < 0.01$, *** $p < 0.001$).

Microscopy: Confocal images were taken with a Zeiss Spinning Disk Axio Observer Z1 with Plan-Apochromat 63x/1.40 oil objective in spinning disc confocal mode using the EVOLVE 512 EMCCD camera or the Axiocam 506 mono, Channel 1 (green, MitoTracker Green, λ_{ex} : 488 nm; λ_{em} : 525/50), Channel 2 (green, doxorubicin derivatives, λ_{ex} : 488 nm; λ_{em} : 595/50 nm, fluorescein derivatives, λ_{ex} : 488 nm; λ_{em} : 525/50 nm), Channel 3 (red, Cy3 and rhodamine derivatives, λ_{ex} : 561 nm; λ_{em} : 595/50 nm), Channel 4 (cyan, Cy5 derivatives): λ_{ex} : 638 nm; λ_{em} : 690/50 nm. The fluorescence images were taken with a Zeiss AX10 Lab A1 fluorescence microscope with a 40x/1.30 Oil DIC objective, Channel 1 (green, doxorubicin derivatives, λ_{ex} : 470/40 nm; λ_{em} : 525/50 nm), Channel 2 (red, MitoSox™, λ_{ex} : 545/25 nm; λ_{em} : 605/70 nm), Channel 3 (blue, Hoechst 33342 λ_{ex} = 365 nm; λ_{em} = 445/50 nm).

A2780 cells were seeded in RPMI 1640 medium (500 μ L) supplemented with 5% FBS, 1% L-glutamine, and 1% penicillin/streptomycin on a 35 mm imaging dish (μ -Dish 35 mm, high, ibidi GmbH, Germany) at a cell density of 80 cells/ μ L and allowed to attach to the surface of the dish for overnight. Then the cells were washed with PBS (2 \times 2 mL) and incubated with the dyes (10 μ M, 2 mL, RPMI 1640 medium supplemented with 5% FBS, 1% L-glutamine, and 1% penicillin/streptomycin, 1% DMSO) for 2 h at 37 °C and 5% CO₂ or MitoTracker Green FM (500 nM, in medium, 2 mL, 0.1% DMSO (Invitrogen, ThermoFisher, US)) for 15 min. Then the cells were washed with PBS (2 \times 2 mL) and either directly subjected to microscopy or methanol (2 mL, −20 °C) was added and incubated for 20 min at −20 °C. The cells were washed again with PBS buffer and a fresh portion of RPMI 1640 medium containing 5% FBS, 1% L-glutamine and 1% penicillin/streptomycin (1 mL) was added. Fluorescent signals were overlapped with DIC images, examples are shown in Figures 3, 4 and S2–S6.

For the colocalization experiments, the cells were treated in the same way, but instead of methanol fixation the cells were washed twice with PBS (2 \times 2 mL) and a fresh portion of medium containing compound **10** (1 μ M, 0.1% DMSO in RPMI 1640 medium supplemented with 5% FBS, 1% L-glutamine, and 1% penicillin/streptomycin, 2 mL) was added and incubated for 15 min at 37 °C and 5% CO₂. The cells were again washed with PBS (2 \times 2 mL) and a fresh portion of medium was added before subjecting the samples to confocal microscopy as described above. The results are shown in Figures 5 and S6–S9.

Du145, A2780 and SBLF9 cells were seeded in the culture medium (500 μ L) at a density of 80 cells/ μ L (or 40 cells/ μ L in case of SBLF9 cells) in imaging dishes 35 mm imaging dish (μ -Dish 35 mm, high, ibidi GmbH, Germany) and incubated overnight. The cells were

then incubated with Hoechst 33342 (1 μ g mL^{−1}, in 2 mL cultivation medium) for 15 min. Subsequently, the cells were washed twice and incubated with the mitochondrial ROS sensor MitoSox™ (5 μ M, in 1 mL Hank's balanced salt solution) for 20 min. The cells were washed again twice prior to imaging. BL2 suspension cells were diluted to a concentration of 1000 cells/ μ L in cultivation medium and treated the same way as adherent cells. Washing was performed by centrifugation (180 rcf, 5 min). Images were taken with the Zeiss Observer with the 40x/1.30 Oil DIC objective: blue channel Ch3: λ_{ex} = 365 nm; λ_{em} = 445/50 nm; red channel Ch2: λ_{ex} = 545/25 nm; λ_{em} = 605/70 nm. Representative images are shown in Figure 7C.

SDS-PAGE: Mitochondrial isolation was performed as described previously.^[46] In brief, two T175 cultivation bottles with 70% confluent A2780 cells were treated with the compounds **8** or **9** (10 μ M, cultivation medium containing 5% FBS, 1% DMSO) for 2 h at 37 °C, 5% CO₂. Cells were lysed in 2 mL PBS (10 mM, pH 7.4, 150 mM NaCl) with freshly added protease inhibitor cocktail in a SONOCOOL sonification bath (100% power, 4 °C, 45 min). The cell lysate was subsequently centrifuged 3 times (1,400 rcf, 10 min, 4 °C) to remove cells that have not been lysed and large cell fragments. For each centrifugation step, the supernatant was transferred into a fresh tube. The supernatant was then centrifuged again (15 000 rcf, 10 min, 4 °C) to pellet mitochondria. The pellet was washed three times by resuspension in ice-cold PBS (2 mL) and repeated centrifugation at (15 000 rcf, 10 min, 4 °C). The pellet was resuspended in 2x Laemmli Sample Buffer (50 μ L, 5 mM tris(2-carboxyethyl)phosphine (TCEP), readjusted to pH 7) and loaded onto a pre-casted SDS gel and run at 200 V until the front ran out. The gels were washed with fixation solution (10% acetic acid (v/v), 20% MeOH (v/v) in water) for 1 h. Fluorescence images were taken with the iBright FL1000 λ_{ex} = 515–545 nm, λ_{em} = 568–617 nm and are shown in Figure 6.

Toxicity test: A2780 cells were seeded in RPMI 1640 medium containing 5% FBS, 1% glutaMAX™, and 1% penicillin/streptomycin in a 96-well microtiter plate (25000 cells per well per 100 μ L) and incubated at 37 °C in the chamber filled with CO₂ (5%) overnight. Stock solutions of **8** and **9** of different concentrations (1 μ L, solvent DMSO, final concentrations in wells were 0.05, 0.1, 0.5, 1, 5, 10, 25, 50 μ M) were added to the wells in triplicate and incubated for 4 h. Then, 3-(4,5-dimethylthiazol-2-yl)-2,5-diphenyltetrazolium bromide (MTT, 20 μ L of the solution prepared by dissolving MTT (5 mg) in DPBS buffer (1 mL)) was added to each well, incubated for 3 h, treated with sodium dodecyl sulfate (SDS) solution (90 μ L, 10% solution in 0.01 M aqueous HCl), and incubated overnight. Afterwards, the intensity of the absorbance at 590 nm was measured. The absorbance at 690 nm was taken as a baseline value. The baseline corrected absorbance at 590 nm ($A_{590\text{ nm}} - A_{690\text{ nm}}$) was applied to calculate the relative cell viability compared to the DMSO control, which was set to 100% viability. Three independent experiments were performed, averages and the standard deviation was calculated and is shown in Figure 6. IC₅₀ values were calculated in Excel. Statistical analysis of the data was conducted using an unpaired Student's t-test from the GraphPad Prism software.

Supporting Information

Further detailed synthetic procedures^[47,48] and characterization data for the control compounds **2**, **11**, **13**, **15**, **17**, **20**. LC-MS spectra for Table 1, additional DIC overlap pictures from confocal microscopy, ¹H NMR, DEPTQ NMR and purity HPLC runs. Additional references are cited within the Supporting Information.^[47,48]

Acknowledgements

The authors are grateful for the support of this project by the Emerging Fields Initiative (EFI, FAU Erlangen-Nürnberg), GRK1910-B3 (DFG; J.K.) and the Graduate School Molecular Science (GSMS; I.K., C.S.). Confocal microscopy was performed on a Zeiss Spinning Disc Axio Observer Z1, funded by the Deutsche Forschungsgemeinschaft (DFG, German Research Foundation) through project 248122450. Open Access funding enabled and organized by Projekt DEAL.

Conflict of Interests

The authors declare no conflict of interest.

Data Availability Statement

The data that support the findings of this study are available in the supplementary material of this article.

Keywords: alkynes · selective targeting · mitochondria · radicals · thiols

- [1] a) L. W. Butz, *J. Am. Chem. Soc.* **1935**, *57*, 1314–1315; b) A. A. Oswald, K. Griesbaum, B. E. Hudson, J. M. Bregman, *J. Am. Chem. Soc.* **1964**, *86*, 2877–2884; c) L. I. Smith, H. R. Davis, Jr, *J. Org. Chem.* **1950**, *15*, 824–831; d) W. E. Truce, H. G. Klein, R. B. Kruse, *J. Am. Chem. Soc.* **1961**, *83*, 4636–4641; e) W. E. Truce, J. A. Simms, H. Hill, *J. Am. Chem. Soc.* **1953**, *75*, 5411–5413.
- [2] a) H. C. Kolb, M. G. Finn, K. B. Sharpless, *Angew. Chem. Int. Ed.* **2001**, *40*, 2004–2021; *Angew. Chem.* **2001**, *113*, 2056–2075; b) S. S. Zaleskiy, N. S. Shlapakov, V. P. Ananikov, *Chem. Sci.* **2016**, *7*, 6740–6745.
- [3] a) S. Lü, Z. Wang, S. Zhu, *Nat. Commun.* **2022**, *13*, 5001; b) Y. Wang, B. J. Bruno, S. Cornillie, J. M. Nogueira, D. Chen, T. E. Cheatham III, C. S. Lim, D. H.-C. Chou, *Chem. Eur. J.* **2017**, *23*, 7087–7092.
- [4] a) H.-Q. Peng, C.-L. Sun, J.-F. Xu, L.-Y. Niu, Y.-Z. Chen, L.-Z. Wu, C.-H. Tung, Q.-Z. Yang, *Chem. Eur. J.* **2014**, *20*, 11699–11702; b) D. Funes-Hernando, P. Hermosilla, E. Vispe, A. Di Giuseppe, R. Castarlenas, L. A. Oro, J. J. Pérez-Torrente, *Polym. Chem.* **2018**, *9*, 1298–1302; c) H. Mutlu, E. B. Ceper, X. Li, J. Yang, W. Dong, M. M. Ozmen, P. Theato, *Macromol. Rapid Commun.* **2019**, *40*, 1800650; d) B. Yao, J. Mei, J. Li, J. Wang, H. Wu, J. Z. Sun, A. Qin, B. Z. Tang, *Macromolecules* **2014**, *47*, 1325–1333.
- [5] a) Z. Hou, D. Wang, Y. Li, R. Zhao, C. Wan, Y. Ma, C. Lian, F. Yin, Z. Li, *J. Org. Chem.* **2020**, *85*, 1698–1705; b) E. Mons, R. Q. Kim, B. R. van Doodewaerd, P. A. van Veelen, M. P. C. Mulder, H. Ovaa, *J. Am. Chem. Soc.* **2021**, *143*, 6423–6433.
- [6] J. V. Burykina, A. D. Kobelev, N. S. Shlapakov, A. Y. Kostyukovich, A. N. Fakhrtudinov, B. König, V. P. Ananikov, *Angew. Chem. Int. Ed.* **2022**, *61*, e202116888; *Angew. Chem.* **2022**, *134*, e202116888.
- [7] a) V. Corcé, L. McSweeney, A. Malone, E. M. Scanlan, *Chem. Commun.* **2015**, *51*, 8672–8674; b) A. Chatterjee, B. König, P. Natarajan, *ChemPhotoChem* **2020**, *4*, 291–293; c) M. Journet, A. Rouillard, D. Cai, R. D. Larsen, *J. Org. Chem.* **1997**, *62*, 8630–8631.
- [8] a) W. E. Truce, J. A. Simms, *J. Am. Chem. Soc.* **1956**, *78*, 2756–2759; b) A. B. Lowe, *Polymer* **2014**, *55*, 5517–5549.
- [9] J. C. Worch, C. J. Stubbs, M. J. Price, A. P. Dove, *Chem. Rev.* **2021**, *121*, 6744–6776.
- [10] T. Talele, *J. Med. Chem.* **2020**, *63*, 5625–5663.
- [11] M. Gehringer, S. A. Laufer, *J. Med. Chem.* **2019**, *62*, 5673–5724.
- [12] a) H. S. Walter, S. A. Rule, M. J. S. Dyer, L. Karlin, C. Jones, B. Cazin, P. Quittet, N. Shah, C. V. Hutchinson, H. Honda, K. Duffy, J. Birkett, V. Jamieson, N. Courtenay-Luck, T. Yoshizawa, J. Sharpe, T. Ohno, S. Abe, A. Nishimura, G. Cartron, F. Morschhauser, C. Fegan, G. Salles, *Blood* **2016**, *127*, 411–419; b) T. Barf, T. Covey, R. Izumi, B. van de Kar, M. Gulrajani, B. van Lith, M. van Hoek, E. de Zwart, D. Mittag, D. Demont, S. Verkaik, F. Krantz, P. G. Pearson, R. Ulrich, A. Kaptein, *J. Pharmacol. Exp. Ther.* **2017**, *363*, 240–252; c) S. H. Wattersson, Q. Liu, M. Beaudoin Bertrand, D. G. Batt, L. Li, M. A. Pattoli, S. Skala, L. Cheng, M. T. Obermeier, R. Moore, Z. Yang, R. Vickery, P. A. Elzinga, L. Discenza, C. D'Arienzo, K. M. Gillooly, T. L. Taylor, C. Pulicicchio, Y. Zhang, E. Heimrich, K. W. McIntyre, Q. Ruan, R. A. Westhouse, I. M. Catlett, N. Zheng, C. Chaudhry, J. Dai, M. A. Galella, A. J. Tebben, M. Pokross, J. Li, R. Zhao, D. Smith, R. Rampulla, A. Allentoff, M. A. Wallace, A. Mathur, L. Salter-Cid, J. E. Macor, P. H. Carter, A. Fura, J. R. Burke, J. A. Tino, *J. Med. Chem.* **2019**, *62*, 3228–3250.
- [13] J. C. Henise, J. Taunton, *J. Med. Chem.* **2011**, *54*, 4133–4146.
- [14] R. Ding, T. Zhang, D. J. Wilson, J. Xie, J. Williams, Y. Xu, Y. Ye, L. Chen, *J. Med. Chem.* **2019**, *62*, 2814–2829.
- [15] E. R. Wood, L. M. Shewchuk, B. Ellis, P. Brignola, R. L. Brashear, T. R. Caferro, S. H. Dickerson, H. D. Dickson, K. H. Donaldson, M. Gaul, R. J. Griffin, A. M. Hassell, B. Keith, R. Mullin, K. G. Petrov, M. J. Reno, D. W. Rusnak, S. M. Tadepalli, J. C. Ulrich, C. D. Wagner, D. E. Vanderwall, A. G. Waterson, J. D. Williams, W. L. White, D. E. Uehling, *Proc. Natl. Acad. Sci. USA* **2008**, *105*, 2773–2778.
- [16] a) C. G. Parker, M. R. Pratt, *Cell* **2020**, *180*, 605–632; b) M. H. Wright, S. A. Sieber, *Nat. Prod. Rep.* **2016**, *33*, 681–708.
- [17] E. Mons, I. D. C. Jansen, J. Loboda, B. R. van Doodewaerd, J. Hermans, M. Verdoes, C. A. A. van Boeckel, P. A. van Veelen, B. Turk, D. Turk, H. Ovaa, *J. Am. Chem. Soc.* **2019**, *141*, 3507–3514.
- [18] a) D. J. Porter, W. G. Chestnut, B. M. Merrill, T. Spector, *J. Biol. Chem.* **1992**, *267*, 5236–5242; b) R. Ekkebus, S. I. van Kasteren, Y. Kulathu, A. Scholten, I. Berlin, P. P. Geurink, A. de Jong, S. Goerdalay, J. Neeffjes, A. J. R. Heck, D. Komander, H. Ovaa, *J. Am. Chem. Soc.* **2013**, *135*, 2867–2870.
- [19] C. Arkona, J. Rademann, *Angew. Chem. Int. Ed.* **2013**, *52*, 8210–8212; *Angew. Chem.* **2013**, *125*, 8368–8370.
- [20] a) E. M. Sletten, C. R. Bertozzi, *Angew. Chem. Int. Ed.* **2009**, *48*, 6974–6998; *Angew. Chem.* **2009**, *121*, 7108–7133; b) J. M. Baskin, J. A. Prescher, S. T. Laughlin, N. J. Agard, P. V. Chang, I. A. Miller, A. Lo, J. A. Codelli, C. R. Bertozzi, *Proc. Natl. Acad. Sci. USA* **2007**, *104*, 16793–16797.
- [21] F. Dénès, M. Pichowicz, G. Povie, P. Renaud, *Chem. Rev.* **2014**, *114*, 2587–2693.
- [22] M. L. Conte, S. Staderini, A. Marra, M. Sanchez-Navarro, B. G. Davis, A. Dondoni, *Chem. Commun.* **2011**, *47*, 11086–11088.
- [23] Y. Li, M. Pan, Y. Li, Y. Huang, Q. Guo, *Org. Biomol. Chem.* **2013**, *11*, 2624–2629.
- [24] S. Sun, B. L. Oliveira, G. Jiménez-Osés, G. J. L. Bernardes, *Angew. Chem. Int. Ed.* **2018**, *57*, 15832–15835; *Angew. Chem.* **2018**, *130*, 16058–16061.
- [25] J. Stubbe, D. G. Nocera, *J. Am. Chem. Soc.* **2021**, *143*, 13463–13472.
- [26] a) L.-M. Altmann, V. Zantop, P. Wenisch, N. Diesendorf, M. R. Heinrich, *Chem. Eur. J.* **2021**, *27*, 2452–2462; b) S. Kindt, K. Wicht, M. R. Heinrich, *Angew. Chem. Int. Ed.* **2016**, *55*, 8744–8747; *Angew. Chem.* **2016**, *128*, 8886–8889.
- [27] M. T. Jeena, S. Kim, S. Jin, J.-H. Ryu, *Cancers* **2020**, *12*, 4.
- [28] Y. Wei, G. Mathies, K. Yokoyama, J. Chen, R. G. Griffin, J. Stubbe, *J. Am. Chem. Soc.* **2014**, *136*, 9001–9013.
- [29] H. J. Forman, H. Zhang, A. Rinna, *Mol. Aspects Med.* **2009**, *30*, 1–12.
- [30] V. Ribas, C. García-Ruiz, J. C. Fernández-Checa, *Front. Pharmacol.* **2014**, *5*, 151.
- [31] V. Reshetnikov, H. G. Özkan, S. Daum, C. Janko, C. Alexiou, C. Sauer, M. R. Heinrich, A. Mokhir, *Molecules* **2020**, *25*, 2545.
- [32] a) L. V. Johnson, M. L. Walsh, L. B. Chen, *Proc. Natl. Acad. Sci. USA* **1980**, *77*, 990–994; b) H. Dong, S. H. Cheung, Y. Liang, B. Wang, R. Ramalingam, P. Wang, H. Sun, S. H. Cheng, Y. W. Lam, *Electrophoresis* **2013**, *34*, 1957–1964.
- [33] I. Yoshifumi, W. Kuni, N. Kyoko, B. Jean-Luc, O. Koichiro, U. Kiitiro, *Chem. Lett.* **1987**, *16*, 1647–1650.
- [34] a) B. D. Fairbanks, E. A. Sims, K. S. Anseth, C. N. Bowman, *Macromolecules* **2010**, *43*, 4113–4119; b) E. G. Jayasree, S. Reshma, *Comput. Theor. Chem.* **2016**, *1098*, 13–21.
- [35] S. Daum, M. S. V. Reshetnikov, M. Sisa, T. Dumych, M. D. Lootsik, R. Bilyy, E. Bila, C. Janko, C. Alexiou, M. Herrmann, L. Sellner, A. Mokhir, *Angew. Chem. Int. Ed.* **2017**, *56*, 15545–15549; *Angew. Chem.* **2017**, *129*, 15751–15755.
- [36] H.-G. Xu, M. Schikora, M. Sisa, S. Daum, I. Klemt, C. Janko, C. Alexiou, G. Bila, R. Bilyy, W. Gong, M. Schmitt, L. Sellner, A. Mokhir, *Angew. Chem. Int. Ed.* **2021**, *60*, 11158–11162; *Angew. Chem.* **2021**, *133*, 11258–11262.
- [37] a) Y. Li, Y. Zhou, X. Yue, Z. Dai, *Adv. Healthcare Mater.* **2020**, *9*, 2001327; b) R. C. Benson, H. A. Kues, *J. Chem. Eng. Data* **1977**, *22*, 379–383.

- [38] a) J. F. Keij, C. Bell-Prince, J. A. Steinkamp, *Cytometry* **2000**, *39*, 203–210; b) S. A. Terlouw, O. Tanriseven, F. G. M. Russel, R. Masereeuw, *J. Pharm. Exp. Ther.* **2000**, *292*, 968–973.
- [39] a) Z. Farhane, F. Bonnier, A. Casey, H. J. Byrne, *Analyst* **2015**, *140*, 4212–4223; b) J.-a. A. Ho, N.-C. Fan, A. Fang-ju Jou, L.-C. Wu, T.-P. Sun, *Talanta* **2012**, *99*, 683–688.
- [40] a) H. Gizem Özkan, V. Thakor, H.-G. Xu, G. Bila, R. Bilyy, D. Bida, M. Böttcher, D. Mougiakakos, R. Tietze, A. Mokhir, *Chem. Eur. J.* **2022**, *28*, e202104420; b) H.-G. Xu, V. Reshetnikov, M. Wondrak, L. Eckhardt, L. A. Kunz-Schughart, C. Janko, R. Tietze, C. Alexiou, H. Borchardt, A. Aigner, W. Gong, M. Schmitt, L. Sellner, S. Daum, H. G. Özkan, A. Mokhir, *Cancers* **2022**, *14*, 208.
- [41] a) M. Alexander, *Crit. Rev. Environ. Sci. Technol.* **1997**, *27*, 383–410; b) S. J. Sumner, T. R. Fennell, *Crit. Rev. Toxicol.* **1994**, *24*, S11–S33.
- [42] G. T. Dempsey, M. Bates, W. E. Kowtoniuk, D. R. Liu, R. Y. Tsien, X. Zhuang, *J. Am. Chem. Soc.* **2009**, *131*, 18192–18193.
- [43] M. Heilemann, E. Margeat, R. Kasper, M. Sauer, P. Tinnefeld, *J. Am. Chem. Soc.* **2005**, *127*, 3801–3806.
- [44] L. M. Hall, M. Gerowska, T. Brown, *Nucleic Acids Res.* **2012**, *40*, e108–e108.
- [45] G.-S. Jiao, L. H. Thoresen, K. Burgess, *J. Am. Chem. Soc.* **2003**, *125*, 14668–14669.
- [46] D. A. Clayton, G. S. Shadel, *Cold Spring Harbor Protocols* **2014**, pdb.top074542.
- [47] M. Niwa, T. Hirayama, K. Okuda, H. Nagasawa, *Org. Biomol. Chem.* **2014**, *12*, 6590–6597.
- [48] M. V. Kvach, A. V. Ustinov, I. A. Stepanova, A. D. Malakhov, M. V. Skorobogatyi, V. V. Shmanai, V. A. Korshun, *Eur. J. Org. Chem.* **2008**, *2008*, 2107–2117.

Manuscript received: April 28, 2023

Accepted manuscript online: May 12, 2023

Version of record online: June 21, 2023

Publication 4:

Reactive oxygen species-responsive RNA interference

Jennifer Rühle,^{#[a]} Insa Klemt,^{#[a]} Tatiana Abakumova,^[b] Olga Sergeeva,^[b] Polina Vetosheva,^[b] Timofei Zatsepin,^{[b,c]} and Andriy Mokhir^{*[a]}*

^[a] *Department of Chemistry and Pharmacy, Organic Chemistry II, Friedrich-Alexander-Universität Erlangen-Nürnberg, Nikolaus-Fiebiger-Str. 10, 91058 Erlangen, Germany*

^[b] *Skolkovo Institute of Science and Technology, Moscow, Russia*

^[c] *Chemistry Department, M.V. Lomonosovo Moscow State University, Leninskie gory, 1-3, Moscow 119992, Russia*

[#]equal contribution

Contribution of I. Klemt:

Design, performance, and data processing of activation experiments in cell free settings and all experiments performed in A2780 cells. Contribution to Publication writing and revision of the manuscript.

The publication and supporting information are found under: DOI: **10.1039/D2CC00651K**



Reactive oxygen species-responsive RNA interference†

 Cite this: *Chem. Commun.*, 2022, 58, 4388

 Received 1st February 2022,
Accepted 8th March 2022

DOI: 10.1039/d2cc00651k

rsc.li/chemcomm

 Jennifer Rühle,^{‡a} Insa Klemt,^{§a} Tatiana Abakumova,^b Olga Sergeeva,^b
Polina Vetosheva,^b Timofei Zatsepin^{§*bc} and Andriy Mokhir^{§*a}

Due to oxidative instability, arylboronic acids are not compatible with the solid-phase synthesis of nucleic acids. We solved this problem and, based on these findings, developed siRNA prodrugs activated in the presence of reactive oxygen species (ROS) *in vivo*. These prodrugs can be used for specific targeting of ROS-rich cancer cells.

Small interfering ribonucleic acids (siRNAs) are short double-stranded RNAs that downregulate gene expression *via* RNA interference (RNAi).¹ The delivery of siRNA conjugates and siRNAs entrapped in lipid nanoparticles (LNPs) to the liver *in vivo* is established.² The current technology is beneficial when all cells in the liver should be affected, *e.g.* for the treatment of metabolic diseases. Targeting siRNAs to specific pathological cells within the normal tissue *in vivo* is still a challenge that limits the number of suitable therapeutic targets.³ Targeted delivery of siRNA can be achieved by the conjugation of various binders of cellular receptors, *e.g.*, aptamers,⁴ antibodies,⁵ and receptor ligands,⁶ either to the carrier part or siRNA in siRNA/carrier constructs. The complementary approach, suitable for targeting cells without known unique receptors, relies on differences in the microenvironment of pathological and normal cells. For example, elevated levels of ROS are a common feature of the majority of cancer cells.⁷ A few “smart” delivery vehicles have already been developed using modified polymers and lipids as reviewed elsewhere.⁸ For example, Shi and co-workers have reported a 3l-NM@siRNA system, which is responsive to endogenous ROS present in tumors.⁹ 3l-NM@siRNA consists of an siRNA and a

ROS-responsive carrier 3l-NM, which is assembled from two different polyacrylamide-based co-polymers decorated with polyethylene glycol, angiopep-2 peptide, guanidinium and phenylboronic acid moieties. Other related examples were reported by Zhou, Shen¹⁰ and T. Sun.¹¹ The transfer of such highly complex delivery systems from the bench to the bedside will be challenging and costly, including possible issues with production, toxicity and unfavourable pharmacokinetics. This justifies the search for alternative, simpler solutions for ROS-responsive siRNAs.

In cells, siRNAs are first phosphorylated at the 5'-terminus of their guide strands with the formation of P-siRNAs that initiate further steps leading to RNAi.^{12,13} “Smart” trigger-responsive RNAi can be realized by reversible blocking of the phosphorylation. To date, known examples include only light-activated siRNAs.^{14–16} We applied this approach to develop siRNAs responsive to H₂O₂, which is the dominating ROS in cancer cells (Fig. 1). Related siRNAs activated by singlet oxygen (¹O₂) are known.¹⁶ Our goal was to prepare these reagents by standard solid-phase RNA synthesis, thereby making them accessible to the scientific community and easily scalable to enable *in vivo* studies. As a ROS-sensitive moiety, we selected a 4-boronobenzyl (4BB) group, which is known to retain its activity *in vivo*.^{17–20}

Contradictory data are available in the literature on the synthesis and coupling of phosphoramidites (Pm's) containing 4BB to 5'-DNA, whereas 4BB-P-RNAs have not been reported. The first successful use of 4BB-Pm's in DNA synthesis was described by Kaiser and Stolowitz.²¹ However, Steinmeyer and Wagenknecht have reported that similar derivatives can be incorporated into DNA only in low yields.²³ Our results obtained for 4BB-Pm confirm the latter conclusion (Fig. 1A). Alternatively, Ikeda and co-workers have reported on the preparation of a 4BB-P-DNA 3 by coupling of the 4BB-diazo reagent to a P-DNA 4 in solution (Fig. 1B).²² Due to the instability of 4BB-diazo, 160 eq excess of this reagent with respect to the DNA was used, which led to conversions of 46%.

In this work, we report for the first time the coupling of 4BB to the 5'-RNA terminus (4BB-P-RNAs 7, Fig. 1C). We applied this

^a Department of Chemistry and Pharmacy, Organic Chemistry II, Friedrich-Alexander-University of Erlangen-Nürnberg (FAU), Nikolaus-Fiebiger Str. 10, 91058 Erlangen, Germany. E-mail: Andriy.Mokhir@fau.de

^b Skolkovo Institute of Science and Technology, Moscow, Russia. E-mail: t.zatsepin@gmail.com

^c Chemistry Department, M. V. Lomonosov Moscow State University, Leninskie gory, 1-3, Moscow 119992, Russia

† Electronic supplementary information (ESI) available. See DOI: 10.1039/d2cc00651k
‡ JR and IK have contributed equally to this paper.

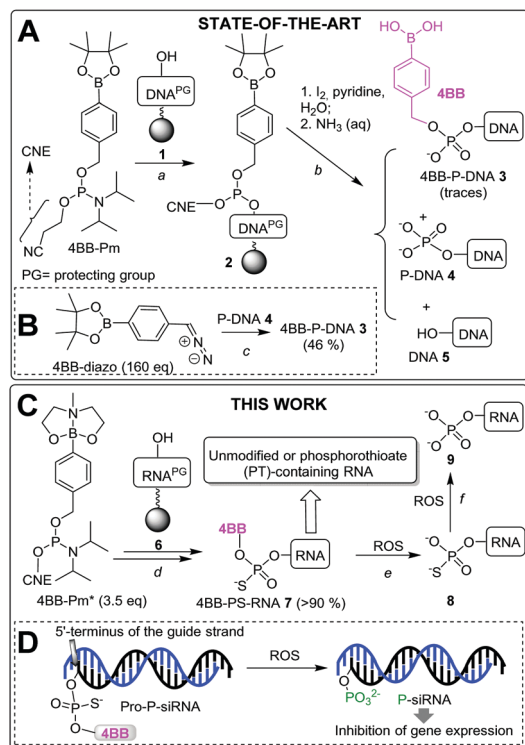
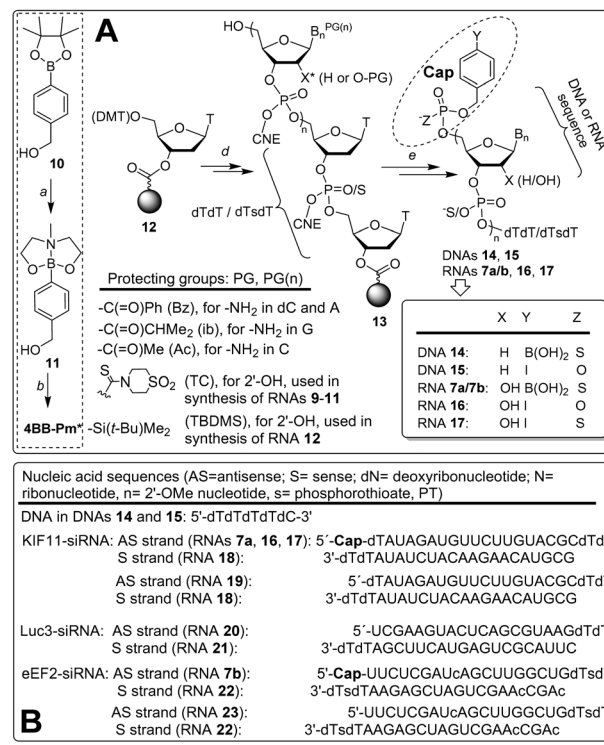


Fig. 1 State-of-the-art in the synthesis of 5'-4BB-modified DNAs: (A) solid-phase synthesis using phosphoramidite **4BB-Pm**,²¹ (B) solution phase synthesis using 4BB-diazo.²² This work: (C) our approach for the synthesis of 5'-4BB-PS-RNA **7**; (D) design of H_2O_2 -responsive siRNAs using 5'-4BB-PS-RNA **7** as a guide strand.

method to prepare ROS-responsive siRNAs (Fig. 1D). One of the reasons why 4BB-Pm is not suitable for the solid-phase synthesis of 4BB-P-DNA **3** could be oxidative cleavage of the B-C bond in the presence of I_2 with the formation of P-DNA in step *b*. To block this side reaction, we replaced bidendate pinacol in **10** with tridentate *N,N*-diethanolmethylamine (DEA) to obtain **11**, where all binding sites at the boron atom are saturated (Scheme 1A). **11** was successfully converted to 4BB-Pm* (Fig. 1C) with an isolated yield of 57%, which increased to 87% upon scaling up.

Next, we coupled this reagent to model DNA **1** followed by oxidation with I_2 and deprotection/cleavage of the product from the solid support by aqueous NH_3 . In the obtained mixture, we observed only 5'-phosphorylated DNA **4** and unmodified DNA **5** and no traces of the expected product 4BB-P-DNA **3** (Fig. S12–S14, ESI†). These data indicated that 4BB-Pm* was initially coupled to **1**, followed by the cleavage of 4BB during the oxidation. In contrast to **3**, its analogue DNA **15**, where a $B(OH)_2$ group was replaced with an I atom, could be obtained under standard conditions (Fig. S19 and S20, ESI†) that underpin the role of the boronic acid in the instability of **3**. By using **11** as a model compound, we confirmed that the B-C bond is cleaved under the conditions used for P(III) oxidation (Fig. S15, ESI†). These data indicated that the protection of the boronic acid in 4BB with DEA does not solve the problem of the instability of a B-C bond under conditions of solid-phase synthesis.



Scheme 1 (A) An outline of the synthesis of ROS-responsive 5'-4BB-oligonucleotides. (B) Sequences of DNAs/RNAs used in this work.

In the results of studies of the sensitivity of the model compound **11** towards different oxidative conditions, we found that it is stable in the presence of 3-ethoxy-1,2,4-dithiazoline-5-one (EDITH) (Fig. S16, ESI†). Based on these data, we replaced I_2 with EDITH in the last oxidation step that allowed us to obtain DNA **14** containing a 5'-4BB moiety linked to the DNA *via* a PS group. We managed to isolate two possible diastereomers of **14** with >90% purity: retention times R_t = 16.78 and 17.65 min (Fig. S17 and S18, ESI†). The product eluted later was obtained at the higher yield that is a common feature in oligonucleotide synthesis.²⁴ Further tests were conducted only with the more abundant isomer. The expected mechanism of DNA **14** transformation in the presence of ROS is outlined in Fig. 2A. In the first step, the B-C bond is cleaved with the formation of phenol derivatives **14_1** and **14_2**, followed by 1,6-elimination of **24** (which is quenched by water forming **25**) leading to a 5'-PS derivative **14_3**. As previously reported, phosphorothioates can be desulfurized under oxidative conditions.²⁵ Correspondingly, **14_4** can be formed as one of the products. We detected the formation of substantial amounts of phenol **14_1** and **14_4** in the DNA **14**/ H_2O_2 mixture (Fig. 2B), which confirms the suggested cleavage mechanism. We found that the cleavage of DNA **14** by H_2O_2 is concentration-dependent. For example, this reaction occurs even at the lowest tested H_2O_2 concentration of 50 μM . Furthermore, we observed that the 5'-4BB group can be cleaved in the presence of ROS types other than H_2O_2 , including HO^\bullet , $O_2^{\bullet-}$, and ONO_2^- . However, it remains stable in the presence of biologically occurring oxidant Cu^{2+} (10 μM) (Fig. 2B).

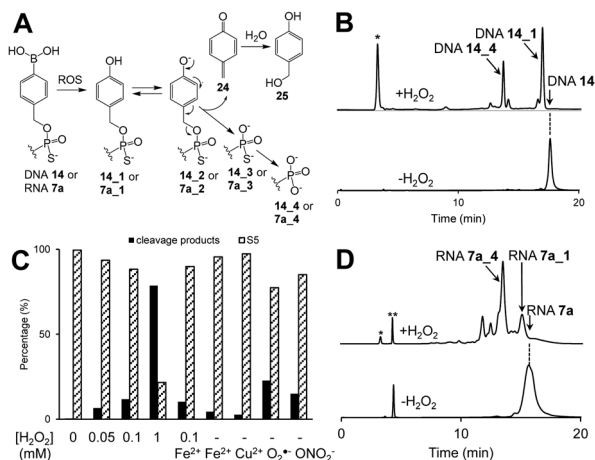


Fig. 2 The mechanism of 5'-4BB group cleavage (A). (B): HPLC-monitored transformation of DNA **14** (130 μ M) dissolved in PBS buffer (10 mM phosphate, pH 7.4, 150 mM NaCl) in the presence of H_2O_2 (200 mM, 1 h incubation at 35 $^\circ\text{C}$, "+ H_2O_2 ") or in its absence ("- H_2O_2 "). (C) Cleavage of **14** in PBS buffer by different oxidants: H_2O_2 (0–1 mM); FeSO_4 (10 μ M), *N,N,N',N'*-ethylenediaminetetracetic acid (EDTA, 10 μ M); CuSO_4 (10 μ M); KO_2 (1 mM) and ONO_2^- –3-morpholinopropanone hydrochloride (SIN-1, 400 μ M). Incubation time – 1 h at 35 $^\circ\text{C}$. Y-Axis: % S5 and cleavage products as determined from HPLC data. Standard deviation is below $\pm 15\%$ of the values shown on the plot. (D) HPLC analysis of RNA **7a** (65 μ M in PBS) in the presence of H_2O_2 (10 mM, 1 h incubation at 35 $^\circ\text{C}$, "+ H_2O_2 ") or in its absence ("- H_2O_2 "). *: a peak derived from H_2O_2 . **: impurity in RNA **7a** (<10%).

Next, we applied the synthesis protocol optimized for DNA **14** to prepare a guide strand RNA **7a** for the siRNA targeting the kinesin family member (KIF11) gene. KIF11 was selected because of the following considerations. First, its downregulation can be easily monitored, since it leads to a simple phenotype: cell cycle arrest in the G2 phase. Second, it is overexpressed at least in some cancers and is a promising target for cancer treatment.²⁶ Third, KIF11 is an essential gene and presents an optimal example of a target that should be selectively downregulated in cancer cells without affecting normal tissue.

We successfully prepared RNA **7a** as a mixture of diastereomers (Fig. S21 and S22, ESI[†]) and confirmed that it reacts with H_2O_2 analogously to DNA **14** (Fig. 2D). Furthermore, we prepared negative control RNA **16** and its PS analogue **17**. In both cases, a 4BB fragment was replaced with a ROS-resistant cap: 4-iodobenzyl. In contrast to **7a**, these RNAs are stable in the presence of H_2O_2 , except that some minor amount of de-sulfurized **16** is formed from **17** under the oxidative conditions (Fig. S32, ESI[†]). These data confirm that the boronic acid moiety is responsible for the observed sensitivity of **7a** to ROS. For cellular assays, we prepared a stock solution of ROS-responsive KIF11-siRNA (10 μ M) by annealing **7a** and **18** (Scheme 1B, ESI[†]). This solution was formulated with Lipofectamine[™] RNAiMAX and applied to human ovarian cancer A2780 cells at two doses of 0.5 and 5 nM. These cells were selected because they contain high levels of intracellular ROS.²⁰ We monitored the expression of the KIF11 gene by detecting its mRNA level using reverse transcription followed by the quantitative polymerase chain reaction (RT-qPCR, Fig. 3). The mRNA amount in untreated

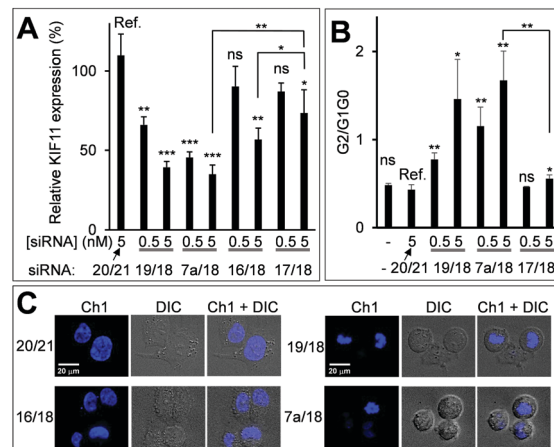


Fig. 3 (A) Relative levels of KIF11 mRNA in A2780 cells treated with the selected siRNAs for 38 h. The data were normalized to the level of KIF11 mRNA in the untreated cells. (B) Effects of the siRNAs on the cell cycle of A2780 cells. G2/G1G0 is a ratio of the number of cells in the G2 phase to that of the cells in the G1 and G0 phases. (C) Fluorescence (Ch1), differential interference contrast (DIC) and combined (Ch1 + DIC) images of A2780 cells treated for 38 h with siRNAs (0.5 nM), followed by the treatment with Hoechst33342 (nuclei stain). Student's *t*-test: * $p < 0.05$, ** $p < 0.01$, *** $p < 0.001$, ns $p \geq 0.05$. Data were compared to the reference (labelled as "ref."), if not otherwise indicated.

cells was set to 100%. We compared relative KIF11 expression (RE) in the presence of **7a/18** with RE in the presence of negative control **20/21**.¹⁶ We observed that after incubation of the cells with **7a/18** (0.5 or 5 nM) for 38 h, RE is decreased down to 40–44% (Fig. 3A, for both doses $p < 0.001$). The difference in RE between the tested doses of **7a/18** is not significant indicating that the effect is saturated already at 0.5 nM. At 0.5 nM, RE, achieved in the presence of positive control **19/18**, is even lower than that of **7a/18** ($40 \pm 2\%$ vs. $68 \pm 5\%$, $p < 0.01$), whereas at 5 nM, the effects of these siRNAs are identical ($44 \pm 5\%$ vs. $45 \pm 5\%$). These data indicate that the conversion of **7a/18** to the active form (5'-phosphorylated **19/18**) occurs efficiently in cells. In contrast, both negative controls **16/18** and **17/18** are substantially less active than **7a/18** at both tested doses (Fig. 3A). Thus, ROS-mediated removal of a 4BB group in **7a/18** is required for the activation of RNAi in cells. Among the negative controls, **16/18** (5 nM) is slightly more active than its PS analogue **17/18** (5 nM, $p < 0.05$) confirming that the PS group is preferable for 5'-blocking in comparison to phosphodiester, due to its higher nuclease resistance.

Furthermore, we demonstrated that the decrease of KIF11 mRNA levels in the presence of **7a/18** (Fig. 3A) correlates with a strong cell cycle arrest in the G2 phase (Fig. 3B). The latter effect is also observed for a positive control **19/18**, but is absent for negative controls **20/21** and **17/18**. Using fluorescence microscopy, we observed compact nuclei in A2780 cells treated with the positive control **19/18** and ROS-responsive siRNA **7a/18**. This feature is characteristic for cells treated with inhibited or downregulated KIF11.²⁷ (45). In contrast, nuclei of the cells treated with the negative controls have larger sizes (Fig. 3C).

To confirm the generality of our prodrug concept, we applied it to design a prodrug targeting another gene: murine

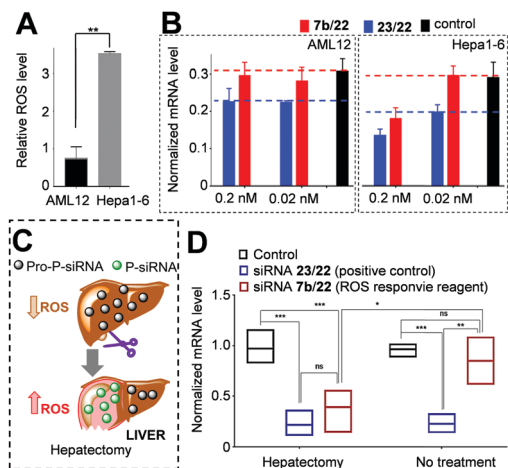


Fig. 4 (A) Flow cytometric analysis of the ROS levels in AML12 and Hepa1-6 cells. (B) Expression of eEF2-mRNA in AML12 and Hep1-6 cells in the presence of **7b/22**, **23/22** and **20/21**. (C) An image illustrating the effect of HE on the ROS level in the liver. (D) *In vivo* downregulation of eEF2 mRNA using **23/22** and **7b/22** in the liver of FvB mice ("without treatment") and in the liver of FvB mice after partial HE. Student's t-test: * - $p < 0.05$, ** - $p < 0.01$, *** - $p < 0.001$, ns - $p \geq 0.05$.

eukaryotic elongation factor 2 (eEF2). An siRNA targeting this gene (**23/22**) was previously reported.²⁸ We converted the guide strand **23** to its ROS-responsive version **7b** (ESI[†]). Furthermore, we studied the effects of siRNA **7b/22** on the expression of eEF2-mRNA in normal (AML12) and cancer (Hep1-6) liver cells. The level of ROS in AML12 cells is lower than that in the Hepa1-6 cells (Fig. 4A), making this pair of cells a good model to study the ROS-dependent prodrug activation. As expected, at both tested doses of 0.02 and 0.2 nM, **7b/22** as well as negative control **23/22** are inactive in AML12 cells (Fig. 4B). In contrast, in the Hepa1-6 cells, **7b/22** exhibits RNAi activity in a concentration-dependent fashion (Fig. 4B).

Encouraged by the promising *in vitro* data, we studied the *in vivo* effects of the prodrug. **7b/22** and control **23/22** were formulated into C12-200 lipid nanoparticles (LNP's, ESI[†]).^{29,30} Intravenous injection of **23/22/LNP** at a dose of 0.02 mg kg⁻¹ to FvB mice resulted in 75–80% eEF2 mRNA downregulation in the liver in 48 h as compared to that of the control (LNP's with siRNA targeting luciferase, Table S1, ESI[†]). In contrast, **7b/22** at the same dose did not affect the eEF2 mRNA level (Fig. 4D), indicating that the prodrug is not activated in healthy mice. To probe whether ROS-induced activation of **7b/22** is possible *in vivo*, we conducted a partial hepatectomy (HE) in the FvB mice, which is known to cause an increase in the ROS levels in the liver (Fig. 4C).³¹ We confirmed that eEF2 mRNA expression is not changed after HE. We conducted HE in FvB mice 24 h after the injection of LNP's with **7b/22** and analyzed the expression of eEF2 mRNA by RT-qPCR after a further 24 h. We were pleased to observe a significant activation of the siRNA prodrug under the HE conditions in comparison to the mock mice (Fig. 4). The efficacy of eEF2 knockdown with the siRNA prodrug under the HE conditions is identical to that of the control siRNA **23/22**.

In summary, we prepared for the first time 5'-modified-siRNA prodrugs responsive to ROS and demonstrated their functionality in cell-free settings, in cells and *in vivo*.

Conflicts of interest

There are no conflicts to declare.

Notes and references

- 1 A. Fire, S. Xu, M. K. Montgomery, S. A. Kostas, S. E. Driver and C. C. Mello, *Nature*, 1998, **391**, 806.
- 2 T. Gökirmak, M. Nikan, S. Wiechmann, T. P. Prakash, M. Tanowitz and P. P. Seth, *Trends Pharmacol. Sci.*, 2021, **42**, 588.
- 3 R. L. Juliano, *NAR Cancer*, 2020, **2**, zcaa025.
- 4 J. P. Dassie, X.-Y. Liu, G. S. Thomas, R. M. Whitaker, K. W. Thiel, K. R. Stockdale, D. K. Meyerholz, A. P. McCaffrey, J. O. McNamara II and P. H. Giangrande, *Nat. Biotechnol.*, 2009, **27**, 839.
- 5 T. Sugo, M. Terada, T. Oikawa, K. Miyata, S. Nishimura, E. Kenjo, M. Ogasawara-Shimizu, Y. Makita, S. Imaichi and S. Murata, *et al.*, *J. Control. Release.*, 2016, **237**, 1.
- 6 B. R. Meade, K. Gogoi, A. S. Hamil, C. Palm-Apergi, A. van den Berg, J. C. Hagopian, A. D. Springer, A. Eguchi, A. D. Kacsinta and C. F. Dowdy, *et al.*, *Nat. Biotechnol.*, 2014, **32**, 1256.
- 7 F. Antunes and R. Cadenas, *FEBS Lett.*, 2000, **475**, 121.
- 8 M. A. Subhan and V. P. Torchilin, *Nanomed.*, 2020, **29**, 102239.
- 9 M. Zheng, Y. Liu, Y. Wang, D. Zhang, Y. Zou, W. Ruan, J. Yin, W. Tao, J. B. Park and B. Shi, *Adv. Mater.*, 2019, 1903277.
- 10 D. Zhu, H. Yan, X. Liu, J. Xiang, Z. Zhou, J. Tang, X. Liu and Y. Shen, *Adv. Funct. Mater.*, 2017, **27**, 1606826.
- 11 C. Ruan, L. Liu, Q. Wang, X. Chen, Q. Chen, Y. Lu, Y. Zhang, X. He, Y. Zhang, Q. Guo, T. Sun and C. Jiang, *et al.*, *ACS Appl. Mater. Interfaces*, 2018, **10**, 10398.
- 12 E. Elkayam, C.-D. Kuhn, A. Tocij, A. D. Haase, E. M. Greene, G. J. Hannon and L. Joshua-Tor, *Cell*, 2012, **150**, 100.
- 13 N. T. Schirle and I. J. MacRae, *Science*, 2012, **336**, 1037.
- 14 S. Shah and S. H. Friedman, *Oligo*, 2007, **17**, 35.
- 15 Y. Ji, J. Yang, L. Wu, L. Yu and X. Tang, *Angew. Chem., Int. Ed.*, 2016, **55**(6), 2152.
- 16 A. Meyer and A. Mokhir, *Angew. Chem., Int. Ed.*, 2014, **53**, 12840.
- 17 J. P. Cadahia, V. Previtali, N. S. Troelsen and M. H. Clausen, *MedChemComm*, 2019, **10**(9), 1531.
- 18 R. Weinstein, E. N. Savariar, C. N. Felsen and R. Y. Tsien, *J. Am. Chem. Soc.*, 2014, **136**(3), 874.
- 19 H. G. Kuivila, *J. Am. Chem. Soc.*, 1954, **76**, 870.
- 20 H. Xu, M. Schikora, M. Sisa, S. Daum, I. Klemm, C. Janko, C. Alexiou, G. Bila, R. Bilyy and W. Gong, *et al.*, *Angew. Chem., Int. Ed.*, 2021, **60**(20), 11158.
- 21 R. J. Kaiser and M. L. Stolowitz, patent US6031117, 29. 02. 2000.
- 22 N. Shirakami, Y. Kawaki, S. L. Higashi, A. Shibata, Y. Kitamura, S. A. Hanifah, L. L. Wah and M. Ikeda, *Chem. Lett.*, 2021, **50**, 1412.
- 23 J. Steinmeyer and H. A. Wagenknecht, *Bioconjugate Chem.*, 2018, **29**(2), 431.
- 24 H. Jahns, M. Roos, J. Imig, F. Baumann, Y. Wang, R. Gilmour and J. Hall, *Nat. Commun.*, 2015, **6**, 6317.
- 25 T. Wu, Q. Huang, X.-L. Wang, T. Shi, L. Bai, J. Liang, Z. Wang, Z. Deng and Y.-L. Zhao, *Sci. Rep.*, 2017, **7**, 42823.
- 26 M. Jiang, H. Zhuang, R. Xia, L. Gan, Y. Wu, J. Ma, Y. Sun and Z. Zhuang, *Oncotarget*, 2017, **8**(54), 92106.
- 27 A.-K. Becker, H. Erfle, M. Gunkel, N. Beil, L. Kaderali and V. Starkuviene, *High-Throughput*, 2018, **7**, 13.
- 28 M. V. Gerashchenko, M. V. Nesterchuk, E. M. Smekalova, J. A. Paulo, P. S. Kallanthothathil, K. A. Akulich, R. Bogorad, S. E. Dmitriev, S. Gygi and T. Zatsepin, *et al.*, *Sci. Rep.*, 2020, **10**, 15473.
- 29 M. Jayaraman, S. M. Ansell, B. L. Mui, Y. K. Tam, J. Chen, X. Du, D. Butler, L. Eltepu, S. Matsuda, J. K. Narayanannair and K. G. Kallanthothathil, *et al.*, *Angew. Chem., Int. Ed.*, 2012, **51**(34), 8529.
- 30 K. T. Love, K. P. Mahon, C. G. Levins, K. A. Whitehead, W. Querbes, J. R. Dorkin, J. Qin, W. Cantley, L. L. Qin and T. Racie, *et al.*, *Proc. Natl. Acad. Sci.*, 2010, **107**(5), 1864.
- 31 S. Ueno, J. Campbell and N. Fausto, *Gastroint.*, 2006, **136**(2), 260.

Publication 5:

Triggering RNA interference by photoreduction under red light irradiation

*Jennifer Rühle,^{#[a]} Insa Klemt,^{#, *[a]} and Andriy Mokhir^{*,[a]}*

^[a] *Department of Chemistry and Pharmacy, Organic Chemistry II, Friedrich-Alexander-Universität Erlangen-Nürnberg, Nikolaus-Fiebiger-Str. 10, 91058 Erlangen, Germany*

[#]equal contribution

Contribution of I. Klemt:

Design, performance, and data processing of experiments performed in A2780 cells. Manuscript writing and revision. Abstract image design.

The publication and supporting information are found under:
DOI: **10.3390/molecules28104204**.

Article

Triggering RNA Interference by Photoreduction under Red Light Irradiation

Jennifer Rühle [†], Insa Klemt ^{*,†}  and Andriy Mokhir ^{*,†} 

Department of Chemistry and Pharmacy, Organic Chemistry II, Friedrich-Alexander-University of Erlangen-Nürnberg (FAU), Nikolaus-Fiebiger Str. 10, 91058 Erlangen, Germany; jennifer.ruehle@fau.de

* Correspondence: insa.klemt@fau.de (I.K.); andriy.mokhir@fau.de (A.M.)

† These authors contributed equally to this work.

Abstract: RNA interference (RNAi) using small interfering RNAs (siRNAs) is a powerful tool to target any protein of interest and is becoming more suitable for in vivo applications due to recent developments in RNA delivery systems. To exploit RNAi for cancer treatment, it is desirable to increase its selectivity, e.g., by a prodrug approach to activate the siRNAs upon external triggering, e.g., by using light. Red light is especially well suited for in vivo applications due to its low toxicity and higher tissue penetration. Known molecular (not nanoparticle-based) red-light-activatable siRNA prodrugs rely on singlet oxygen (¹O₂)-mediated chemistry. ¹O₂ is highly cytotoxic. Additionally, one of the side products in the activation of the known siRNA prodrugs is anthraquinone, which is also toxic. We herein report on an improved redlight-activatable siRNA prodrug, which does not require ¹O₂ for its activation. In fact, the 5' terminus of the antisense strand is protected with an electron-rich azobenzene moiety. It is reduced and cleaved upon red light exposure in the presence of Sn(IV)(pyropheophorbide a)dichloride acting as a catalyst and ascorbate as a bulk reducing agent. We confirmed the prodrug activation upon red light irradiation both in cell-free settings and in human ovarian cancer A2780 cells.

Keywords: siRNA prodrug; selective cancer targeting; red light activation; photoreduction; RNAi; azobenzene; moiety



Citation: Rühle, J.; Klemt, I.; Mokhir, A. Triggering RNA Interference by Photoreduction under Red Light Irradiation. *Molecules* **2023**, *28*, 4204. <https://doi.org/10.3390/molecules28104204>

Academic Editor: Rafik Karaman

Received: 28 April 2023

Revised: 14 May 2023

Accepted: 16 May 2023

Published: 20 May 2023



Copyright: © 2023 by the authors. Licensee MDPI, Basel, Switzerland. This article is an open access article distributed under the terms and conditions of the Creative Commons Attribution (CC BY) license (<https://creativecommons.org/licenses/by/4.0/>).

1. Introduction

Due to recent developments in in vivo oligonucleotide delivery systems, RNA-based therapeutic approaches are becoming more and more enticing. Hence, alongside, for example, RNA-based vaccines, five silencing RNA (siRNA) drugs have been clinically approved (patisiran, givosiran, lumasiran, inclisiran, and vutrisiran) that act via the mechanism of RNA interference (RNAi) to downregulate specific genes [1–5]. All five siRNA drugs on the market treat metabolic or neurodegenerative diseases. As an alternative application, targeting cancer cells by the downregulation of genes that are essential for mitosis, for example, would be attractive as well. In that way, proteins that are considered undruggable could also be targeted. However, similar to small molecular drug approaches, the mere targeting of mitosis and thus fast-dividing cells, results in dose-limiting side effects concerning non-cancerous cells that rely on fast proliferation, resulting in myelosuppression, cytopenia, hepatotoxicity, etc. One possible solution to increase cancer selectivity is the application of prodrugs that are activated in a specific cancer microenvironment or upon an external trigger. Accordingly, few examples of siRNA prodrugs have been reported [6–8]. Following this approach, we have already developed ROS-responsive siRNAs that are activated by elevated H₂O₂ concentrations [9], a hallmark of many cancers [10]. In addition, we reported on red-light-responsive siRNAs (Figure 1), in which the passenger strand is modified with a photosensitizer that generates ¹O₂ upon red light irradiation. The on-demand-generated ¹O₂ cleaves the 9-anthracenyl moiety on the antisense strand, yielding the active siRNA,

and while the activation is efficient, side effects by these harsh oxidative conditions are to be expected, especially for in vivo applications. This can be one of the reasons why this system has never been applied in vivo. In search of alternative promoieties, which are not activated under strong oxidative conditions, we explored azobenzenes. The application of azobenzene triggers in a biological context comes with some challenges, as two distinct processes can be initiated, the first one being photoisomerization and the second one being reduction. The photoisomerization of azobenzenes is in most cases triggered by UV light, which is toxic to cells and does not show significant tissue penetration. Nevertheless, some stable azobenzenes were successfully applied in living cells or in vivo to activate certain processes (e.g., disassembly of complex biomolecules) by photoswitching to the *cis* isomer [11–13]. Exploiting the second process, few approaches have also been developed towards reducible azobenzenes, e.g., as sensors of hypoxia [14,15]. For this study, we aimed for a stable azobenzene moiety to avoid the unspecific intracellular reduction of the siRNA prodrug. However, upon an external trigger, the promoiety should be reduced efficiently. We therefore selected electron-rich azobenzene “RF” (Scheme 1), which was shown to be non-cleavable under conditions mimicking the cellular environment [16]. We hoped that this residue would still be photo-reducible in the presence of catalyst Sn(IV)(pyropheophorbide a)dichloride (SnPPA) (Figure 1). We selected SnPPA based on our previous report [16], in which we established that in contrast to free PPA and its complexes (e.g., In(III)(pyropheophorbide a) chloride, InPPA), SnPPA is able to mediate the photoreduction by electron transfer to organic substrates.

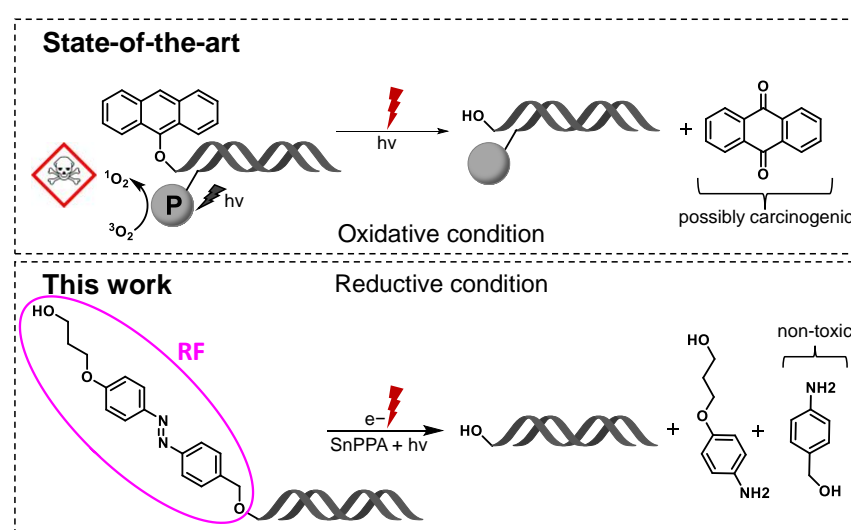
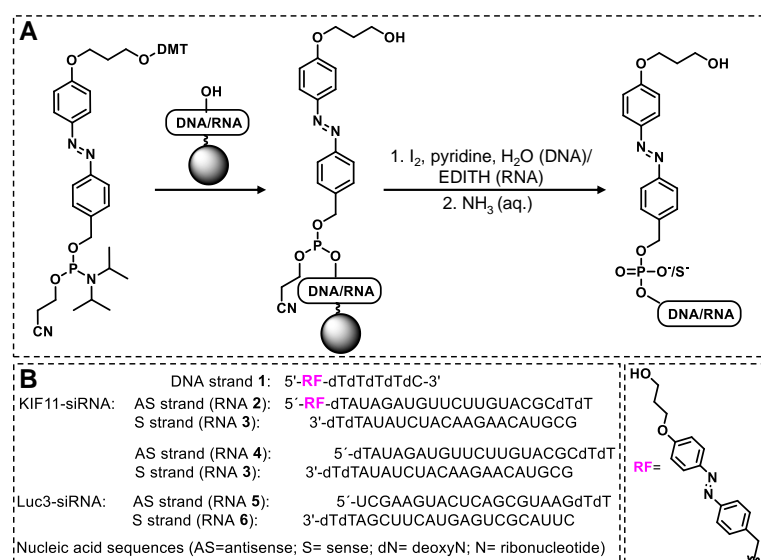


Figure 1. The state of the art in siRNA prodrugs. The 9-anthracenyl promoiety on the guide strand of the siRNA is cleaved by $^1\text{O}_2$ that is photogenerated on the passenger strand upon red light irradiation. The $^1\text{O}_2$, as well as the anthraquinone side product, is potentially harmful to the cells and the surrounding tissue. In this work, we report on an improved siRNA prodrug, which does not require $^1\text{O}_2$ for the activation: it is activated upon red light-induced electron transfer in the presence of photosensitizer SnPPA.

In preliminary tests, an RF-DNA model strand (DNA 1) was synthesized, characterized, and its stability in the presence of various potentially reactive molecules found in the intracellular environment (H_2O_2 , NaSH, KO_2 , and sodium ascorbate) was confirmed. In contrast, we observed that DNA 1 is indeed activated upon irradiation with red light in the presence of photosensitizer SnPPA and ascorbate as an electron source. Next, the RF-RNA guide strand (RNA 2) was synthesized and its similarity to DNA 1's behavior was confirmed in cell-free settings. Finally, the corresponding siRNA prodrug (RNA 2/3) was assembled. As a gene target, *KIF11* was chosen because it is an essential gene for mitosis that is overexpressed in some cancers, making it a promising target for cancer treat-

ment [17]. However, it is an essential gene expressed in many organs [18], which makes it necessary to activate the inhibition of siRNA specifically in cancer cells to achieve the favorable therapeutic effect. We investigated the RNAi efficiency of the siRNA prodrug in human ovarian carcinoma cells A2780 by reverse-transcription quantitative PCR (RT-qPCR) in the presence and absence of the photosensitizer SnPPA, showing selective activation and good knockdown efficiency upon irradiation with red light.



Scheme 1. (A) Synthesis scheme of DNA 1/RNA 2 by solid-phase synthesis. While the 5' P(III) of DNA 1 was oxidized by I_2 , pyridine in H_2O , the 5' P(III) of RNA 2 was oxidized with 3-ethoxy-1,2,4-thiazoline-5-one (EDITH), giving rise to the phosphodiester and the phosphorothioate, respectively. (B) Structure of promoiety RF and sequences of DNA/RNAs used in this work.

2. Results

2.1. Design, Synthesis, and Characterization of DNA 1 and RNA 2

The RF-phosphoramidite (Scheme S1) was synthesized as described earlier [16] and applied for the solid-phase synthesis of model strand DNA 1 using commercially available standard DNA phosphoramidites (Schemes 1 and S2, Supporting Information (further SI)). The analytical HPLC profile of the crude synthesis mixture indicates that the overall yield is higher than 50% and is shown in Figure 2A. The purification of the DNA by reversed-phase chromatography gives rise to the analytically pure product as confirmed by HPLC (Figure 2B). We identified the obtained product by MALDI-TOF-MS. In particular, we observed two peaks eluted after 18 min and 25 min with the identical mass of 1791 Da (Figure 2C,D) that correspond to the expected brutto formula of DNA 1 (calculated for $C_{65}H_{82}N_{13}O_{37}P_5 [M - H^+]^-$: $m/z = 1791$ Da). We calibrated MALDI-TOF-MS by using an external standard, which gives rise to an accuracy of determination in $m/z = 0.1\%$ of the detected mass (e.g., for a peak with $m/z = 1791$ Da, the expected deviation would be ± 1.8 Da). Thus, the product is a mixture of two isomers corresponding to the *cis* and the *trans* forms of the azobenzene-DNA.

We prepared the RNA part of the RF-RNA strand 2 (Schemes 1 and S3) by solid-phase RNA synthesis using commercially available dioxo-thiomorpholine (TC) RNA phosphoramidites according to the manufacturer's recommendations. We conducted the coupling of the azobenzene phosphoramidite RF analogously to DNA 1 synthesis, except that we performed the oxidation step with 3-ethoxy-1,2,4-thiazoline-5-one (EDITH) to yield the corresponding phosphorothioate. This modification was utilized, as it shows improved stability towards unspecific phosphatases in cells. The characterization (analytical HPLC and MALDI-TOF-MS spectra) is shown in Figure 2E,F. As expected, again two distinct peaks with identical mass were observed (calculated for $C_{216}H_{266}N_{71}O_{152}P_{21}S [M - H^+]^-$:

$m/z = 6970$ Da; found: $m/z = 6971$ Da), corresponding to the *cis* and the *trans* isomers of RNA 2. The sense-strand RNA 3, the unmodified *KIF11* RNA antisense strand RNA 4, and the RNA strands for a control (scrambled) siRNA without any cellular target (RNA 5 and RNA 6) were custom-made by Sigma Aldrich (Scheme 1). We annealed the RNA strands via temperature gradient (from 90 °C for 15 min to 22 °C in 45 min) in the presence of high salt concentrations (500 mM NaCl) and ethylenediaminetetraacetic acid (EDTA, 10 mM).

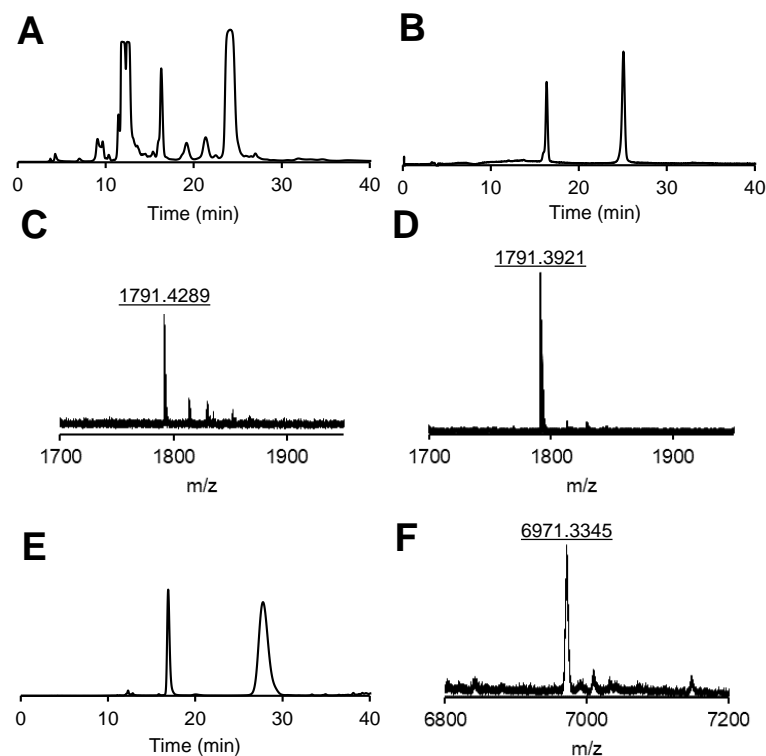


Figure 2. Crude (A) and analytical (B) HPLC profile of DNA 1 and MALDI-TOF-MS spectra of the peaks in (B) eluted after 18 min (C) and 25 min (D). Analytical HPLC of RNA 2 (E) and corresponding MALDI-TOF-MS spectra of the peak eluted after 28 min (F). Reversed-phase HPLC was performed with a gradient of solution B (ACN) in solution A (TEAA buffer, 150 mM, 5% ACN, pH 7.4): From 0 to 10 min to 15% B until 15 min; from 15 to 20 min to 20% B until 35 min (DNA 1) and from 0 to 10 min to 15% B until 20 min, then from 20 to 40 min to 30% B (RNA 2) by monitoring the absorbance at 260 nm.

2.2. *Cis–Trans* Isomerization of DNA 1 and Its Photoreduction

To investigate the *cis–trans* isomerization of DNA 1 (Figure 3A) and to further prove the identity of the two elution peaks in the HPLC profile, a UV-vis spectrum of DNA 1 was recorded before and after irradiation with 365 nm for 1 min (Figure 3B). As expected, the absorbance at 365 nm, which is characteristic of the *trans* isomer, decreases upon irradiation, while the absorbance at 440 nm, characteristic of the *cis* isomer, increases. In the HPLC profile, light irradiation shifts the equilibrium toward the peak that is eluted first (compare Figure 3C,D), indicating that this peak corresponds to the *cis* isomer. Already five minutes after the irradiation, the equilibrium shifts nearly completely back to the initial state (Figure 3E).

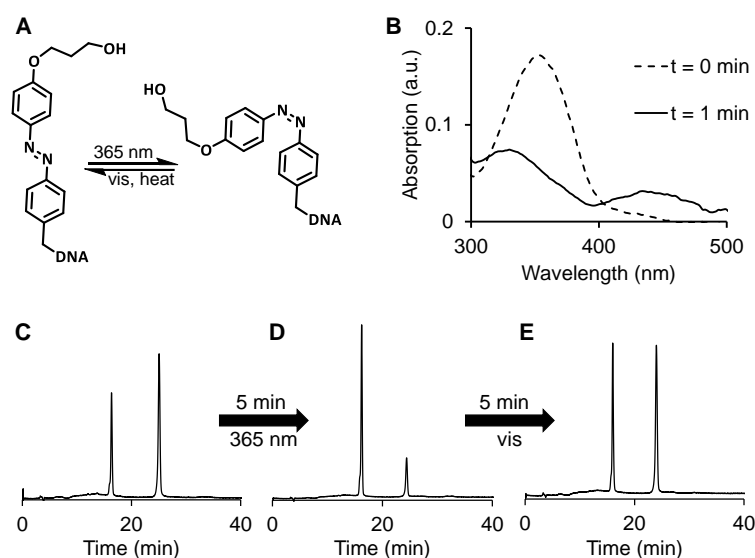


Figure 3. Cis-trans isomerization of DNA **1** (A) as observed by UV vis absorbance (B) before and after 1 min irradiation at 365 nm. HPLC profile (absorbance at 260 nm) of DNA **1** before (C) and after (D) 5 min irradiation at 365 nm and after an additional 5 min at room light (E), using a gradient of solution B (ACN) in solution A (TEAA buffer, 150 mM, 5% ACN, pH 7.4): From 0 to 10 min to 15% B until 15 min; from 15 to 20 min to 20% B until 35 min.

To investigate the cleavage of DNA **1** by photoreduction, we incubated DNA **1** with sodium ascorbate in the presence (“sample”) or absence (“blank”) of photosensitizer SnPPA. The photosensitizer was selected as a catalyst of photoreduction based on our previously published study (synthesis as described in [16], for MS spectra, see Figure S1, SI). The samples were either irradiated with red light (660 nm) (+ $h\nu$) or kept in the dark (− $h\nu$), and the absorbance at 351 nm (characteristic of the more abundant *trans* isomer of DNA **1**, see Figure 3B) was recorded after 20 min and 40 min (Figure 4A). In the presence of the photosensitizer and red light, the bleaching of the azobenzene takes place as detected by the reduced absorbance. In contrast, in the absence of either light or a catalyst, no degradation of DNA **1** is detectable. These data confirm the first step of the mechanism of DNA **1** photoreduction outlined in Scheme 2.

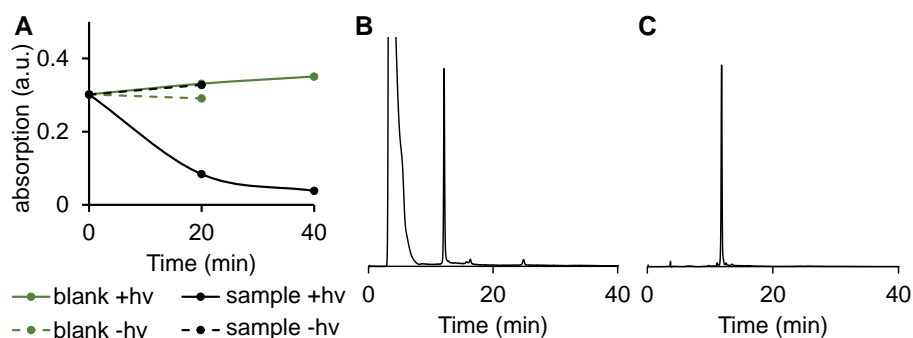
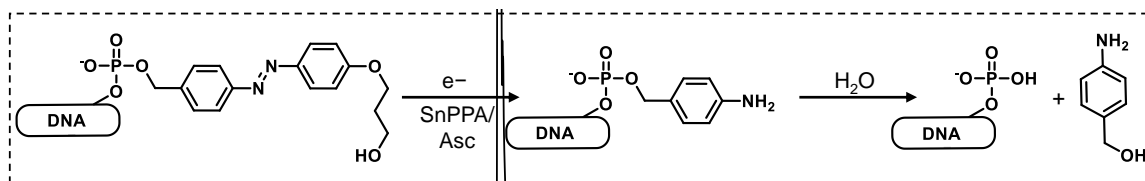


Figure 4. Photoreduction of DNA **1** in PBS (10 mM, 150 mM NaCl, 10 mM sodium ascorbate, pH 7.4) in the presence (“sample”) or absence (“blank”) of SnPPA (4 μ M). The mixtures were either irradiated with red light (+ $h\nu$) or kept in the dark (− $h\nu$). UV-vis absorbance at 351 nm was recorded after 20 and 40 min (A). HPLC profile of the 20 min irradiated sample containing SnPPA using a gradient of solution B (ACN) in solution A (TEAA buffer, 150 mM, 5% ACN, pH 7.4): From 0 to 10 min to 15% B until 15 min. From 15 to 20 min to 20% B until 35 min (B). All peaks were collected and analyzed by MALD-MS spectrometry (see Figure S2, SI). HPLC profile of 5'-phosphorylated DNA strand (C).



Scheme 2. Cleavage mechanism of DNA 1 upon irradiation with red light in the presence of SnPPA and ascorbate (Asc).

To identify the product(s) formed in the latter reaction, we subjected the sample after 40 min irradiation in the presence of SnPPA to HPLC. The corresponding profile (Figure 4B) shows one major peak (approximately 80% of eluted peaks after injection peak), that is eluted after 11.8 min. The corresponding MALDI-TOF-MS spectrum (Figure S3, SI) indeed shows the mass (calculated for $C_{49}H_{66}N_{11}O_{35}P_5$ $[M - H^+]^-$: $m/z = 1523$ Da, found: $m/z = 1524$ Da) of the expected 5'-phosphorylated DNA after azobenzene reduction and subsequent 1,6-elimination of para-quinone methide followed by its quenching with water with the formation of 4-hydroxymethylaniline (Scheme 2). As an additional control, we synthesized the 5'-phosphorylated DNA strand and subjected it to HPLC (Figure 4C), showing the same elution time (11.8 min) as the product of the photoreduction, further confirming the identity of the cleavage product.

2.3. DNA 1 Cleavage Selectivity and RNA 2 Photoreduction

To challenge the selectivity of RF cleavage by red-light-induced electron transfer, DNA 1 was incubated with biorelevant redox species, namely, H_2O_2 (200 mM), KO_2 (100 μ M), and NaSH (630 μ M), for 1 h. As shown in Figure 5A–D, no cleavage products could be detected under these conditions. Note that the large injection peak in B is caused by H_2O_2 light absorption. This proves the selectivity of RF cleavage by electron transfer, forming a solid foundation for applications in a biological context.

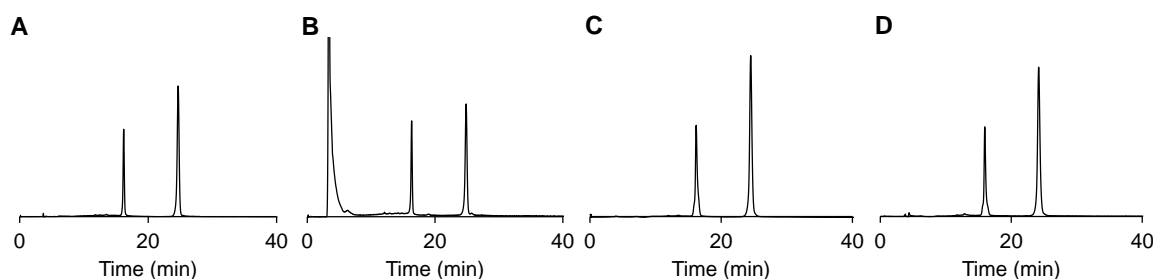


Figure 5. DNA 1 stability in PBS (10 mM, 150 mM NaCl pH 7.4) (A), in the presence of 200 mM H_2O_2 (B), KO_2 (100 μ M (1% DMSO)) (C), or NaSH (630 μ M) (D) after 1 incubation at 37 °C as analyzed by HPLC using a gradient solution B (ACN) in solution A (TEAA buffer, 150 mM, 5% ACN, pH 7.4): From 0 to 10 min to 15% B until 15 min; from 15 to 20 min to 20% B until 35 min.

To approach our goal of *in vitro* application, we repeated the cleavage experiments on an RNA level by incubation of RNA 2 with sodium ascorbate and the photosensitizer SnPPA in the absence or presence of red light. In the dark, no cleavage takes place (compare Figure 6A,B). However, upon irradiation, two major cleavage products could be detected (Figure 6C). The first one, eluted after 12 min, corresponds to the phosphorylated RNA strand (calculated for $C_{200}H_{250}N_{69}O_{151}P_{21}$ $[M - H^+]^-$: $m/z = 6685$ Da; found: $m/z = 6676$), according to the MALDI-TOF-MS spectra (Figure S3, SI). The second one, eluted 1 min later, corresponds to the thiophosphorylated RNA strand (calculated for $C_{200}H_{250}N_{69}O_{150}P_{21}S$ $[M - H^+]^-$: $m/z = 6701$ Da; found: $m/z = 6703$ Da). Both species would catalyze RNAi in a cellular context.

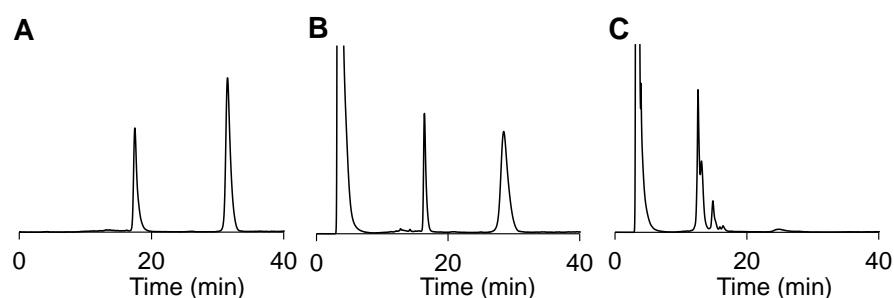


Figure 6. Photoreduction of RNA 2 in PBS buffer (10 mM, 150 mM NaCl, pH 7.4) containing sodium ascorbate (10 mM) and SnPPA (10 μ M) as observed by HPLC. The sample was either directly injected into HPLC (A), incubated in the dark (B), or irradiated with red light for 30 min (C). A gradient of solution B (ACN) in solution A (TEAA buffer, 150 mM, 5% ACN, pH 7.4), from 0 to 10 min to 15% B until 20 min, then from 20 to 40 min to 30% B, was used. HPLC fractions were analyzed by MALDI-TOF-MS (see Figure S3, SI).

2.4. Knockdown Efficacy of RNA 2/3

Encouraged by these results, we annealed RNA 2 with its corresponding passenger strand RNA 3 and formulated it with the standard commercially available transfection agent LipofectamineTM RNAiMAX for the transfection of A2780 cancer cells. As a target gene, we selected *KIF11*, a member of the kinesin-5 family, an essential enzyme for mitosis in most organisms. The inhibition of *KIF11* is reflected in the accumulation of cells in a G2 phase and an increase in the ratio of cell numbers in G2 and G1 states (G2/G1) [19]. We applied the unmodified *KIF11* siRNA 4/3 as a positive control and the scrambled siRNA 5/6 as a negative control. Upon completed transfection (14 h), we added the photosensitizer SnPPA. Then, 30 min later, all samples were irradiated with red light (660 nm) for 30 min. After an additional 23 h, the relative *KIF11* expression was quantified by RT-qPCR. The overall incubation time of the cells with the prodrug and controls was 38 h. It is expected that, upon light irradiation, the azobenzyl group at the 5' end of the antisense strand is cleaved, allowing the siRNA to be activated by the RNA-induced silencing complex (RISC) (Figure 7A). The siRNA antisense strand then serves as a template for the selective binding of mRNAs with the corresponding sequence (in this case: *KIF11*), followed by mRNA degradation. By RT-qPCR, the relative mRNA content of single genes can be quantified and normalized to that of a consecutively expressed housekeeping gene (in this case: GAPDH). As shown in Figure 7B, RNA 2/3, indeed, significantly decreased the *KIF11* mRNA concentration in the presence of the photosensitizer as compared to cells only treated with the photosensitizer ($p < 0.01$, unpaired Student's *t* test). In contrast, no significant RNAi could be observed in the absence of SnPPA. These results not only demonstrate the successful activation of RNA 2/3 in cells but also its selective on-demand activation in the presence of the photosensitizer SnPPA.

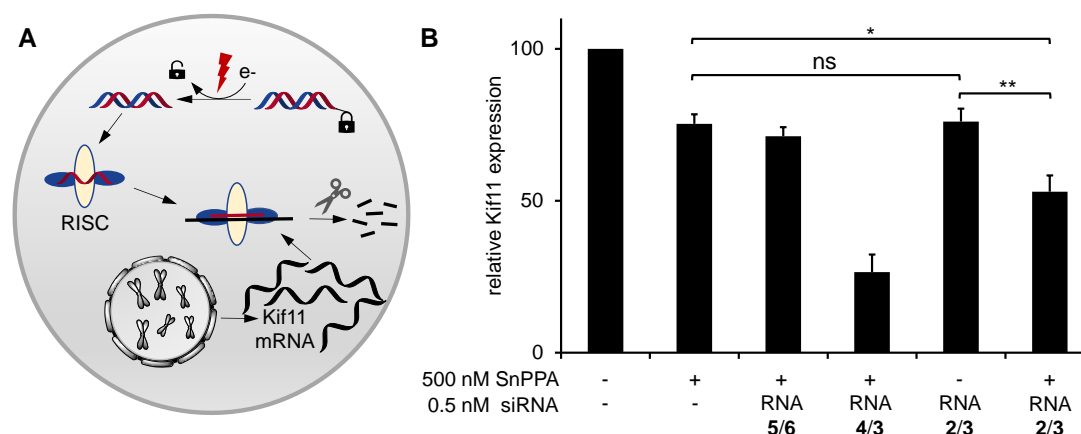


Figure 7. (A) After the photoreduction of the siRNA prodrug, the guide strand of the siRNA is uptaken into the RNA-induced silencing complex (RISC) to selectively cleave the complementary *KIF11* mRNA, resulting in reduced *KIF11* expression. (B) Relative *KIF11* mRNA concentrations of A2780 cells treated with 0.5 nM the unmodified *KIF11* siRNA 4/3 or the modified analog siRNA 2/3 for 38 h. As a negative control, siRNA 5/6, which has no target mRNA in the cells, was applied. After 14 h incubation, SnPPA (500 nM, 0.1% DMSO, end concentration) was added to the indicated samples and incubated for 30 min. All samples were irradiated for 30 min with red light, and subsequently incubation was continued in the dark. As a housekeeping gene, GAPDH was used. $2^{-\Delta Ct}$ values were calculated and normalized to those of untreated cells. Three independent experiments were performed. Error bars indicate standard deviation. An unpaired Student's *t*-test was performed for statistical analysis: * $p < 0.05$; ** $p < 0.01$; ns $p \geq 0.05$.

3. Materials and Methods

3.1. Synthesis of Modified Oligonucleotides

Automated oligonucleotide synthesis was performed on a 1 μ mol scale by using the standard ($3' \rightarrow 5'$) synthesis according to the recommendations of the manufacturer. For DNA synthesis, dC(bz) CPG (1000 Å, 28 μ mol/g) was used, and for RNA synthesis, dT CPG (1000 Å, 25–35 μ mol/g) was used. The phosphoramidite-carrying RF was coupled manually under argon atmosphere for 10 min. For this, the phosphoramidite in water-free acetonitrile (0.1 mL, 0.1 M) was mixed in the solid phase with a solution of ETT activator in acetonitrile (0.1 mL, 0.5 M). After oxidation with a standard iodine solution and DMT-deprotection, coupling was repeated. For RNA 2, oxidation was performed with 3-ethoxy-1,2,4-thiazoline-5-one (EDITH, 0.05 M, in acetonitrile) with 20 s oxidation time. The synthesized and chemically modified oligonucleotides were purified on reversed-phase HPLC with a gradient of solution B (ACN) in solution A (TEAA buffer, 150 mM, 5% ACN, pH 7.4). For DNA, a gradient from 0 to 10 min to 15% B until 15 min and then from 15 to 20 min to 20% B until 35 min was used. RNA was purified with a gradient from 0 to 10 min to 15% B until 20 min, then from 20 to 40 min to 30% B. Concentrations of modified and non-modified RNAs and DNAs were determined by measuring the absorption at 260 nm. Annealing of RNA/DNA strands (10 μ M each strand) was performed in Tris buffer (100 mM Tris, pH 7.8, 500 mM NaCl, and 10 mM EDTA) by heating the mixture to 90 °C for 15 min and cooling it by 3 °C per 2 min to 22 °C.

3.2. Cis-Trans Isomerization of DNA 1

UV-vis absorbance of DNA 1 (15 μ M) in PBS (10 mM, 150 mM NaCl, pH 7.4) was measured before ($t = 0$ min) and after irradiation with 365 nm light for 1 min (Figure 3B). In addition, DNA 1 (20 μ M) in PBS (10 mM, 150 mM NaCl, pH 7.4) was injected into HPLC before (Figure 2C) and after 5 min irradiation at 365 nm (Figure 3D) and after 5 min irradiation with 365 nm plus an additional 5 min incubation (Figure 3E) using a gradient of solution B (ACN) in solution A (TEAA buffer, 150 mM, 5% ACN, pH 7.4): From 0 to 10 min to 15% B until 15 min. From 15 to 20 min to 20% B until 35 min.

3.3. DNA 1 Cleavage by Red-Light-Induced Photoreduction

DNA 1 (50 μ M) was dissolved in PBS (10 mM, 150 mM NaCl, 10 mM sodium ascorbate, pH 7.4) in the presence or absence of SnPPA (4 μ M) (for synthesis and structure see [16]). The mixtures were either irradiated (+hv) or kept in the dark (−hv) and UV-Vis spectra were recorded after 20 and 40 min (351 nm) (Figure 4A). The 20 min irradiated sample containing SnPPA was additionally injected into HPLC using a gradient of solution B (ACN) in solution A (TEAA buffer, 150 mM, 5% ACN, pH 7.4): From 0 to 10 min to 15% B until 15 min. From 15 to 20 min to 20% B until 35 min (Figure 4B). All peaks were collected and analyzed by MALD-MS spectrometry (see SI, Figure S2). The HPLC profile was compared to that of the unmodified DNA strand (Figure 4C).

3.4. Stability in Presence of Oxidizing/Reducing Agents

DNA 1 (75 μ M) was dissolved in PBS (10 mM, 150 mM NaCl pH 7.4) (Figure 5A) in presence of 200 mM H₂O₂ (Figure 5B), in presence of KO₂ (100 μ M (1% DMSO)) (Figure 5C), or in presence of NaSH (630 μ M) (Figure 5D) and incubated for 1 h at 37 °C. Solutions were injected to reversed-phase HPLC using a gradient solution B (ACN) in solution A (TEAA buffer, 150 mM, 5% ACN, pH 7.4): From 0 to 10 min to 15% B until 15 min. From 15 to 20 min to 20% B until 35 min.

3.5. RNA 2 Cleavage by Red-Light-Induced Photoreduction

RNA 2 (50 μ M) was dissolved in PBS buffer (10 mM, 150 mM NaCl, pH 7.4) containing sodium ascorbate (10 mM) and SnPPA (10 μ M) and directly injected into HPLC (Figure 6A) or kept in the dark (−hv) (Figure 6B) or irradiated with red light for 30 min at 23 °C (Figure 6C) and subsequently injected into HPLC using a gradient solution B (ACN) in solution A (TEAA buffer, 150 mM, 5% ACN, pH 7.4): from 0 to 10 min to 15% B until 20 min, then from 20 to 40 min to 30% B. HPLC fractions were analyzed by MALDI-TOF-MS (see Figure S3, SI)

3.6. Transfection

A2780 were seeded in 6-well plates (100 cells/ μ L, 2 mL RPMI 1640, containing FBS (5%), penicillin/streptomycin (1%), and L-Glutamine (1%) per well). For the transfection, 1 pmol (for 0.5 nM end concentration) siRNA in biograde water (10 μ L) was diluted with Gibco™ Opti-MEM™ Reduced Serum Media (Opti-MEM) (40 μ L). In addition, Lipofectamine™ RNAiMAX (1.5 μ L) was diluted in Opti-MEM (48.5 μ L) and incubated for 5 min at 22 °C before both solutions were combined. The transfection solution was then incubated for 20 min at 23 °C with recurring shaking every 5 min. The cells were washed with PBS (2.5 mL per well) and a fresh portion of RPMI 1640 medium (1.9 mL per well) containing FBS (5%), penicillin/streptomycin (1%), and L-Glutamine (1%) was added. Finally, the 100 μ L transfection solution was added to the cells. The samples were incubated for 14 h.

3.7. Relative Gene Expression Quantification by RT-qPCR

SnPPA (500 nM, 0.1% DMSO) was added to the cells. As a control, to one of the siRNA 2/3-treated sample, no SnPPA was added. The samples were incubated for 30 min in the dark, and subsequently irradiated for 30 min with a red LED lamp consisting of eighteen 2-watt super-bright red LEDs (λ = 660 nm, Flux = 1086 lm, efficacy: 56.6 lm/w; half width at half maximum = 26.4 nm; distance to samples = 30 cm). The samples were incubated for 23 h in the dark. To isolate total RNA from cells, the cultivation medium was removed, the cells were washed with PBS, and TRI reagent® (1 mL/well) was added for lysis. After 5 min incubation at 22 °C, the cell lysate was transferred into 1.5 mL Eppendorf tubes, and the aqueous phase of the samples was extracted by adding chloroform (200 μ L, 4 °C) followed by thorough mixing and centrifugation (12,000 \times g, 4 °C, 15 min). The aqueous phase was mixed with ethanol (400 μ L, 4 °C) and transferred onto Zymo-Spin IC Columns. The samples were subsequently centrifuged (1 min, 8000 \times g, 4 °C). The eluate was discarded.

The RNA on the column was washed first with sodium acetate buffer (3 M, 500 μ L, 4 $^{\circ}$ C, pH = 5.2) and secondly with ethanol (500 μ L, 75%, *v/v*, in water, 4 $^{\circ}$ C), in three steps: solvent addition, subsequent centrifugation as above, and eluate removal. Finally, pure ethanol (500 μ L, 4 $^{\circ}$ C) was added and the samples were centrifuged (3 min, 10,000 \times *g*, 4 $^{\circ}$ C) to dry the column. The RNA was eluted by adding RNase-free water (25 μ L), followed by incubation for 5 min at 22 $^{\circ}$ C, and subsequent centrifugation (2 min, 8000 \times *g*, 4 $^{\circ}$ C). To transcribe the isolated RNA into cDNA, RNA (1 μ g in 12.5 μ L RNase-free water) was incubated (65 $^{\circ}$ C for 5 min) with random hexamer primer (1 μ L). Subsequently, reverse transcriptase (0.5 μ L), RT 5 \times buffer (4 μ L), and dNTPs (2 μ L) were added per sample. Finally, the reverse-transcription protocol (10 min at 25 $^{\circ}$ C; 60 min at 42 $^{\circ}$ C; 10 min at 70 $^{\circ}$ C; forever at 4 $^{\circ}$ C) was run at the Dual Block Gradient PCR Thermal Cycler. For the relative quantification of the genes of interest, LightCycler[®] 480 SYBR[®] Green Master (5 μ L) (Roche Diagnostics Deutschland GmbH, Mannheim, Germany) was mixed with a primer pair (1 μ L) and cDNA (4 μ L, 1:10 diluted) and subjected to the LightCycler[®] 480 (Roche Diagnostics Deutschland GmbH, Mannheim, Germany). The applied primer sequences were CAGCTGAAAAGGAAACAGCC; ATGAACAATCCACACCAGCA for *KIF11* and CTCACCACCATGGAGGAGGC; GGCATGGACTGTGGTCATGAG for the housekeeping gene GAPDH. The reaction mixtures were initially heated at 95 $^{\circ}$ C for 5 min, followed by 45 cycles, which consisted of 10 s at 95 $^{\circ}$ C, 30 s 60 $^{\circ}$ C, and 10 s at 72 $^{\circ}$ C. The Ct value of the *KIF11* cDNA amplification of each sample was subtracted by the Ct value of the GAPDH cDNA amplification of the same sample (Δ Ct). For the evaluation of the fold change, the $2^{-\Delta$ Ct} value was calculated. The $2^{-\Delta$ Ct} value of untreated cells was set to 100. Three independent experiments were performed and the mean \pm standard deviation were calculated and are shown in Figure 7.

3.8. Statistical Analysis of Data

For statistical analysis of data, an unpaired Student's *t*-test was performed using GraphPad Prism Software: * $p < 0.05$; ** $p < 0.01$. Difference between experimental average values, for which $p \geq 0.05$, were considered to be statistically not significant (ns).

4. Conclusions

In this study, we present electron-rich azobenzene "RF" as a suitable promoiety for the design of siRNAs activated under reductive conditions upon irradiation with red light. This can be achieved in the presence of SnPPA acting as a photocatalyst mediating the transfer of electrons from intracellular electron sources (e.g., ascorbate) to the azobenzene. In particular, the RF-based prodrug is not reduced either in the dark or upon irradiation with red light in the presence of bioavailable redox species such as H₂O₂, NaSH, KO₂, or ascorbate if SnPPA is not present. We first characterized the promoiety on a DNA model strand in cell-free settings and then successfully synthesized and characterized an RF-carrying RNA strand. Finally, we transferred the concept into cells, by application of an RF-siRNA prodrug, which was transfected with a standard transfection agent into ovarian carcinoma cells (A2780). We also showed that, in cells, the siRNA is selectively activated upon red light irradiation in the presence of the photosensitizer SnPPA inducing *KIF11* knockdown. With this siRNA prodrug approach, we avoid the formation of toxic metabolites such as ¹O₂ and anthraquinone, making this concept superior to the previously published one. The RNAi is triggered by biologically tolerated red light, due to the application of the catalyst SnPPA, which uses naturally abundant metabolites, such as ascorbic acid, as electron sources. Presumably, the promoiety described here can be easily attached to any siRNA sequence by the presented synthesis route and the resulting prodrug can be formulated with standard transfection reagents, making this approach a versatile tool to improve siRNA selectivity.

Supplementary Materials: The following supporting information can be downloaded at <https://www.mdpi.com/article/10.3390/molecules28104204/s1>, with details about applied chemicals and instruments, Scheme S1: Structure of DMT-RF-carrying phosphoramidite, Scheme S2: Structure of DNA 1, Scheme S3: Structure of RNA 2, Figure S1: High-resolution mass spectrum of SnPPA,

Figure S2: MALDI-TOF-MS spectra of DNA 1 stability test, Figure S3: MALDI-TOF-MS spectra of DNA 1 cleavage experiments, details about cells and cell culture.

Author Contributions: Conceptualization, A.M.; methodology, J.R. and I.K.; synthesis, J.R.; Analytics, J.R.; cell experiments, I.K.; writing—original draft preparation, I.K.; writing—review and editing, A.M.; visualization, I.K.; supervision, A.M.; funding acquisition, A.M. All authors have read and agreed to the published version of the manuscript.

Funding: This research was funded by the joint program of German Research Council (DFG, project 1419/11-1).

Data Availability Statement: Data is contained within the article and the Supplementary Material.

Acknowledgments: We thank Subrata Dutta for the synthesis of SnPPA.

Conflicts of Interest: The authors declare no conflict of interest.

Sample Availability: Not applicable.

References

1. Scott, L.J. Givosiran: First Approval. *Drugs* **2020**, *80*, 335–339. [CrossRef] [PubMed]
2. Scott, L.J.; Keam, S.J. Lumasiran: First Approval. *Drugs* **2021**, *81*, 277–282. [CrossRef] [PubMed]
3. Wood, H. FDA approves patisiran to treat hereditary transthyretin amyloidosis. *Nat. Rev. Neurol.* **2018**, *14*, 570. [CrossRef] [PubMed]
4. Lamb, Y.N. Inclisiran: First Approval. *Drugs* **2021**, *81*, 389–395. [CrossRef] [PubMed]
5. Keam, S.J. Vutrisiran: First Approval. *Drugs* **2022**, *82*, 1419–1425. [CrossRef] [PubMed]
6. Han, S.P.; Scherer, L.; Gethers, M.; Salvador, A.M.; Salah, M.B.H.; Mancusi, R.; Sagar, S.; Hu, R.; DeRogatis, J.; Kuo, Y.H.; et al. Programmable siRNA pro-drugs that activate RNAi activity in response to specific cellular RNA biomarkers. *Mol. Ther. Nucleic Acids* **2022**, *27*, 797–809. [CrossRef] [PubMed]
7. Hayashi, J.; Nishigaki, M.; Ochi, Y.; Wada, S.I.; Wada, F.; Nakagawa, O.; Obika, S.; Harada-Shiba, M.; Urata, H. Effective gene silencing activity of prodrug-type 2'-O-methyldithiomethyl siRNA compared with non-prodrug-type 2'-O-methyl siRNA. *Bioorg. Med. Chem. Lett.* **2018**, *28*, 2171–2174. [CrossRef] [PubMed]
8. Mikat, V.; Heckel, A. Light-dependent RNA interference with nucleobase-caged siRNAs. *RNA* **2007**, *13*, 2341–2347. [CrossRef] [PubMed]
9. Rühle, J.; Klemm, I.; Abakumova, T.; Sergeeva, O.; Vetosheva, P.; Zatsepin, T.; Mokhir, A. Reactive oxygen species-responsive RNA interference. *Chem. Commun.* **2022**, *58*, 4388–4391. [CrossRef] [PubMed]
10. Antunes, F.; Cadenas, E. Estimation of H₂O₂ gradients across biomembranes. *FEBS Lett.* **2000**, *475*, 121–126. [CrossRef] [PubMed]
11. Rybak, C.J.; Andjaba, J.M.; Fan, C.; Zeller, M.; Uyeda, C. Dinickel-Catalyzed N=N Bond Rotation. *Inorg. Chem.* **2023**, *62*, 5886–5891. [CrossRef] [PubMed]
12. Johnson, T.G.; Sadeghi-Kelishadi, A.; Langton, M.J. A Photo-responsive Transmembrane Anion Transporter Relay. *J. Am. Chem. Soc.* **2022**, *144*, 10455–10461. [CrossRef] [PubMed]
13. Samanta, S.; Beharry, A.A.; Sadowski, O.; McCormick, T.M.; Babalhavaeji, A.; Tropepe, V.; Woolley, G.A. Photoswitching azo compounds in vivo with red light. *J. Am. Chem. Soc.* **2013**, *135*, 9777–9784. [CrossRef] [PubMed]
14. Tian, X.; Li, Z.; Sun, Y.; Wang, P.; Ma, H. Near-Infrared Fluorescent Probes for Hypoxia Detection via Joint Regulated Enzymes: Design, Synthesis, and Application in Living Cells and Mice. *Anal. Chem.* **2018**, *90*, 13759–13766. [CrossRef] [PubMed]
15. Guisán-Ceinos, S.; Rivero, A.R.; Romeo-Gella, F.; Simón-Fuente, S.; Gómez-Pastor, S.; Calvo, N.; Orrego, A.H.; Guisán, J.M.; Corral, I.; Sanz-Rodríguez, F.; et al. Turn-on Fluorescent Biosensors for Imaging Hypoxia-like Conditions in Living Cells. *J. Am. Chem. Soc.* **2022**, *144*, 8185–8193. [CrossRef] [PubMed]
16. Dutta, S.; Rühle, J.; Schikora, M.; Deussner-Helfmann, N.; Heilemann, M.; Zatsepin, T.; Duchstein, P.; Zahn, D.; Knör, G.; Mokhir, A. Red light-triggered photoreduction on a nucleic acid template. *Chem. Commun.* **2020**, *56*, 10026–10029. [CrossRef] [PubMed]
17. Jiang, M.; Zhuang, H.; Xia, R.; Gan, L.; Wu, Y.; Ma, J.; Sun, Y.; Zhuang, Z. KIF11 is required for proliferation and self-renewal of docetaxel resistant triple negative breast cancer cells. *Oncotarget* **2017**, *8*, 92106–92118. [CrossRef] [PubMed]
18. Kinesin Family Member 11 [Homo sapiens (Human)]. Available online: <https://www.ncbi.nlm.nih.gov/gene/3832> (accessed on 14 April 2023).
19. Meyer, A.; Mokhir, A. RNA Interference Controlled by Light of Variable Wavelength. *Angew. Chem. Int. Ed.* **2014**, *53*, 12840–12843. [CrossRef] [PubMed]

Disclaimer/Publisher's Note: The statements, opinions and data contained in all publications are solely those of the individual author(s) and contributor(s) and not of MDPI and/or the editor(s). MDPI and/or the editor(s) disclaim responsibility for any injury to people or property resulting from any ideas, methods, instructions or products referred to in the content.

Publication 6:

An Endoplasmic Reticulum Specific Pro-amplifier of Reactive Oxygen Species in Cancer Cells

Hong-Gui Xu,^[a] Margot Schikora,^[a] Miroslav Sisa,^[a] Steffen Daum,^[a] Insa Klemt,^[a] Christina Janko,^[b] Christoph Alexiou,^[b] Galyna Bila,^[c] Rostyslav Bilyy,^[c] Wenjie Gong,^[d] Michael Schmitt,^[d] Leopold Sellner,^[d] Andriy Mokhir,^[a]

^[a] Department of Chemistry and Pharmacy, Organic Chemistry II, Friedrich-Alexander-Universität Erlangen-Nürnberg, Nikolaus-Fiebiger-Str. 10, 91058 Erlangen, Germany

^[b] Else Kröner-Fresenius-Stiftung-Professorship, Department of Otorhinolaryngology, Head and Neck Surgery Section of Experimental Oncology and Nanomedicine (SEON), Universitätsklinikum Erlangen, Glücksstraße 10a, 91054 Erlangen, Germany

^[c] Danylo Halytsky Lviv National Medical University, Pekarska str. 69, 79010 Lviv (Ukraine)

^[d] Department of Medicine V, Heidelberg University Hospital, Im Neuenheimer Feld 410, 69120 Heidelberg, Germany

Contribution of I. Klemt:

Design and performance of confocal microscopy, qPCR assay and cellular experiments on SBLF9. Manuscript proof reading.

The publication and supporting information are found under: DOI: [10.1002/anie.202100054](https://doi.org/10.1002/anie.202100054).

Prodrugs

How to cite: *Angew. Chem. Int. Ed.* **2021**, *60*, 11158–11162

International Edition: doi.org/10.1002/anie.202100054

German Edition: doi.org/10.1002/ange.202100054

An Endoplasmic Reticulum Specific Pro-amplifier of Reactive Oxygen Species in Cancer Cells

Hong-Gui Xu, Margot Schikora, Miroslav Sisa, Steffen Daum, Insa Klemt, Christina Janko, Christoph Alexiou, Galyna Bila, Rostyslav Bilyy, Wenjie Gong, Michael Schmitt, Leopold Sellner, and Andriy Mokhir*

Abstract: The folding and export of proteins and hydrolysis of unfolded proteins are disbalanced in the endoplasmic reticulum (ER) of cancer cells, leading to so-called ER stress. Agents further augmenting this effect are used as anticancer drugs including clinically approved proteasome inhibitors bortezomib and carfilzomib. However, these drugs can affect normal cells, which also rely strongly on ER functions, leading, for example, to accumulation of reactive oxygen species (ROS). To address this problem, we have developed ER-targeted prodrugs activated only in cancer cells in the presence of elevated ROS amounts. These compounds are conjugates of cholic acid with N-alkylaminoferrrocene-based prodrugs. We confirmed their accumulation in the ER of cancer cells, their anticancer efficacy, and cancer cell specificity. These prodrugs induce ER stress, attenuate mitochondrial membrane potential, and generate mitochondrial ROS leading to cell death via necrosis. We also demonstrated that the new prodrugs are activated in vivo in Nemeth-Kellner lymphoma (NK/Ly) murine model.

According to estimation of European Cancer Information System (ECIS) in the European Union 1.3 millions of people will die from cancer and over 2.7 million of new cases (excluding non-melanoma skin cancer) will be diagnosed in 2020.^[1] Treatment of this disease is complicated, since cancer and normal cells are related and, correspondingly, precise targeting/killing of the former cells without affecting of the latter ones is a challenging and not yet fully solved problem. In particular, currently available, clinically approved chemo-

therapeutics exhibit dose-limiting side effects, which adversely and sometimes irreversibly affect the quality of life of patients.^[2] Cancer cells can be addressed specifically by making use of their unique features, for example, the presence of some overexpressed receptors,^[3] altered glycolysis,^[4] and elevated amounts of reactive oxygen species (ROS = H₂O₂, O₂^{•-} and HO[•]).^[5,6] The endoplasmic reticulum (ER) has been recognized as an especially attractive target due to the following reasons.^[7] In cancer cells the balance between folding/transport of proteins and degradation of misfolded proteins is disturbed that leads to the so called ER stress. Further potentiation of the stress by chemical agents induces cancer cell death, whereas normal cells initially lacking the ER stress withstand the drug effect. Though some cancer cell selectivity can be achieved, side effects are also expected. They include, but not limited to induction of moderate ER stress in normal cells leading to unfolded protein response (UPR), elevation of intracellular amounts of ROS and disbalance of Ca²⁺ homeostasis. All these factors contribute to genome instability that stimulate carcinogenesis.^[8]

Herein we addressed this problem by the development of ER targeting prodrugs **4a-g**, which are activated only in cancer cells, but remain inactive in normal cells (Scheme 1, Scheme 2). These compounds are based on N-substituted aminoferrrocene (AF) drugs. After their formation in cells these drugs cycle between reduced (AF) and oxidized (AF⁺) forms catalyzing the formation of highly reactive ROS O₂^{•-} (from O₂) and HO[•] (from H₂O₂) that leads to cell death.^[9]

[*] M. Sc. H.-G. Xu, M. Sc. M. Schikora, Dr. M. Sisa, Dr. S. Daum, M. Sc. I. Klemt, Prof. Dr. A. Mokhir
Friedrich-Alexander University Erlangen-Nürnberg (FAU)
Department of Chemistry and Pharmacy
Organic Chemistry Chair II
Nikolaus-Fiebiger-Str. 10, 91058 Erlangen (Germany)
E-mail: Andriy.Mokhir@fau.de

Dr. M. Sisa
Institute of Experimental Botany AS CR
Prague (Czech Republic)

Dr. C. Janko, Prof. Dr. C. Alexiou
Else Kröner-Fresenius-Stiftung-Professorship
Department of Otorhinolaryngology, Head and Neck Surgery
Section of Experimental Oncology and Nanomedicine (SEON)
Universitätsklinikum Erlangen
Glückstraße 10a, 91054 Erlangen (Germany)

M. Sc. G. Bila, Prof. Dr. R. Bilyy
Danylo Halytsky Lviv National Medical University
Pekarska str. 69, 79010 Lviv (Ukraine)

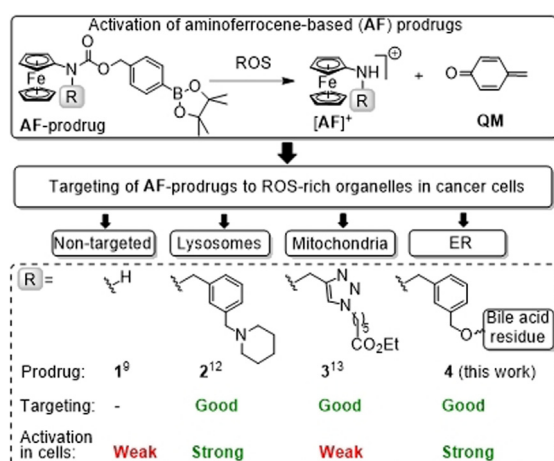
Dr. W. Gong, Prof. Dr. M. Schmitt, Dr. L. Sellner
Department of Medicine V, Heidelberg University Hospital
Im Neuenheimer Feld 410, 69120 Heidelberg (Germany)

Dr. W. Gong
Hematology Department
First Affiliated Hospital of Soochow University, Suzhou (China)

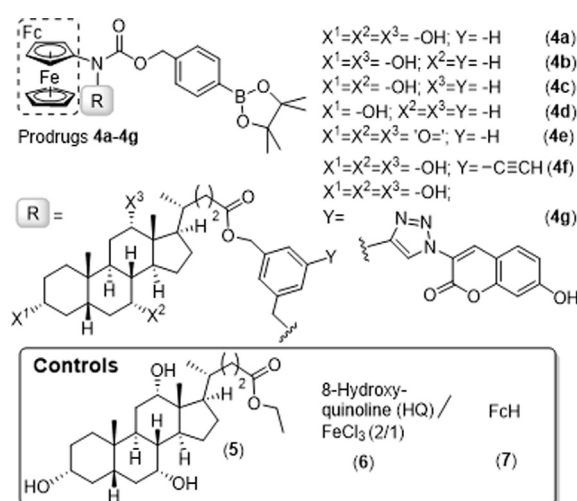
Dr. L. Sellner
Takeda Pharma Vertrieb GmbH & Co. KG
Jägerstr. 27, 1017 Berlin (Germany)

Supporting information and the ORCID identification number for one of the authors of this article can be found under: <https://doi.org/10.1002/anie.202100054>.

© 2021 The Authors. Angewandte Chemie International Edition published by Wiley-VCH GmbH. This is an open access article under the terms of the Creative Commons Attribution Non-Commercial NoDerivs License, which permits use and distribution in any medium, provided the original work is properly cited, the use is non-commercial and no modifications or adaptations are made.



Scheme 1. The mechanism of activation of AF-based prodrugs and state-of-the-art in the targeting of these prodrugs to organelles in cancer cells.



Scheme 2. Structures of AF prodrugs targeting ER (**4a–g**) and control compounds.

These and other ferrocene-based biologically active compounds were described in several recent reviews.^[10] The AFs are protected in prodrugs **4** with a 4-(carbonyloxymethyl)-phenylboronic acid pinacol ester group.^[9] The latter group is labile under oxidative conditions and was, therefore, expected to be cleaved especially well within the ER of cancer cells, which is known to have more oxidative environment than the cytoplasm.^[11]

Our research group has substantial experience with AF-based prodrugs. We have previously investigated their mode of action^[9,12] and developed compounds targeting lysosomes (LY)^[13] and mitochondria (Mit)^[14] in cancer cells (Scheme 1). However, ER specific AF-prodrugs were not available before this work. P. Cloetens, G. Jaouen and S. Bohic have recently reported on anticancer osmocenyl-tamoxifen prodrugs, which are accumulated in endomembrane system of breast cancer MDA-MB-231 cells including, apart from ER, nuclear envelope, endosomes and lysosomes.^[15] Another example of an ER-targeting prodrug is disulfiram. Its mode of action

relies on the activation by binding of Cu ions in cells. Apart from inducing ER stress via proteasome inhibition and ROS production,^[16] it affects other targets including inhibition of aldehyde dehydrogenase (ALDH) and the STAT3 signaling pathway,^[17] modulation of DNA-topoisomerases and methyltransferases as well as glutathione S-transferase.^[18] Thus, the known anticancer prodrugs are not ER specific.

Previously reported ER-carriers are usually hydrophobic structures, for example, cyanine dye DiOC6, hexyl rhodamine B, polyethylene glycol (PEG), long alkyl chains, derivatives of p-methylphenylsulfonamides.^[19] Since water solubility of AF-prodrugs is limited ($\leq 50 \mu\text{M}$),^[9,12–14] their further modification with the known ER-carriers would with high probability lead to non-soluble in water compounds. Therefore, we searched for alternative modifiers. We selected bile acids, since along with their hydrophobic core, they carry polar groups (alcohol or carbonyl), which could provide for water solubility. To find the best modifier, we introduced a series of bile acid fragments (substituent R, Scheme 2) to obtain prodrugs **4a–4e** as described in the supporting information (SI). We were pleased to observe that all prepared prodrugs are soluble at least up to $50 \mu\text{M}$ in aqueous solution (Table S1, SI). All prodrugs affect the viability of Burkitt's lymphoma BL-2 cells (Table S2, SI), selected as a representative cancer cell line. Derivatives of cholic (**4a**, $IC_{50} = 9 \pm 2 \mu\text{M}$) and dehydrocholic acid (**4e**, $IC_{50} = 9 \pm 2 \mu\text{M}$) are most potent in this series. They exhibit a stronger anticancer effect than the non-targeted control **1**^[9] ($IC_{50} = 34 \pm 3 \mu\text{M}$, $p < 0.001$) and the Mit-targeting prodrug **3**^[14] ($IC_{50} = 35 \pm 2 \mu\text{M}$, $p < 0.001$) reaching the potency of the best previously reported LY-targeting prodrug **2**^[13] ($IC_{50} = 5 \pm 2 \mu\text{M}$). Based on these data and due to its easier synthesis, prodrug **4a** was selected for more detailed studies.

As previously established, prodrugs containing arylboronic acid pinacol ester are hydrolyzed in aqueous buffered at pH 7 solutions within $\leq 1 \text{ h}$.^[20] Therefore, the active form of **4a** will be the boronic acid **4a_BA**. We determined n-octanol/water partition coefficient ($\log P$) of **4a_BA** to be substantially higher (5.9 ± 0.2 , Table S3, SI) than that of parent prodrug **1_BA** (2.7 ± 0.2). The high lipophilicity of **4a_BA** was expected to facilitate its accumulation in the ER.^[19]

To investigate the mechanism of **4a** activation in the presence of H_2O_2 , we applied electrospray ionization (ESI) mass spectrometry (MS). We confirmed that **4a** is first hydrolyzed in aqueous solution forming **4a_BA**. In the presence of H_2O_2 AF-drug **4a_2** is formed (Figures S29–S34, SI), which can donate an electron to H_2O_2/O_2 leading to formation of ferrocenium **4a_2⁺** and highly toxic $HO^{\bullet}/O_2^{\bullet-}$. We confirmed experimentally formation of $HO^{\bullet}/O_2^{\bullet-}$ in mixtures of **4a** and H_2O_2 by using 2',7'-dichlorodihydrofluorescein (DCFH) (Figure S35, Table S4, SI). In particular, we found that **4a** accelerates the rate of DCFH oxidation by 3.2-fold with respect to the rate of its spontaneous oxidation by H_2O_2 . All together these data indicate that **4a** is activated as outlined in Scheme 1 similarly to other known AF-prodrugs.^[9,12–14]

Further, we confirmed that apart from BL-2 cells prodrug **4a** exhibits anticancer activity towards other cancer cell lines including ovarian cancer A2780 ($IC_{50} = 5.4 \pm 0.7 \mu\text{M}$) and T-

cell leukemia Jurkat ($IC_{50} = 18 \pm 1 \mu\text{M}$). The anticancer activity of LY-targeting prodrug **2**^[13] is similar towards A2780 cells ($IC_{50} = 7 \pm 2 \mu\text{M}$) and higher towards Jurkat cells ($IC_{50} = 7.2 \pm 0.1 \mu\text{M}$, $p < 0.001$), whereas that of Mit-targeting **3**^[14] is substantially lower for both cell lines ($p < 0.001$, Tables S5, S6, SI). For Jurkat cells we observed that **4a** induces cell death mainly via necrosis and partially via apoptosis (Figure S36A, SI) that was reproduced for A2780 cells (Figure S37, SI). Since necrotic cells are usually immunogenic, it is possible that the initial direct anticancer effect of **4a** will be facilitated by the action of immune system in vivo. We observed that the anticancer activity of **4a** in Jurkat cells is decreased in the presence of the ROS inhibitor N-acetylcysteine (NAC)^[21] (Figure S36B, SI). These data confirm that ROS is involved in the intracellular activation of **4a**.

Next, we investigated the mechanism of action of **4a** in cells. In the first experiment, we incubated A2780 cells with prodrug **4a** as well as controls **1** and **2** for time periods between 1–24 h followed by their staining with organelle-specific dyes (ER: ER-tracker-green, ERTgrn; LY: acridine orange, AO; Golgi: Golgi-Staining-Green, GO; Mit: rhodamine 123, R123) and evaluation of their fluorescence by using flow cytometry (Figure 1). The fluorescence intensity of the cells treated with medium only (carrier) was used as a reference. We observed that non-targeted control **1** weakly affects the ER-specific fluorescence at 1 h incubation (but not at 4 h incubation) and does not affect the LY-, Golgi- and Mit-specific fluorescence at both 1 and 4 h incubation times. A weak decrease of the Mit-specific fluorescence was observed at the highest incubation time of 24 h. As expected, LY-targeted **2** strongly reduces the LY-specific fluorescence of the cells. Additionally, it also affects ER and especially Mit that can be a follow up effect after the initial lysosomal disruption as previously reported.^[13] The effect of **4a** on the ER-specific

fluorescence of the cells for both 1 and 4 h incubation times was found to be strongest within the studied series of the prodrugs ($p < 0.001$, Figure 1A). Using confocal microscopy we observed that the ER tracker dye is leaking into the nuclei and the cytoplasm of a large proportion of **4a**-treated cells indicating that **4a** induces the ER disruption (Figure S38). In contrast to **2**, prodrug **4a** does not affect the LY-specific signal (Figure 1B), but at the early incubation time (1 h) decreases slightly the Golgi-specific fluorescence and does not affect the Mit-specific fluorescence. At the later incubation times the effects on Golgi and Mit become stronger. These data indicate that the ER is a primary site of action for **4a** (the strong effect is seen already at 1h-incubation), whereas the effects on Golgi and Mit are secondary (≥ 4 h incubation is needed to observe strong effects).

By using quantitative PCR, we observed that the expression of mRNA of CCAAT-enhancer-binding protein homologous protein (CHOP), which is a marker of the ER stress,^[22] is significantly increased in **4a**-treated A2780 cells ($p < 0.05$). In contrast, neither unspecific **1** nor LY-targeting **2** affected the expression of the CHOP-mRNA (Table S7, SI). These data indicate that **4a** exhibits its anticancer activity via the induction of the ER stress.

Next, we evaluated the ability of **4a** to modulate the oxidative stress in cells (Figure 2A,B). We observed that this prodrug increases the total intracellular ROS amount (tROS)

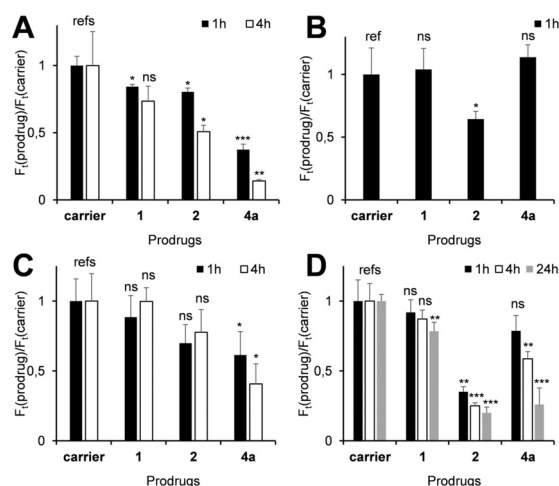


Figure 1. Effect of prodrugs and controls on relative organelle-specific staining ($F_1(\text{prodrug})/F_1(\text{carrier})$), where F is emission at 525 nm ($\lambda_{\text{ex}} = 488$ nm). Incubation times with prodrugs (1, 4, or 24 h) are indicated on the plots. A) ER staining with ERTgrn. B) LY staining with AO. C) Golgi staining with GO. D) Mit staining with R123. References are indicated with “ref”. The experimental data were compared by using Student’s t test: $p < 0.05$ (*), $p < 0.01$ (**), $p < 0.001$ (***), $p \geq 0.05$ (ns).

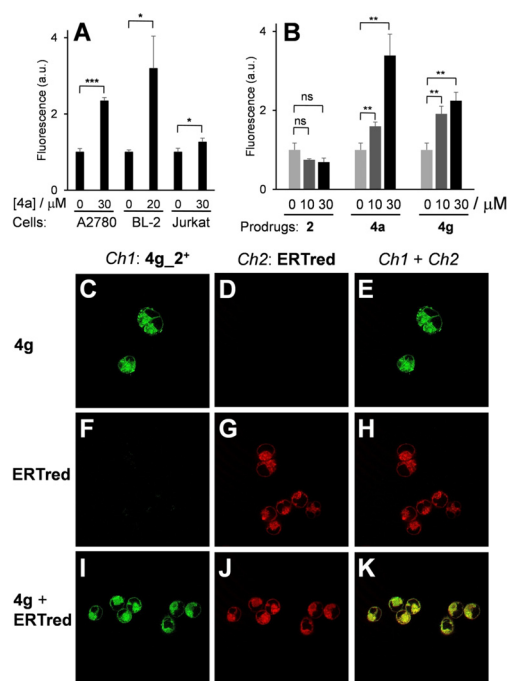


Figure 2. A) Increase of the mean fluorescence ($\lambda_{\text{ex}} = 488$ nm, $\lambda_{\text{em}} = 530$ nm) of 5-(6-(6-chloromethyl)-2',7'-dichlorodihydrofluorescein diacetate (CM-DCFH-DA)-loaded cells incubated with **4a** for 2 h (A2780 and BL-2 cells) or 1 h (Jurkat cells). B) Increase of the mean fluorescence ($\lambda_{\text{ex}} = 488$ nm, $\lambda_{\text{em}} = 585$ nm) of A2780 cells incubated with **4a** for 2 h followed by MitosoxTM for 20 min. C–K) Images of A2780 cells stained with **4g** (C–E), ERTred (F–H), and a mixture of **4g** and ERTred (I–K). Fluorescent channels: $Ch1$ (green)— λ_{ex} : 335–383 nm; λ_{em} : 420–470 nm (detection of **4g**); $Ch2$ (red)— λ_{ex} : 538–562 nm; λ_{em} : 570–640 nm (detection of ERTred).

in all studied cell lines significantly. However, the overall magnitude of the tROS increase was substantially lower than that found for LY-targeting **2**.^[13] In contrast, we observed the strong dose-dependent increase of mitochondrial ROS (mROS) in A2780 cells treated with **4a**, whereas control **2** did not affect mROS at any concentration tested (0–30 μM). Thus, the mode of action of **4a** (the induction of ER stress, the increase of mROS) is distinct from that implicated for all previously known AF-prodrugs.^[9,12–14,20]

To find out whether **4a** is directly accumulated in ER or induces its effects on the ER indirectly, we prepared its fluorogenic analogue **4g** containing a fluorescent dye 7-hydroxycoumarin (*SI*). We confirmed that **4g** and **4a** are analogues. For example, they have similar solubility in aqueous solution (Table S1, *SI*), lipophilicity (Table S3, *SI*) and exhibit similar anticancer activity towards A2780 cells ($\text{IC}_{50} = 6.2 \pm 2.4$ vs. $\text{IC}_{50} = 5.4 \pm 0.7$ μM correspondingly).

Prodrug **4g** is practically not fluorescent due to photo-induced electron transfer (PET) from the ferrocene moiety to the dye. Analogously to **4a**, it is converted to AF-drug **4g.2⁺** in the presence of H_2O_2 (Figure S29, S30) that is accompanied by the strong (up to 50-fold) fluorescence increase (Figure S39). We found that **4g** is accumulated and activated in A2780 cells leading to formation of fluorescent products (most probably **4g.2⁺**) that could be monitored by flow cytometry (Figure S40, Table S9). By using fluorescence microscopy we confirmed that the fluorescent product derived from **4g** is accumulated in ER (Figure 2C–K). This is evident from the efficient overlap (Pearson's R value = 0.85, Figure S41, *SI*) of the signal of the fluorescent product **4g.2⁺** derived from **4g** (green color) and the signal of ER-specific stain ERTred (red color, Figure 2K). It should be mentioned that previously reported fluorogenic versions of LY-targeting **2**^[13] and Mit-targeting **3**^[14] are substantially less active than their unlabeled counterparts. These compounds are suitable for the study of the mechanism of prodrug action, but not as therapeutic agents. In contrast, **4g** is the first truly teranostic AF-based prodrug.

To evaluate the cancer cell specificity of the ER-targeting AF-prodrugs, we conducted two complementary experiments. For the first one we selected a pair of genetically related primary cancer (chronic lymphocytic leukemia: CLL) and normal cells (mononuclear cells: MNC's). MNC's is a mixture of cells containing primary B cells, which are parent for CLL cells. We observed that **4a** is significantly more toxic towards CLL cells ($\text{IC}_{50} = 5.6 \pm 0.7$ μM) than normal MNC's ($\text{IC}_{50} = 18.3 \pm 7.5$ μM , $p < 0.05$) (Figure S42, *SI*). Furthermore, by using fluorescence microscopy we confirmed that **4g** (the fluorogenic analogue of **4a**) is activated only in cancer (A2780), but not in normal (SBLF9 fibroblasts) cells (Figure S43, *SI*). We selected the SBLF9 cells as representative normal cells, since they are adherent and, therefore, better suitable for the fluorescence microscopy than the non-adherent MNC's.

Finally, we evaluated the activation of **4g** in vivo in C57/BL6N mice with Nemeth-Kellner lymphoma (NK/Ly), which grow in the form of ascites (*SI*). First, we took ascite probes from untreated mice (time point 0) as a reference. Then prodrug **4g** at the dose of 40 mg kg^{-1} was injected i.p. every

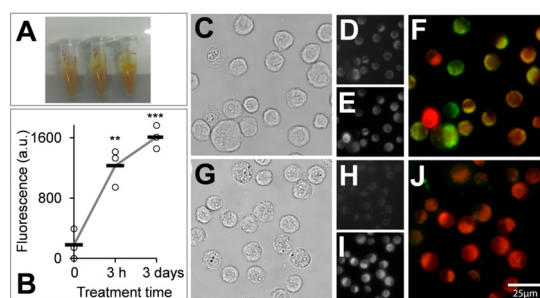


Figure 3. A) Photograph of ascite suspensions isolated from C57/BL6N mice carrying NK/Ly and treated with **4g** for 3 days. B) Increase of the mean fluorescence ($\lambda_{\text{ex}} = 340\text{--}380$ nm; $\lambda_{\text{em}} = 435\text{--}485$ nm) of ascites isolated from the C57/BL6N mice treated with **4g** for 0, 3 h and 3 days: circles: individual data, horizontal bars: means of the individual data. Student's t test: ** – $p < 0.01$; *** – $p < 0.001$; the untreated sample was used as a reference. C) Bright-field images of ascites isolated from the C57/BL6N mice treated with **4g** for 3 days. D, E) Fluorescence image of the same cells as in (C): $\lambda_{\text{ex}} = 290\text{--}410$ nm; $\lambda_{\text{em}} = 415\text{--}465$ nm (D) and $\lambda_{\text{ex}} = 530\text{--}570$ nm; $\lambda_{\text{em}} = 570\text{--}650$ nm (E). F) Overlay of images shown in (D) (green color) and (E) (red color). G–J) Controls; the same as (C–F) for untreated ascites.

day for 3 days. Ascite probes were taken 3 h and 3 days after the beginning of the treatment. The cell suspensions appeared yellow indicating the prodrug uptake (Figure 3A). Furthermore, the fluorescence of ascites ($\lambda_{\text{ex}} = 360/20$ nm, $\lambda_{\text{em}} = 460/25$ nm) was quantified by using a fluorescence plate reader (*SI*). We observed the significant ($p < 0.01$ for 3 h incubation and $p < 0.001$ for 3 days incubation) time-dependent fluorescence increase in the treated animals compared to the non-treated ones (Figure 3B) that is in agreement with the activation of **4g** in vivo. These results were confirmed by imaging of the live ascites by using vital fluorescence microscopy (3 days incubation, Figure 1C–J). In particular, we imaged the cells at two settings (Ch1 and Ch2), which allowed detecting the products of **4g** activation (Ch1: $\lambda_{\text{ex}} = 290\text{--}410$ nm; $\lambda_{\text{em}} = 415\text{--}465$ nm) and the ER-tracking dye ERTred (Ch2: $\lambda_{\text{ex}} = 530\text{--}570$ nm; $\lambda_{\text{em}} = 570\text{--}650$ nm, added to the isolated ascites shortly before the measurements). For the ascites from the treated group we observed an intense signal in the Ch1 indicating the **4g** activation. The latter signal overlaps with that in the Ch2 indicating that **4g** is accumulated and activated in the ER of the ascites in vivo. As expected, no signal in the Ch1 was observed in the ascites isolated from the control (untreated) group. These data are in agreement with our in vitro studies (Figure 2C–K).

In summary, we successfully prepared cholic acid-conjugated AF-prodrug **4a** as well as its fluorogenic version **4g**, which is the first reported teranostic AF-prodrug. We demonstrated fast (≤ 1 h incubation) accumulation and activation of these prodrugs in the ER of cancer cells that leads to the significant ER stress (upregulation of CHOP-mRNA) and the production of both mitochondrial and total ROS. We have confirmed the excellent cancer cell specificity of prodrugs **4a/4g** and demonstrated that **4g** is efficiently activated in vivo in the NK/Ly murine model. The prodrugs **4a/4g** described in this paper and the previously reported LY-targeting **2**^[13] exhibit comparable anticancer effects. However, due to different mechanisms of action, these drugs are

complementary to each other. We assume that **4a/4g** may find applications in cases when **2** is not suitable. Furthermore, the simultaneous use of these prodrugs would be an interesting option due to the possible synergistic effects between them.

Acknowledgements

Leonard Mach has conducted preliminary studies, which were not included in this publication. This project has received funding from the German Research Council (DFG, MO1418/7-2) and the European Union's Horizon 2020 research and an innovation program FET Open under grant agreement No 861878 (project "NeuroCure"). C.A. acknowledges funding from Manfred Roth-Stiftung, Fürth, the Forschungsstiftung Medizin am Universitätsklinikum Erlangen (Germany) and Hans Wormser, Herzogenaurach (Germany). Confocal microscopy was conducted at the Optical Imaging Centre Erlangen (OICE). Open access funding enabled and organized by Projekt DEAL.

Conflict of interest

The authors declare no conflict of interest.

Keywords: aminoferrocene · cancer · endoplasmic reticulum · prodrugs · reactive oxygen species

- [1] ECIS—European Cancer Information System: from <https://ecis.jrc.ec.europa.eu>, accessed on 25/08/2020 © European Union, 2020.
- [2] V. Schirmacher, *Int. J. Oncol.* **2019**, *54*, 407–419.
- [3] T. Vu, F. X. Claret, *Front. Oncol.* **2012**, *2*, 62.
- [4] a) W. H. Koppenol, P. L. Bounds, C. V. Dang, *Nat. Rev. Cancer* **2011**, *11*, 325–337; b) O. Warburg, *Science* **1956**, *123*, 309–314.
- [5] F. Antunes, R. Cadenas, *FEBS Lett.* **2000**, *475*, 121–126.
- [6] a) T. P. Szatrowski, C. F. Nathan, *Cancer Res.* **1991**, *51*, 794–798; b) B. Halliwell, *Biochem. J.* **2007**, *401*, 1–11.
- [7] A. P. King, J. J. Wilson, *Chem. Soc. Rev.* **2020**, *49*, 8113–8136.
- [8] N. Siwecka, W. Rozpędek, D. Pytel, A. Wawrzynkiewicz, A. Dziki, Ł. Dziki, J. A. Diehl, I. Majsterek, *Int. J. Mol. Sci.* **2019**, *20*, 4354.
- [9] S. Daum, V. Chekhun, I. Todor, N. Lukianova, Y. Shvets, L. Sellner, K. Putzker, J. Lewis, T. Zenz, I. Graaf, G. Groothuis, A. Casini, O. Zozulia, F. Hampel, A. Mokhir, *J. Med. Chem.* **2015**, *58*, 2015–2024.
- [10] a) S. Peter, B. A. Aderibigbe, *Molecules* **2019**, *24*, 3604; b) M. Patra, G. Gasser, *Nat. Rev. Chem.* **2017**, *1*, 0066.
- [11] C. Hwang, A. J. Sinskey, H. F. Lodish, *Science* **1992**, *257*, 1496–1502.
- [12] S. Daum, S. Babiy, H. Konovalova, W. Hofer, A. Shtemenko, N. Shtemenko, C. Janko, C. Alexiou, A. Mokhir, *J. Inorg. Biochem.* **2018**, *178*, 9–17.
- [13] S. Daum, V. Reshetnikov, M. Sisa, T. Dumych, M. D. Lootsik, R. Bilyy, E. Bila, C. Janko, A. Alexiou, M. Herrmann, L. Sellner, A. Mokhir, *Angew. Chem. Int. Ed.* **2017**, *56*, 15545–15549; *Angew. Chem.* **2017**, *129*, 15751–15755.
- [14] a) V. Reshetnikov, S. Daum, C. Janko, W. Karawacka, R. Tietze, C. Alexiou, S. Paryzhak, T. Dumych, R. Bilyy, P. Tripal, B. Schmid, R. Palmisano, A. Mokhir, *Angew. Chem. Int. Ed.* **2018**, *57*, 11943–11946; *Angew. Chem.* **2018**, *130*, 12119–12122; b) V. Reshetnikov, H. G. Özkan, S. Daum, C. Janko, C. Alexiou, C. Sauer, M. R. Heinrich, A. Mokhir, *Molecules* **2020**, *25*, 2545.
- [15] F. Fus, Y. Yang, H. Z. S. Lee, S. Top, M. Carriere, A. Bouron, A. Pacureanu, J. Cesar da Silva, M. Salmain, A. Vessières, P. Cloetens, G. Jaouen, S. Bohic, *Angew. Chem. Int. Ed.* **2019**, *58*, 3461–3465; *Angew. Chem.* **2019**, *131*, 3499–3503.
- [16] a) D. Chen, Q. C. Cui, H. Yang, Q. P. Dau, *Cancer Res.* **2006**, *66*, 10425–10433; b) K. Butcher, V. Kannappan, R. S. Kilari, M. R. Morris, C. McConville, A. L. Armesilla, W. Wang, *BMC Cancer* **2018**, *18*, 753.
- [17] Q. Yang, Y. Yao, K. Li, L. Jiao, J. Zhu, C. Ni, M. Li, Q. P. Dou, H. Yang, *Curr. Pharm. Des.* **2019**, *25*, 3248–3256.
- [18] E. Ekinci, S. Rohondia, R. Khan, Q. P. Dou, *Recent Pat. Anti-Cancer Drug Discovery* **2019**, *14*, 113–132.
- [19] P. Gao, W. Pan, N. Li, B. Tang, *Chem. Sci.* **2019**, *10*, 6035–6071.
- [20] S. Daum, J. Toms, V. Reshetnikov, H. G. Özkan, F. Hampel, S. Maschauer, A. Hakimioun, F. Beierlein, L. Sellner, M. Schmitt, O. Prante, A. Mokhir, *Bioconjugate Chem.* **2019**, *30*, 1077–1086.
- [21] S. Y. Sun, *Cancer Biol. Ther.* **2010**, *9*, 109–110.
- [22] S. Oyamomari, M. Mori, *Cell Death Differ.* **2004**, *11*, 381–389.

Manuscript received: January 3, 2021
Accepted manuscript online: March 3, 2021
Version of record online: April 8, 2021

Publication 7:

A prodrug activated by H₂O₂ and mitochondrial hydroxide: an improvement of cancer cells *versus* neutrophils selectivity

Insa Klemt,^{[a]#} Viktor Reshetnikov,^{[a]#} Subrata Dutta,^[a] Galyna Bila,^[b] Rostyslav Bilyy,^[b] Itziar Cossío Cuartero,^[c] Andrés Hidalgo,^[c] Adrian Wünsche,^[a] Maximilian Böhm,^[a] Marit Wondrak,^[d] Leoni A. Kunz-Schughart,^[d,e] Rainer Tietze,^[f] Frank Beierlein,^[g] Petra Imhof,^[g] Sabrina Gensberger-Reigl,^[h] Monika Pischetsrieder,^[h] Marlies Rippl,^[a] Tina Jost,^[i] and Andriy Mokhir^[a]

^[a]Friedrich-Alexander-University of Erlangen-Nürnberg (FAU), Department of Chemistry and Pharmacy, Organic Chemistry II, 91058 Erlangen, Germany

^[b]Danylo Halytsky Lviv National Medical University, Department of Histology, Cytology and Embryology Pekarska str. 69, 79010 Lviv, Ukraine

^[c]Program of Cardiovascular Regeneration, Centro Nacional de Investigaciones Cardiovasculares Carlos III (CNIC), C. Melchor Fernández Almagro, 3, 28029 Madrid, Spain

^[d]OncoRay, National Center for Radiation Research in Oncology, Faculty of Medicine and University Hospital Carl Gustav Carus, TU Dresden and Helmholtz-Zentrum Dresden-Rossendorf, Dresden, Germany

^[e]National Center for Tumor Diseases (NCT), Partner Site Dresden, Germany

^[f]FAU, University Hospital, Department of Otorhinolaryngology, Head and Neck Surgery, Section of Experimental Oncology and Nanomedicine (SEON), Glückstraße 10a, 91054 Erlangen, Germany

^[g] FAU, Erlangen National High Performance Computing Center (NHR@FAU), 91058 Erlangen, Germany; FAU, Computer-Chemistry-Center, Department of Chemistry and Pharmacy, Food Chemistry, 91058, Erlangen, Germany

^[h]FAU, Department of Chemistry and Pharmacy, Food Chemistry, 91058 Erlangen, Germany

^[i]FAU, University Hospital, Department of Radiation Oncology, 91054 Erlangen, Germany

#equal contribution

Contribution of I. Klemt:

UV-visible spectra of the prodrug and intermediate H₂N-L-E-cpt; Dynamic light scattering (DLS) of solutions of the prodrug and H₃N⁺-L-E-cpt; Stability of the prodrug and control FcNF-L-E-cpt at different pH's in the presence and absence of H₂O₂ monitored by fluorescence spectroscopy; Study of activation of the prodrug and control FcNF-L-E-cpt in the presence of different concentrations of H₂O₂ (0-10 mM); Monitoring release of iron ions from the prodrug; Monitoring the reaction of the prodrug with H₂O₂ by using HPLC; Preparation of intermediate H₃N⁺-L-E-cpt; Monitoring HO-cpt release from the prodrug by using HPLC coupled to the mass detector; Monitoring the reaction of FcN^{PG2/PG1}-L-E-dmb with H₂O₂ by using HPLC; fluorescence signal characteristic for camptothecin derivatives, except R123 colocalization; Reaction of the prodrug with H₂O₂ in cells; species (ROS) in A2780 cells; Effect of the prodrug on cell cycle of A2780 cells; all experiments with neutrophils; Contribution to Publication writing and revision of the manuscript.

The publication and supporting information are found under: DOI: **10.26434/chemrxiv-2023-69qzs**.

A prodrug activated by H₂O₂ and mitochondrial hydroxide: an improvement of cancer cells *versus* neutrophils selectivity

Insa Klemt,^{[a]†} Viktor Reshetnikov,^{[a]†} Subrata Dutta,^[a] Galyna Bila,^[b] Rostyslav Bilyy,^[b] Itziar Cossío Cuartero,^[c] Andrés Hidalgo,^[c] Adrian Wünsche,^[a] Maximilian Böhm,^[a] Marit Wondrak,^[d] Leoni A. Kunz-Schughart,^[d,e] Rainer Tietze,^[f] Frank Beierlein,^[g] Petra Imhof,^[g] Sabrina Gensberger-Reigl,^[h] Monika Pischetsrieder,^[h] Marlies Körber,^[a] Tina Jost,^[i] Andriy Mokhir*^[a]

[a] Friedrich-Alexander-University of Erlangen-Nürnberg (FAU), Department of Chemistry and Pharmacy, Organic Chemistry II, 91058 Erlangen, Germany, E-mail: Andriy.Mokhir@fau.de

[b] Danylo Halatsky Lviv National Medical University, Department of Histology, Cytology and Embryology, 79010 Lviv, Ukraine

[c] Program of Cardiovascular Regeneration, Centro Nacional de Investigaciones Cardiovasculares Carlos III (CNIC), C. Melchor Fernández Almagro, 3, 28029 Madrid, Spain

[d] OncoRay, National Center for Radiation Research in Oncology, Faculty of Medicine and University Hospital Carl Gustav Carus, TU Dresden and Helmholtz-Zentrum Dresden-Rossendorf, Dresden, Germany

[e] National Center for Tumor Diseases (NCT), Partner Site Dresden, Germany

[f] FAU, University Hospital, Department of Otorhinolaryngology, Head and Neck Surgery, Section of Experimental Oncology and Nanomedicine (SEON), 91054 Erlangen, Germany

[g] FAU, Erlangen National High Performance Computing Center (NHR@FAU), 91058 Erlangen, Germany; FAU, Computer-Chemistry-Center, Department of Chemistry and Pharmacy, 91054 Erlangen, Germany

[h] FAU, Department of Chemistry and Pharmacy, Food Chemistry, 91058 Erlangen, Germany

[i] FAU, University Hospital, Department of Radiation Oncology, 91054 Erlangen, Germany

† VR and IK have contributed equally

Many known chemotherapeutic anticancer agents exhibit neutropenia as a dose-limiting side effect. In this paper we suggest a prodrug concept solving this problem for camptothecin (HO-cpt). The prodrug is programmed according to Boolean “AND” logic. It requires for its activation the simultaneous presence of triggers T1 (H₂O₂) and T2 (pH 8 in mitochondria: Mit). The level of H₂O₂ in cancer cells is higher than that in normal cells. Thus, T1 discriminates cancer cells from the majority of normal cells excluding neutrophils, known to produce elevated levels of H₂O₂. T2 discriminates cancer cells from neutrophils, since the former cells have a higher number of Mit. We demonstrated that our prodrug exhibits antitumor activity both *in vitro* and *in vivo*, but is not toxic to normal cell and neutrophils in contrast to known single trigger prodrugs and the parent drug HO-cpt.

Introduction

Chemotherapy is one of the three major concepts in current cancer treatment along with surgery and radiotherapy. Clinically used chemotherapeutics include both natural and synthetic compounds, e.g., camptothecins,^[1] bleomycin,^[2] doxorubicin,^[3] paclitaxel^[4] and Pt(II) complexes (cisplatin, oxaliplatin).^[5] Their common side effect is neutropenia,^[1-5] a condition characterized by the low number of neutrophils. Since neutrophils belong to the first line of defense against infections, neutropenia causes strong suppression of the immune system in patients and, as a consequence, even minor infections can become life threatening.

Side effects of drugs can be eliminated by converting them to prodrugs, which are activated under cancer specific conditions, but remain inactive in other cells.^[6] For example, we^[7] and others^[8] have used differences in the amount of H₂O₂ in cancer and normal cells^[9] to design H₂O₂-responsive anticancer prodrugs. However, neutrophils also produce large amounts of H₂O₂ that can activate the prodrugs causing neutropenia. Representative examples include H₂O₂-responsive prodrugs of (a) gemcitabine exhibiting residual neutrophil toxicity compared to the vehicle^[10] and (b) N-alkylaminoferrocene (AF) causing death of neutrophils via formation of neutrophil extracellular traps (NETs).^[11] These literature data indicate that improved concepts for H₂O₂-responsive prodrugs are warranted.

Since the number of mitochondria (Mit) in cancer cells is substantially higher than that in neutrophils (Figure 1A),^[12] we hypothesized that a combination of the H₂O₂-mediated activation with the Mit-driven chemistry can be used to improve cancer cells *versus* neutrophils specificity of H₂O₂-responsive prodrugs. Herein, we report on a proof-of-concept studies confirming the feasibility of this hypothesis.

We developed a prodrug of an inhibitor of topoisomerase I (TOPI) camptothecin (HO-cpt) AF^{PG2/PG1}-L-E-cpt (Figures 1, 2). HO-cpt was selected, since alone with the strong anticancer activity it exhibits severe neutropenia.^[1] Two HO-cpt derivatives (irinotecan and topotecan) are already used in clinics.^[1] Single trigger H₂O₂-activated prodrugs of HO-cpt have been previously reported.^[13] In contrast, the AF^{PG2/PG1}-L-E-cpt (further prodrug) is dependent on two triggers: H₂O₂ (T1) and a Mit-associated trigger (T2) (Figures 1B, C). As T2 we used OH⁻ present at elevated amounts (pH 8) in Mit (OH⁻_{Mit}).^[14] Single trigger prodrugs activated by OH⁻_{Mit} have been previously described.^[15]

The prodrug reported in this paper exhibits low μM anticancer activity *in vitro* towards a variety of human cancer cell lines representing blood, ovarian, prostate, pharynx and tongue, but is not toxic towards normal cells including PMA-primed neutrophils. Its anticancer activity is potentiated by ionizing radiation. The prodrug retains its activity *in vivo* in Nemeth-Kellner lymphoma model of murine cancer. In contrast to HO-cpt, it does not induce neutropenia *in vivo*.

Results and Discussion

A previously reported $\text{FcN}^{\text{PG2/PG1}}\text{-X}$, where X = a fluorescein derivative, is hydrolyzed within <2h in aqueous solution with formation of the boronic acid $\text{FcN}^{\text{PG2}}\text{-X}$ (a1, Figure 1B).^[7b] The $\text{FcN}^{\text{PG2}}\text{-X}$ is taken up by both normal and cancer cells, but is activated only in H_2O_2 -rich, cancer cells via steps *b1-c1* with formation of a ferrocenium $\text{Fc}^+\text{NH-X}$, found to be accumulated in Mit.^[7b] The $\text{Fc}^+\text{NH-X}$ is decomposed forming not identified polar products. The T1-responsive moiety of the $\text{FcN}^{\text{PG2/PG1}}\text{-X}$ was applied to design the prodrug reported in this paper.

Design of a T1/T2-responsive prodrug

The proposed activation mechanism of the prodrug and its chemical structure are shown in Figures 1C and 2.

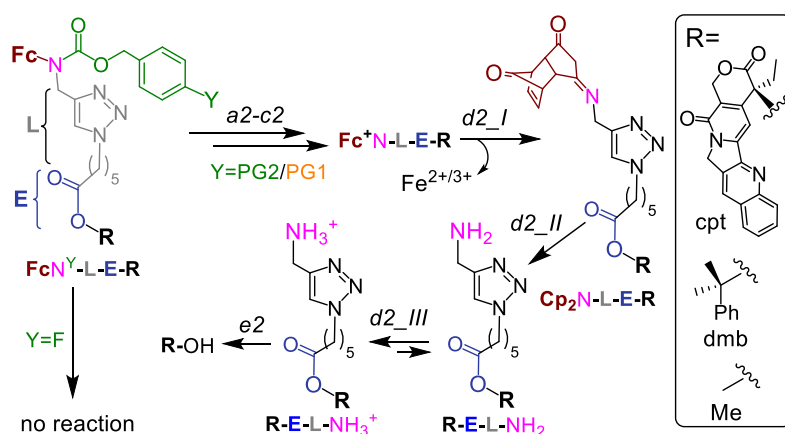


Figure 2. The mechanism of activation of the prodrug. A control $\text{FcN}^{\text{F}}\text{-L-E-cpt}$ is unreactive under these conditions. Steps *a2-c2* and *e2* are described in the caption to Figure 1C. Steps *d2_I* and *d2_II* occur spontaneously.

The prodrug includes three elements: moieties responsive to T1 ($\text{FcN}^{\text{PG2/PG1}}$ ^[7b]) and T2 (L-E) as well as a drug fragment (cpt), deactivated by acylation of the critical for the activity HO group with formation of an ester E.^[16] Ideally, the E is cleaved in the presence of both H_2O_2 (T1) and HO^{Mit} (T2) releasing the active drug HO-cpt (cancer cell: T1⁺/T2⁺), but remains intact when one of the triggers is absent (normal cell: T1⁻/T2⁺; neutrophil: T1⁺/T2⁻). This goal is achieved in the following way. The prodrug is designed to be lipophilic enough to exist in the oligomer-form in aqueous solution (aggregate I, Figure 1C). In aggregate I the hydrophobic L-E moiety is buried in the interior and, therefore, not accessible to the hydrolysis by hydrophilic T2. A polar boronic acid moieties PG2/PG1 are located at the exterior of the aggregate and accessible to T1. Assuming that the T1-responsive $\text{FcN}^{\text{PG2/PG1}}$ moiety^[7b] retains its properties in the prodrug, its activation induced by T1 will occur as outlined in Figure 2. In steps *b2* and *c2*, the PG2/PG1 will be cleaved by T1 forming a $\text{Fc}^+\text{NH-L-E-cpt}$. A positive charge of this intermediate should destabilize the aggregate, thereby favoring the monomeric species. In cells, the de-aggregation will be further supported by loading of the $\text{Fc}^+\text{NH-L-E-cpt}$ into Mit (Figure 1C). In this state the ester E will be

accessible for T2 and can, therefore, be hydrolyzed forming HO-cpt as indicated with a dashed arrow in Figure 1C. As it is described in the experimental part, the latter reaction occurs stepwise ($d2+e2$) via a H_3N^+ -L-E-cpt. In step $f2$, the drug is accumulated in the nucleus, where it inhibits TOPI.

Activation of the prodrug by T1 and T2 in cell free settings

Synthesis of the prodrug and controls is described in the supporting information (SI). Their purity was confirmed by C, H, N elemental analysis and was found to be >95%. The characterization and confirmation of prodrug stability in solid state and solution are provided in Figures S1-S24 (SI).

Aggregation of the prodrug The prodrug is lipophilic as evidenced by its high n-octanol/water partition coefficient (logP) of 4.27 ± 0.04 (Table S1, SI). However, it is still moderately soluble at $\leq 30 \mu\text{M}$ in Dulbecco's phosphate-buffered saline (DPBS) (Table S2, SI). To investigate the aggregation phenomena in the aqueous solutions, we recorded UV-visible spectra of the prodrug at concentrations up to $25 \mu\text{M}$ (Figure 3A). As expected, the spectra are dominated by the cpt chromophore ($\lambda_{\text{max}} = 369$ and 394 nm), whereas the ferrocenyl moiety is not visible due to its low extinction coefficient. Absorbance at these maxima does not obey Beer-Lambert law (Figure 3B: representative data for $\lambda_{\text{max}} = 369 \text{ nm}$) indicating the presence of more than one cpt-chromophore-containing species in solution. Interestingly, the significant absorbance >500 nm is also observed (Figures 3A, D). Since the prodrug has no chromophores absorbing >500 nm, this feature can be interpreted by Reyleigh light scattering on aggregate 1. By using dynamic light scattering (DLS) we confirmed the formation of aggregate 1 with sizes ranging from 350 ± 21 to $535 \pm 65 \text{ nm}$. The λ_{max} values of the prodrug (369 / 394 nm) are close to those observed for the solution of HO-cpt dissolved in unpolar solvent toluene (369 / 386 nm), but do not match those of HO-cpt dissolved in polar water (355 / 368 nm).^[17] These data indicate that the cpt moiety is located in the hydrophobic interior of aggregate 1. Since the E-L is directly linked to the cpt, it will also be located in the hydrophobic interior that will protect it from the attack by T2 (Figure 1C).

Reaction of the prodrug with H_2O_2 The prodrug as well as the control FcN^F -L-E-cpt are practically not fluorescent in aqueous solutions (Figure 4A), possibly due to (a) photo-induced electron transfer (PET) from the Fc moiety to the excited state of the cpt and (b) aggregation. We observed the H_2O_2 -dose dependent increase of the fluorescence characteristic for the cpt fluorophore ($\lambda_{\text{ex}} = 365 \text{ nm}$, $\lambda_{\text{em}} = 460 \text{ nm}$) in the mixtures of prodrug ($20 \mu\text{M}$) and H_2O_2 ($10 \mu\text{M}$ to 10 mM , Figures 4A, B). Further data obtained at pH 7, 8 and 10 are shown in Figure S25, SI. This reaction is facilitated at higher pH: it is 1.5- and 1.9-fold faster at pH 8 and 10 than at pH 7 (Table S3, SI). Importantly, the prodrug activation by H_2O_2 is not affected by the physiological concentration of glutathione (GSH, 5 mM) (Figure 4C) indicating that the reaction is possible within living cells

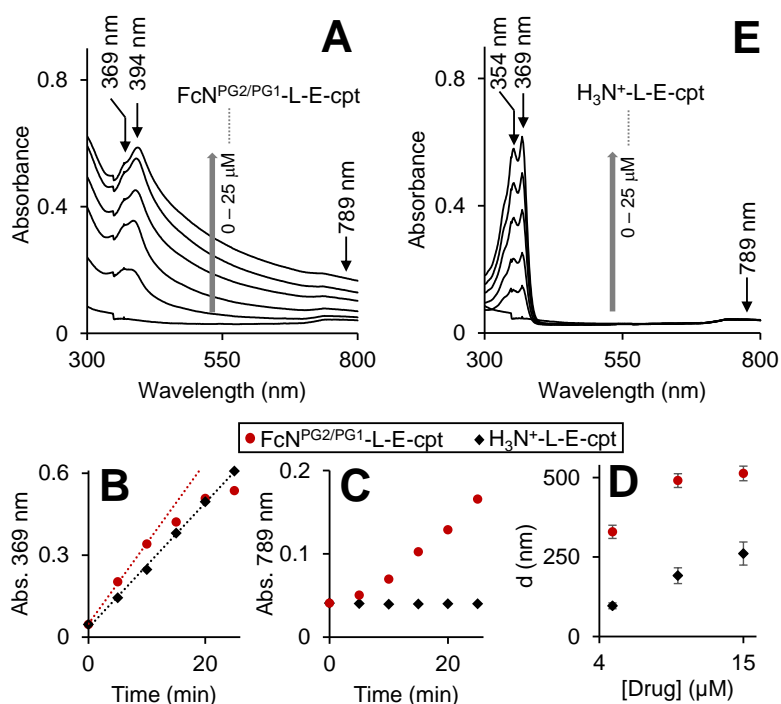


Figure 3. UV-visible spectra of the prodrug (**A**) and $\text{H}_3\text{N}^+\text{-L-E-cpt}$ (**E**) in triethylammonium acetate (TEAA) buffer (150 mM, pH 8, CH_3CN 15 % v/v, DMSO 1%, v/v) at concentrations 0, 10, 15, 20 and 25 μM . Plots of absorbance at 369 and 789 nm versus time obtained from the spectra shown in **A** and **E** are provided in insets **B** and **C**, correspondingly. Linear fits of the initial time periods (0-10 min) are provided as dotted lines. **D**: DLS data for aqueous solutions (same as in **A** and **E**) of the prodrug (red circles) and $\text{H}_3\text{N}^+\text{-L-E-cpt}$ (black diamonds): “d” is the mean size of the aggregates detected.

Furthermore, the activation relies on the presence of the PG2/PG1 group, since the control $\text{FcN}^{\text{F}}\text{-L-E-cpt}$ lacking this group remains non-emissive even in the presence of the highest H_2O_2 concentration tested (10 mM, Figure 4A, red colored trace). Importantly, both the prodrug and the control $\text{FcN}^{\text{F}}\text{-L-E-cpt}$ are stable at pH 7 and 8 in the absence of H_2O_2 , indicating that the direct hydrolysis of the ester E does not take place. Compared to pH 7, the direct hydrolysis is facilitated at pH 10 by 6-fold for the prodrug and 2.5-fold for the control (Table S3, S1). The fluorescent product generated upon the prodrug activation can be both HO-cpt and other fluorescent intermediates as will be discussed later. To identify these products, we first examined the release of Fe ions in the mixture of the prodrug (20 μM) and H_2O_2 (10 mM) by making use of the formation of red colored complex of Fe^{2+} with ferrozine.^[18] We detected no Fe^{2+} both at pH 7 and 8 after 2h incubation (S1). However, when the mixtures were first reduced by hydroxylamine to convert Fe^{3+} to Fe^{2+} , followed by addition of ferrozine, the characteristic red solution was obtained at both pH 7 and 8: representative data

obtained at pH 8 are shown in Figure 4D. This indicates the H₂O₂-mediated release of Fe³⁺, occurring in the result of the decomposition of Fc⁺NH-L-E-cpt (Figure 2).

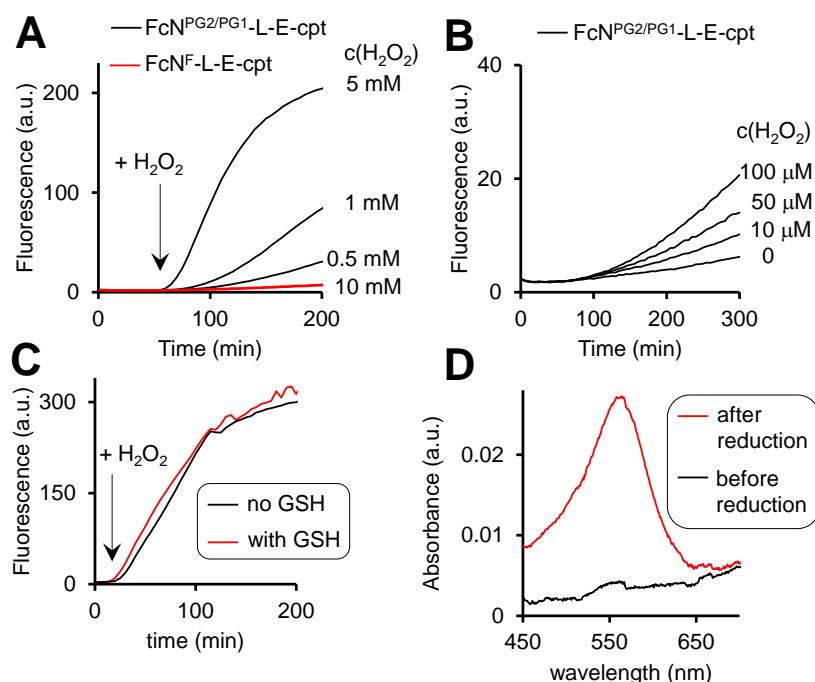


Figure 4. The fluorescence increase ($\lambda_{\text{ex}} = 365 \text{ nm}$, $\lambda_{\text{em}} = 400 \text{ nm}$) in aqueous solutions of the prodrug (10 μM , pH 8) in the presence of H₂O₂ (**A**: 0.5 – 10 mM; **B**: 0 – 100 μM). **C**: Data indicating that GSH (5 mM) does not affect the activation of the prodrug by H₂O₂ (10 mM). **D**: Detection of Fe²⁺ (“before reduction”) and the sum of Fe³⁺ and Fe²⁺ (“after reduction”) in the solution of the prodrug (20 μM , pH 8) incubated with H₂O₂ (10 mM) for 2 h. Other experimental details are provided in the *SI*.

Furthermore, the activation relies on the presence of the PG2/PG1 group, since the control FcN^F-L-E-cpt lacking this group remains non-emissive even in the presence of the highest H₂O₂ concentration tested (10 mM, Figure 4A, red colored trace). Importantly, both the prodrug and the control FcN^F-L-E-cpt are stable at pH 7 and 8 in the absence of H₂O₂, indicating that the direct hydrolysis of the ester E does not take place. Compared to pH 7, the direct hydrolysis is facilitated at pH 10 by 6-fold for the prodrug and 2.5-fold for the control (Table S3, *SI*). The fluorescent product generated upon the prodrug activation can be both HO-cpt and other fluorescent intermediates as will be discussed later. To identify these products, we first examined the release of Fe ions in the mixture of the prodrug (20 μM) and H₂O₂ (10 mM) by making use of the formation of red colored complex of Fe²⁺ with ferrozine.^[18] We detected no Fe²⁺ both at pH 7 and 8 after 2h incubation (*SI*). However, when the mixtures were first reduced by hydroxylamine to convert Fe³⁺ to Fe²⁺, followed by addition of ferrozine, the characteristic red solution was obtained at both pH 7 and 8: representative data obtained at pH 8 are shown in Figure 4D. This indicates the H₂O₂-mediated release of Fe³⁺, occurring in the result of the decomposition of Fc⁺NH-L-E-cpt (Figure 2).

Other intermediates and HO-cpt were identified by using HPLC coupled to UV-light (LC-UV) and electrospray ionization MS detectors (LC-MS, Figure 5).

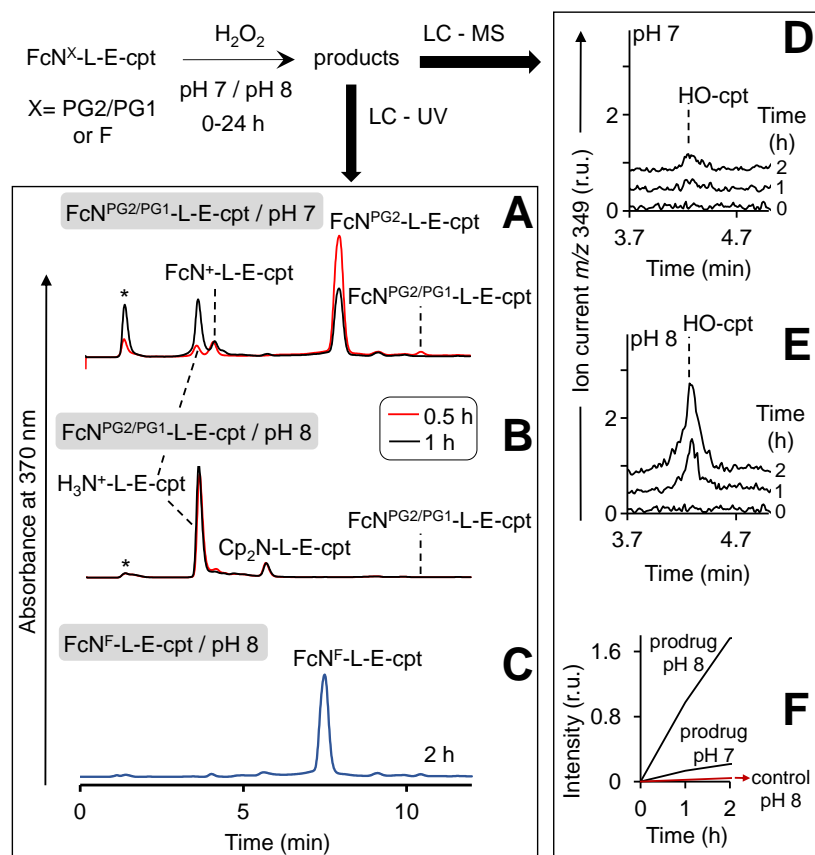


Figure 5. Study of the reaction of the prodrug and the control FcN^F-L-E-cpt with H₂O₂ at pH 7 and 8 by using HPLC. HPLC profiles (detection of absorbance at 370 nm) are shown in **A** and **B**. Solutions of the prodrug (20 μM) at pH 7 (**A**) or pH 8 (**B**) were incubated for 0.5 – 1 h in the presence of H₂O₂ (10 mM) and analysed. Injection peak is indicated with *. **C**: The same as in **B**, except that the prodrug was replaced with FcN^F-L-E-cpt and the incubation time was extended to 2h. **D**, **E**: Analysis of the prodrug/H₂O₂ mixtures (incubation times are shown on the plot) by using LC – quadrupole-time-of-flight mass detector (detection of positive ion current at m/z 349 Da: protonated HO-cpt). **F**: Dependence of peak areas at m/z 349 Da observed in experiments shown in **D** and **E** from the time of incubation with H₂O₂.

In particular, at pH 7 traces of the prodrug are observed at the retention time $R_t = 10.5$ min (m/z 986 [M-e]⁺) after 30 min incubation with H₂O₂ (10 mM) (red line, Figure 5A). After 1h incubation it is not detectable anymore (black line). The major peak at both 30 min and 1 h incubation at pH 7 is the hydrolyzed prodrug FcN^{PG2}-L-E-cpt: $R_t = 7.8$ min (m/z 904 [M-e]⁺). Further detected intermediates include a Fc⁺NH-L-E-cpt ($R_t = 4.1$ min, m/z 726 [M]⁺) and its decomposition product H₃N⁺-L-E-cpt ($R_t = 3.7$ min, m/z 543 [M]⁺). The formation of the latter intermediate is in agreement with the release of Fe³⁺ (Figure 4D). At 30 min incubation ferrocenium/amine ratio is equal to 3/4, whereas at 1h incubation it is 1/9. At pH 8 the same intermediates are formed. However, the reaction is substantially faster. Already after 30 min, neither prodrug nor its hydrolyzed form are detectable, whereas the ferrocenium intermediate is present only as traces. The major

product is $\text{H}_3\text{N}^+\text{-L-E-cpt}$. Additionally, a weak peak is observed at $R_t = 5.6$ min (m/z 701 $[\text{M}]^+$), which corresponds to $\text{Cp}_2\text{N-L-E-cpt}$ formed in the result of decomposition of $\text{Fc}^+\text{NH-L-E-cpt}$ (Figure S27, *S/*).

We observed that at the separation conditions selected for LC-UV (Figure 5A-B) both HO-cpt and $\text{H}_3\text{N}^+\text{-L-E-cpt}$ (Figure S28, *S/*) elute at the same time (3.7 min) that did not allow for the accurate quantification of HO-cpt. We solved this problem by using more efficient chromatographic separation with high-resolution mass spectrometry (Figure S29, *S/*). The data obtained are provided in Figures 5D, E. In Figure 5F, areas of the peaks corresponding to HO-cpt are plotted as a function of time. In the prodrug / H_2O_2 mixture at pH 7 a HO-cpt peak is observed only after 2h incubation (Figure 5D). In contrast, at pH 8 this peak is detectable already after 1h and the peak intensity is increased after 2h. Importantly, practically no HO-cpt could be detected in the mixture of the control $\text{FcN}^{\text{F-L-E-cpt}} / \text{H}_2\text{O}_2$ at pH 8 (red trace, Figure 5F) indicating that the direct hydrolysis of E does not take place.

To investigate whether the latter reaction sequence is specific for cpt derivatives, we prepared a $\text{FcN}^{\text{PG2/PG1-L-E-dmb}}$ containing 1,1-dimethylbenzyl in place of the cpt moiety. By using LC-UV-MS we confirmed that this compound forms related intermediates as the $\text{FcN}^{\text{PG2/PG1-L-E-cpt}}$ in the presence of H_2O_2 (Figure S30A, *S/*). The reaction was also found to be facilitated at pH 8 as compared to pH 7. By using GC-MS we confirmed the formation of HO-dmb in the $\text{FcN}^{\text{PG2/PG1-L-E-dmb}}/\text{H}_2\text{O}_2/\text{pH 8}$ mixture (Figure S30B, *S/*). Thus, these data indicate that the reaction sequence reported in this paper is not restricted to the cpt-prodrugs. It can potentially be applied to design prodrugs of other anticancer drugs, which possess a critical for their activity tertiary OH group. Possible examples of such drugs are clinically used irinotecan and topotecan.^[1]

The mechanism of the reaction of the prodrug with H_2O_2 at pH 8

According to the data discussed above the prodrug is aggregated in aqueous solution that blocks the reactivity of the L-E (Figures 3A-D). In the presence of H_2O_2 the prodrug is converted to the $\text{H}_3\text{N}^+\text{-L-E-cpt}$ (Figure 5A, B). This compound is monomeric according to the following experimental evidences. First, its UV-visible spectra at 0 to 25 μM are characteristic for a monomeric cpt derivative. In particular, the absorbance maxima (354 / 369 nm) are close to those observed for HO-cpt dissolved water (355 / 368 nm).^[17] Absorbance at these maxima obey Beer-Lambert law (Figure 3B, black trace). No absorbance is observed at >500 nm, indicating the absence of aggregates able to scatter light. Finally, DLS data indicate the absence of aggregates larger than 100 nm at the compound concentration $< 5 \mu\text{M}$. This indicates that the cpt in $\text{H}_3\text{N}^+\text{-L-E-cpt}$ is exposed to the solvent.

To find out whether the hydrolysis is facilitated by the intramolecular interactions, we analyzed possible conformations of $\text{H}_3\text{N}^+\text{-L-E-cpt}$ in aqueous solution by molecular dynamics (MD) simulations (Figures S31A-F, *S/*). We observed only low probabilities for conformations where hydrogen bonding between the ammonia and the C=O (E) is possible (Figures S31A-C, *S/*). Combined quantum mechanical/molecular mechanical (QM/MM) simulation of the hydrolysis reaction by an OH^- ion on $\text{H}_3\text{N}^+\text{-L-E-cpt}$ in a stretched conformation, i.e. with the ammonium group far from the E, show a step-wise

reaction, in which the rate-determining step is the OH⁻ attack with formation of a tetrahedral intermediate with a feasible free energy barrier of 34.0 ± 0.7 kcal/mol (Figures S31E-F, S). In simulations, in which the ammonium group has been constrained to be close to the C=O (E), the free energy barrier for the nucleophilic attack does not change significantly (36.1 ± 0.6 kcal/mol) compared to the simulations without this distance constraint (Figure S31F). This indicates that hydrolysis of E does not rely on intramolecular interactions involving the ammonium group. It is therefore conceivable that the hydrolysis occurs by direct OH⁻ attack of the E of H₃N⁺-L-E-cpt.

Effect of the prodrug on viability of cancer and normal cells

We selected several representative human cancer cell lines from different organs, including Burkitt's lymphoma BL-2 (blood), A2780 (ovary), DU-145 (prostate), SAS (tongue) and FaDu (pharynx), known to produce elevated ROS amounts.^[7,19,20] Incubation of these cells with the prodrug for 96 h affects strongly their viability. In particular, half inhibitory concentration (IC₅₀) ranges from 0.3 ± 0.1 μM (for most sensitive BL-2 cells) to 1.1 ± 0.5 μM (for least sensitive DU-145 cells) (Table 1). Experiments with controls revealed the importance of the individual components of the prodrug. In particular, the control FcN^{PG2/PG1}-L-E-Me^[7b] lacking the cpt fragment is from 34- to 93-fold and the control FcN^F-L-E-cpt lacking the H₂O₂-responsive fragment is from 4.3 to 27.5-fold less active than the prodrug (Table 1). The trend is retained at the shorter incubation times of 24 and 48 h (Tables S5, S6, S). Importantly, the prodrug does not affect the viability of representative normal cell lines, producing low amounts of intracellular ROS: normal human dermal fibroblasts (NHDF), IC₅₀ > 20 μM; retinal pigment epithelia (ARPE-19) cells, IC₅₀ > 10 μM and primary human fibroblasts (HF), IC₅₀ > 10 μM (Table S6, Figure S32, S).

Table 1. Effect of the prodrug/controls on viability of selected cancer cell lines.

Prodrug/ controls	Cancer cell lines / IC ₅₀ , μM				
	BL-2 ^[a]	A2780 ^[a]	DU-145 ^[a]	SAS ^[b]	FaDu ^[b]
FcN ^{PG2/PG1} -L-E-cpt	0.3 ± 0.1	1.0 ± 0.2	1.1 ± 0.5	4 ± 2	8 ± 2
FcN ^{PG2/PG1} -L-E-Me	28 ± 5	34 ± 5	>50	-	-
FcN ^F -L-E-cpt	1.3 ± 0.2	8.0 ± 0.2	>30	>40	>40
HO-cpt	0.02±0.01	0.08±0.02	0.03±0.01	-	-

^[a] 96 h incubation; ^[b] 48 h incubation.

The differences in the anticancer effects of the prodrug and the controls can be caused by the different uptake efficacy. To evaluate this possibility, we studied the uptake of the latter compounds in representative cancer cells – BL-2 (Tables S8, S9 S). We found that the uptake of FcN^F-L-E-cpt is more efficient than that of the prodrug, whereas FcN^{PG2/PG1}-L-E-Me^[7b] and the prodrug are taken up with almost the same

efficacy. Thus, the stronger anticancer effect of the prodrug than that of the controls is not caused by the differences in their uptake efficacy.

Enhancement of the prodrug efficacy

The anticancer effect of the prodrug is 13 to 37-fold weaker than that of HO-cpt (Table 1) suggesting that its intracellular activation is not complete. Since ionizing irradiation (IR) increases ROS in cells,^[21] we assumed that it could also facilitate the prodrug activation.^[22] We tested this hypothesis in two representative cell lines, SAS and FaDu, which are cancer models established in our laboratory for exploring synergistic effects between IR and new drugs.^[22]

First, we confirmed that the prodrug inhibits growth of both SAS ($IC_{50} = 4 \pm 2 \mu\text{M}$) and FaDu cells ($IC_{50} = 8 \pm 2 \mu\text{M}$) at 48 h incubation time. At the concentration of $0.5 \mu\text{M}$ (but not $0.2 \mu\text{M}$) it also inhibits the capacity of these cells to form colonies ($p < 0.01$). Next, we investigated inhibition of colony formation capacity of SAS and FaDu cells by the combination of the prodrug and IR. The prodrug at non-toxic ($0.2 \mu\text{M}$) and moderately toxic ($0.5 \mu\text{M}$) concentrations and IR at doses ranging from 0 to 10 Gy were used. For the highest IR dose of 10 Gy and one representative cell line (FaDu) the IR-induced increase of the intracellular ROS level was confirmed (Figure S33, *SI*). We were pleased to observe that the effect of the prodrug at both tested concentrations on both cell lines is strongly enhanced by IR ($p < 10^{-3}$) (Figure S34, *SI*). In contrast, the H_2O_2 -resistant control $\text{FcN}^{\text{F}}\text{-L-E-cpt}$ exhibits practically no synergy with IR (Figure S34, *SI*).

A mechanism of anticancer activity of the prodrug

The prodrug is not fluorescent (Figure 4A). When it reacts with H_2O_2 two long- ($\text{H}_3\text{N}^+\text{-L-E-cpt}$ and HO-cpt) and one short-living ($\text{Fc}^+\text{NH-L-E-cpt}$) fluorescent products are formed, each exhibiting a broad emission in the range of 420 - 470 nm (Figures 4A, 5A, B, D, E). Further, we will call a mixture of these compounds **prodrug-derived fluorescent products** (PDFPs). $\text{H}_2\text{N-L-E-cpt}$ and $\text{Fc}^+\text{NH-L-E-cpt}$ are inactive cpt esters unable to bind TOPI, whereas HO-cpt is a TOPI inhibitor and a highly potent anticancer drug. Thus, the fluorescence increase in the reaction of the prodrug with H_2O_2 will not necessarily correlate with the high anticancer activity, but is rather an indication of the first step of the activation. We investigated formation and intracellular localization of PDFPs (blue channel) in representative cancer A2780 cells. Mit was labelled with rhodamine 123 (R123: green channel) and nuclei – with NUCLEAR-ID[®] Red dye (NIRD: red channel). As shown in Figure 6A, the blue signal is clustered in particular regions. This signal is co-localized with both R123 (green, Pearson's coefficient $r = 0.68$) and NIRD (red, $r = 0.81$) confirming that the PDFPs are present in Mit and in nuclei of the cells. We observed that the signal of PDFPs is practically absent in A2780 cells pretreated with ROS scavenger N-acetylcystein (NAC, Figure 6A, right image) indicating that PDFPs are formed in cells in the ROS-dependent reaction. This data are in agreement with the suggested mechanism (Figure 1C) including formation of $\text{Fc}^+\text{NH-L-E-cpt}$ in the cytoplasm, its accumulation in Mit, where it is transformed via the

sequence of the OH⁻Mit-mediated reactions to HO-cpt. The drug then migrates to the nucleus, where it is trapped by binding to its target TOPI.^[23]

Next, we investigated whether the prodrug acts as a cpt-derivative releasing HO-cpt in cells or as a typical AF-prodrug. HO-cpt affects intracellular ROS levels weakly, but is known to induce a strong cell cycle arrest in S and G2 phases as reflected, amongst others, in altered static DNA histograms (Figures 6B, C). In contrast, the typical effect of AF prodrugs is amplification of intracellular ROS (e.g. control FcN^{PG2/PG1}-L-E-Me,^[7b] Figures S37, S38, S), whereas no major effect on the cell cycle distribution - rather a slight increase in the G1 phase cell fraction - is observed.^[7,19] The prodrug practically does not facilitate ROS production (Figures S37-S39, S), but causes changes of cell cycle distribution characteristic for HO-cpt (Figures 6B, C). It is therefore likely that HO-cpt is intracellularly released from the prodrug.

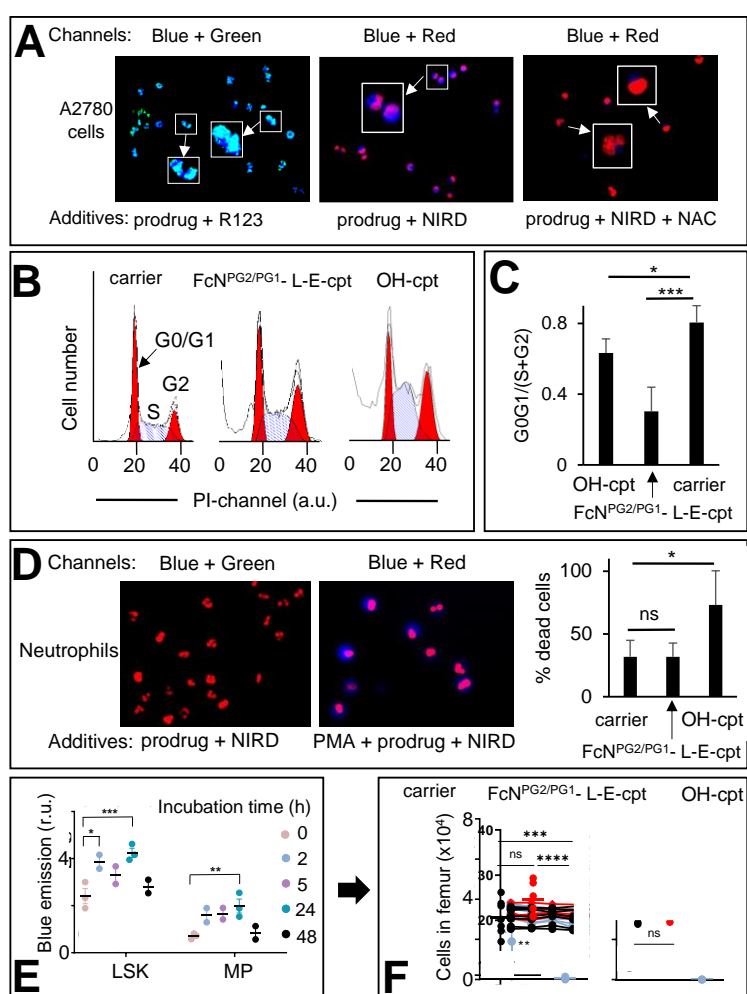


Figure 6. **A:** Left image— A2780 cells incubated with the prodrug (20 μ M) and Mit-specific dye R123 (1 μ M). Two channels were used for emission monitoring: Ch1 - λ_{ex} = 365 nm, λ_{em} = 420–470 nm (for detecting PDFFPs) and Ch2 - λ_{ex} = 430–510 nm, λ_{em} = 475-575 nm (for detecting R123). Ch1+Ch2 combination is provided. Middle image— A2780 cells incubated with the prodrug (20 μ M) and nuclei-labelling NUCLEAR-ID[®] Red dye (NIRD). Two channels were used for emission monitoring: Ch1 and Ch3 - λ_{ex} = 538–562 nm, λ_{em} = 570–640 nm (for NIRD). Ch1+Ch3 combination is shown. Right image: the same as the middle image, except that N-acetyl cysteine (NAC, 2 mM) was added. Zoomed-in (x2.5) images are shown in white boxes.

B: Cell cycle distribution of A2780 cells treated for 72 h either with DMSO (1 %, v/v, carrier) or HO-cpt (5 nM) or the prodrug (0.5 μ M). **C:** Quantification of the data shown in **B**. G0G1/(S+G2) - the number of cells in phases G0 and G1 divided by the number of cells in phases S and G2. **D:** The prodrug (20 μ M) and NIRD incubated either with human neutrophils (left image) or human neutrophils pre-incubated with PMA (right image). Combined “Ch1+Ch2” images are shown (Ch1 and Ch2 are defined in inset **A**). Right plot- % dead cells in human neutrophils incubated with the carrier, the prodrug and HO-cpt (both 20 μ M) for 2h. **E:** Monitoring the fluorescence characteristic for PDFPs in immature cells (lineageNEG Sca-1+ c-Kit+ (LSK) and myeloid progenitor (MP) cells) from BM in mice injected i.p. on days 0, 2 and 4 with the prodrug (12 mg/kg). **F:** Monitoring of the number of LSK and MP cells in BM of mice treated as described in **E**. The analysis was conducted on day 7. Paired t-test was conducted between days 0 and 7. *: $p < 0.05$; **: $p < 0.01$; ***: $p < 0.001$.

Effects of the prodrug on neutrophils

We investigated the activation of the prodrug with formation of PDFPs in human neutrophils from healthy individuals. Nuclei of the neutrophils were counter-stained with NIRD (red channel). As shown in Figure 6D (left image), the blue signal is absent in the cells incubated with the prodrug for 2 h indicating that the latter compound remains intact. In contrast, neutrophils primed with phorbol myristate acetate (PMA, 50 nM), inducing H₂O₂ generation, feature the evenly distributed, intense blue signal indicating PDFPs formation (Figure 6D, right image). However, HO-cpt does not seem to be formed under these conditions, since the prodrug does not enhance the PMA toxicity of neutrophils (Figure 6D, right plot). In contrast, HO-cpt is toxic under the same conditions.

Next, we assessed the characteristic for PDFPs fluorescence in neutrophils of blood and bone marrow (BM) as well as in immature BM cells (LineageNEG Sca-1+ c-Kit+ (LSK) and myeloid progenitor (MP) cells) from mice treated with the prodrug. At the early incubation time of 2h, we observed some minor ($p < 0.05$) increase of the fluorescence of blood neutrophils (Figure S40A, S1). The more pronounced fluorescence increase was observed in LSK (2 / 24h incubation) and MP cells (24 h) (Figure 6E). These data indicate formation of PDFPs *in vivo*. However, this does not correlate with a decrease of the number of the corresponding cells in blood and BM (Figures 6F, S40B and C, S1), thereby allowing concluding that toxic drug HO-cpt is not formed at these conditions. Thus, the *in vivo* data are also in agreement with the suggested mechanism of action of the prodrug (Figure 1C).

Antitumor activity of the prodrug in vivo

Encouraged by the excellent *in vitro* properties of the prodrug, we studied its toxicity and antitumor activity *in vivo*. We observed that at doses of 3 to 24 mg/kg (interperitoneal (i.p.) injections on days 0, 2 and 4), it does not affect weight of Balb/c mice in a 7-day experiment (Figure S41, Table S10, S1). On day 7, the animals were sacrificed and their internal organs inspected. We detected no apparent damage (Figure S42, S1). Further, we extracted the prodrug and PDFPs from the organs and measured the fluorescence of the extracts at $\lambda_{\text{ex}} = 365$ nm, $\lambda_{\text{em}} = 450$ nm (parameters characteristic for PDFPs). We observed no fluorescence increase between untreated

and prodrug-treated groups (Figure S43, S1). After the extracts were treated with H₂O₂ to activate the prodrug, significant signals could be detected in extracts from blood ($p < 0.001$), spleen ($p < 0.001$), adipose tissue ($p < 0.01$) and peritoneum ($p < 0.01$) (Figure S44, S1). Thus, the prodrug is accumulated in the mentioned organs, but remains there in the intact state. All these data indicate that at doses ≤ 24 mg/kg, the prodrug does not exhibit acute toxicity. In contrast, at 6 mg/kg, HO-cpt exhibits acute toxicity reflected in its negative effect on weight of mice (Figure 7A). At the dose of 24 mg/kg a precipitate of the prodrug was detected on the surface of internal organs of peritoneal cavity and, locally, near the i.p. injection site. All further experiments were conducted at the highest tested dose, at which no precipitates of the prodrug were detected *in vivo*: 12 mg/kg (Figure S42, S1). We studied the antitumor effect of the prodrug in the Nemeth-Kellner (NK) lymphoma (Ly) NK/Ly model. The prodrug was injected i.p. on days 1, 3, 6, 8, 10, 13, 15, 17 and 20 at the dose of 12 mg/kg. The control group received only the carrier (DMSO). We observed statistically significant ($p < 0.05$) prolongation of mice survival ($t_{1/2}$) in the treated group to 55 days *versus* 33 days in the control group (Figure 7B).

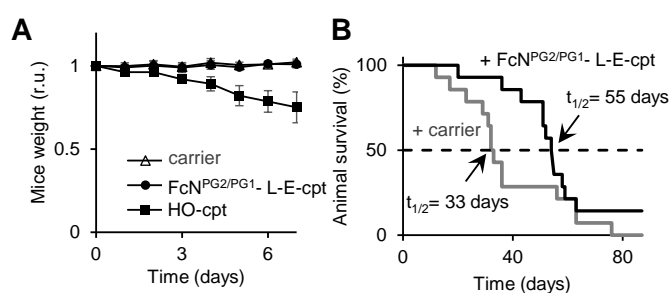


Figure 7. A: Change of weight of wild type mice treated either with DMSO only (carrier: “-”) or the prodrug (12 mg/kg) or drug HO-cpt (6 mg/kg), which were injected i.p. on days 0, 2 and 4. **B:** Effects of the prodrug (12 mg/kg) and the carrier injected i.p. on days 1, 3, 6, 8, 10, 13, 15, 17, 20 and 22 on survival of mice carrying Nemeth-Kellner lymphoma (Kaplan-Meier plot). The prodrug prolongs mice survival from 33 to 55 days ($p < 0.05$).

Conclusion

We developed the dual camptothecin prodrug, which is activated in cancer cells in the presence of H₂O₂ and HO⁻Mit. This mode of action relies on aggregation-derived blocking of the HO⁻Mit-sensitive ester E in the prodrug, which is released by de-aggregation in the presence of H₂O₂. The prodrug discriminates cancer cells from primed (H₂O₂-rich) neutrophils, since the latter cells have the low number of mitochondria and correspondingly lack the HO⁻Mit- trigger. We confirmed the effects in cell free settings. The prodrug exhibits high nM to low μ M anticancer activity towards a variety of cancer cell lines derived from blood, ovary, prostate, tongue and pharynx *in vitro* and towards Nemeth-Kellner lymphoma *in vivo*, but do not induce usual for camptothecins neutropenia both *in vitro* and *in vivo*. We demonstrated that the prodrug concept reported in this paper is not restricted to the derivatives of cpt and can

potentially be applied to other drugs containing the critical for their activity tertiary HO group.

Acknowledgements

We thank German Research Council (DFG) (AM 1418 / 7-2) and European Commission (861878 - NeuroCure) for funding this study. The CNIC is supported by the MCIN and the Pro CNIC Foundation and is a Severo Ochoa Center of Excellence (CEX2020-001041-S). The contribution of DFG to the mass spectrometry unit (timsTOF Pro) is highly appreciated (INST 90/950-1). The authors acknowledge the scientific support and HPC resources provided by the Erlangen National High Performance Computing Center (NHR@FAU) of the Friedrich-Alexander-Universität Erlangen-Nürnberg (FAU). The hardware is funded by the DFG. Open access funding enabled and organized by Projekt DEAL.

References

- [1] a) Y. Pommier, *Nature Cancer Rev.* **2006**, *6*(10), 789-802; b) W. J. Slichenmyer, E. K. Rowinsky, R. C. Donehower, S. H. Kaufmann, *J. Nat. Cancer Institute* **1993**, *85*(4), 271-291.
- [2] J. Chen, Stubbe, J., *Nature Cancer Rev.* **2005**, *5*(2), 102-112.
- [3] D. C. Dale, G. M. McCarter, J. Crawford, G. H. Lyman, *J. Nat. Compr. Cancer Network* **2003**, *1*(3), 440-454.
- [4] a) M. A. Jordan, L. Wilson, *Nature Rev. Cancer* **2004**, *4*(4), 253-265; b) E. K. Rowinsky; R. C. Donehower, *New England J. Med.* **1995**, *332*(15), 1004-1014.
- [5] a) L. Kelland, *Nature Rev. Cancer* **2007**, *7*(8), 573-584; b) R. Oun, Y. Moussa, N. J. Wheate, *Dalton Trans.* **2018**, *47*(19), 6645-6653.
- [6] J. Rautio, H. Kumpulainen, T. Heimbach, R. Oliyai, D. Oh, T. Jaervinen, J. Savolainen, *Nature Rev. Drug. Discovery* **2008**, *7*(3), 255-270.
- [7] a) H.-G. Xu, M. Schikora, M. Sisa, S. Daum, I. Klemm, C. Janko, C. Alexiou, G. Bila, R. Bilyy, W. Gong, M. Schmitt, L. Sellner, A. Mokhir, *Angew. Chem. Int. Ed.* **2021**, *60*, 11158-11162; *Angew. Chem.* **2021**, *133*, 11258-11262; b) V. Reshetnikov, S. Daum, C. Janko, W. Karawacka, R. Tietze, C. Alexiou, S. Paryzhak, T. Dumych, R. Bilyy, P. Tripal, B. Schmid, R. Palmisano, A. Mokhir, *Angew. Chem. Int. Ed.* **2018**, *57*, 11943-11946; *Angew. Chem.* **2018**, *130*, 12119-12122; c) S. Daum, V. Reshetnikov, M. Sisa, T. Dumych, M. D. Lootsik, R. Bilyy, E. Bila, C. Janko, C. Alexiou, M. Herrmann, L. Sellner, A. Mokhir, *Angew. Chem. Int. Ed.* **2017**, *56*, 15545-15549; *Angew. Chem.* **2017**, *129*, 15751-15755.
- [8] a) G. Jaouen, Vessières, S. Top, *Chem. Soc. Rev.* **2015**, *44*, 8802-8817; b) M. F. Renschler, *Eur. J. Cancer* **2004**, *40*, 1934-1940; c) M. Doering, L. A. Ba, N. Lilienthal, C. Nicco, C. Scherer, M. Abbas, A. A. Peer Zada, R. Coriat, T. Burkholz, L. Wessjohann, M. Diederich, F. Batteux, M. Herling, C. Jacob, *J. Med. Chem.* **2010**, *53*, 6954-6963.

- [9] a) D. Hanahan, R. A. Weinberg, *Cell* **2011**, *144*(5), 646-674; b) L. M. Coussens, Z. Werb, *Nature*, **2002**, *420*(6917), 860-867; c) M. Valko, D. Leibfritz, J. Moncol, M. T. D. Cronin, M. Mazur, J. Telser, *Int. J. Biochem. Cell. Biol.* **2006**, *39*(1), 44-84; d) F. Antunes, R. Cadenas, *FEBS Lett.* **2000**, *475*, 121-126; e) T. P. Szatrowski, C. F. Nathan, *Cancer Res.* **1991**, *51*, 794-798.
- [10] K. Matsushita, T. Okuda, S. Mori, M. Konno, H. Eguchi, A. Asai, J. Koseki, Y. Iwagami, D. Yamada, H. Akita, T. Asaoka, T. Noda, K. Kawamoto, K. Gotoh, S. Kobayashi, Y. Kasahara, K. Morihira, T. Satoh, Y. Doki, M. Mori, H. Ishii, S. Obika, *ChemMedChem* **2019**, *14*(15), 1384-1391.
- [11] M. Euler, M. H. Hoffmann, *Biochem. Soc. Trans.* **2019**, *47*(6), 1921-1930.
- [12] N. A. Maianski, J. Geissler, S. M. Srinivasula, E. S. Alnemri, D. Roos, T. W. Kuijpers, *Cell Death Diff.* **2004**, *11*, 143-153.
- [13] a) L. Wang, S. Xie, L. Ma, Y. Chen, W. Lu, *Eur. J. Med. Chem.* **2016**, *116*, 84-89; b) S. Ayyanaar, M. P. Kesavan, G. Sivaraman, R. P. Raja, V. Vijayakumar, J. Rajesh, G. Rajagopal, *J. Drug. Deliv. Sci. Tech.* **2019**, *52*, 722-729; c) T. Zhang, X. Ma, S. Bai, Y. Wang, X. Zhang, Y. Lu, F. Wen, P. Xue, Y. Kang, Z. Xu, *J. Mater. Chem. B* **2020**, *8*, 1245-1255; d) B. Chu, Y. Qu, X. He, Y. Hao, C. Yang, Y. Yang, D. Hu, F. Wang, Zh. Qian, *Adv. Func. Mat.* **2020**, *30*, 2005918; e) X. Luo, X. Chi, Y. Lin, Zh. Yang, H. Lin, J. Gao, *Chem. Comm.* **2021**, *57*, 11033-11036.
- [14] H. Cho, Y.-Y. Cho, M. S. Shim, J. Y. Lee, H. S. Lee, H. C. Kang, *Biochim. Biophys. Acta. – Mol. Basis Dis.* **2020**, *1866*(8), 165808.
- [15] a) Y. Tan, Y. Zhu, Y. Zhao, L. Wen, T. Meng, X. Liu, X. Yang, S. Dai, H. Yuan, F. Hu *Biomaterials* **2018**, *154*, 169-181; b) B.-Y. Liu, X.-L. Yang, X. Xing, J. Li, Y.-H. Liu, N. Wang, X.-Q. Yu, *ACS Macro. Lett.* **2019**, *8*(6), 719-723.
- [16] M. R. Redinbo, L. Stewart, P. Kuhn, J. J. Champoux, W. G. J. Hol, *Science* **1998**, *279*(5356), 1504-1513.
- [17] D. Dvoranová, M. Bobeničová, S. Čoralová, M. Breza, *Chem. Phys. Lett.* **2013**, *580*, 141-144.
- [18] E. Kinski, P. Marzenell, W. Hofer, H. Hagen, J. A. Raskatov, K. X. Knaup, E. M. Zolnhofer, K. Meyer, A. Mokhir, *J. Inorg. Biochem.* **2016**, *160*, 218-224.
- [19] P. Marzenell, H. Hagen, L. Sellner, T. Zenz, R. Grinyte, V. Pavlov, S. Daum, A. Mokhir, *J. Med. Chem.* **2013**, *56*, 6935-6944.
- [20] S. Daum, S. Babiy, H. Konovalova, W. Hofer, A. Shtemenko, N. Shtemenko, C. Janko, C. Alexiou, A. Mokhir, *J. Inorg. Biochem.* **2017**, *178*, 9-17.
- [21] E. I. Azzam, J.-P. Jay-Gerin, D. Pain, *Cancer Lett.* **2012**, *327*(0), 48-60.
- [22] H.-G. Xu, V. Reshetnikov, M. Wondrak, L. Eckardt, L. A. Kunz-Schughart, C. Janko, R. Tietze, C. Alexiou, H. Borchardt, A. Aigner, W. Gong, M. Schmitt, L. Sellner, S. Daum, H. G. Özkan, A. Mokhir, *Cancers* **2022**, *14*(1), 208.
- [23] Y. Mao, I. R. Mehl, M. T. Muller, *Proc. Natl. Acad. Sci.* **2002**, *99*(3), 1235-1240.

4. References

- [1] H. Sung, J. Ferlay, R. L. Siegel, M. Laversanne, I. Soerjomataram, A. Jemal, F. Bray, *CA: a cancer journal for clinicians* **2021**, *71*, 209-249.
- [2] D. L. Stoler, N. Chen, M. Basik, M. S. Kahlenberg, M. A. Rodriguez-Bigas, N. J. Petrelli, G. R. Anderson, *Proceedings of the National Academy of Sciences of the United States of America* **1999**, *96*, 15121-15126.
- [3] D. Hanahan, R. A. Weinberg, *Cell* **2000**, *100*, 57-70.
- [4] C. Donato, L. Kunz, F. Castro-Giner, A. Paasinen-Sohns, K. Strittmatter, B. M. Szczerba, R. Scherrer, N. Di Maggio, W. Heusermann, O. Biehlmaier, C. Beisel, M. Vetter, C. Rochlitz, W. P. Weber, A. Banfi, T. Schroeder, N. Aceto, *Cell reports* **2020**, *32*, 108105.
- [5] R. A. Gatenby, R. J. Gillies, *Nature Reviews Cancer* **2004**, *4*, 891-899.
- [6] X. Xu, P. E. Saw, W. Tao, Y. Li, X. Ji, S. Bhasin, Y. Liu, D. Ayyash, J. Rasmussen, M. Huo, J. Shi, O. C. Farokhzad, *Advanced materials (Deerfield Beach, Fla.)* **2017**, *29*.
- [7] M. Redza-Dutordoir, D. A. Averill-Bates, *Biochimica et Biophysica Acta (BBA) - Molecular Cell Research* **2016**, *1863*, 2977-2992.
- [8] aR. Fato, C. Bergamini, S. Leoni, P. Strocchi, G. Lenaz, *Neurochemical Research* **2008**, *33*, 2487-2501; bL. K. Sharma, J. Lu, Y. Bai, *Current medicinal chemistry* **2009**, *16*, 1266-1277.
- [9] Y. S. Bae, H. Oh, S. G. Rhee, Y. D. Yoo, *Molecules and Cells* **2011**, *32*, 491-509.
- [10] T. Kurz, A. Terman, U. T. Brunk, *Archives of Biochemistry and Biophysics* **2007**, *462*, 220-230.
- [11] S. Kanemura, M. Okumura, K. Yutani, T. Ramming, T. Hikima, C. Appenzeller-Herzog, S. Akiyama, K. Inaba, *The Journal of biological chemistry* **2016**, *291*, 23952-23964.
- [12] J. M. Roscoe, C. S. Sevier, *Cells* **2020**, *9*, 2314.
- [13] aA. Terman, T. Kurz, B. Gustafsson, U. T. Brunk, *IUBMB life* **2006**, *58*, 531-539; bC. Kubota, S. Torii, N. Hou, N. Saito, Y. Yoshimoto, H. Imai, T. Takeuchi, *The Journal of biological chemistry* **2010**, *285*, 667-674.
- [14] Z. Yu, H. L. Persson, J. W. Eaton, U. T. Brunk, *Free radical biology & medicine* **2003**, *34*, 1243-1252.
- [15] H. Sies, V. V. Belousov, N. S. Chandel, M. J. Davies, D. P. Jones, G. E. Mann, M. P. Murphy, M. Yamamoto, C. Winterbourn, *Nature Reviews Molecular Cell Biology* **2022**, *23*, 499-515.
- [16] R. Bennett, B. Demple, **2013**.
- [17] S. Kanvah, J. Joseph, G. B. Schuster, R. N. Barnett, C. L. Cleveland, U. Landman, *Acc Chem Res* **2010**, *43*, 280-287.
- [18] C. A. Juan, J. M. Pérez de la Lastra, F. J. Plou, E. Pérez-Lebeña, *International Journal of Molecular Sciences* **2021**, *22*, 4642.
- [19] D. K. Yadav, S. Kumar, E.-H. Choi, S. Chaudhary, M.-H. Kim, *Scientific Reports* **2019**, *9*, 4496.
- [20] B. Yang, K. L. Fritsche, D. Q. Beversdorf, Z. Gu, J. C. Lee, W. R. Folk, C. M. Greenlief, G. Y. Sun, *Frontiers in Neurology* **2019**, *10*.
- [21] M. Bandoowala, P. Sengupta, *The International journal of neuroscience* **2020**, *130*, 1047-1062.
- [22] E. A. Veal, A. M. Day, B. A. Morgan, *Molecular cell* **2007**, *26*, 1-14.
- [23] J. van der Reest, S. Lilla, L. Zheng, S. Zanivan, E. Gottlieb, *Nature Communications* **2018**, *9*, 1581.
- [24] Y. Li, J. D. Paonessa, Y. Zhang, *PLoS One* **2012**, *7*, e35122.
- [25] M. Sundaresan, Z.-X. Yu, V. J. Ferrans, K. Irani, T. Finkel, *Science* **1995**, *270*, 296-299.
- [26] K. Irani, Y. Xia, J. L. Zweier, S. J. Sollott, C. J. Der, E. R. Fearon, M. Sundaresan, T. Finkel, P. J. Goldschmidt-Clermont, *Science* **1997**, *275*, 1649-1652.

- [27] F. Weinberg, R. Hamanaka, W. W. Wheaton, S. Weinberg, J. Joseph, M. Lopez, B. Kalyanaraman, G. M. Mutlu, G. R. S. Budinger, N. S. Chandel, *Proceedings of the National Academy of Sciences* **2010**, *107*, 8788-8793.
- [28] aM. Krauthammer, Y. Kong, B. H. Ha, P. Evans, A. Bacchicocchi, J. P. McCusker, E. Cheng, M. J. Davis, G. Goh, M. Choi, S. Ariyan, D. Narayan, K. Dutton-Regester, A. Capatana, E. C. Holman, M. Bosenberg, M. Sznol, H. M. Kluger, D. E. Brash, D. F. Stern, M. A. Materin, R. S. Lo, S. Mane, S. Ma, K. K. Kidd, N. K. Hayward, R. P. Lifton, J. Schlessinger, T. J. Boggon, R. Halaban, *Nature Genetics* **2012**, *44*, 1006-1014; bC. Zhou, S. Licciulli, J. L. Avila, M. Cho, S. Troutman, P. Jiang, A. V. Kossenkov, L. C. Showe, Q. Liu, A. Vachani, S. M. Albelda, J. L. Kissil, *Oncogene* **2013**, *32*, 903-909.
- [29] aG. Delaney, S. Jacob, C. Featherstone, M. Barton, *Cancer* **2005**, *104*, 1129-1137; bO. World Health, *Assessing national capacity for the prevention and control of noncommunicable diseases: report of the 2019 global survey*, World Health Organization, Geneva, **2020**.
- [30] M. J. LaRiviere, P. M. G. Santos, C. E. Hill-Kayser, J. M. Metz, *Hematology/oncology clinics of North America* **2019**, *33*, 989-1009.
- [31] X. Deng, H. Wu, F. Gao, Y. Su, Q. Li, S. Liu, J. Cai, *International journal of clinical oncology* **2017**, *22*, 641-650.
- [32] B. Li, H. L. Chan, P. Chen, *Current medicinal chemistry* **2019**, *26*, 3009-3025.
- [33] S. Jin, Y. Sun, X. Liang, X. Gu, J. Ning, Y. Xu, S. Chen, L. Pan, *Signal transduction and targeted therapy* **2022**, *7*, 39.
- [34] A. Mullard, *Nature Reviews Drug Discovery* **2017**, *16*, 669-669.
- [35] Z. S. Guo, *BMC cancer* **2018**, *18*, 1086.
- [36] aA. A. Al-Badr, M. M. Alodhaib, *Profiles of drug substances, excipients, and related methodology* **2016**, *41*, 323-377; bS. Dasari, P. Bernard Tchounwou, *European Journal of Pharmacology* **2014**, *740*, 364-378; cC. Carvalho, R. X. Santos, S. Cardoso, S. Correia, P. J. Oliveira, M. S. Santos, P. I. Moreira, *Current medicinal chemistry* **2009**, *16*, 3267-3285; dS. M. Hecht, *Journal of natural products* **2000**, *63*, 158-168.
- [37] D. B. Longley, D. P. Harkin, P. G. Johnston, *Nature reviews. Cancer* **2003**, *3*, 330-338.
- [38] P. B. Schiff, S. B. Horwitz, *Proceedings of the National Academy of Sciences* **1980**, *77*, 1561-1565.
- [39] Y. Pommier, *Nature reviews. Cancer* **2006**, *6*, 789-802.
- [40] aL. Qi, Q. Luo, Y. Zhang, F. Jia, Y. Zhao, F. Wang, *Chemical research in toxicology* **2019**, *32*, 1469-1486; bW. J. Slichenmyer, E. K. Rowinsky, R. C. Donehower, S. H. Kaufmann, *JNCl: Journal of the National Cancer Institute* **1993**, *85*, 271-291; cD. C. Dale, G. C. McCarter, J. Crawford, G. H. Lyman, *Journal of the National Comprehensive Cancer Network : JNCCN* **2003**, *1*, 440-454.
- [41] A. Ramos, S. Sadeghi, H. Tabatabaeian, *Int J Mol Sci* **2021**, *22*.
- [42] aU. Jungwirth, C. R. Kowol, B. K. Keppler, C. G. Hartinger, W. Berger, P. Heffeter, *Antioxidants & redox signaling* **2011**, *15*, 1085-1127; bB. Rosenberg, *Cancer treatment reports* **1979**, *63*, 1433-1438.
- [43] A. D. Kelman, H. J. Peresie, *Cancer treatment reports* **1979**, *63*, 1445-1452.
- [44] K. L. Haas, K. J. Franz, *Chemical reviews* **2009**, *109*, 4921-4960.
- [45] H. Hagen, P. Marzenell, E. Jentsch, F. Wenz, M. R. Veldwijk, A. Mokhir, *J Med Chem* **2012**, *55*, 924-934.
- [46] D. Wang, Y. Zhang, Q. Guo, *Int J Nanomedicine* **2018**, *13*, 7987-7996.
- [47] L. Feng, Y. Geisselbrecht, S. Blanck, A. Wilbuer, G. E. Atilla-Gokcumen, P. Filippakopoulos, K. Kräling, M. A. Celik, K. Harms, J. Maksimoska, R. Marmorstein, G. Frenking, S. Knapp, L.-O. Essen, E. Meggers, *Journal of the American Chemical Society* **2011**, *133*, 5976-5986.
- [48] aE. I. Edwards, R. Epton, G. Marr, *Journal of Organometallic Chemistry* **1975**, *85*, C23-C25; bR. Rubbiani, O. Blacque, G. Gasser, *Dalton transactions (Cambridge, England : 2003)* **2016**, *45*, 6619-6626.

- [49] Y. Z. Voloshin, O. A. Varzatskii, I. I. Vorontsov, M. Y. Antipin, A. Y. Lebedev, A. S. Belov, N. G. Strizhakova, *Russian Chemical Bulletin* **2004**, *53*, 92-98.
- [50] J. Blechinger, O. A. Varzackii, V. Kovalska, G. E. Zelinskii, Y. Z. Voloshin, E. Kinski, A. Mokhir, *Bioorganic & medicinal chemistry letters* **2016**, *26*, 626-629.
- [51] M. Siepi, J. Politi, P. Dardano, A. Amoresano, L. de Stefano, D. Maria Monti, E. Notomista, *Nanotechnology* **2017**, *28*.
- [52] C. T. Jafvert, P. P. Kulkarni, *Environmental science & technology* **2008**, *42*, 5945-5950.
- [53] B. Abuaita, G. Sule, F. Gao, J. Knight, M. O'Riordan, *The IRE1 α stress signaling axis is a key regulator of neutrophil antimicrobial effector function*, **2019**.
- [54] aH. Dong, S. H. Cheung, Y. Liang, B. Wang, R. Ramalingam, P. Wang, H. Sun, S. H. Cheng, Y. W. Lam, *Electrophoresis* **2013**, *34*, 1957-1964; bJ. Zielonka, J. Joseph, A. Sikora, M. Hardy, O. Ouari, J. Vasquez-Vivar, G. Cheng, M. Lopez, B. Kalyanaraman, *Chemical reviews* **2017**, *117*, 10043-10120; cL. V. Johnson, M. L. Walsh, L. B. Chen, *Proceedings of the National Academy of Sciences of the United States of America* **1980**, *77*, 990-994.
- [55] aM. H. Wright, S. A. Sieber, *Natural product reports* **2016**, *33*, 681-708; bC. G. Parker, M. R. Pratt, *Cell* **2020**, *180*, 605-632.
- [56] aH. S. Walter, S. A. Rule, M. J. Dyer, L. Karlin, C. Jones, B. Cazin, P. Quittet, N. Shah, C. V. Hutchinson, H. Honda, K. Duffy, J. Birkett, V. Jamieson, N. Courtenay-Luck, T. Yoshizawa, J. Sharpe, T. Ohno, S. Abe, A. Nishimura, G. Cartron, F. Morschhauser, C. Fegan, G. Salles, *Blood* **2016**, *127*, 411-419; bT. Barf, T. Covey, R. Izumi, B. van de Kar, M. Gulrajani, B. van Lith, M. van Hoek, E. de Zwart, D. Mittag, D. Demont, S. Verkaik, F. Krantz, P. G. Pearson, R. Ulrich, A. Kaptein, *The Journal of pharmacology and experimental therapeutics* **2017**, *363*, 240-252; cS. H. Watterson, Q. Liu, M. Beaudoin Bertrand, D. G. Batt, L. Li, M. A. Pattoli, S. Skala, L. Cheng, M. T. Obermeier, R. Moore, Z. Yang, R. Vickery, P. A. Elzinga, L. Discenza, C. D'Arienzo, K. M. Gillooly, T. L. Taylor, C. Pulicicchio, Y. Zhang, E. Heimrich, K. W. McIntyre, Q. Ruan, R. A. Westhouse, I. M. Catlett, N. Zheng, C. Chaudhry, J. Dai, M. A. Galella, A. J. Tebben, M. Pokross, J. Li, R. Zhao, D. Smith, R. Rampulla, A. Allentoff, M. A. Wallace, A. Mathur, L. Salter-Cid, J. E. Macor, P. H. Carter, A. Fura, J. R. Burke, J. A. Tino, *J Med Chem* **2019**, *62*, 3228-3250; dJ. C. Henise, J. Taunton, *J Med Chem* **2011**, *54*, 4133-4146; eR. Ding, T. Zhang, D. J. Wilson, J. Xie, J. Williams, Y. Xu, Y. Ye, L. Chen, *J Med Chem* **2019**, *62*, 2814-2829.
- [57] aE. Mons, I. D. C. Jansen, J. Loboda, B. R. van Doodewaerd, J. Hermans, M. Verdoes, C. A. A. van Boeckel, P. A. van Veelen, B. Turk, D. Turk, H. Ovaa, *J Am Chem Soc* **2019**, *141*, 3507-3514; bD. J. Porter, W. G. Chestnut, B. M. Merrill, T. Spector, *The Journal of biological chemistry* **1992**, *267*, 5236-5242; cR. Ekkebus, S. I. van Kasteren, Y. Kulathu, A. Scholten, I. Berlin, P. P. Geurink, A. de Jong, S. Goerdalay, J. Neefjes, A. J. Heck, D. Komander, H. Ovaa, *J Am Chem Soc* **2013**, *135*, 2867-2870; dC. Arkona, J. Rademann, *Angewandte Chemie (International ed. in English)* **2013**, *52*, 8210-8212.
- [58] M. L. Conte, S. Staderini, A. Marra, M. Sanchez-Navarro, B. G. Davis, A. Dondoni, *Chemical Communications* **2011**, *47*, 11086-11088.
- [59] F. Dénès, M. Pichowicz, G. Povie, P. Renaud, *Chemical reviews* **2014**, *114*, 2587-2693.
- [60] M. T. Jeena, S. Kim, S. Jin, J. H. Ryu, *Cancers* **2019**, *12*.
- [61] J. Köckenberger, I. Klemt, C. Sauer, A. Arkhypov, V. Reshetnikov, A. Mokhir, M. R. Heinrich, *Chemistry – A European Journal*, *n/a*, e202301340.
- [62] J. Rautio, J. Kärkkäinen, K. B. Sloan, *European Journal of Pharmaceutical Sciences* **2017**, *109*, 146-161.
- [63] J. E. Hardebo, C. Owman, *Annals of Neurology* **1980**, *8*, 1-11.
- [64] M. Miwa, M. Ura, M. Nishida, N. Sawada, T. Ishikawa, K. Mori, N. Shimma, I. Umeda, H. Ishitsuka, *European journal of cancer (Oxford, England : 1990)* **1998**, *34*, 1274-1281.

- [65] J. L. Major Jourden, S. M. Cohen, *Angewandte Chemie (International ed. in English)* **2010**, *49*, 6795-6797.
- [66] T. Gökirmak, M. Nikan, S. Wiechmann, T. P. Prakash, M. Tanowitz, P. P. Seth, *Trends in Pharmacological Sciences* **2021**, *42*, 588-604.
- [67] A. Liu, C. Liang, J. Liu, Y. Huang, M. Wang, L. Wang, *ACS Applied Materials & Interfaces* **2022**, *14*, 17022-17031.
- [68] M. Jiang, H. Zhuang, R. Xia, L. Gan, Y. Wu, J. Ma, Y. Sun, Z. Zhuang, *Oncotarget* **2017**, *8*, 92106-92118.
- [69] aM. A. Subhan, V. P. Torchilin, *Nanomedicine: Nanotechnology, Biology and Medicine* **2020**, *29*, 102239; bY. Ji, J. Yang, L. Wu, L. Yu, X. Tang, *Angewandte Chemie International Edition* **2016**, *55*, 2152-2156; cA. Meyer, A. Mokhir, *Angewandte Chemie International Edition* **2014**, *53*, 12840-12843; dS. Shah, S. H. Friedman, *Oligonucleotides* **2007**, *17*, 35-43.
- [70] J.-R. Meunier, A. Sarasin, L. Marrot, *Photochemistry and Photobiology* **2002**, *75*, 437-447.
- [71] aK. Athreya, M. F. Xavier, *Nutrition and cancer* **2017**, *69*, 1099-1104; bM. H. Raza, S. Siraj, A. Arshad, U. Waheed, F. Aldakheel, S. Alduraywish, M. Arshad, *Journal of cancer research and clinical oncology* **2017**, *143*, 1789-1809.
- [72] P. Marzenell, H. Hagen, L. Sellner, T. Zenz, R. Grinyte, V. Pavlov, S. Daum, A. Mokhir, *J Med Chem* **2013**, *56*, 6935-6944.
- [73] V. Reshetnikov, H. G. Özkan, S. Daum, C. Janko, C. Alexiou, C. Sauer, M. R. Heinrich, A. Mokhir, *Molecules* **2020**, *25*.
- [74] S. Daum, M. S. V. Reshetnikov, M. Sisa, T. Dumych, M. D. Lootsik, R. Bilyy, E. Bila, C. Janko, C. Alexiou, M. Herrmann, L. Sellner, A. Mokhir, *Angewandte Chemie International Edition* **2017**, *56*, 15545-15549.
- [75] V. Reshetnikov, S. Daum, A. Mokhir, *Chemistry* **2017**, *23*, 5678-5681.
- [76] P. Gao, W. Pan, N. Li, B. Tang, *Chemical Science* **2019**, *10*, 6035-6071.
- [77] G. H. Lyman, E. Abella, R. Pettengell, *Critical reviews in oncology/hematology* **2014**, *90*, 190-199.
- [78] K. Matsushita, T. Okuda, S. Mori, M. Konno, H. Eguchi, A. Asai, J. Koseki, Y. Iwagami, D. Yamada, H. Akita, T. Asaoka, T. Noda, K. Kawamoto, K. Gotoh, S. Kobayashi, Y. Kasahara, K. Morihira, T. Satoh, Y. Doki, M. Mori, H. Ishii, S. Obika, *ChemMedChem* **2019**, *14*, 1384-1391.
- [79] N. A. Maianski, J. Geissler, S. M. Srinivasula, E. S. Alnemri, D. Roos, T. W. Kuijpers, *Cell death and differentiation* **2004**, *11*, 143-153.
- [80] V. Reshetnikov, S. Daum, C. Janko, W. Karawacka, R. Tietze, C. Alexiou, S. Paryzhak, T. Dumych, R. Bilyy, P. Tripal, B. Schmid, R. Palmisano, A. Mokhir, *Angew Chem Int Ed Engl* **2018**, *57*, 11943-11946.